2010

Unzipping Amyloid Fibrils: How a Novel Calcium-Binding Protein, NUCB1, Prevents the Formation of Amyloid Fibrils

Neeraj Kapoor

UNZIPPING AMYLOID FIBRILS

HOW A NOVEL CALCIUM-BINDING PROTEIN, NUCB1, PREVENTS THE FORMATION OF AMYLOID FIBRILS

A Thesis Presented to the Faculty of

The Rockefeller University

In Partial Fulfillment of the Requirements for

the degree of Doctor of Philosophy

by

Neeraj Kapoor

June 2010

UNZIPPING AMYLOID FIBRILS

HOW A NOVEL CALCIUM-BINDING PROTEIN , NUCB1, PREVENTS THE FORMATION OF AMYLOID FIBRILS

Neeraj Kapoor, Ph.D.

The Rockefeller university, 2010

Nucleobindin 1 (NUCB1) is a widely expressed multi-domain Ca^{2+}-binding protein whose precise physiological and biochemical functions are not well understood. We engineered and heterologously expressed a soluble form of NUCB1 (*s*NUCB1) and characterized its biophysical and biochemical properties. We show that *s*NUCB1 exists as a dimer in solution and that each monomer binds two divalent Ca^{2+} cations. Ca^{2+}-binding causes conformational changes in *s*NUCB1 as judged by circular dichroism and fluorescence spectroscopy experiments. Earlier reports suggested that NUCB1 might interact with heterotrimeric G protein α-subunits. We show that dimeric Ca^{2+}-free *s*NUCB1 binds to heterologously expressed $G\alpha_{i1}$ and that Ca^{2+}-binding inhibits this interaction. We further show that the binding of *s*NUCB1 to $G\alpha_{i1}$ inhibits its basal rate of GDP release and slows its rate and extent of GTPγS uptake. We conclude that *s*NUCB1 is a Ca^{2+}-dependent guanine-nucleotide dissociation inhibitor (GDI) for $G\alpha_{i1}$. To our knowledge

*s*NUCB1 is the first example of a calcium-dependent GDI for heterotrimeric G proteins.

In addition, we also established novel and unique anti-amyloidogenic functional ability of *s*NUCB1. We show that Ca^{2+}-free *s*NUCB1 can inhibit fibril formation by highly amyloidogenic human Islet Amyloid PolyPeptide (hIAPP) and Amyloid-β 42 (Aβ42) peptides, as relevant to Type-2 Diabetes and Alzheimer's disease. In addition, we also show that Ca^{2+}-free *s*NUCB1 can effectively dissociate amyloid fibrils formed by both hIAPP and Aβ42. Interestingly, Ca^{2+} disrupts this unique functional ability of *s*NUCB1. In order to circumvent this, we designed and purified a Ca^{2+}-insentive mutant namely *s*NUCB1(tetramutant) that is functionally similar to *s*NUCB1 even in the presence of excess Ca^{2+} in the reaction mixture. Mechanistically, we show that *s*NUCB1 inhibits fibril formation by capping the ends of high molecular mass prefibrillar species. Subsequently, we also isolated a 39-amino-acid long C-terminal (CT) peptide fragment of NUCB1 namely NUCB1(381-419) which, similar to *s*NUCB1, inhibits and disaggregates hIAPP fibrillization. Finally we have also extended this work to other amyloidogenic proteins namely tau K19(C322S), a synthetic construct comprising microtubule binding domain of human tau protein. Specifically, we show that Ca^{2+}-free *s*NUCB1 effectively inhibits amyloid fibril formation by tauK19(C322S).

ACKNOWLEDGEMENTS

A compilation of work presented in this thesis would not have been possible without the experience, hard work and guidance of a number of people. First and foremost, I would like to sincerely thank my thesis advisor Dr Thomas P Sakmar, whose constant encouragement and kind help throughout the course of my thesis work has been instrumental in shaping the overall architecture and progress of the research undertaken. His constant support even while working on subjects orthogonal to the principal scientific realm and interest of the lab has overall made this an immensely intellectually challenging and gratifying experience.

A big proportion of the work presented in this thesis would not have been possible without the overzealous and unrelenting enthusiasm, dedication and attention to detail of my colleague Dr Ruchi Gupta. Her curiosity to understand things at molecular detail have truly been refreshing and a strong inspiration for me. Next, I would like to thank Dr Santosh T Menon, whose guidance and constant help were pivotal towards gradually developing a keen interest in biophysics and biochemistry. In addition to learning biophysical techniques, the Sakmar lab has also provided me with a nice blend and great environment to both learn and utilize cell biology tools. In this regard, I am especially thankful to Dr Pallavi Sachdev for her kind help with patiently teaching me the basics of several important cell biology techniques. I am also particularly thankful to Manija Kazmi who has been great help and resource with several cell and molecular biology tools through the course of my stay in the Sakmar Lab. In addition, I am also thankful to Dr Thomas Huber for guidance and critical analysis with experimental understanding and data interpretation. Finally, in general I would like to personally thank all the members of Sakmar Lab for all their constant help, support and motivation through the course of my thesis work in the Sakmar Lab.

Next, the TEM facility under the electron microscopy resource center at Rockefeller Univerisity has been greatly helpful for our experiments and data analysis. In this regard, I would like to sincerely thank Dr Eleana Sphicas and Dr Kunihiro Uryu for their consistent help and guidance with the usage of the instrument and data analysis. As a long-term collaborator, I am also grateful to Dr Daniel P Raleigh from Stony Brook univeristy for generous supply of purified material and helpful guidance / suggestions through the course of the study.

I am also grateful to my committee members Dr Erec C Stebbins, Dr Tom Muir, Dr David Eliezer and Dr Tadgh P Begley (former member), whose constant help and motivation throughout the course of this work has been an immense source of inspiration and intellectual curiosity. I am also thankful to the training program in chemical biology (TPCB) and David Rockefeller Graduate program at Rockefeller Univerisity for providing me with an opportunity to work in exciting areas of chemical biology at Rockefeller Univerisity.

On a personal note, I would like to present my sincerest gratitude towards my family (especially my mother) and friends, without whose unwavering faith and strong support the accomplishments of this thesis work would not have been possible.

TABLE OF CONTENTS

CHAPTER 3

LIST OF FIGURES

LIST OF ABBREVIATIONS

ADP . . . . . Adenosine di-phosphate

AGS . . . . . Activator of G protein Signaling

Apo E . . . . . Apolipoprotein E

APP . . . . . Amyloid Precursor Protein

ATP . . . . . Adenosine Tri-Phosphate

Aβ . . . . . Amyloid-β

BODIPY 4,4-difluoro-4-bora-3a,4a-diaza-*s*-indacene

cAMP . . . . . cyclic Adenosine Mono Phosphate

CD . . . . . Circular Dichroism

CREB . . . . . CRE Response Element Binding protein

CT . . . . . C-Terminal

DLS . . . . . Dynamic Light Scattering

DMEM . . . . . Dulbecco's modified eagle medium

DMSO . . . . . Dimethyl Sulfoxide

DTT . . . . . Dithiothreitol

EDTA . . . . . Ethylene Diamine Tetraacetic acid

EGTA Ethylene Glycol-bis-(2-aminoethyl)-N,N,N', N'-Tetraacetic acid

ER . . . . . Endoplasmic Reticulum

FRET . . . . . Fluorescence Resonance Energy Transfer

GDI . . . . . Guanine nucleotide Dissociation Inhibitor

GDP . . . . . Guanosine Di-Phosphate

GoLoco . . . . . $G_{i/o}$ Loco

GSH . . . . . Glutathione reduced

GST . . . . . Glutathione S-Transferase

GTPγS . . . . . Guanosine 5'-O-(3-thiotriphosphate)

HFIP . . . . . Hexafluoro Isopropanol

hIAPP . . . . . human Islet Amyloid Polypeptide

HPLC . . . . . High Performance Liquid Chromatography

Hsp . . . . . Heat shock protein

IDE . . . . . Insulin Degrading Enzyme

IPTG . . . . . Isopropylthio-β-D-Galactoside

LC - MS . . . . . Liquid Chromatography Mass Spectroscopy

LDL . . . . . Low Density Lipoprotein

LRP . . . . . Low Density Lipoprotein Related protein

LZ . . . . . Leucine Zipper

MALS . . . . . Multi-Angle Light Scattering

MANT . . . . . 2',3'-O-(N-methyl-anthraniloyl)

MMP . . . . . Matrix MetalloProteinase

MTT 3-(4,5-Dimethyl-2-thiazolyl)-2,5-diphenyl-2H-tetrazolium bromide

MVB . . . . . Multi-Vesicular Body

Nano-Au . . . . . Nano gold maleimide

Ni-NTA . . . . . Nickel Nitrilo Triacetic acid

NT . . . . . N-Terminal

NUCB1 . . . . . Nucleobindin 1

PAGE . . . . . Polyacrylamide gel electrophoresis

PBS . . . . . phosphate buffer saline

PC12 . . . . . Pheochromocytoma 12

PKA . . . . . Protein kinase A

PMSF . . . . . Phenylmethane sulfonyl fluoride

RGS . . . . . Regulator of G protein signaling

SDS . . . . . Sodium dodecyl sulfate

SEC . . . . . Size exclusion chromatography

sHsp . . . . . small heat shock protein

STEM . . . . . Scanning Transmission Electron Microscopy

TCEP . . . . . Tris Carboxyethyl phosphine

TEM . . . . . Transmission Electron Microscopy

Thio-T . . . . . Thioflavin-T

TMV . . . . . Tobacco Mosaic Virus

Tris 2-amino-2-hydroxymethyl-propane-1,3-diol

UA . . . . . Uranyl Acetate

UV. . . . . Ultraviolet

CHAPTER 1

Nucleobindin 1 is a Calcium Regulated Guanine Nucleotide Dissociation Inhibitor of $G\alpha_{i1}$

1.0 INTRODUCTION

Heterotrimeric guanine nucleotide-binding proteins, G proteins, couple to heptahelical cell surface G protein-coupled receptors (GPCRs) and participate in intracellular signaling events. The G protein heterotrimer is composed of the GTPase Gα subunit and the Gβγ heterodimer. Upon ligand-mediated activation, GPCRs catalyze the exchange of GDP for GTP on Gα leading to dissociation of the heterotrimer into Gα•GTP and Gβγ subunits (*1-3*). These individual subunits then regulate downstream signaling cascades involving effector systems like adenylyl cyclases, Ca^{2+} and K^{+} channels, phospholipase C isozymes and cyclic nucleotide phosphodiesterases (*4, 5*). Thereafter, the intrinsic GTPase activity of Gα reverts it back to the GDP-bound state, which can reassociate with Gβγ. This inhibits the interaction of G protein subunits with downstream effectors, which results in turning-off of the signaling pathways. Hence, signaling by heterotrimeric G proteins is directly dependent on the lifetime of the GTP-bound state of Gα. This lifetime is regulated by GTPase accelerating proteins (GAPs), which catalyze the rapid hydrolysis of the Gα bound GTP to GDP and by guanine nucleotide dissociation inhibitors (GDIs), which inhibit the exchange of GDP for GTP in the catalytic pocket of Gα (*6*).

Together, GAPs and GDIs exert a regulatory control on G protein signaling. In recent years, novel interacting partners of heterotrimeric G proteins called the regulators of G protein signaling or RGS proteins have been discovered that possess GAP activity (*7, 8*). Interestingly, RGS12 and RGS14 in addition to functioning as GAPs, can also act as GDIs (*9, 10*). In 1999, Lanier and coworkers used yeast two-hybrid analysis to identify distinct receptor independent activators of G protein signaling or AGS proteins (*11*). Several members of this AGS family (AGS3-6) have been shown to function as GDIs of $G\alpha_i$ subunits (*12*). The observed GDI activity of both AGS and RGS proteins towards $G\alpha_{i/o}$ is attributed to a 19-amino-acid consensus sequence called the GoLoco motif (*9, 13, 14*). Earlier in 1995, in an independent yeast two-hybrid screen, Mochizuki *et al*. established the interaction of a novel Golgi-resident Ca^{2+}-binding protein Nucleobindin 1 or NUCB1, specifically with the heterotrimeric G protein α-subunit, $G\alpha_{i2}$ (*15*). Subsequently, Lin *et al.* demonstrated that NUCB1 interacts exclusively with the adenylyl cyclase inhibitory ($G\alpha_i$) and stimulatory ($G\alpha_s$) classes of $G\alpha$ subunits (*16*). In a recent study it was shown that overexpression of NUCB1 causes redistribution of only the $G\alpha_{i1}$ subunits and not the $G\beta\gamma$ subunits to the plasma membrane and regulated secretion granules (*17*). However, a role of NUCB1 in modulating $G\alpha_{i1}$ activation has not been observed so far.

NUCB1 is a 55 kDa multi-domain Ca^{2+}-binding protein that was first identified as a novel B cell growth and differentiation factor associated with lupus syndrome (*18*). NUCB1 derives its trivial name, Calnuc, from its Ca^{2+}-binding and DNA-binding ability (*19*). The DNA-binding domain of basic residues (172-218) lies at the N-terminus following the signal sequence. The Ca^{2+}-binding domain is at the core of the protein sequence comprising of two EF hand motifs with an intervening acidic region (253-316). The Ca^{2+}-binding domain is followed by a leucine zipper domain (347-389), which has been postulated to induce NUCB1 dimerization (*20*) (Fig.1.1). The C-terminal (CT) region following the leucine zipper domain is predicted to be intrinsically disordered and unstructured (*21*). Intriguingly, NUCB1 is strongly conserved from flies to humans (*22*) and is widely distributed amongst Golgi (*16, 23*), nucleus (*19, 24*), endoplasmic reticulum (*25, 26*) and cytoplasm (*17*). The N-terminal signal sequence of NUCB1 targets it to different membrane compartments and its deletion renders NUCB1 cytosolic.

Recently, Brodeur *et al.* reported the role of NUCB1 in LDLR related protein 9 (LRP9) trafficking where the cytosolic NUCB1 fraction helps in LRP9 endosomal sorting and prevents its delivery to lysosomes (*27*). The ubiquitous expression of NUCB1 in various cell and tissue types results in a diverse interactome comprising interacting partners like G protein α-subunits, cyclooxygenases and amyloid precursor protein (*16, 26-28*).

Several classes of Gα subunits have been shown to interact with NUCB1 (*16, 26-28*). Yeast-two hybrid experiments performed with various deletion constructs of either $G\alpha_{i3}$ or NUCB1 mapped the CT α5 helix domain of G protein and the acidic region of NUCB1 (264-305) to be necessary for interaction (*29*). Immuno-fluorescence based studies showed that NUCB1 and $G\alpha_i$ protein subunits co-localize on the Golgi lumen and regulated secretion granules (*17*). Since Gα subunits are ubiquitously involved in numerous signal transduction pathways in different tissue types, their interaction with NUCB1 might regulate downstream signaling events.

We are interested in understanding the role of α5 helix of G protein α subunits in regulating nucleotide exchange rates (*30-32*). Since the α5 helix of Gα is involved in interaction with NUCB1, we characterized and studied the interaction of NUCB1 with $G\alpha_{i1}$ in detail. In the current study, we present the detailed biophysical and biochemical characterization of the Ca^{2+}-binding ability and oligomeric state of a heterologously expressed N-terminally truncated soluble form of NUCB1, termed *s*NUCB1 (Fig.1.1). We show that *s*NUCB1 binds Ca^{2+} and exists as a dimer in solution. Ca^{2+}-free *s*NUCB1 preferentially binds wild-type (WT) $G\alpha_{i1}$ and inhibits its GDP release as demonstrated by several independent assays. We conclude that *s*NUCB1 serves as a novel Ca^{2+}-regulated GDI

of $G\alpha_{i1}$. Our findings suggest that NUCB1 is involved in regulating cytoplasmic G protein signaling and trafficking.

1.1 MATERIALS AND METHODS

1.1.1 REAGENTS

Guanosine 5'-diphosphate (GDP) sodium salt and guanosine 5'-O-(3-thiotriphosphate) (GTPγS) tetralithium salt were purchased from Sigma-Aldrich (St. Louis, MO). The fluorescent GTPγS analogue, mant (2',3'-O-(N-methyl-anthraniloyl) - GTPγS was purchased from Jena Biosciences (Jena, Germany) whereas BODIPY (4,4-difluoro-4-bora-3a,4a-diaza-*s*-indacene)-FL-GTPγS was purchased from Molecular Probes (Invitrogen). The His_6-tagged truncation and point mutants of *s*NUCB1 were generated by site-directed mutagenesis using the high-fidelity thermostable DNA polymerase *Pfu* (Stratagene, CA). All reagents and chemicals used were of highest available purity.

1.1.2. Heterologous expression of *s*NUCB1 and heterotrimeric G protein α-subunit $G\alpha_{i1}$

The cDNA clones for human NUCB1 and rat $G\alpha_{i1}$ were obtained from ATCC and cDNA.org respectively. DNA fragment for the soluble form of NUCB1 or *s*NUCB1, corresponding to residues 31-461 of the human NUCB1 protein without the N-terminal signal sequence (residues 1-31) was cloned into the pET28a(+) expression vector (Amersham Biosciences). Similarly the DNA fragment corresponding to full-length

WT rat $G\alpha_{i1}$ subunit (residues 1–354) was cloned into the pET28a(+) expression vector. The vector was used to transform BL21 (DE3) cells to express a N-terminal His_6-tag protein containing a PreScission protease site directly after the His_6-tag. The expressed construct for *s*NUCB1 served as a template for introducing site-specific mutations using the Quick Change system (Stratagene, La Jolla, CA) to generate *s*NUCB1(W232A/W333A) or for introducing a missense mutation to generate the truncated version of the protein, namely *s*NUCB1(W333Ter). All proteins were expressed in BL21 (DE3) cells grown in the presence of 50 μg / ml kanamycin. Cells were grown at 37 ^{o}C to A_{600nm} of ~ 0.8 and then induced with 500 μ M isopropylthio-β-D-galactoside (IPTG) (US Biological). Post induction the culture was grown overnight at 17 ^{o}C and subsequently harvested. The resulting pellets were re-suspended in a buffer containing 50 mM Tris-HCl pH 8.0, 150 mM NaCl, 50 mM β-mercaptoethanol, bovine lung aprotinin (20 mg / ml), 2 mM phenylmethane sulfonyl fluoride (PMSF) and complete EDTA-free protease inhibitor cocktail tablets (Roche). Thereafter the cells were lysed and the expressed His_6-tag protein was purified from crude extract by using affinity chromatography using Ni-NTA column pre-equilibrated with buffer A (50 mM Tris, pH 8.0, 150 mM NaCl, 50 mM β-mercaptoethanol) for *s*NUCB1 and its variants and buffer A' (50 mM Tris pH 8.0, 150 mM NaCl, 2 mM $MgCl_2 \bullet 6H_2O$, 10 μM GDP, 50 mM β-mercaptoethanol) for WT $G\alpha_{i1}$. The bound His_6-tag protein was eluted

from the column by using buffer A or buffer A' supplemented with 500 mM imidazole. The His_6-tag was cleaved by a GST-tagged PreScission™ protease, which was subsequently removed from the solution using GSH-Sepharose column chromatography. In order to remove Ca^{2+} from *s*NUCB1 or its variants, the proteins were extensively dialyzed against buffer A supplemented with 5 mM EGTA and 1 mM EDTA, which were also eventually removed through dialysis. Finally, size exclusion chromatography (SEC) was done using Superdex200 26 / 60 HR column equilibrated with buffer S (50 mM Tris, pH 8.0, 150 mM NaCl) for *s*NUCB1 and its variants and equilibrated in buffer S' (50 mM Tris, pH 8.0, 150 mM NaCl, 2 mM $MgCl_2.6H_2O$, 10 μM GDP, 1mM DTT) for WT $G\alpha_{i1}$ to obtain homogenously pure protein. The typical yield for *s*NUCB1 and its variants was ~ 5-7 mg / L and for WT $G\alpha_{i1}$ ~ 12-15 mg / L. The purity of the proteins was assessed by Coomassie brilliant blue staining after the proteins were separated through SDS-PAGE. The purity of all proteins was greater than 95%.

1.1.3 Isothermal Titration Calorimetry (ITC)

ITC was performed at 25 °C (298 K) using a MicroCal VP-ITC (MicroCal, Northhampton, MA) calorimeter. In order to measure quantitatively the binding of Ca^{2+} or WT $G\alpha_{i1}$•GDP to *s*NUCB1, 2 ml of 50 μM *s*NUCB1 (Ca^{2+}-free) and 700 μl of either 500 μM $CaCl_2$•$6H_2O$

(prepared in 50 mM Tris, pH 8.0, 150 mM NaCl) or 600 μM WT $G\alpha_{i1}$•GDP (prepared in 50 mM Tris, pH 8.0, 150 mM NaCl, 2 mM $MgCl_2.6H_2O$, 10 μM GDP, 1 mM TCEP) was used and thoroughly degassed. Contents of the sample cell were stirred continuously at 280 rpm during the experiment. A typical titration of *s*NUCB1 involved 50 injections each of 5 μl of $CaCl_2.6H_2O$ (500 μM) or WT $G\alpha_{i1}$•GDP (600 μM) into a sample cell containing 1.4 ml of *s*NUCB1 (50 μM). The heat of dilution of the titrant ($CaCl_2$•$6H_2O$ or WT $G\alpha_{i1}$•GDP) was subtracted from the titration data for base-line correction. The base line-corrected data were analyzed with MicroCal OriginTM 6.0 software to determine the change in enthalpy (ΔH) and association constant (K_a). Thermal titration data fit showed two-sets of binding sites for Ca^{2+} to *s*NUBC1. Additionally, the data analysis also showed that one WT $G\alpha_{i1}$•GDP subunit interacts with a dimer of Ca^{2+}-free *s*NUCB1. The parameters were calculated based on 3 or more independent titration experiments. Each numerical value reported is the mean ± S.E.M. amongst the independent data sets.

1.1.4 Size Exclusion Chromatography (SEC)

Complex formation between sNUCB1 and WT $G\alpha_{i1}$

Complex formation between *s*NUCB1 and $G\alpha_{i1}$ was monitored using SEC. 150 μM of *s*NUCB1 (- Ca^{2+} / +Ca^{2+}) was incubated with 256 μM

$G\alpha_{i1}$•(GDP / GTPγS) in 20 mM Tris, pH 8.0, 100 mM NaCl, 10 mM $MgCl_2$, 10 μM GDP and 1 mM DTT at 30 ^oC for 20 min with minimal shaking to enable saturation binding. WT $G\alpha_{i1}$ in the GTPγS-bound state was generated by incubating WT $G\alpha_{i1}$•GDP with 5 mM GTPγS for 30 min at 30 ^oC to ensure complete exchange of nucleotide. Further the complete exchange was confirmed by AlF_4^- exchange assay. About 200 μl of the reaction mixture was injected onto a buffer equilibrated Superdex200 10 / 30 GL column attached to AKTA FPLC (GE Healthcare) and run at 4 ^oC. Sample Elution was performed with the incubation buffer at a flow rate of 0.5 ml / min with 0.35 ml fractions collected. Peak fractions were analyzed through SDS-PAGE followed by Coomassie staining to analyze the complex formation.

Estimation of sNUCB1 molecular mass using heavy molecular weight standards

Purified *s*NUCB1 or the heavy molecular weight standards (GE Healthcare) were injected onto a Superdex200 10 / 30 GL column pre-equilibrated with Buffer S and the normalized absorbance of the eluting peak was plotted. A calibration curve of K_{av} $[(V_e-V_o)/(V_c-V_o)]$ vs Log(molecular weight) was plotted, where V_e is the elution volume, V_o is the column void volume corresponding to the elution of Blue Dextran and V_c is the geometric column volume. The data were fit to a straight-line

curve like Y = A + Bx where A = 1.915 and B = 0.311 were obtained from the fit. Therefore for a Y = K_{av} value, the corresponding value of Log(Molecular weight) was obtained to estimate the molecular mass of *s*NUCB1 and *s*NUCB1(W333Ter).

1.1.5 Light Scattering

Multi-angle light scattering (MALS) and Dynamic Light Scattering (DLS)

The light scattering data were collected using a Superdex200 10 / 30 HR SEC column (GE Healthcare, Piscataway, NJ), connected to High Performance Liquid Chromatography System (HPLC), Agilent 1200, (Agilent Technologies, Wilmington, DE) equipped with an autosampler. The elution from SEC was monitored by a photodiode array (PDA) UV / VIS detector (Agilent Technologies, Wilmington, DE), differential refractometer (OPT-Lab rEx Wyatt Corp., Santa Barbara, CA), static and dynamic, multiangle laser light scattering (LS) detector (HELEOS II with QELS capability, Wyatt Corp., Santa Barbara, CA). The SEC-UV / LS / RI system was equilibrated in buffer (50 mM Tris, pH 8.0, 150 mM NaCl) for *s*NUCB1 alone and in buffer (50 mM Tris, pH 8.0, 100 mM NaCl, 10 mM $MgCl_2$, 10 μM GDP, 1 mM DTT) for WT and truncated *s*NUCB1 / G protein complex at the flow rate of 1.0 ml / min. Two software packages were used for data collection and analysis: the Chemstation software

(Agilent Technologies, Wilmington, DE) controlled the HPLC operation and data collection from the multi-wavelength UV/VIS detector, while the ASTRA software (Wyatt Corp., Santa Barbara, CA) collected data from the refractive index (RI) detector and the LS detectors, and recorded the UV trace at 280 nm sent from the PDA detector. The weight-average molecular masses, *Mw*, were determined across the entire elution profile in the intervals of 1 s from static LS measurement using ASTRA software as previously described (*33*). The approach uses a Rayleigh-Debye-Gans light scattering model (equation 1), which relates the amount of scattered light to the concentration and weight average molecular weight of solute and second virial coefficient:

$$\frac{K^* c}{R(\theta)} = \frac{1}{M_w} + 2A_2 c \qquad (1)$$

where, *R(θ)* is the intensity of excess scattered light at angle θ*, c* is the concentration of the solute, *Mw* is the weight average molecular weight of the solute, A_2 is the second virial coefficient, *K** is an optical parameter equal to $4\pi^2 n^2 \frac{(dn/dc)^2}{\lambda_0^4 N_A}$, where *n* is the refractive index, dn / dc is the refractive index increment for the solute, N_A is Avogadro's number, and λ_0 is the wavelength of the scattered light.

DLS measurements were made "on line" at an angle of 100° with a 2 s collection time. Time resolved scatter intensity fluctuations were analyzed using ASTRA Software (Wyatt Corp., Santa Barbara, CA), which implements the cumulants method (*34*) to determine the time dependence of diffusive motion also referred to as the intensity correlation function, *G(T),* (*35*):

$$G(T) = B\{1 + \alpha[\exp(-D_T q^2 t)]^2\} \quad (2)$$

where, B is the average baseline intensity, α is an instrument-specific correction factor, D_T is the concentration-dependent translational diffusion constant of the solute, t is a delay time, and q is the scattering vector equal to $\frac{4\pi n}{\lambda}\sin\theta/2$, where n is the refractive index of the solvent, λ is the wavelength of the scattered light and θ is the scattering angle. Equation 2 describes the relationship between the time dependency of fluctuation in scatter intensity and the translational diffusion coefficient. The value of D_T can be used to estimate the apparent hydrodynamic radius of an equivalent sphere using Stokes-Einstein relationship (equation 3):

$$R_h = \frac{kT}{6\pi\eta D_T} \quad (3)$$

where, k is the Boltzmann constant, T is the absolute temperature, and η is the temperature corrected viscosity of the solution.

Determination of dimerization equilibrium constant from SEC-UV/LS/RI

The concentration dependent changes in the weight-average molar mass (*Mw*) determined for the apex of the eluting peak for *s*NUBC1 were used to determine the dimerization constant. The weight-average molar masses were plotted as a function of protein concentration for *s*NUCB1; error bars represent ± 3 % of *Mw* for concentration above 100 μg / ml; ± 5 % of *Mw* for concentration between 1-100 μg / ml and ± 10 % of *Mw* for concentration below 1 μg / ml. Lines represent the non-linear least-square fits to a monomer-dimer association model for *s*NUCB1 dimerization.

Determination of K_d of complex formation from SEC-UV / LS / RI

The concentration dependent changes in the weight average molar mass (*Mw*) determined for the apex of the eluting peak were used to determine the complexation of $G\alpha_{i1}$ with *s*NUCB1 / *s*NUCB1(W333Ter). The weight-average molar mass values were plotted as a function of total protein concentration for complexation; error bars represent ± 3 % of *Mw* for concentration above 100 μg / ml; ± 5 % of *Mw* for concentration between 1-100 μg / ml and ± 10 % of *Mw* for concentration below 1 μg / ml. Lines represent the non-linear least-square fits to a stimulated complexation model using Origin 6.0.

1.1.6 Steady State Fluorescence Spectroscopy

Steady-state Trp fluorescence upon Ca^{2+}-binding

Steady-state fluorescence measurements for *s*NUCB1 were carried out in a SPEX τ3 spectrofluorimeter (Jobin-Yvon Instruments, NJ) at 25 °C. The excitation wavelength was set at 295 nm, while emission spectra were collected from 310 nm to 460 nm. The excitation and emission slit widths were 2.5 nm and 5.0 nm, respectively. 178 nM of Ca^{2+}-free *s*NUCB1 equilibrated in buffer containing 50 mM Tris, pH 8.0, 100 mM NaCl was incubated with increasing concentrations of Ca^{2+} with constant stirring for 5 min. Thereafter, Trp emission fluorescence spectra were collected for each concentration of Ca^{2+} added.

Quenching of tryptophan fluorescence by small molecule quenchers

The excitation wavelength was set at 295 nm and the emission spectra were collected from 315-460 nm with the excitation slit and emission slit width being 2.5 nm and 5 nm, respectively. 333 nM of protein was equilibrated in buffer containing 50 mM Tris, pH 8.0 and 100 mM NaCl. In order to study the interaction between the protein and the quenchers, small aliquots of the quenchers were added incrementally from a concentrated stock solution. In the case of potassium iodide, a small quantity of $Na_2S_2O_3$ (0.1 mM) was added to prevent it from forming free

triiodide (I_3^-). The accessibility of Trp was monitored by analyzing the quenching data using Stern-Volmer equation (equation 4):

$$F_0 / F = 1 + K_{SV} [Q] \quad (4)$$

Where F_0 and F are the fluorescence intensities in the absence and presence of quenchers respectively, [Q] is the concentration of the quenching molecules and K_{SV} is the Stern-Volmer quenching constant. In the case of purely collisional quenching mechanism, the Stern-Volmer plot of F_0 / F versus [Q] is linear with a slope equal to K_{SV}.

Fluorescence-based mant-GTPγS (mGTPγS) binding assays

Steady-state fluorescence measurements experiments were carried out in a SPEX τ3 spectrofluorimeter (Jobin-Yvon Instruments, NJ) at 25 °C. 15 μM of WT $G\alpha_{i1}$ was incubated with 50 μM of *s*NUCB1(W232A/W333A) in the reaction buffer (50 mM Tris-HCl, pH 8.0, 150 mM NaCl, 2 mM $MgCl_2$ and 1 mM DTT) for 5 min with constant stirring. Thereafter, mGTPγS (15 μM) was added to the reaction mixture. FRET was monitored by exciting the intrinsic Trp fluorescence at 295 nm and measuring the fluorescence emission from 310 nm to 540 nm. In all cases, blank spectra containing buffer with *s*NUCB1(W232A/W333A) alone were subtracted from the final spectra.

1.1.7 Time based fluorescence spectroscopy

Time-based fluorescence measurements were performed in a SPEX Fluorolog-2 spectrofluorometer (SPEX Industries, Edison, NJ) at 25^{o}C. The excitation wavelength was set at 295 nm specifically for Trp residues, while emission wavelength was set at 340 nm. The excitation and emission slit width were 5 nm each.

AlF_4^- uptake assay

WT $G\alpha_{i1}$ was incubated at 25^{o}C in reaction buffer K (50 mM Tris-HCl, pH 8.0, 150 mM NaCl, 2 mM $MgCl_2$ and 1 mM DTT) with increasing amounts of *s*NUCB1(W232A/W333A) for 10 mins with constant stirring. Thereafter for AlF_4^- dependent activation of $G\alpha_{i1}$, a premixed solution of $AlCl_3^-$ (20 mM) and NaF (1 M), respectively, was injected at 180 s. A time course of enhancement in Trp fluorescence coupled to activation was monitored in the presence of increasing concentrations of *s*NUCB1(W232A/W333A) in the reaction mixture.

GTPγS nucleotide exchange assay

WT $G\alpha_{i1}$ was incubated at 25 ^{o}C with increasing concentration of *s*NUCB1(W232A/W333A) in reaction buffer K for 10 min with constant stirring. The base line fluorescence was monitored for 200 s after which

GTPγS (20 μM) was injected into the reaction mixture and the relative increase in intrinsic Trp fluorescence (λ_{ex} = 295 nm, λ_{em} = 340 nm) was measured as a function of time for each concentration of *s*NUCB1(W232A/W333A).

BODIPY-FL-GTPγS nucleotide exchange assay

WT $G\alpha_{i1}$ (20 μM) was incubated at 25°C in reaction buffer K with increasing concentration of Ca^{2+}-free *s*NUCB1 for 10 min with constant stirring. BODIPY -FL-GTPγS (20 μM) was added to the reaction mixture and the relative increase in intrinsic fluorescence (λ_{ex} = 485 nm, λ_{em} = 512 nm) was measured for each concentration of Ca^{2+}-free *s*NUCB1 as a function of time.

BODIPY FL-GTPγS nucleotide binding assay

WT $G\alpha_{i1}$ (20 μM) was incubated alone and with Ca^{2+}-free *s*NUCB1 (100 μM) at room temperature in reaction buffer K. 10 μl samples were withdrawn from each reaction mixture at various time points and loaded onto a pre-equilibrated Zeba™ micro-desalt spin columns to remove the unbound nucleotide. The columns were spun at 1000 g for 1 min and the flowthrough collected. The amount of bound nucleotide in each flowthrough was measured by using BODIPY absorbance at 504 nm (ε =

80,000 M^{-1} cm^{-1}). The absorbance at 280 nm was also monitored to ensure that the same amount of protein was being collected in each flowthrough sample.

1.1.8 Circular Dichroism (CD) Spectroscopy

Wavelength scan: All CD experiments were performed using an Aviv 62A DS CD spectrophotometer. Far-UV CD spectra were recorded at the end of each kinetic run. Spectra were recorded over the wavelength range of 190-250 nm at 1 nm intervals with an averaging time of 3 s using a 0.1 cm path length cell. Background spectrum was subtracted from each of the collected data sets. Each spectrum obtained was an average of 3 scans. The recorded spectra in millidegrees of ellipticity was converted to mean residue ellipticity in $deg.cm^2dmol^{-1}$ using the following equation (equation 5):

$$[\theta] = \frac{\theta}{10 \times c \times l \times n} \tag{5}$$

where [θ] is the mean residue ellipticity in $deg_*cm^2dmol^{-1}$, θ is the ellipticity in mdeg, c is the concentration in M, l is the path length in cm and n is the number of peptide bonds.

***Thermal unfolding*:** The unfolding of the protein (8 μM) with temperature was monitored using CD at a wavelength of 222 nm, which is characteristic of an α-helix. The data points were averaged over 30 s for every unit increment in temperature. A plot of CD signal versus temperature was fit to the equation (equation 6):

$$f(T) = \frac{\alpha_N + \beta_N \times T + (\alpha_D + \beta_D \times T) \bullet e^{\frac{-\Delta G^o_{D-N}(T)}{RT}}}{1 + e^{\frac{-\Delta G^o_{D-N}(T)}{RT}}} \qquad (6)$$

where,

$$-\Delta G^o_{D-N}(T) = -\Delta H^o_{D-N}(T_m) * (1 - \frac{T}{T_m}) - \Delta C^o_p * \{(T_m - T) + T * \ln\frac{T}{T_m}\}$$

f(T) is the signal as a function of temperature, T is the temperature, R is the gas constant, α_N defines the intercept and β_N is the slope of the post-transition region of the curve, α_D defines the intercept and β_D is the slope of the pre-transition region of the curve, ΔG^o is the free energy change for the unfolding reaction, $\Delta H^o_{D\text{-}N}$ is the change in enthalpy for unfolding at the T_m and $\Delta C_p{}^o$ is the change in heat capacity. Using the above expressions, T_m, the mid-point transition temperature was estimated along with the change in enthalpy $\Delta H^o_{D\text{-}N}$, for the unfolding reaction at that T_m.

1.1.9 Radioligand [GTPγ^{35}S] based nucleotide-exchange assay

The effect of Ca^{2+}-free *s*NUCB1 or Ca^{2+}-free *s*NUCB1(W333Ter) binding to WT $G\alpha_{i1}$•GDP on the nucleotide exchange was monitored using [^{35}S]GTPγS exchange assay. 20 µM WT $G\alpha_{i1}$•GDP alone or with 100 µM of Ca^{2+}-free *s*NUCB1 / *s*NUCB1(W333Ter) was incubated in Buffer (10 mM Tris pH 7.5, 100 mM NaCl, 2 mM $MgCl_2$, 2 mM DTT) for 20 min at 30 ^{o}C. After incubation, [^{35}S]GTPγS solution diluted with GTPγS was added to the reaction mixtures such that the final GTPγS concentration in each reaction mixture was 100 µM with an associated radioactivity of 50 nCi / 8 µl of reaction volume. Thereafter 8 µl samples (50 nC_i) were withdrawn from each reaction mixture and added to Buffer equilibrated nitrocellulose filters. Subsequently, the filters were extensively washed with Wash Buffer (50 mM Tris pH 7.5, 5 mM $MgCl_2$) to remove excess radioligand. For data analysis the counts were recorded and the value for buffer alone was subtracted from each reading. Each individual data point was scaled to the value of radioactivity within 8 µl of reaction volume to get the pmoles of radioligand bound to WT $G\alpha_{i1}$ in each reaction. As a positive control, the CT GoLoco motif peptide from RGS14 namely R14GL(496-531) was used in an identical experimental setup.

1.1.10 Analytical UltraCentrifugation (AUC)

Sedimentation equilibrium studies were carried out at different centrifugal speeds and protein concentrations for *s*NUCB1 and *s*NUCB1(W333Ter). AUC experiments for *s*NUCB1 (- / $+Ca^{2+}$) were done at 25^{o}C with protein concentrations of 50 μM, 100 μM and 150 μM each at speeds of 20,000 rpm, 30,000 rpm and 40,000 rpm. Similarly for *s*NUCB1(W333Ter), AUC experiments were done with 32 μM, 70 μM and 150 μM protein concentrations each at speeds of 25,000 rpm, 30,000 rpm and 40,000 rpm. The individual protein samples were run for sufficiently long periods of time to allow for the equilibrium to generate a time invariant concentration gradient balanced by diffusion of the macromolecular species. The speeds were decided based on the molecular weight of the protein. Under no net transport conditions, the following correlation should be observed between concentration and the radial distance (*36*) (equation 7):

$$C_r = C_{r_o} * e^{\frac{(\sigma * r)}{2}(r^2 - r_o^2)} \tag{7}$$

where,

$$\sigma = M(1 - \nu\rho) * \frac{\omega^2}{RT}$$

Cr is the concentration of macrosolute at any radial distance r, Cr_o is the concentration of the macrosolute at the reference radial distance r_0, ν is the partial specific volume, ω is the angular velocity, ρ is the density, R is the

gas constant, T is the absolute temperature and M is the molecular mass. The data were analyzed using Optima^{TM} XL-A/XL-I Data Analysis Software (Beckman, 2001).

1.2 RESULTS

1.2.1 Ca^{2+}-binding to EF hand domains of *s*NUCB1 induces conformational changes

A soluble form of NUCB1 namely *s*NUCB1 was engineered, expressed in *E.coli* and purified to homogeneity (Figs. 1.1, 1.2A). The domain architecture of *s*NUCB1 shows two EF hand Ca^{2+}-binding regions sandwiched between a N-terminal DNA binding domain and a CT leucine zipper (*20*). The thermodynamics of Ca^{2+}-binding to *s*NUCB1 were studied using Isothermal Titration Calorimetry (ITC). The Ca^{2+} binding was exothermic with $\Delta H_1° = -2.1 \pm 0.06$ kcal mol^{-1} and $\Delta S_1° = 16.5$ cal mol^{-1} K^{-1} for the first EF hand and $\Delta H_2° = -0.62 \pm 0.31$ kcal mol^{-1} and $\Delta S_2° = 17.1$ cal mol^{-1} K^{-1} for Ca^{2+} binding to the second EF hand, suggesting a spontaneous uptake of Ca^{2+} by Ca^{2+}-free *s*NUCB1. The recorded data were best fit to a "two-set of binding sites" model giving K_d values of 6.3 μM and 73.5 μM for Ca^{2+}-binding (Fig. 1.2B). The difference in binding affinities arises due to the presence of a non-canonical Arg residue substituting for the canonical Gly at the sixth position of the 12-residue Ca^{2+}-binding loop of the second EF hand. Our results show that the two EF hands in *s*NUCB1 bind to Ca^{2+} differentially with an order of magnitude difference in their K_d values. In 2004, de Alba *et al.* heterologously expressed and purified only the EF hand domain (228-326) of NUCB1 and also reported two Ca^{2+}-binding sites with different affinities (*21*).

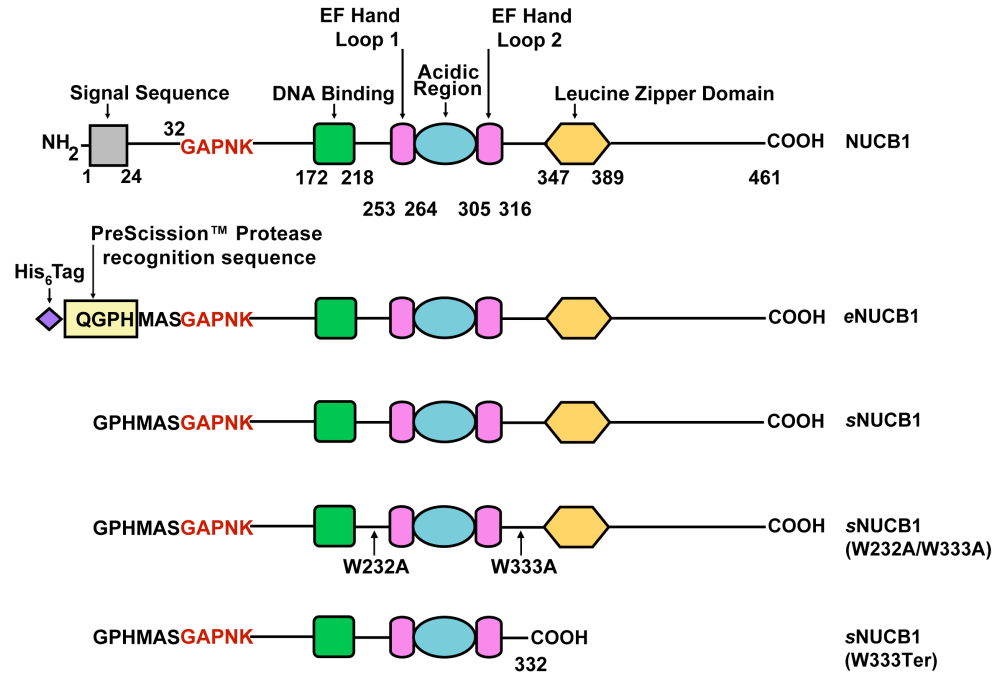

Figure 1.1. Domain architecture of human NUCB1 and engineered NUCB1 variants **(A)** The modular nature of the NUCB1 protein structure is depicted schematically with its N-terminal signal sequence (grey square), putative DNA binding domain (green square), two EF hand loops (magenta rectangles), acidic region (blue oval) and leucine zipper domain (yellow hexagon). The amino acid residues at domain borders are numbered. We engineered a construct for expression in *E. coli* of a soluble form of NUCB1 that included an N-terminal hexa-His tag and a PreScission protease recognition sequence with an intervening spacer sequence as shown. Endoprotease cleavage yields a soluble form of NUCB1 that begins with the amino acid sequence GPHMAS and continues with the remainder of the native sequence beginning at Gly32. We refer to this expressed protein construct as soluble NUCB1 or *s*NUCB1 throughout the text. We also constructed a Trp double-replacement mutant *s*NUCB1(W232A/W333A) and a truncation mutant *s*NUCB1(W333Ter) as shown.

The EF hand regions undergo conformational changes upon Ca^{2+}-binding, which can be monitored through change in intrinsic Trp fluorescence of *s*NUCB1. *s*NUCB1 has two Trp residues at position 232 and 333 lying sequentially before and after the EF hand domain, respectively. Steady-state fluorescence measurements show a blue shift of 15 nm and an enhancement in fluorescence intensity as more Ca^{2+} was added to Ca^{2+}-free *s*NUCB1 (Fig. 1.2C). Thus, Ca^{2+}-binding causes a conformational change in *s*NUCB1 causing reorientation of the Trp residues from a solvent exposed polar to a hydrophobic environment. Fluorescence quenching experiments with acrylamide and iodide were performed to probe these conformational changes around the Trp residues upon Ca^{2+} binding. Acrylamide is a diffusible neutral quencher of Trp fluorescence unaffected by the charges surrounding the fluorophore. I^-, on the other hand, is an anionic quencher for surface exposed fluorophores only (*37*). Quenching experiments show that Trp residues are more accessible to acrylamide than I^- for quenching. On binding to Ca^{2+}, acrylamide quenching decreases much more than I^- quenching (Fig. 1.2D). F_0 / F *vs* quencher concentration gave a straight-line indicative of a dynamic quenching rather than static quenching. These observations suggest that conformational changes associated with Ca^{2+}-binding make Trp residues less accessible by reorienting them into a hydrophobic environment.

Figure 1.2. Purification and effect of Ca^{2+}-binding to *s*NUCB1. (A) The SDS-PAGE analysis of *s*NUCB1 shows a single band after final step of purification. The protein band migrates at ~ 51 kDa. *s*NUCB1 possesses two Ca^{2+}-binding EF hand motifs. **(B)** We used isothermal titration calorimetry (ITC) to measure the Ca^{2+} binding affinity of *s*NUCB1. *s*NUCB1 presumably binds one Ca^{2+} cation at each of its two EF hand domains and a non-linear least squares fit of the calculated values using the "two-set of sites" model resulted in an excellent fit as shown in the *inset*. The calculated dissociation constants for Ca^{2+}-binding to the two EF hand domains of *s*NUCB1 are 6.3 ± 0.18 μM and 73.5 ± 0.19 μM. **(C)** Ca^{2+}-free *s*NUCB1 was used for determining the conformational changes associated with Ca^{2+}-binding to *s*NUCB1. 178 nM *s*NUCB1 was titrated with increasing amounts of Ca^{2+} while fluorescence emission was collected from 310 to 460 nm with the excitation set at 295 nm. Black trace indicates Ca^{2+}-free *s*NUCB1, while the red, green, navy blue, yellow, light blue and pink traces represent 1 mM, 2 mM, 5 mM, 7 mM, 10 mM and 15 mM Ca^{2+} added to the protein solution. Inset: Change in the fluorescence intensity is indicated by black circles, while the red circles indicate the blue shift of the Trp fluorescence. With increasing concentration of Ca^{2+}, the emission intensity enhanced by 50%, while there was a 15 nm blue shift on binding to Ca^{2+} to *s*NUCB1 indicative of the movement of Trp residues from a polar environment to a non-polar, hydrophobic region. **(D)** We measured the accessibility of Trp residues of *s*NUCB1 to small molecule quenchers, acrylamide and iodide, in the presence and absence of Ca^{2+}. Steady-state fluorescence measurements were done at 25 °C with the excitation at 295 nm, while the emission spectra were collected from 315 nm to 460 nm. Stern-Volmer plot was calculated by taking the emission maxima at 330 nm. The top panel shows the quenching of *s*NUCB1 Trp residues in the presence (black trace) and absence (red trace) of Ca^{2+}. The bottom panel shows quenching of *s*NUCB1 Trp residues by ionic quencher iodide in the presence (black

trace) and absence (red trace) of Ca^{2+}. F_o / F vs quencher concentration gave a straight line indicative of a dynamic quenching rather than static quenching. The quenching by acrylamide both in the presence and absence of Ca^{2+} was larger than the iodide showing that the two Trp residues are in different environments. Ca^{2+}-binding to *s*NUCB1 caused a considerably greater decrease in the observed acrylamide quenching relative to iodide. This shows that the conformational change associated with Ca^{2+}-binding reorients the Trp residues in an environment inaccessible to either quencher.

Figure 1.2

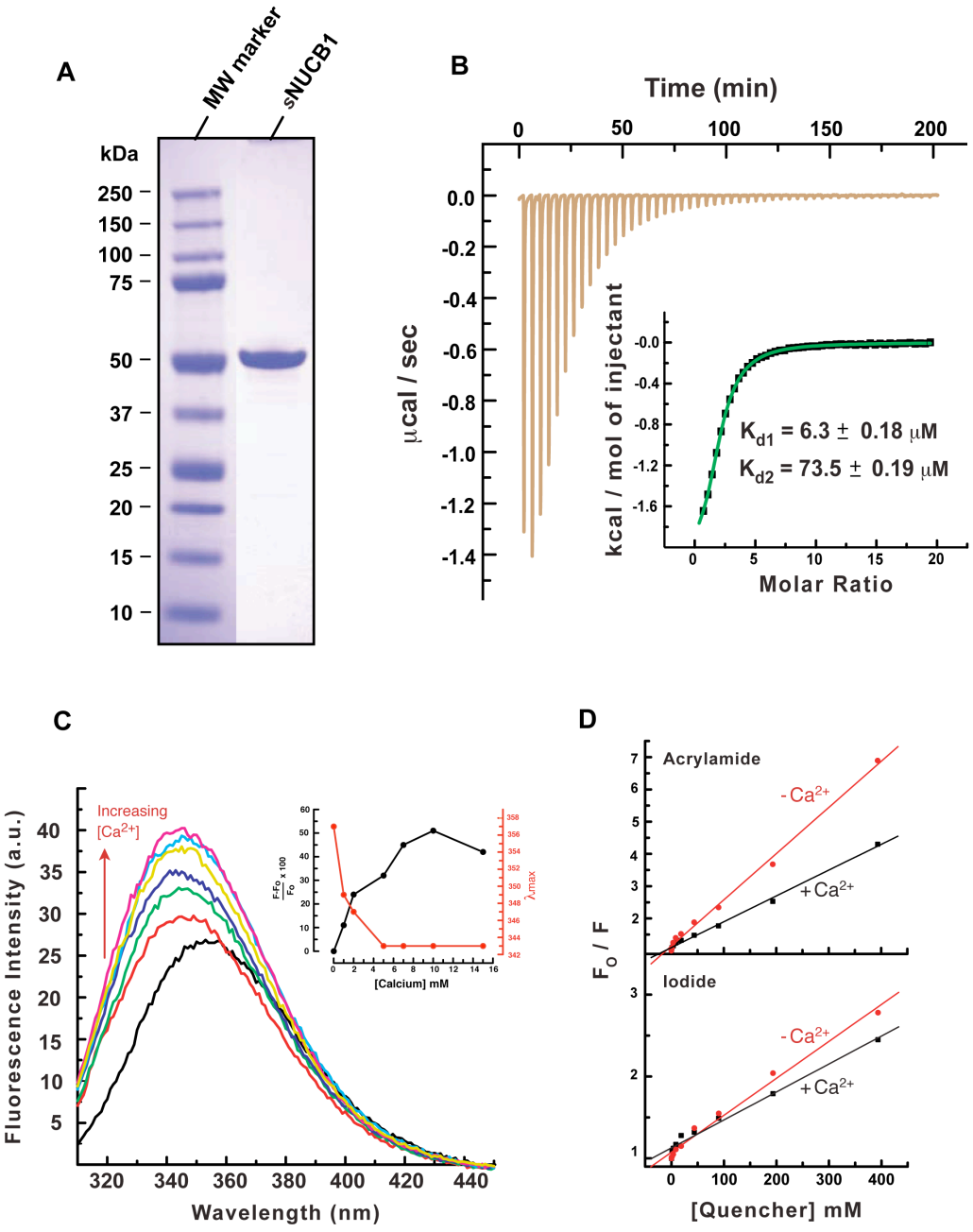
A
MW marker
sNUCB1
kDa
250
150
100
75
50
37
25
20
15
10
B
Time (min)
0
50
100
150
200
0.0
-0.2
-0.4
-0.6
-0.8
-1.0
-1.2
-1.4
µcal / sec
kcal / mol of injectant
-0.0
-0.4
-0.8
-1.2
-1.6
0
5
10
15
20
Molar Ratio
K_{d1} = 6.3 ± 0.18 µM
K_{d2} = 73.5 ± 0.19 µM
C
Increasing
[Ca2+]
Fluorescence Intensity (a.u.)
40
35
30
25
20
15
10
5
320
340
360
380
400
420
440
Wavelength (nm)
[Calcium] mM
λmax
D
Acrylamide
-Ca2+
+Ca2+
Iodide
-Ca2+
+Ca2+
Fo / F
[Quencher] mM

The binding of Ca^{2+} to an EF hand motif forms an octahedral co-ordination sphere, which can cause structural rearrangement in the protein (*38*). This secondary structural change can in principle be followed by circular dichroism (CD) spectroscopy. Ca^{2+}-binding to *s*NUCB1 causes only a slight increase in helicity. Intriguingly, the far-UV CD spectra of *s*NUCB1 show a smooth structural transition from an α-helical secondary structure at lower concentrations to a predominant β-sheet structure at higher concentrations. These concentration-dependent structural changes were observed both in the absence and presence of Ca^{2+} (Fig. 1.3A). Furthermore, the thermal unfolding data for *s*NUCB1 showed an increase in apparent T_m of 4 ^oC on binding to Ca^{2+}. The folding of *s*NUCB1 was observed to be non-cooperative and irreversible both in the absence and presence of Ca^{2+} (Fig. 1.3B). The increase in stabilization on binding to Ca^{2+} suggests a structural ordering of *s*NUCB1.

1.2.2 NUCB1 is a dimer

The domain diagram of NUCB1 reveals the presence of a CT-domain leucine zipper, which is a canonical structural motif known to cause dimerization (*39*) (Fig. 1.1). The oligomeric state of NUCB1 was evaluated through sedimentation equilibrium experiments using Analytical Ultra-Centrifugation (AUC). This experiment is insensitive to the shape of the molecule, and directly reports on the molar mass of the sedimenting

Figure 1.3. Secondary structure transition in *s*NUCB1 (- / + Ca^{2+}) with increasing concentration. Far-UV circular dichroism spectra of **(A)** Ca^{2+}-free or **(B)** Ca^{2+}-bound *s*NUCB1 were collected with increasing concentration. At lower concentrations, i.e. 4 μM (red), 8 μM (green), 16 μM (yellow) and 24 μM (blue), CD spectra show that *s*NUCB1 is mainly helical. At 32 μM (pink), the CD spectrum shows a reduction in the helical content. Higher concentrations of *s*NUCB1, i.e. 40 μM (cyan), 50 μM (brown) and 64 μM (orange), show primarily β-sheet secondary structure. We also monitored thermal unfolding of *s*NUCB1. **(B)** Thermal unfolding transitions of recombinant Ca^{2+}-free (*top*) and Ca^{2+}-bound (*bottom*) *s*NUCB1 (8 μM) were monitored by recording CD signal at 222 nm at a heating rate of 1 ^{o}C / min. The trace is indicative of a multistep non-cooperatively folded protein. The T_m for the Ca^{2+}-bound sNUCB1 is higher than T_m for the Ca^{2+}-free protein, indicating the enhanced stability of the protein in the Ca^{2+}-bound state. **(C)** The CD spectrum for *s*NUCB1(W333Ter) at 50 μM concentration displays a majorly helical secondary structure. In each experiment, the spectrum for buffer (50 mM Tris pH 8.0, 150 mM NaCl) alone was subtracted from each of the spectra.

Figure 1.3

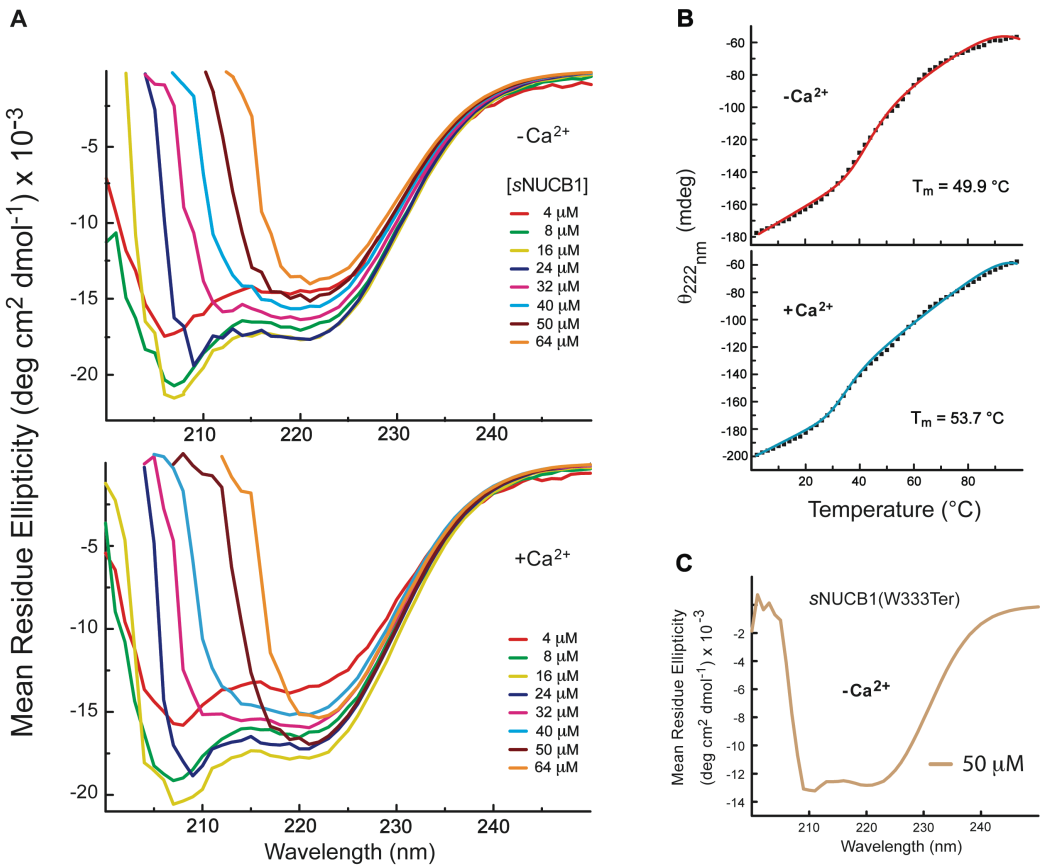
A
Mean Residue Ellipticity (deg cm2 dmol-1) x 10-3
-Ca2+
[sNUCB1]
4 µM
8 µM
16 µM
24 µM
32 µM
40 µM
50 µM
64 µM
+Ca2+
Wavelength (nm)
B
θ222nm (mdeg)
-Ca2+
Tm = 49.9 °C
+Ca2+
Tm = 53.7 °C
Temperature (°C)
C
sNUCB1(W333Ter)
-Ca2+
50 µM
Mean Residue Ellipticity (deg cm2 dmol-1) x 10-3
Wavelength (nm)

species characterized by Boltzmann distribution. Sedimentation equilibrium measurements were performed with Ca^{2+}-free *s*NUCB1 for concentrations varying from 50 μM to 150 μM. The data could be well fit to a monomer-Nmer model, which gave a molecular mass of ~100 kDa corresponding to a dimer of *s*NUCB1 in solution (Fig. 1.4A). AUC analysis of Ca^{2+}-bound *s*NUCB1 indicated that it is also primarily dimeric in solution (Fig. 1.4A, inset). In order to confirm that the dimerization of *s*NUCB1 is caused by the leucine zipper domain, a CT truncation mutant, *s*NUCB1(W333Ter), lacking the leucine zipper was designed and heterologously expressed. The far-UV CD spectrum of *s*NUCB1(W333Ter) showed an α-helical secondary structure even at high protein concentrations in contrast to the concentration dependent transition observed for *s*NUCB1 (Fig.1.3C). AUC analysis of *s*NUCB1(W333Ter) revealed a monomeric species in solution over the concentration range of 32μM to 150μM (Fig. 1.4B). Similar to *s*NUCB1, the association state of *s*NUCB1(W333Ter) was unaffected upon binding to Ca^{2+}. The experiments with the truncation mutant confirm that the leucine zipper domain of *s*NUCB1 is essential for the dimeric state of the protein in solution.

The thermodynamics of the dimerization of *s*NUCB1 was further investigated using Multi-Angle Light Scattering (MALS). In a series of size-exclusion chromatography (SEC) experiments, Ca^{2+}-free *s*NUCB1

was analyzed by gel filtration using a Superdex 200 10/30 HR column. The eluted protein peak was fractionated and subjected to MALS analysis at seven different angles to estimate the molecular mass of the eluting species. As shown in Fig.1.4C, a gradual increase in the weight-average molecular mass of the eluting species was observed with increasing concentration of the protein. At concentrations around 10 nM, *s*NUCB1 exists as a monomer. As the concentration is gradually increased, a monomer-dimer equilibrium is observed with dimeric *s*NUCB1 dominating at concentrations greater than 1μM. The data collected at different angles for each run were fit to a monomer-dimer equilibrium model giving a dissociation constant, K_d of dimerization, for *s*NUCB1 of 0.26 ± 0.12 μM. *s*NUCB1(W333Ter) in MALS measurements continued to exist as a monomer even at high protein concentrations. Thus the leucine zipper region is responsible for the dimeric state of *s*NUCB1 in solution under physiological conditions.

1.2.3 *s*NUCB1 is structurally asymmetric with an elongated CT

Ca^{2+}-free *s*NUCB1 in SEC experiments elutes at a much higher volume than a globular protein with molecular mass similar to that of a *s*NUCB1 monomer or a dimer (Fig. 1.4D). A plot of the elution parameter, K_{av}, vs log(molecular mass) for a number of globular protein standards was utilized to estimate an apparent molecular mass of 300 kDa for *s*NUCB1

Figure 1.4. *s*NUCB1 forms a stable non-globular dimer mediated by its leucine zipper domain. (A) We carried out analytical ultracentrifugation (AUC) experiments to determine the oligomeric state of *s*NUCB1 in solution. The sedimentation equilibrium plot for Ca^{2+}-free *s*NUCB1 (50 μM monomeric concentration) shows the evolution of a sample concentration curve resulting from the applied centrifugal force. The data were fit to a monomer-Nmer equilibrium model, which gave a measured molecular mass of 98.9 ± 0.41 kDa, consistent with a dimeric structure for *s*NUCB1 in solution (the theoretical molecular mass of monomeric *s*NUCB1 is ~51 kDa). The inset shows the sedimentation equilibrium plot for Ca^{2+}-bound *s*NUCB1, which gave essentially an identical molecular mass of 99.4 ± 0.78 kDa. Thereafter, **(B)** AUC experiments were carried out on the truncation mutant, *s*NUCB1(W333Ter), which lacked the Leucine zipper domain in the C-terminal region of the protein. The AUC sedimentation equilibrium plot for Ca^{2+}-free *s*NUCB1(W333Ter) (70 μM monomeric concentration) gave a molecular mass of 35.2 ± 0.05 kDa, consistent with a monomeric species in solution (the theoretical molecular mass of *s*NUCB1(W333Ter) is ~36.8 kDa). **(C)** We studied the monomer-dimer equilibrium of *s*NUCB1 with multi-angle light scattering (MALS) of fractions with increasing protein concentration collected from Superdex200 10/30 HR size exclusion chromatography in 50 mM Tris-HCl (pH 8.0), 150 mM NaCl. The weight-average molecular mass of the complex at a given protein concentration was determined from a non-linear least-square fit of a collection of values determined for the apex fractions of each eluting peak. A monomer-dimer association model of the values as a function of *s*NUCB1 concentration gave an apparent dissociation constant (K_d) for dimerization of 0.26 ± 0.12 μM. The error bars indicate the extent of variation in molecular mass determination originating from the light scattering measurement. **(D)** SEC of *s*NUCB1, heavy molecular weight standards along with known globular proteins was done using a Superdex200 10/30 HR column. Proteins were

individually injected onto the column and the elution profile for each protein was recorded as a function of elution volume. The void volume (V_o) of the column was derived from the elution of Blue Dextran, whereas elution volume (V_e) for each protein was obtained from the corresponding peak for each sample. In order to estimate the molecular mass of *s*NUCB1 and *s*NUCB1(W333Ter), a calibration curve was prepared by plotting K_{av} $[(V_e-V_o)/(V_c-V_o)]$ vs Log(molecular weight) where V_c is the geometric volume of the column. The data were fit to a linear equation. The estimated molecular mass of *s*NUCB1 and *s*NUCB1(W333Ter) were obtained from the plot by using their corresponding K_{av} values. The estimated masses suggest that *s*NUCB1 has a non-globular structure due to which it elutes at a higher volume compared to globular proteins of similar masses. We next measured dynamic light scattering (DLS) chromatograms for **(E)** *s*NUCB1 and **(F)** *s*NUCB1(W333Ter). Each protein sample was injected onto a Superdex200 10/30 HR column and the refractive index detector was used to analyze the protein peak. The change in refractive index as a function of protein concentration was used to compute the molecular mass as shown in green for *s*NUCB1 and red for *s*NUCB1(W333Ter). The molecular mass corresponds to a dimer for *s*NUCB1 and a monomer for *s*NUCB1(W333Ter). The insets show the correlation functions as each protein diffuses through the solution in the DLS experiment. The diffusion coefficient from the correlation function gives the hydrodynamic radius (R_h) using Stokes equation. The computed R_h values were 6.2 nm and 3.03 nm for *s*NUCB1 and *s*NUCB1(W333Ter), respectively.

Figure 1.4

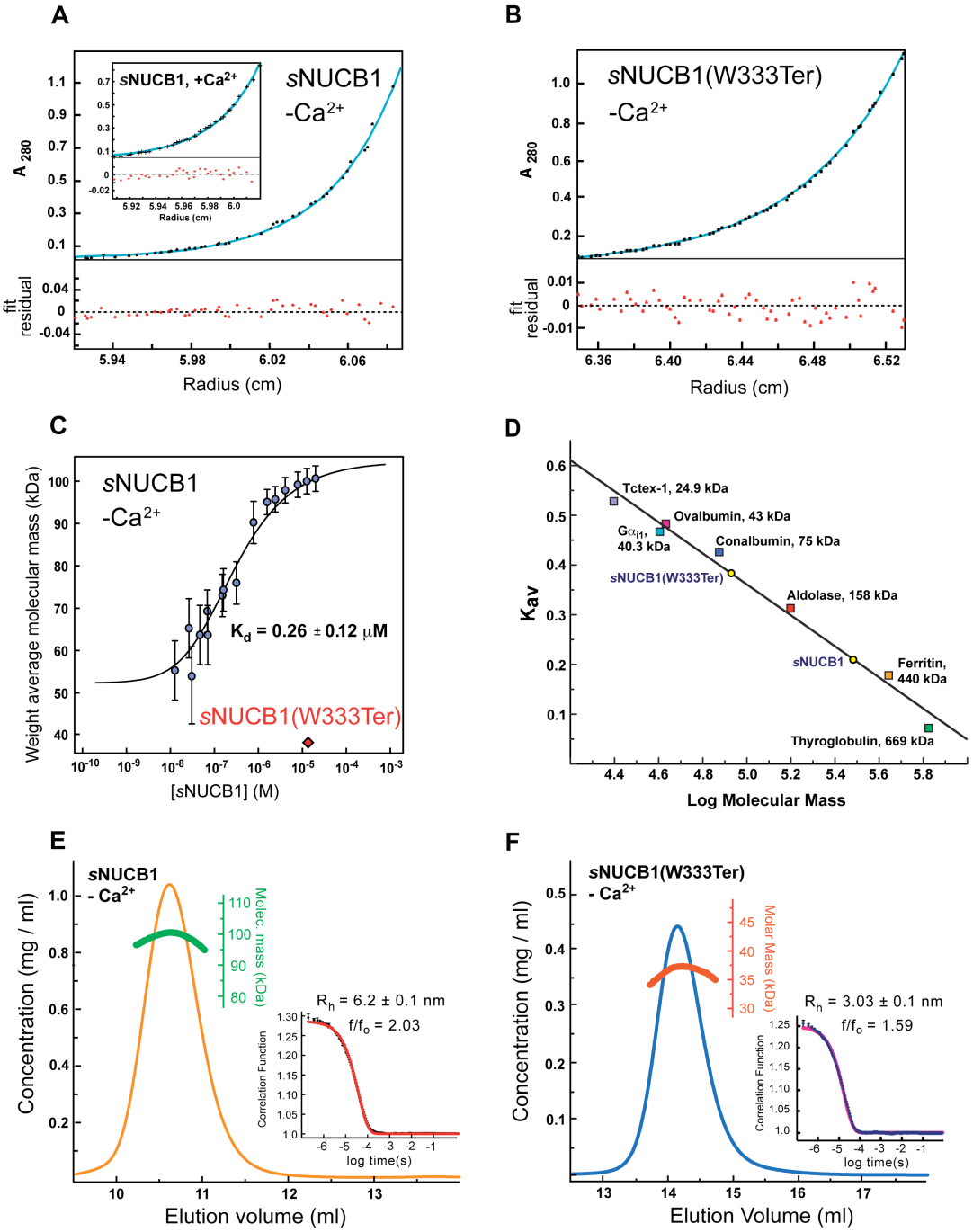
A
sNUCB1, +Ca2+
sNUCB1
-Ca2+
A 280
fit residual
Radius (cm)
B
sNUCB1(W333Ter)
-Ca2+
A 280
fit residual
Radius (cm)
C
sNUCB1
-Ca2+
Kd = 0.26 ± 0.12 μM
sNUCB1(W333Ter)
Weight average molecular mass (kDa)
[sNUCB1] (M)
D
Tctex-1, 24.9 kDa
Ovalbumin, 43 kDa
Gαi1, 40.3 kDa
Conalbumin, 75 kDa
sNUCB1(W333Ter)
Aldolase, 158 kDa
sNUCB1
Ferritin, 440 kDa
Thyroglobulin, 669 kDa
Kav
Log Molecular Mass
E
sNUCB1
- Ca2+
Molec mass (kDa)
Rh = 6.2 ± 0.1 nm
f/fo = 2.03
Correlation Function
log time(s)
Concentration (mg / ml)
Elution volume (ml)
F
sNUCB1(W333Ter)
- Ca2+
Molar Mass (kDa)
Rh = 3.03 ± 0.1 nm
f/fo = 1.59
Correlation Function
log time(s)
Concentration (mg / ml)
Elution Volume (ml)

(Fig.1.4D). This implies that either *s*NUCB1 exists as a trimer of dimers (3 x 100 kDa) or is asymmetric in its shape. Since AUC and MALS analysis convincingly ruled out any association of *s*NUCB1 dimers into higher order structures, we proceeded to derive structural information on *s*NUCB1 through Dynamic Light Scattering (DLS). DLS analysis of Ca^{2+}-free *s*NUCB1 yields a hydrodynamic radius (R_h) of 6.2 nm and a frictional coefficient (f/f_o) of 2.03 (Fig.1.4E). The frictional coefficient of globular proteins usually lies in the range of 1.1 - 1.25 (*40*). A value of 2.03 for *s*NUCB1 indicates an asymmetric shape for the dimer, deviating considerably from a sphere. Interestingly, Ca^{2+}-free *s*NUCB1(W333Ter) has a R_h of 3.3 nm and a f/f_o of 1.59 showing that the deletion of CT domain reduces the radius of hydration by almost 50% (Fig. 1.4F). This suggests that while the N-terminus of *s*NUCB1 is relatively more compact and globular, the CT domain of the protein is elongated, contributing to the observed asymmetry in the shape of *s*NUCB1.

1.2.4 *s*NUCB1 selectively interacts with GDP-bound WT $G\alpha_{i1}$ in the absence of Ca^{2+}

NUCB1 is a Ca^{2+}-binding protein that has been shown to interact with G_i and G_s classes of α-subunits (*16*). Physiologically, Gα subunits can individually exist both in the "inactive" or GDP-bound state and the "active" or GTP-bound state. To investigate the interaction of *s*NUCB1

with WT $G\alpha_{i1}$, *s*NUCB1 was incubated with WT $G\alpha_{i1}$•GDP (Fig. 1.5, top left) and WT $G\alpha_{i1}$•GTPγS (Fig. 1.5, top right), respectively, and the complex formation was analyzed by SEC using a Superdex200 10/30 HR column. As shown in the top panels of Fig. 1.5, the Coomassie stained gels of the fractionated peaks show elution of the complex containing both *s*NUCB1 and $G\alpha_{i1}$ with excess $G\alpha_{i1}$ fractionating at higher elution volume. The amount of $G\alpha_{i1}$ eluting with *s*NUCB1 was significantly higher when $G\alpha_{i1}$ was present in the GDP-bound state rather than in the GTPγS-bound state. Thus Ca^{2+}-free *s*NUCB1 preferentially interacts with $G\alpha_{i1}$ in the GDP-bound form. Interestingly, the interaction with $G\alpha_{i1}$ in both the GDP- and GTPγS-bound states is absent when *s*NUCB1 is bound to Ca^{2+} as shown in the lower panels of Fig. 1.5. The two protein subunits elute out as individual components as the complex is disrupted in the presence of Ca^{2+}. The inhibition of the complex formation between *s*NUCB1 and $G\alpha_{i1}$ in the presence of Ca^{2+} can be explained by the structural rearrangement of EF hands upon Ca^{2+}-binding. Yeast two-hybrid analysis for interaction of Gα with deletion mutants of NUCB1 as bait proposed the EF hand intervening acidic region of NUCB1 to be involved in G protein binding (*16*). The conformational change induced upon Ca^{2+}-binding can possibly result in the masking of the acidic region sandwiched between the two EF hands, thereby making it inaccessible for G protein binding.

The thermodynamics of Ca^{2+}-free *s*NUCB1 complex formation with $G\alpha_{i1}$•GDP was investigated using ITC. The exothermic nature of the reaction shows a thermodynamically favorable binding event between the two protein subunits with ΔH^o = -1.45 ± 0.17 kcal mol^{-1} and ΔS^o = 16.9 cal mol^{-1} K^{-1}. The data were best fit to a "one-set of binding sites" model with dimeric *s*NUCB1 and monomeric G protein as the interacting partners. The fit provides a K_d value of 18.3 ± 1.45 μM suggesting that *s*NUCB1 interacts relatively weakly with GDP-bound $G\alpha_{i1}$ (Fig.1.6A). The association between Ca^{2+}-free *s*NUCB1 and $G\alpha_{i1}$•GDP was also monitored using light scattering. Protein samples with increasing concentrations of *s*NUCB1-$G\alpha_{i1}$•GDP complex were injected onto a Superdex200 10/30 HR column and MALS was done on the complex elution peak. The analysis shows that binding of $G\alpha_{i1}$•GDP to *s*NUCB1 initiates only after dimerization of Ca^{2+}-free *s*NUCB1. At lower concentrations, dimerization of *s*NUCB1 from molecular mass of 50 kDa to 100 kDa was traced. Once the dimer was formed, binding of one $G\alpha_{i1}$•GDP subunit to *s*NUCB1 was evident from increase in molecular mass to 140 kDa (Fig.1.6B). The trace observed for *s*NUCB1-$G\alpha_{i1}$•GDP complex formation can be understood from the experimental K_d values. The K_d for *s*NUCB1 dimerization is much smaller than K_d for binding to $G\alpha_{i1}$•GDP, resulting in *s*NUCB1 dimerization prior to $G\alpha_{i1}$•GDP binding. However *s*NUCB1-$G\alpha_{i1}$•GDP association curve does not rule out the ability of *s*NUCB1 monomer to interact with $G\alpha_{i1}$•GDP.

Figure 1.5. *s*NUCB1 forms a stable complex with $G\alpha_{i1}$•GDP only in the absence of Ca^{2+}. We used size-exclusion chromatography to determine the nature of the interaction between *s*NUCB1 and $G\alpha_{i1}$ in solution under several conditions. *s*NUCB1 and $G\alpha_{i1}$•GDP were incubated together in the absence (*upper left*), or presence (*lower left*) of Ca^{2+} and the mixture was subjected to size-exclusion chromatography using a Superdex200 10/30 HR column. Peak fractions were analyzed by SDS-PAGE with Coomassie-brilliant blue staining as shown in the insets. In the absence of Ca^{2+}, *s*NUCB1 and $G\alpha_{i1}$•GDP formed a complex as judged by (i) the slight shift (from approximately 11.2 ml to 10.6 ml) and enhancement of the peak containing only *s*NUCB1 in the presence of Ca^{2+}, and both *s*NUCB1 and $G\alpha_{i1}$, in the absence of Ca^{2+}, and (ii) the depletion, in the absence of Ca^{2+}, of the peak eluting at about 14.6 ml, which contained only $G\alpha_{i1}$. The same experiment was repeated with *s*NUCB1 and $G\alpha_{i1}$•GTPγS in the absence (*upper right*), or presence (*lower right*) of Ca^{2+}. Although the same general trend and Ca^{2+} dependency were observed, the apparent ability of $G\alpha_{i1}$•GTPγS to form a stable complex with *s*NUCB1 was markedly diminished compared to that of $G\alpha_{i1}$•GDP.

Figure 1.5

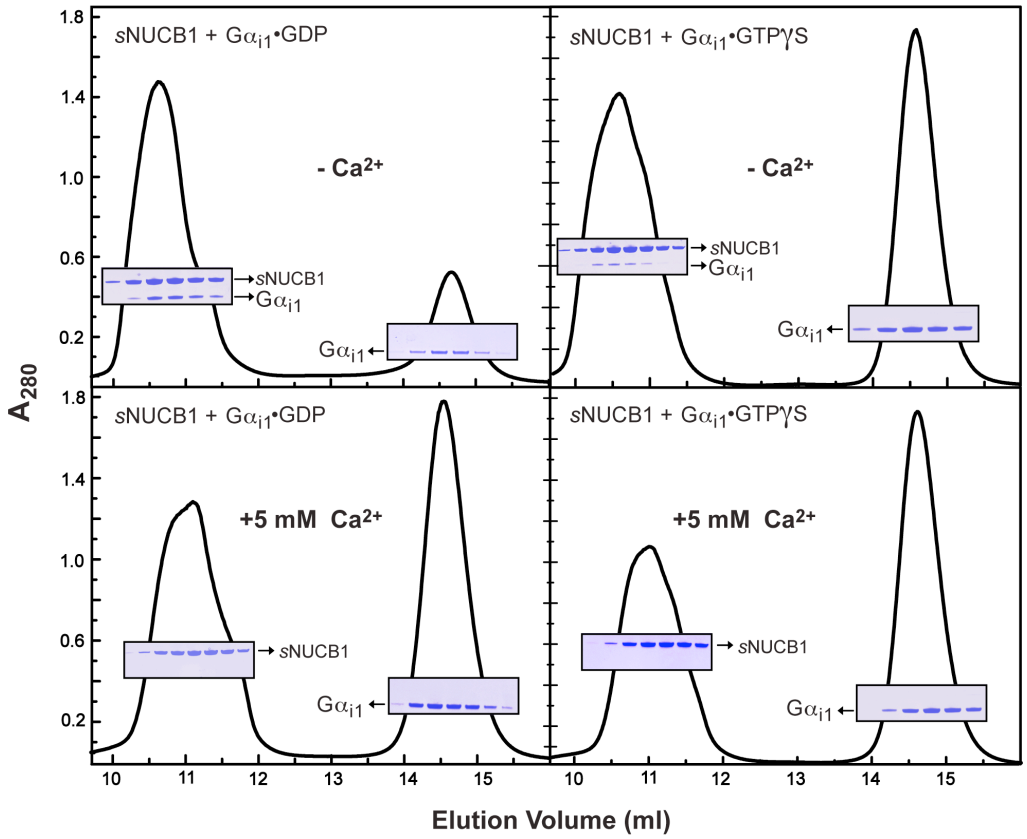
sNUCB1 + Gαi1•GDP
- Ca2+
sNUCB1
Gαi1
Gαi1
sNUCB1 + Gαi1•GTPγS
- Ca2+
sNUCB1
Gαi1
Gαi1
sNUCB1 + Gαi1•GDP
+5 mM Ca2+
sNUCB1
Gαi1
sNUCB1 + Gαi1•GTPγS
+5 mM Ca2+
sNUCB1
Gαi1
A280
Elution Volume (ml)

MALS experiments were also conducted with the monomeric truncation mutant *s*NUCB1(W333Ter). A plot of the weight-average molecular mass obtained from light scattering plotted vs the protein concentration shows that monomeric Ca^{2+}-free *s*NUCB1(W333Ter) forms a 1:1 complex with $G\alpha_{i1}$•GDP. The fit yields a K_d value of 1.99 ± 0.26 μM showing that the interaction of *s*NUCB1 with WT $G\alpha_{i1}$•GDP becomes stronger on deletion of the CT region of *s*NUCB1 (Fig.1.6C). This suggests that the CT region of *s*NUCB1 possibly acts as a regulatory domain modulating the interaction of *s*NUCB1 with G protein α-subunit. Alternatively, the structural rearrangement associated with dimerization can also result in the reduced affinity of *s*NUCB1 for $G\alpha_{i1}$ in comparison with *s*NUCB1(W333Ter).

1.2.5 *s*NUCB1 affects nucleotide-exchange by WT $G\alpha_{i1}$•GDP

GPCRs activate heterotrimeric G proteins by catalyzing the exchange of GTP for GDP on Gα subunits. The receptor facilitates the nucleotide exchange by using the CT-linked α5 helix of Gα subunits. The α5 helix region is postulated to be a molecular micro domain on Gα that allosterically couples the activation signal from the receptor to the catalytic pocket of G proteins (*30, 31, 41, 42*). Farquhar and coworkers have

Figure 1.6. Interaction of *s*NUCB1 and $G\alpha_{i1}$•GDP. **(A)** We used ITC to measure the binding of Ca^{2+}-free *s*NUCB1 to $G\alpha_{i1}$•GDP. The heat released per injection of aliquots of a solution of $G\alpha_{i1}$•GDP (200 μM) into a buffered solution of Ca^{2+}-free *s*NUCB1 (50 μM) was recorded and the area under the curve was integrated. The heat of dilution for the addition of $G\alpha_{i1}$•GDP to buffer alone was subtracted. A non-linear least squares fit of the calculated values using the "one-set of sites" model for dimeric *s*NUCB1 resulted in a satisfactory fit with a dissociation constant of 18.3 ± 1.45 μM as shown in the *inset*. We used multi-angle light scattering (MALS) to measure the formation of a complex between **(B)** *s*NUCB1 and $G\alpha_{i1}$•GDP or **(C)** the truncation mutant *s*NUCB1(W333Ter) and $G\alpha_{i1}$•GDP. MALS data were collected on protein complex peaks eluting from Superdex200 10/30 HR size exclusion chromatography connected to a high performance liquid chromatography system equipped with an autosampler. Samples with increasing protein concentrations were successively injected onto the column, and the eluate was monitored using a photo-diode UV/Vis detector, a differential refractometer, and a static multi-angle laser light scattering detector. The weight-average molecular mass of the complex was determined as a function of increasing protein concentration. The magenta curve in **(B)** inset and the red curve in **(C)** indicate non-linear least-square fits for a complex formation model of weight average molecular mass values determined for the apex of each eluting peak at various concentrations. The error bars indicate extent of variation in molecular mass determination originating from the light-scattering measurement. The data for *s*NUCB1-$G\alpha_{i1}$•GDP complex formation shows that association between the protein subunits occurs only after dimerization of *s*NUCB1 (blue curve). The data suggest that one $G\alpha_{i1}$ subunit binds to a dimer of *s*NUCB1 and a monomer of *s*NUCB1(W333Ter), respectively, and that the binding site for $G\alpha_{i1}$ lies in the *s*NUCB1(W333Ter) sequence.

Figure 1.6

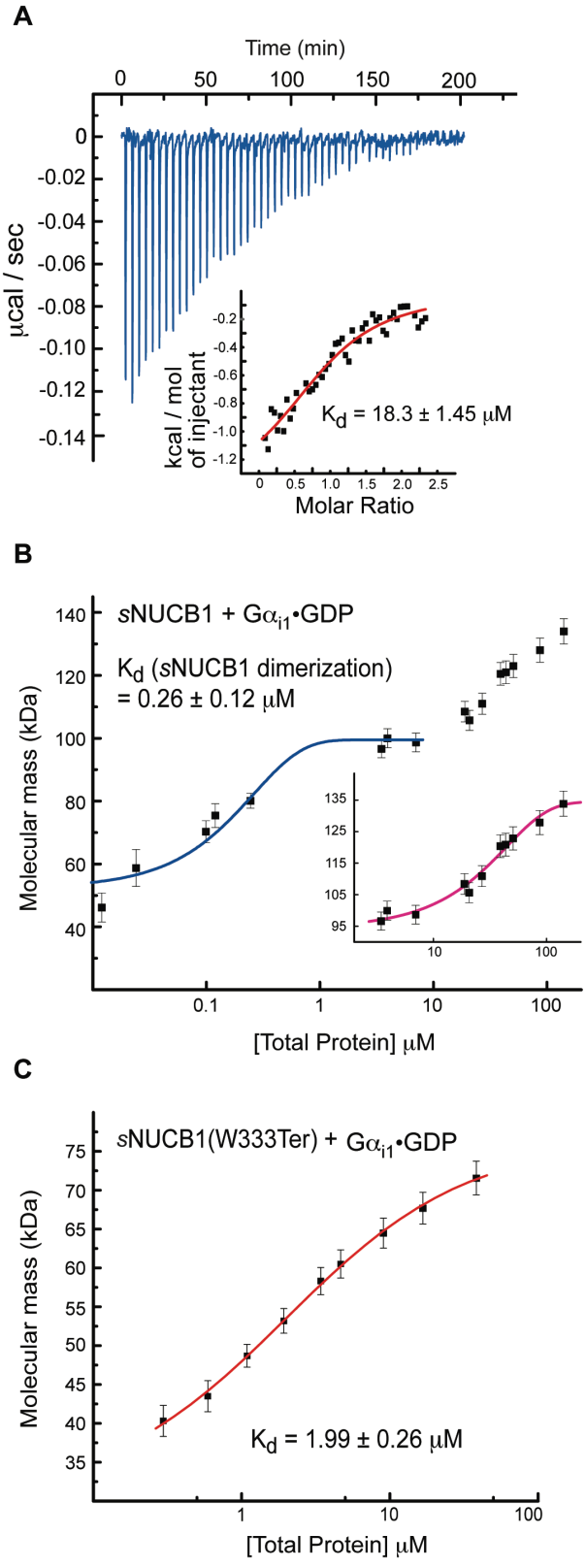
A
Time (min)
0
50
100
150
200
0
-0.02
-0.04
-0.06
-0.08
-0.10
-0.12
-0.14
µcal / sec
kcal / mol of injectant
-0.2
-0.4
-0.6
-0.8
-1.0
-1.2
0
0.5
1.0
1.5
2.0
2.5
Molar Ratio
Kd = 18.3 ± 1.45 µM
B
sNUCB1 + Gαi1•GDP
Kd (sNUCB1 dimerization)
= 0.26 ± 0.12 µM
Molecular mass (kDa)
140
120
100
80
60
40
135
125
115
105
95
10
100
0.1
1
10
100
[Total Protein] µM
C
sNUCB1(W333Ter) + Gαi1•GDP
Molecular mass (kDa)
75
70
65
60
55
50
45
40
35
Kd = 1.99 ± 0.26 µM
1
10
100
[Total Protein] µM

shown that NUCB1 possibly interacts with the CT α5 helix region of $G\alpha_{i3}$ (*29*). Thus, we measured the nucleotide exchange on Gα in the presence of Ca^{2+}-free *s*NUCB1. The concentrations of both *s*NUCB1 and $G\alpha_{i1}$ were kept above the determined K_d for *s*NUCB1-$G\alpha_{i1}$ complex formation. Steady-state and time-based fluorescence experiments were performed by monitoring the enhancement in Trp fluorescence, which is coupled to activation of $G\alpha_{i1}$. Any potential contribution from the Trp residues of *s*NUCB1 was eliminated by mutating both W232 and W333 to Ala, thereby generating *s*NUCB1(W232A/W333A) (Fig.1.1). Both AlF_4^- uptake (Fig.1.7A) and GTPγS binding (Fig.1.7B) to $G\alpha_{i1}$•GDP showed an increase in Trp fluorescence as $G\alpha_{i1}$ molecules were activated with time. However, Fig.1.7A and B show that binding to Ca^{2+}-free *s*NUCB1(W232A/W333A) decreases the observed fluorescence enhancement observed for Trp residues coupled to activation of $G\alpha_{i1}$. This suggests that Ca^{2+}-free *s*NUCB1(W232A/W333A) possibly affects the nucleotide exchange by inhibiting the activation process. Furthermore, the G protein activation was also monitored using a fluorescent nucleotide analogue, BODIPY FL-GTPγS. The fluorescence of BODIPY FL-GTPγS in solution is self-quenched by the guanine ring of GTPγS. However, binding of the fluorescent nucleotide in the catalytic pocket of $G\alpha_{i1}$ relieves the self-quenching leading to the enhancement in the observed fluorescence of the bound fluorophore (*43*). As shown in Fig1.7C,

Figure 1.7. *s*NUCB1 affects nucleotide-exchange by WT $G\alpha_{i1}$. (A) We employed a time-based intrinsic Trp fluorescence assay to measure the rate of spontaneous nucleotide exchange by $G\alpha_{i1}$•GDP in the presence of increasing concentrations of *s*NUCB1. The fluorescence emission of Trp211, which is situated on the Switch II region of $G\alpha_{i1}$ increases dramatically on binding of AlF_4^- to $G\alpha_{i1}$•GDP. To eliminate the influence of intrinsic Trp fluorescence from *s*NUCB1 on the measured activation rates, we used site-directed mutagenesis to engineer a Trp free version of *s*NUCB1, *s*NUCB1(W2323A/W333A). $G\alpha_{i1}$•GDP alone (20 μM, black trace) was allowed to equilibrate while Trp fluorescence emission was recorded at 340 nm. Thereafter, AlF_4^- (20 mM) was injected at 180 seconds and the fluorescence time course was monitored. The same experiment was repeated in the presence of increasing concentrations of *s*NUCB1(W232A/W333A). The rate of $G\alpha_{i1}$•GDP activation by AlF_4^- is considerably decreased upon preincubation with equimolar (red) or excess (green) *s*NUCB1(W2323A/W333A). As a control, *s*NUCB1(W232A/W333A) alone shows no enhancement in Trp fluorescence upon addition of AlF_4^- (blue). **(B)** In an analogous experiment, we monitored the enhancement in fluorescence emission of Trp211 upon exchange of GDP for GTPγS, a non-hydrolyzable analogue of GTP. The results show that the rate and extent of GTPγS-mediated activation is less when $G\alpha_{i1}$•GDP is bound to Ca^{2+}-free *s*NUCB1(W232A/W333A). **(C)** In addition to measuring intrinsic Trp fluorescence, we also monitored nucleotide exchange by using the fluorescent analogue of GTPγS, BODIPY FL-GTPγS. BODIPY FL-GTPγS was added to a buffered solution of 20 μM $G\alpha_{i1}$•GDP alone or $G\alpha_{i1}$•GDP precomplexed with increasing concentrations of *s*NUCB1. The binding of BODIPY FL-GTPγS to the catalytic pocket leads to enhancement of BODIPY fluorescence since self-quenching by guanine ring in solution is relieved. The observed time-based fluorescence

enhancement of BODIPY fluorophore on binding to $G\alpha_{i1}$ decreased as increasing concentrations of Ca^{2+}-free *s*NUCB1 were used. The data show that Ca^{2+}-free *s*NUCB1 decreases the rate and extent of BODIPY FL-GTPγS mediated activation of $G\alpha_{i1}$•GDP. In a FRET based experiment **(D)** $G\alpha_{i1}$•GDP activation was monitored through exchange of bound GDP for fluorescent mant-GTPγS nucleotide. Upon uptake of mant-GTPγS by $G\alpha_{i1}$, Trp211 moves into the catalytic pocket and forms a productive FRET pair which can transfer energy to the nucleotide analogue mant-GTPγS. FRET from Trp211 of $G\alpha_{i1}$ to bound mant-GTPγS was measured at different times after addition of mant-GTPγS. The same experiment was carried out in the presence of *s*NUCB1(W2323A/W333A). The addition of *s*NUCB1(W2323A/W333A) caused a decrease in the rate of FRET increase, indicating that uptake of mant-GTPγS by $G\alpha_{i1}$ was inhibited. Maximum FRET intensity at 425 nm with increasing time was plotted. A fit to each data set clearly shows attenuation of FRET intensity for $G\alpha_{i1}$ complexed to Ca^{2+}-free *s*NUCB1(W232A/W333A) in comparison to $G\alpha_{i1}$ alone, suggesting that Ca^{2+}-free *s*NUCB1(W232A/W333A) inhibits nucleotide exchange.

Figure 1.7

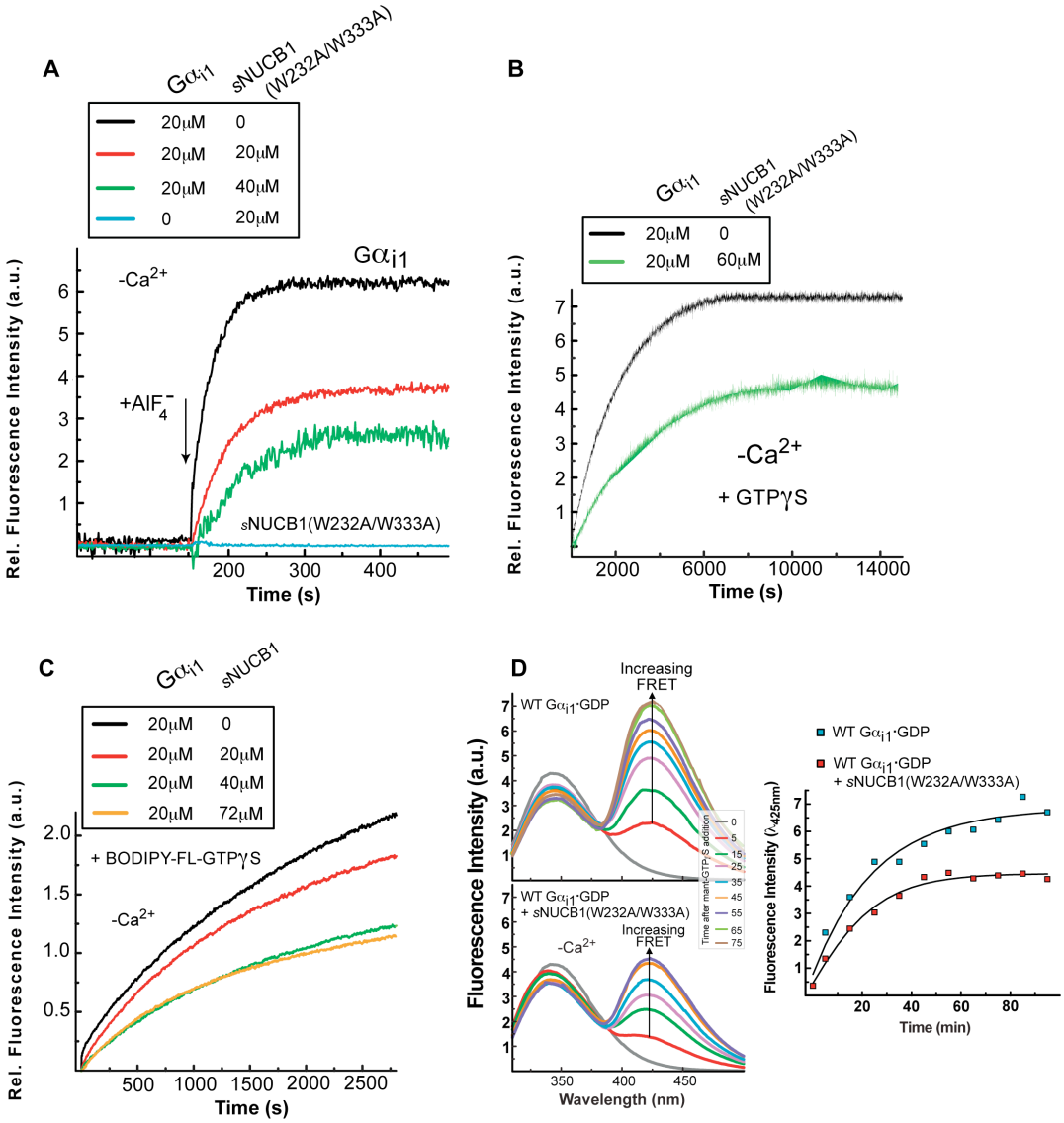
A
Gαi1
sNUCB1 (W232A/W333A)
20μM 0
20μM 20μM
20μM 40μM
0 20μM
-Ca2+
+AlF4-
Gαi1
sNUCB1(W232A/W333A)
Rel. Fluorescence Intensity (a.u.)
Time (s)
B
Gαi1
sNUCB1 (W232A/W333A)
20μM 0
20μM 60μM
-Ca2+
+ GTPγS
Rel. Fluorescence Intensity (a.u.)
Time (s)
C
Gαi1
sNUCB1
20μM 0
20μM 20μM
20μM 40μM
20μM 72μM
+ BODIPY-FL-GTPγS
-Ca2+
Rel. Fluorescence Intensity (a.u.)
Time (s)
D
Increasing FRET
WT Gαi1·GDP
WT Gαi1·GDP + sNUCB1(W232A/W333A)
-Ca2+
Time after mantGTP-S addition
Fluorescence Intensity (a.u.)
Wavelength (nm)
WT Gαi1·GDP
WT Gαi1·GDP + sNUCB1(W232A/W333A)
Fluorescence Intensity (λ425nm)
Time (min)

incubation of increasing concentrations of Ca^{2+}-free *s*NUCB1 with $G\alpha_{i1}$•GDP leads to decrease in the fluorescence enhancement of BODIPY fluorophore suggesting that Ca^{2+}-free *s*NUCB1 affects nucleotide-exchange by inhibiting it.

To monitor simultaneously the activation associated conformational change in $G\alpha_{i1}$ and the uptake of nucleotide, a mant-GTPγS based FRET assay was also performed. The binding of mant-GTPγS in the catalytic pocket of $G\alpha_{i1}$ brings it in close vicinity of Trp211 on the switch II region of $G\alpha_{i1}$. Hence, FRET can be observed between the Trp and mant fluorophores upon $G\alpha_{i1}$ activation (*44*). As shown in Fig.1.7D, the FRET intensity for $G\alpha_{i1}$ alone at each time point is significantly higher in comparison to the FRET intensity for $G\alpha_{i1}$ associated with Ca^{2+}-free *s*NUCB1(W232A/W333A). A plot of the λ_{max} at 425 nm with time shows that the FRET signal is significantly inhibited in the presence of *s*NUCB1(W232A/W333A) (Fig.1.7D). These experiments suggest towards a possible inhibitory effect of Ca^{2+}-free *s*NUCB1 towards nucleotide-exchange.

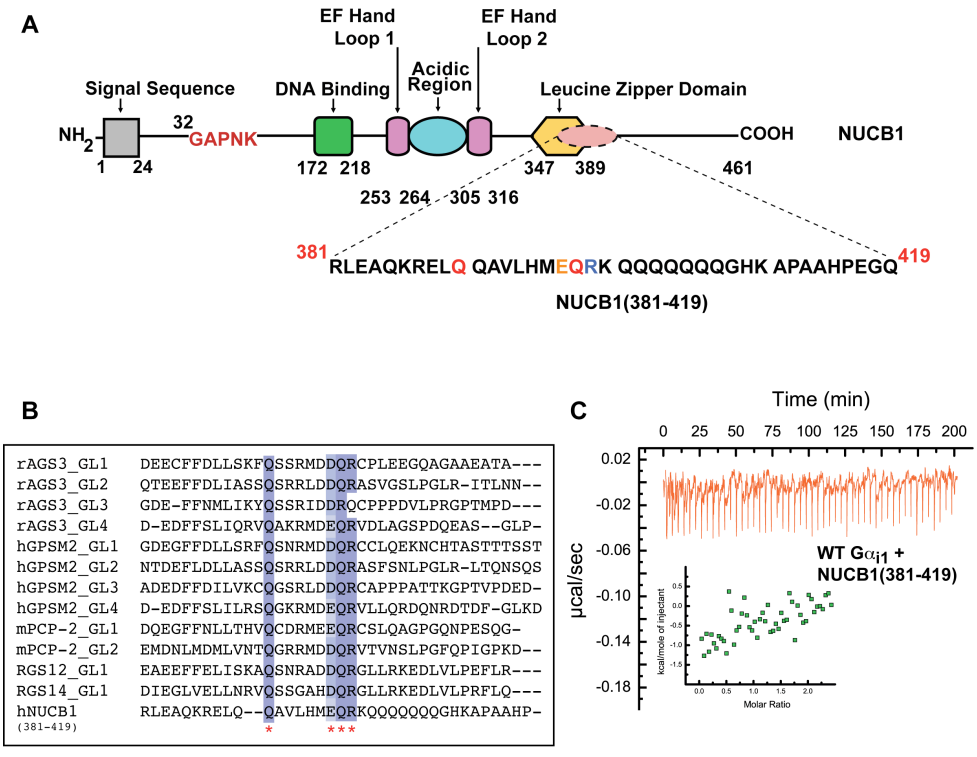

Figure 1.8. NUCB1(381-419) does not bind to WT $G\alpha_{i1}$•GDP. (A) A CT 39 mer sequence of NUCB1 (residues 381-419) consist of the Glu-Gln-Arg (397-399) triad preceded by an upstream Gln390. **(B)** The sequence alignment of NUCB1(381-419) with various GoLoco motif peptides shows the presence of the conserved Gln and the Asp/Glu-Gln-Arg motif in the sequence. The stars indicate the positions of the conserved residues amongst different sequences. **(C)** We further used ITC to measure the binding of NUCB1(381-419) to WT $G\alpha_{i1}$•GDP. NUCB1(381-419) (600 µM) was injected into a buffered solution of WT $G\alpha_{i1}$•GDP (40 µM) in the reaction cell and the heat released per injection was recorded. The heat of dilution for the addition of $G\alpha_{i1}$•GDP to buffer alone was subtracted. The isotherm shows complete absence of any binding event indicating that NUCB1(381-419) does not interact with WT $G\alpha_{i1}$•GDP.

1.2.6 The CT *s*NUCB1 peptide NUCB1(381-419) does not bind to WT $G\alpha_{i1}$•GDP

The GDI activity of several G protein interacting partners is attributed to the presence of a GoLoco motif region, which directly binds to WT $G\alpha_{i1}$•GDP and inhibits nucleotide exchange. The GoLoco motif region is a 36-39 mer long structured fragment that consists of a conserved Gln residue followed by the presence of a conserved downstream Asp/Glu-Gln-Arg triad wherein the Arg residue directly projects into the catalytic pocket and interacts with the bound GDP and stabilizes it (*54*). As shown in Fig.1.8A, the CT region of NUCB1 (residues 381-419) consists of a Gln at position 390 followed by a downstream Glu-Gln-Arg motif. A sequence alignment of NUCB1(381-419) with GoLoco motif sequences from various GDIs for $G\alpha_{i1}$ shows that NUCB1(381-419) consists of the conserved Gln followed by the triad (Fig.1.8B). Hence in order to evaluate the binding of the NUCB1(381-419) to WT $G\alpha_{i1}$•GDP, we performed ITC experiment by incubating 40 μM WT $G\alpha_{i1}$•GDP in the reaction cell and using 600 μM of NUCB1(381-419) as the injectant. The isotherm shows that NUCB1(381-419) does not bind to WT $G\alpha_{i1}$•GDP (Fig. 1.8C). Hence the isolated CT NUCB1 peptide fragment NUCB1(381-419) does not bind to WT $G\alpha_{i1}$•GDP which indicates that the peptide alone cannot act as a GDI for G protein activation.

1.2.7 *s*NUCB1 is a Guanine-Nucleotide Dissociation Inhibitor (GDI) of $G\alpha_{i1}$

WT $G\alpha_{i1}$•GDP subunit can readily self-exchange GDP for GTP albeit with poor efficiency. Our earlier results show that Ca^{2+}-free *s*NUCB1 can affect nucleotide exchange by WT $G\alpha_{i1}$•GDP. However for Ca^{2+}-free *s*NUCB1 to be a GDI of nucleotide-exchange, it must cause a decrease in the number of sites for binding of GTP / GTPγS. In order to investigate the GDI activity, we incubated 20 μM WT $G\alpha_{i1}$•GDP alone or in the presence of 100 μM Ca^{2+}-free *s*NUCB1 with 100 μM BODIPY FL-GTPγS present in the reaction mixture at 25 ^{o}C. Samples were withdrawn at various time points and amount of bound BODIPY FL-GTPγS was estimated by measuring the absorbance at 504 nm. The data shows that Ca^{2+}-free *s*NUCB1 significantly inhibits the nucleotide-exchange by WT $G\alpha_{i1}$•GDP by decreasing the number of binding sites available for BODIPY FL-GTPγS (Fig.1.9A). In order to further substantiate the observed GDI acitivity of Ca^{2+}-free *s*NUCB1, we monitored the exchange of radioligand GTPγ^{35}S by WT $G\alpha_{i1}$•GDP in the presence and absence of Ca^{2+}-free *s*NUCB1 / *s*NUCB1(W333Ter). The results show that both Ca^{2+}-free *s*NUCB1 or *s*NUCB1(W333Ter) possess similar GDI activity (~ 58 % inhibition) suggesting that the C-terminus is not necessary for the activity (Fig.1.9B). As a positive control we also used a C-terminal peptide from RGS14 protein namely RGS14(496-531) which has been shown to possess GDI activity due to the presence of a canonical GoLoco motif.

Figure 1.9. *s*NUCB1 acts as a GDI of $G\alpha_{i1}$. (A) We determined the number of available nucleotide binding sites on $G\alpha_{i1}$ in the absence or presence of Ca^{2+}-free *s*NUCB1 by monitoring the absorbance of $G\alpha_{i1}$-bound BODIPY FL-GTPγS at 504 nm. $G\alpha_{i1}$•GDP alone (20 μM, blue) or in complex with Ca^{2+}-free *s*NUCB1 (100 μM, orange) was allowed to undergo nucleotide exchange with 100 μM BODIPY FL-GTPγS in the reaction mixture. Samples were withdrawn at different time points and unbound BODIPY FL-GTPγS was removed using a micro-spin desalting column. The amount of bound BODIPY FL-GTPγS was measured using the UV/VIS absorbance spectroscopy at each time point. A relative decrease in the number of nucleotide binding sites on $G\alpha_{i1}$ was observed on association with *s*NUCB1. This shows that Ca^{2+}-free *s*NUCB1 binds to $G\alpha_{i1}$ in its GDP-bound form and inhibits nucleotide exchange. We further investigated the **(B)** guanine-nucleotide inhibitory activity of Ca^{2+}-free *s*NUCB1 using the radioligand based assay. 20 μM WT Gαi1•GDP was incubated alone (blue) or with 100 μM Ca^{2+}-free *s*NUCB1 (green) / *s*NUCB1(W333Ter) (red) in the presence of GTPγ^{35}S and samples were withdrawn at various time points to estimate the amount of radioligand bound upon nucleotide exchange. As a positive control, 100 μM of a CT GoLoco motif peptide from RGS14 namely RGS14(496-531) with established GDI activity was used as a positive control (magenta). The data shows that both Ca^{2+}-free *s*NUCB1 or Ca^{2+}-free *s*NUCB1(W333Ter) considerably inhibit nucleotide exchange with similar potency. The GDI peptide RGS14(496-531) shows complete inhibition of nucleotide exchange. Each experiment was repeated atleast 3 times and the data was plotted as mean ± S.E.M. amongst the independent measurements.

Figure 1.9

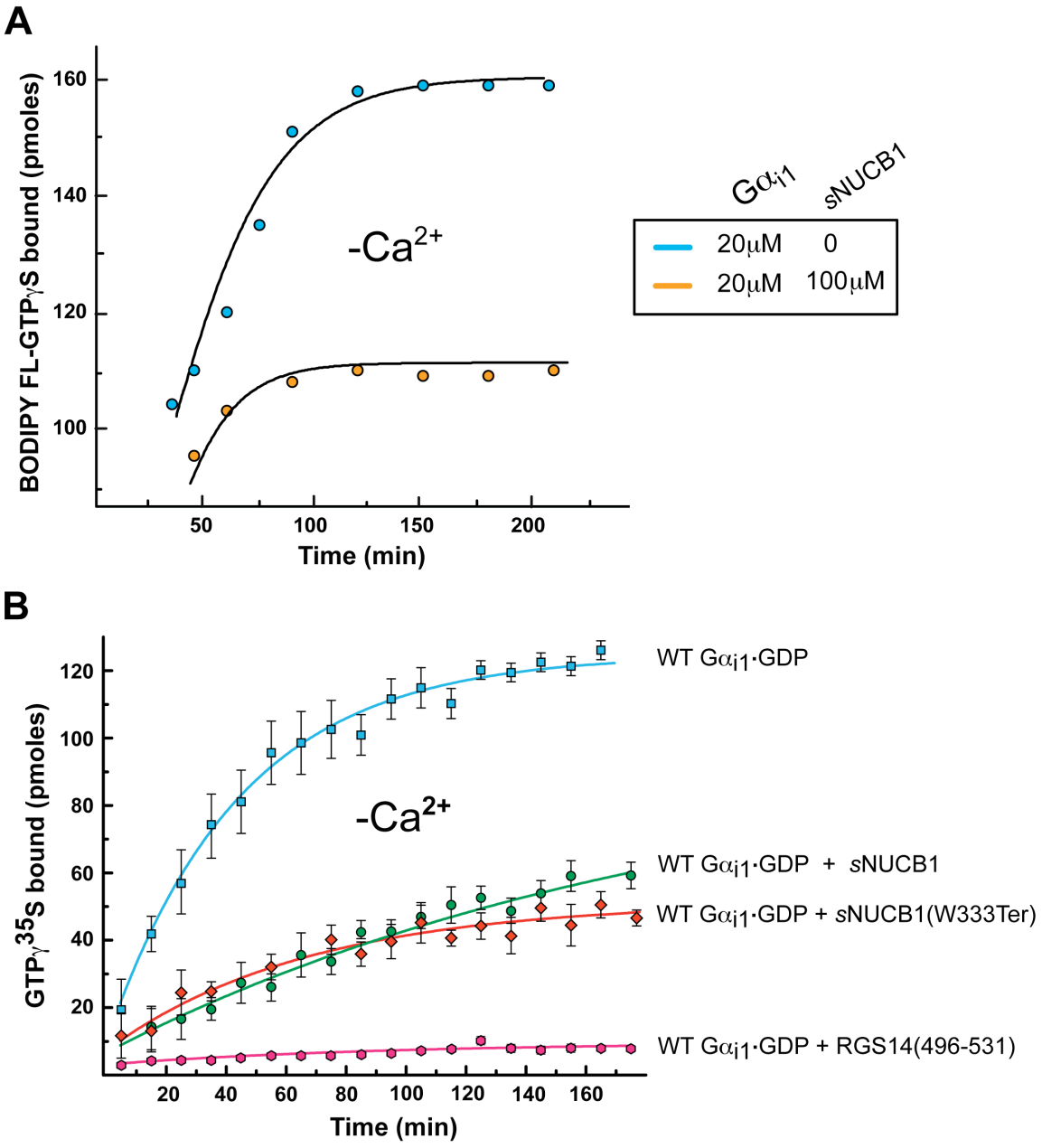
A
BODIPY FL-GTPγS bound (pmoles)
160
140
120
100
50
100
150
200
Time (min)
-Ca2+
Gαi1
sNUCB1
20μM 0
20μM 100μM
B
GTPγ35S bound (pmoles)
120
100
80
60
40
20
20
40
60
80
100
120
140
160
Time (min)
-Ca2+
WT Gαi1·GDP
WT Gαi1·GDP + sNUCB1
WT Gαi1·GDP + sNUCB1(W333Ter)
WT Gαi1·GDP + RGS14(496-531)

1.3 DISCUSSION

NUCB1 is a ubiquitously expressed multi-domain Ca^{2+}-binding protein whose physiological role(s) is not well understood. Our results provide the first direct evidence that NUCB1 is a Ca^{2+}-regulated GDI of $G\alpha_{i1}$. SEC experiments showed that Ca^{2+}-free *s*NUCB1 interacts primarily with the GDP-bound state of $G\alpha_{i1}$, and that no interaction occurs when *s*NUCB1 is bound to Ca^{2+} (Fig.1.5,1.6). The role of Ca^{2+}-binding as a regulatory switch for *s*NUCB1 association with $G\alpha_{i1}$ can be explained structurally through the involvement of the acidic region of *s*NUCB1. The acidic region has been previously shown to be a G protein interaction site (*29*). Earlier, yeast two-hybrid experiments had suggested that the CT-linked α5 helix of G protein interacts with NUCB1 (*29*). Interestingly, the α5 helix is conformationally identical in both the $G\alpha_{i1}$•GDP and $G\alpha_{i1}$•GTPγS structures. However, as Gα undergoes transition from the inactive to the active state, the structurally dynamic switch regions (switch I to IV) of Gα subunits change conformation (*45*). Thus, the preferential binding of Ca^{2+}-free *s*NUCB1 to $G\alpha_{i1}$•GDP, which can modulate G protein activation, points toward a possible participation of switch regions in this interaction.

The domain diagram of NUCB1 shows the presence of a CT leucine zipper domain that can facilitate dimerization (Fig.1.1). Our sedimentation equilibrium experiments using AUC alongwith MALS analysis show that

NUCB1 is a dimer in solution. Furthermore, analysis of the dimer of *s*NUCB1 using dynamic light scattering revealed that it is considerably asymmetric in its shape with a long axis of 12.4 nm (Fig1.4E,F). This elongated shape may facilitate simultaneous interaction of *s*NUCB1 with both the α5 helix and the switch regions of $G\alpha_{i1}$•GDP. Interestingly, deletion of the leucine zipper domain along with the CT region of *s*NUCB1 increased the binding affinity of monomeric *s*NUCB1(W333Ter) for $G\alpha_{i1}$•GDP and decreased the R_h to 3.3 nm (Fig.1.6C). This suggests that the deleted CT of *s*NUCB1 may play a regulatory role in *s*NUCB1-$G\alpha_{i1}$•GDP interaction.

NUCB1 is a major Ca^{2+}-binding protein of Golgi. In 1998, Lin *et al.* used labeling studies to show that NUCB1 is concentrated on the membranes of the stacked Golgi cisternae and associated vesicles on the cis side (*16*). NUCB1 assists in Ca^{2+} uptake, storage and release from the Golgi apparatus (*46*). Optimal Golgi Ca^{2+} levels are required for anterograde (ER to Golgi), retrograde (Golgi to ER) and intra-Golgi transport (*47*). Thus, NUCB1 along with Cab45 (*48*), the only other known Ca^{2+}-binding Golgi resident protein, may be involved in maintaining the essential Ca^{2+} levels and gradient from cis to trans Golgi. The Ca^{2+} concentration in the cis-Golgi is around 0.3 mM under unstimulated conditions (*47*). Thus, the NUCB1 pool in Golgi should largely be Ca^{2+} bound given the K_d values for Ca^{2+}-binding. However, at cytosolic Ca^{2+} concentrations (100-125 nM)

(*49*), NUCB1 should essentially be in a Ca^{2+}-free state, suggesting that this Ca^{2+}-free cytosolic pool of NUCB1 can interact with cytosolic $G\alpha_{i1}$. NUCB1, like heterotrimeric G proteins, exists in both the cytosolic and membrane fractions (*17*). Co-immunoprecipitation and FRET analysis have convincingly shown that NUCB1 interacts with $G\alpha_i$ and co-localizes on Golgi lumen (*50*). Our MALS analysis alongwith the results from ITC experiments establish the interaction of one $G\alpha_{i1}$•GDP subunit with a dimer of Ca^{2+}-free *s*NUCB1.

Earlier work by Siderovski and coworkers has unraveled several interacting partners of $G\alpha_{i1}$•GDP namely, RGS12, RGS14, AGS3, GPSM2, PCP-2 and G18, all of which possess GDI activity (*9, 14, 51-53*). The GDI activity was attributed to the presence of a single or tandem repeats of a 19-amino-acid long conserved GoLoco motif region present in each of these proteins. The crystal structure of $G\alpha_{i1}$•GDP complexed to RGS14 derived GoLoco peptide showed that the conserved CT of the 19-amino-acid GoLoco motif makes contacts with both the switch I region and the bound nucleotide. Each GoLoco motif ends in a conserved triad of Asp/Glu-Gln-Arg. On binding to $G\alpha$, the Arg side chain extends into the catalytic pocket to interact directly with the bound GDP and stabilize it. In addition, the highly conserved Asp/Glu and Gln residues are absolutely essential for binding to G protein α-subunit as they are involved in both intra- and inter-molecular H-bonding interactions (*54*). A sequence

alignment of CT residues 381-419 of NUCB1 with GoLoco motif regions of several GDIs of $G\alpha_i$ subunits reveals that NUCB1 also possesses the highly conserved triad of Glu-Gln-Arg preceded by a conserved upstream Gln (Fig.1.8B). The other residues in the aligned sequence of NUCB1 show relatively poor conservation across the GoLoco motif. Nevertheless, the presence of the most conserved regions suggests that mechanistically NUCB1 might act as a GDI by stabilizing the GDP-bound state of $G\alpha_{i1}$ in a manner analogous to GoLoco region of RGS14.

Nucleotide-exchange assays with GTPγS and its fluorescent analogues showed that Ca^{2+}-free *s*NUCB1 interacts with WT $G\alpha_{i1}$•GDP and can possibly affect the nucleotide exchange (Fig.1.7). The results show an inhibition in fluorescence intensity of Trp residues of $G\alpha_{i1}$ on addition of Ca^{2+}-free *s*NUCB1 / *s*NUCB1(W232A/W333A) indicating that Ca^{2+}-free *s*NUCB1 inhibits conformational changes in WT $G\alpha_{i1}$•GDP associated with nucleotide exchange. In order to directly show that Ca^{2+}-free *s*NUCB1 is a GDI, we used BODIPY FL-GTPγS and radioligand (GTPγ^{35}S) binding assays to measure the number binding sites available on WT $G\alpha_{i1}$•GDP (Fig.1.9). Our results show that Ca^{2+}-free *s*NUCB1 significantly inhibits nucleotide exchange by $G\alpha_{i1}$•GDP. Interestingly, even the truncation mutant *s*NUCB1(W333Ter) possesses the ability to inhibit nucleotide exchange suggesting that the C-terminal domain of

*s*NUCB1 is not essential for its GDI activity. Hence unlike other GDIs with GoLoco motifs, the GDI activity of NUCB1 is not due to the presence of a conserved CT Glu-Gln-Arg triad characteristic of a GoLoco motif.

As shown by the sequence alignment, the core GoLoco motifs between different GDIs are highly conserved, whereas the residues C-terminus to it are quite divergent. Evidently, longer GoLoco peptides with additional CT residues display significantly higher affinity towards $G\alpha_i$ than the minimal 19-amino-acid peptides. The GoLoco motif peptides derived from RGS proteins have nanomolar binding affinity for $G\alpha_i$•GDP in comparison to micromolar binding affinities observed for GPSM2, PCP-2 or G18 derived GoLoco motif peptides. The binding affinities for full length GDIs like RGS14, GPSM2 and others with GoLoco motif regions towards $G\alpha_i$•GDP is unknown. Unlike these, our *in vitro* assays estimate that the binding affinity of full-length ~100 kDa *s*NUCB1 dimer to $G\alpha_{i1}$ is 18.3 μM (Fig.1.6A). The crystal structure of RGS14 GoLoco motif region bound to $G\alpha_{i1}$ showed numerous stabilizing interactions between the residues CT to the GoLoco motif and $G\alpha_{i1}$•GDP. The activation studies with chimeric Gα subunits showed that both the CT region of the GoLoco motif and the helical domain of Gα determine binding of the GoLoco motif towards a particular class of Gα subunits (*54*). Yeast two-hybrid analysis by Lin *et*

al. showed that NUCB1 preferentially interacts with $G\alpha_{i1}$ and $G\alpha_{i3}$ with higher affinity than with $G\alpha_{i2}$ and $G\alpha_s$ (*16*). Future studies of NUCB1 interaction with different classes of $G\alpha$ subunits are planned to reveal the selectivity of its GDI activity. Our G protein interaction and nucleotide exchange studies with the truncation mutant *s*NUCB1(W333Ter) (Fig.1.6C, 1.9B) suggest that unlike known GDIs, *s*NUCB1 interacts with $G\alpha_{i1}$•GDP in a novel manner. A co-crystal structure of the minimum subunit of NUCB1 bound to $G\alpha_{i1}$•GDP that has GDI activity would be immensely helpful in understanding the precise molecular details of this interaction and may provide understanding of the Ca^{2+}-dependence of this interaction.

G proteins are widely expressed in different tissue types and are involved in various signal transduction pathways interacting with a number of binding partners. The interaction of NUCB1 with $G\alpha_{i1}$ has been previous established but no GEF or GDI activity was observed because the experimental concentrations used were below the K_d value of association. Our results show that the interaction of $G\alpha_{i1}$ with *s*NUCB1 is regulated by Ca^{2+}-binding. We have evaluated this interaction in terms of cytosolic Ca^{2+} concentrations where NUCB1 should exist in a Ca^{2+}-free state capable of binding to $G\alpha_{i1}$. Based on the available evidence, we propose a model for the role of a cytosolic pool of NUCB1 in regulating G protein

signaling. According to the model, G protein heterotrimer (Gαβγ) upon activation by GPCRs, dissociates into Gα and Gβγ subunits to initiate downstream signaling cascades. RGS proteins acting as GAPs, rapidly accelerate the hydrolysis of GTP to GDP, thereby bringing the α-subunit back to the GDP-bound state. Thereafter, the GDP-bound state of $G\alpha_{i1}$ can be stabilized by the Ca^{2+}-free cytosolic pool of NUCB1 to inhibit basal nucleotide exchange. The GDI activity of NUCB1 would inhibit the self-activation of $G\alpha_{i1}$ subunit and in turn augment the Gβγ-dependent signaling cascade. Subsequently, NUCB1 would be displaced by Gβγ at the plasma membrane to promote formation of the heterotrimer, thereby initiating another cycle of receptor mediated G protein signal transduction. Future cell-based assays should provide information about the physiological importance of this interaction and how it affects the ligand mediated signal transduction cascade which involves activation of heterotrimeric G proteins.

In summary, our results show that *s*NUCB1 is a physiological dimer, which interacts with the GDP-bound $G\alpha_{i1}$. This association inhibits the nucleotide exchange by $G\alpha_{i1}$, thus demonstrating the GDI activity of NUCB1. Ca^{2+}-binding to *s*NUCB1 regulates NUCB1-$G\alpha_{i1}$•GDP complex formation and possibly modulates this interaction in different cellular compartments. NUCB1 is a novel Ca^{2+}-binding GDI with a role in

trafficking and Ca^{2+} buffering. In addition, NUCB1 also has a nuclear localization signal sequence within the DNA binding region. Recently, its role in affecting the biogenesis of amyloid precursor protein was reported (*16*). Such a potential for diverse functionality makes the comprehensive understanding of the physiological role of NUCB1 difficult. Based on our current knowledge, NUCB1 seems to be neither a RGS nor an AGS protein. Future experiments will unravel the functional relevance of the interaction of NUCB1 with other Gα subunits. Understanding the role of NUCB1 in the context of different Gα subunits will highlight the signaling pathways modulated by NUCB1. Our discovery of the Ca^{2+}-regulated GDI activity of NUCB1 adds a new level of understanding to the role of NUCB1 and to the complexity of G protein-mediated signal regulation.

CHAPTER 2

Nucleobindin 1 and its Engineered Mutant Disaggregate human Islet Amyloid Polypeptide fibrils and Inhibit its Aggregation by forming Dead-end Prefibrillar Species

2.0 INTRODUCTION

Amyloid deposition is an underlying pathophysiological hallmark of a number of severe biological disorders like Alzheimer's Disease, Creutzfeldt-Jacob disease, Parkinson's disease, Huntington's disease and Type 2 diabetes (T2D) (*55, 56*). Amyloid deposits are insoluble fibrous aggregates with a β-pleated sheet structure, formed by aggregation of natively unfolded or misfolded / partially denatured proteins or peptides. In T2D, aggregation of human islet amyloid polypeptide (hIAPP) results in islet amyloid deposits, which has been proposed as an aetiological factor contributing to the observed pathology in T2D (*57, 58*). T2D is a metabolic disorder that stems from disruption of glucose homeostasis caused by reduced insulin secretion from pancreatic islets and enhanced insulin resistance of peripheral tissues. In addition, extensive islet amyloid deposits have been observed extracellularly and adjacent to islet capillaries in 70-90% of T2D patients (*59-61*). These amyloid deposits are composed of unstructured and highly hydrophobic 37-amino-acid long polypeptide called human Islet Amyloid Polypeptide (hIAPP) or Amylin

(*62, 63*). Once formed, these amyloid deposits are highly toxic and cause β-cell death. This irreversible loss of β-cell results in insulin depletion and aggravates T2D. Physiologically, hIAPP is present in both normal and diabetic individuals but is somehow kept from aggregating into toxic deposits in non-diabetic populations. The physiological checkpoints / factors that keep this most amyloidogenic sequence from aggregating into insoluble and toxic amyloid deposits are poorly understood. Thus arises a need for investigation of factors that can inhibit the aggregation process and preferably disaggregate the pre-formed fibrils to facilitate their clearance from the system.

hIAPP is a glucomodulatory polypeptide co-secreted with insulin from pancreatic β-cells in response to glucose uptake. The gene for IAPP is located on the short arm of chromosome 12 and transcribes a 89-amino-acid long precursor protein. This larger precursor is sequentially processed by proconvertases PC1/3 and PC2 to generate the mature 37-amino-acid long polypeptide, which has a free N-terminus and an amidated C-terminus with a disulfide bond between Cys2 and Cys7 (*58*) (Fig.2.1). The mature form of hIAPP is a natively unstructured neuroendocrine hormone that regulates food intake and fat storage (*64*). It suppresses glucagon secretion and inhibits the secretion of gastric acid, bile and pancreatic enzymes (*65*). These functions of hIAPP allow for both exogenous and endogenous modulation of the rate of glucose appearance in the blood.

Thus, hIAPP together with insulin constitutes an essential glucoregulatory cascade (*66*). The aggregation of hIAPP into amyloid deposits, however, disrupts this underlying cascade and promotes β-cell death resulting in the loss of β-cell mass (*67*).

hIAPP is a very hydrophobic peptide with a significantly high propensity to rapidly aggregate in aqueous solution at low micromolar concentrations. Physiologically, the concentration of hIAPP in the secretory granules can vary from 100 μM to 4 mM. However, even at such high concentrations, hIAPP does not aggregate under normal environment of secretory granules (*65*). Several studies have shown that the physiological molar ratio of IAPP to insulin, proinsulin and C-peptide protects against IAPP aggregation (*68, 69*). Additionally, transgenic mice under normal metabolic conditions did not develop any amyloid deposits (*70*). Thus synthesis and secretion of IAPP alone is not sufficient for islet amyloidosis. Rather, defects in either IAPP biosynthesis, folding, trafficking or processing have been postulated as possible mechanisms facilitating the initiation of amyloid formation (*57, 58, 71-73*) Furthermore, the role of several chaperones and proteases has come to light explaining how the physiological defense mechanisms prevent these naturally occurring amyloidogenic proteins from aggregating in healthy individuals. In particular, heat shock proteins Hsp70 and sHsp20 have been shown to inhibit amyloidogenesis of Aβ which contributes to the

pathophysiology of Alzheimer's disease (*74, 75*). Additionally, the extracellular chaperone Clusterin has been shown to inhibit the aggregation of prion protein, Aβ and Apolipoprotein C-II (*76, 77*) into amyloid fibrils. Along with the chaperones, Insulin Degrading Enzyme (IDE), a Zn^{2+}-dependent metallo-endoprotease, has been shown to proteolytically cleave monomeric hIAPP and may play an important role in regulating the physiological concentration and eventual clearance of the peptide (*78, 79*). In addition, a number of novel approaches towards preventing both *in vivo* and *in vitro* amyloid formation by IAPP have been undertaken. Administration of drugs that increase insulin sensitivity in transgenic mouse model of hIAPP overexpression and thereby decrease β-cell demand to produce more IAPP have shown to reduce amyloid formation (*80*). Several peptide fragments and derivatives of hIAPP have been identified that inhibit fibril formation *in vitro* by targeting the amyloidogenic region (residues 8-20 and 20-29) of hIAPP (*81-84*). However we still lack a deeper understanding of the physiological factors that inhibit aggregation of hIAPP into amyloid fibrils and help keep it in a soluble form. In this study, we present the anti-amyloidogenic properties of a ubiquitously expressed mammalian protein Nucleobindin 1 (NUCB1) or commonly known as Calnuc in inhibiting the progression of hIAPP aggregation into amyloid fibrils and more importantly, in disaggregating the formed fibrils.

NUCB1 is a 55 kDa protein, which was first reported as a growth and differentiation factor associated with lupus syndrome (*19*) (Fig.2.1). Since then NUCB1 has been postulated to be involved in several important cellular functions like matrix modulation and maintaining Ca^{2+}-homeostasis in Golgi (*46*). NUCB1 has also been shown to interact with heterotrimeric G protein α-subunits leading to possible intervention in the regulation of downstream signaling events (*16, 29, 50*). However, the selective pathways associated with the functionality of NUCB1, which require its strong conservation across the animal kingdom, still remain elusive. Since its discovery, NUCB1 has been reported to be widely expressed in cells and tissues and is conserved from flies to humans (*85*). This suggests that NUCB1 is an essential Ca^{2+}-binding protein present in the eukaryotic proteome. It is primarily a Golgi-resident protein found in both cytosolic and membrane fractions (*16*). NUCB1 shows high homology with the ER resident protein Calreticulin and displays properties suggesting its role in both Ca^{2+}-storage and homeostasis in Golgi.

Recent *in vitro* studies have suggested that overexpression of NUCB1 down-regulates the mRNA production of Amyloid precursor protein (APP) and inhibits its biogenesis. It was further shown that the expression level of NUCB1 is decreased by 50% in the brains of Alzheimer's disease

Figure 2.1. Modular structure of human NUCB1 and the engineered NUCB1 variants. The domain diagram of NUCB1 is depicted schematically with its N-terminal signal sequence (grey square), putative DNA binding domain (green square), two EF hand loops (magenta rectangles), acidic region (blue oval) and leucine zipper domain (yellow hexagon). The amino acid residues at domain borders are numbered. We engineered a construct for expression in E. coli of a soluble form of NUCB1 that included an N-terminal hexa-His tag and a PreScission protease recognition sequence with an intervening spacer sequence as shown for *e*NUCB1. Endoprotease cleavage yields a soluble form of NUCB1 that begins with the amino acid sequence GPHMAS and continues with the remainder of the native sequence beginning at Gly32. We refer to this expressed protein construct as soluble NUCB1 or *s*NUCB1. Thereafter we used the *s*NUCB1 template to make point mutations in each EF hand as indicated by the arrows to generate *s*NUCB1(tetramutant) which lacks the ability to bind to Ca^{2+}.Finally, we also generated a variant of *s*NUCB1 whereby the Ser44 was substituted by a Cys residue to generate *s*NUCB1(S44C), which was used for labeling studies. We also generated a CT peptide fragment of *s*NUCB1 namely NUCB1(381-419) which consists of residues 381-419. Thereafter the complete sequences for the mature human Islet Amyloid PolyPeptide (hIAPP) and its non-aggregating synthetic analog namely Pramlintide are listed. Both peptides have a free N-terminus and an amidated C-terminus. The highlighted residues (red) in the sequence of Pramlintide show prolines, which are absent in hIAPP.

Figure 2.1

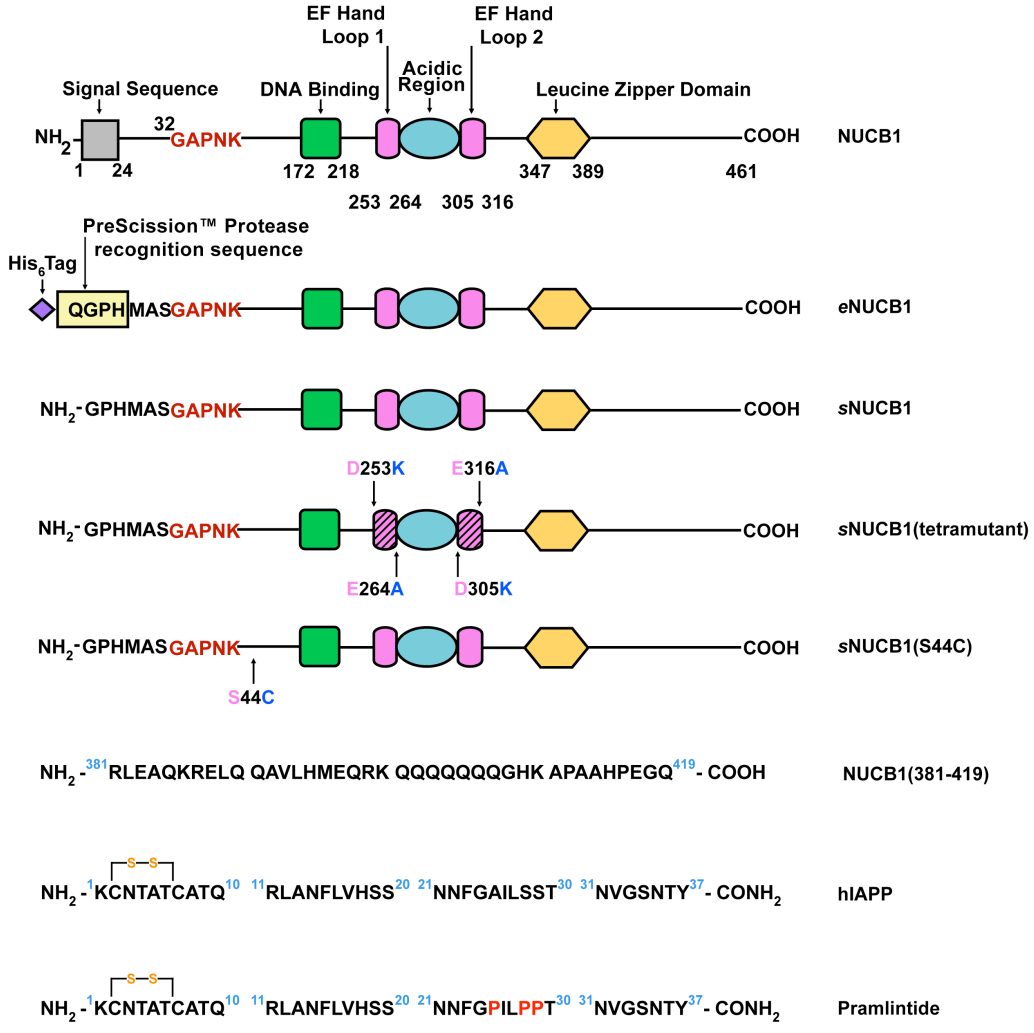
EF Hand Loop 1
EF Hand Loop 2
Acidic Region
Signal Sequence
DNA Binding
Leucine Zipper Domain
NH2
32
GAPNK
COOH
NUCB1
1 24
172 218
253 264 305 316
347 389
461
PreScission™ Protease recognition sequence
His6Tag
QGPHMASGAPNK
eNUCB1
NH2-GPHMASGAPNK
sNUCB1
D253K
E316A
sNUCB1(tetramutant)
E264A
D305K
S44C
sNUCB1(S44C)
NH2 -381RLEAQKRELQ QAVLHMEQRK QQQQQQQGHK APAAHPEGQ419- COOH
NUCB1(381-419)
S—S
NH2 -1KCNTATCATQ10 11RLANFLVHSS20 21NNFGAILSST30 31NVGSNTY37- CONH2
hIAPP
NH2 -1KCNTATCATQ10 11RLANFLVHSS20 21NNFGPILPPT30 31NVGSNTY37- CONH2
Pramlintide

patients (*28*). Thus in order to test for potent anti-amyloidogenic property and to understand the possible mechanism of action, we investigated the ability of NUCB1 towards inhibiting fibril formation by the highly amyloidogenic hIAPP .

In the present study we show that soluble form of NUCB1, *s*NUCB1 (Fig.2.1), inhibits hIAPP fibril formation at sub-stoichiometric amounts and also effectively disaggregates preformed fibrils in a Ca^{2+}-dependent manner. Interestingly, the anti-amyloidogenic functional ability of *s*NUCB1 is completely absent when bound to Ca^{2+}. In order to circumvent this, we designed a mutant of *s*NUCB1 namely *s*NUCB1(tetramutant), which similar to *s*NUCB1 can effectively inhibit hIAPP fibril formation and disaggregate hIAPP fibrils even in the presence of excess Ca^{2+}. Interestingly, Ca^{2+}-free *s*NUCB1 can bind to Zn^{2+} and ATP but does not possess protease activity towards hIAPP nor can it protect firefly Luciferase against heat denaturation. We further show that mechanistically Ca^{2+}-free *s*NUCB1 binds to and stabilizes a prefibrillar species of hIAPP by "capping" the ends to inhibit their further association to form fibrils. Interestingly, these Ca^{2+}-free *s*NUCB1 bound prefibrilar species form dead-end products incapable of seeding the aggregation reaction of hIAPP. Finally we also isolated a small peptide fragment from the C-terminal (CT) region of NUCB1 namely NUCB1(381-419) (Fig.2.1), which similar

to *s*NUCB1, inhibits hIAPP fibril formation and can also facilitate disaggregation of amyloid fibrils.

2.1 MATERIALS AND METHODS

2.1.1 REAGENTS

Thioflavin-T was purchased from Fisher Scientific and Uranyl Acetate was purchased from SPI-Chem^{TM}. For TEM, 300 mesh carbon coated Cu grids were purchased from EMS diasum (Hatfield, PA). Nano-Au Maleimide was purchased from Invitrogen Molecular Probes (Cat # 20345). Rabbit polyclonal hIAPP prediluted antibody (Cat # GTX15128) was purchased from Genetex Inc. (Irvine, CA) and Rabbit polyclonal NUCB1 antibody (Cat # P102230_T100) was purchased from Aviva Systems Biology (San Diego, CA). NUCB1(381-419) was purchased from Keck facility at Yale University. All reagents and chemicals used were of the highest available purity.

2.1.2 Heterologous expression and purification of *s*NUCB1 and its variants

The cDNA clone for human NUCB1 was obtained from ATCC and the DNA fragment for the soluble form of NUCB1 or sNUCB1, corresponding to residues 31-461 of the human NUCB1 protein without the N-terminal signal sequence (residues 1-31) was cloned into a pET28a(+) expression vector (Amersham Biosciences) to generate a N-terminal His_6-tagged construct. The construct for *s*NUCB1 served as a template to generate the His_6-tagged mutants of *s*NUCB1 namely

*s*NUCB1(tetramutant) and *s*NUCB1(S44C). For *s*NUCB1(tetramuant) the coding sequence changes leading to generation of D253K, E264A, D305K and E316A mutations were introduced by site-directed mutagenesis using the Quick Change system (Stratagene, La Jolla, CA) whereas a coding sequence for Ser44 was mutated to Cys to generate *s*NUCB1(S44C) . The vectors were then used to transform BL21 (DE3) cells to express a N-terminal His_6-tag protein containing a PreScission protease site following the His_6-tag. Both proteins were expressed in BL21 (DE3) cells grown in the presence of 50 μg / ml kanamycin. Cells were grown at 37 ^{o}C to A_{600nm} of ~ 0.7 and then induced with 500 μ M isopropylthio-β-D-galactoside (IPTG) (US Biological). Post induction the culture was grown overnight at 17 ^{o}C and subsequently harvested. The resulting pellets were re-suspended in a buffer containing 50 mM Tris-HCl pH 8.0, 150 mM NaCl, 50 mM β-mercaptoethanol, bovine lung aprotinin (20 mg/ml), 2 mM phenylmethane sulfonyl fluoride (PMSF) and complete EDTA-free protease inhibitor cocktail tablets (Roche). Thereafter the cells were lysed and the expressed His_6-tag protein was purified from crude extract by using affinity chromatography using Ni-NTA column pre-equilibrated with buffer A (50 mM Tris, pH 8.0, 150 mM NaCl, 50 mM β-mercaptoethanol). The bound His_6-tag protein was eluted from the column by using buffer A supplemented with 500 mM imidazole. The His_6-tag was cleaved by PreScission^{TM} protease, which was subsequently removed. In order to remove Ca^{2+} from *s*NUCB1 or its variant, the proteins were extensively

dialyzed against buffer A supplemented with 5 mM EGTA and 1 mM EDTA, which were also eventually removed through dialysis. Finally, size exclusion chromatography (SEC) was done using Superdex200 26/60 HR column equilibrated with buffer S (50 mM Tris, pH 8.0, 150 mM NaCl, 1 mM DTT) to obtain homogenously pure protein. The typical yield for sNUCB1 and its variant was ~ 5 mg / L. The purity of the proteins was assessed by Coomassie brilliant blue staining after the proteins were separated through SDS-PAGE. The purity of both the proteins was greater than 95%.

2.1.3 Solid phase peptide synthesis and purification of hIAPP

Wild type human IAPP (hIAPP) was synthesized and purified by Ruchi Gupta at Stony Brook University, NY in the lab of Dr Daniel P Raliegh.

2.1.4 Monitoring hIAPP aggregation kinetics using thioflavin-T fluorescence

The kinetics of aggregation of hIAPP was monitored in the absence and presence of Ca^{2+}-free *s*NUCB1 using thioflavin-T or thio-T fluorescence. All fluorescence measurements were done on a Jobin Yvon Horiba fluorescence spectrophotometer using an excitation wavelength of 450 nm and an emission wavelength of 485 nm. The emission and excitation slits

were both set to 5 nm and a 1.0 cm cuvette was used. Experiments were performed by diluting a stock of hIAPP in 20 mM Tris pH 7.5. Each stock solution was filtered through a 0.45 μm pore size GHP Acrodisc syringe filter prior to the experiment. The final reaction mixture contained hIAPP with or without a particular concentration Ca^{2+}-free *s*NUCB1 along with 32 μM thio-T in the reaction buffer at 25 ^{o}C with constant stirring. The fluorescence intensity observed for binding of thio-T to Ca^{2+}-free *s*NUCB1 alone was subtracted from each kinetic curve.

2.1.5 Transmission Electron Microscopy (TEM)

TEM was performed at the Bioimaging facility at Rockefeller University. Samples were prepared by placing 5 μl of solution onto formvar coated 300 mesh copper grids and counterstained with 2% aqueous uranyl acetate solution. Samples were viewed with a FEI Tecnai12 BioTwinG^2 transmission electron microscope at 80 kV. Digital images were acquired with an AMT XR-60 CCD Digital Camera System and compiled using Adobe Photoshop CS2 and Image J.

2.1.6 Size Exclusion Chromatography (SEC)

Size exclusion chromatography (SEC) was done using a Superose 6 10 / 30 GL column attached to an AKTA explorer FPLC. 200 μl of a reaction

mixture with Ca^{2+}-free *s*NUCB1 (32 µM) alone in 20 mM Tris pH 7.5 or Ca^{2+}-free *s*NUCB1 preincubated with equimolar amount of hIAPP in reaction buffer were injected onto a buffer equilibrated Superose 6 10 / 30 GL column. The chromatogram corresponding to absorbance at 280 nm for each reaction was plotted as a function of elution volume.

2.1.7 Dot Blot Assay

Dot blot was done by blotting samples onto an activated polyvinylidene fluoride (PVDF) membrane and allowed to dry followed by blocking with 5 % milk solution in TBS (20 mM Tris, pH 7.5, 150 mM NaCl) at room temperature. Subsequently the membrane was incubated with a solution of rabbit polyclonal primary antibody against hIAPP (1:2 dilution of prediluted stock) or NUCB1 (1:500 dilution of 1 µg / µl stock) in TBS for 1 h at room temperature followed by three washes with TBS-T (20 mM Tris pH 7.5, 150 mM NaCl, 0.05 % Tween-20) for 5 min each. After this, the membranes were incubated with horseradish peroxidase conjugated anti-rabbit secondary antibody (1:8000 dilution of the stock) in TBS for 30 min at room temperature followed by two washes with TBS-T for 5 min each and a subsequent wash with TBS for 5 min. The blots were developed using the supersignal west femto maximum sensitivity substrate (Thermo Scientific).

2.1.8 Light Scattering

The light scattering data was collected using a Superose6 10/30 GL SEC column (GE Healthcare, Piscataway, NJ), connected to High Performance Liquid Chromatography System (HPLC), Agilent 1200, (Agilent Technologies, Wilmington, DE) equipped with an autosampler. The elution from SEC was monitored by a photodiode array (PDA) UV / VIS detector (Agilent Technologies, Wilmington, DE), differential refractometer (OPT-Lab rEx Wyatt Corp., Santa Barbara, CA), static and dynamic, multiangle laser light scattering (LS) detector (HELEOS II with QELS capability, Wyatt Corp., Santa Barbara, CA). The SEC-UV / LS / RI system was pre-equilibrated in buffer (20 mM Tris pH 7.5) and 200 µl of reaction mixture containing either Ca^{2+}-free *s*NUCB1 alone or incubated with equimolar amount of hIAPP were injected onto the column. Two software packages were used for data collection and analysis: the Chemstation software (Agilent Technologies, Wilmington, DE) controlled the HPLC operation and data collection from the multi-wavelength UV / VIS detector, while the ASTRA software (Wyatt Corp., Santa Barbara, CA) collected data from the refractive index (RI) detector, the light scattering detectors, and recorded the UV trace at 280 nm sent from the PDA detector. Molecular masses were determined across the entire elution profile for each observed peak in the intervals of 1 sec from static LS measurement using ASTRA software as previously described (*33*). The approach uses a Rayleigh-Debye-Gans light scattering model

(equation 1), which relates the amount of scattered light to the concentration and molecular mass of solute and second virial coefficient:

$$\frac{K^* c}{R(\theta)} = \frac{1}{M_w} + 2A_2 c \qquad (1)$$

where *R(θ)* is the intensity of excess scattered light at angle θ, *c* is the concentration of the solute, *Mw* is the weight average molecular weight of the solute, A_2 is the second virial coefficient, *K** is an optical parameter equal to $4\pi^2 n^2 \frac{(dn/dc)^2}{\lambda_0^4 N_A}$, where *n* is the refractive index, dn/dc is the refractive index increment for the solute, N_A is Avogadro's number, and λ_0 is the wavelength of the scattered light.

Dynamic light scattering (DLS) measurements were made "on line" at an angle of 100° with a 2 sec collection time across the elution peaks. Time resolved scatter intensity fluctuations were analyzed using ASTRA Software (Wyatt Corp., Santa Barbara, CA) which implements the cumulants method (Koppel, 1972) to determine the time dependence of diffusive motion also referred to as the intensity correlation function, *G(τ), (35)*:

$$G(T) = B\{1 + \alpha[\exp(-D_T q^2 t)]^2\} \qquad (2)$$

where *B* is the average baseline intensity, α is an instrument-specific correction factor, D_T is the concentration-dependent translational

diffusion constant of the solute, t is a delay time, and q is the scattering vector equal to $\frac{4\pi n}{\lambda}\sin\theta/2$, where n is the refractive index of the solvent, λ is the wavelength of the scattered light and θ is the scattering angle. Equation 2 describes the relationship between the time dependency of fluctuation in scatter intensity and the translational diffusion coefficient. The value of D_T was used to estimate the apparent hydrodynamic radius of an equivalent sphere using Stokes-Einstein relationship (equation 3):

$$R_h = \frac{kT}{6\pi\eta D_T} \tag{3}$$

where k is the Boltzmann constant, T is the absolute temperature, and η is the temperature corrected viscosity of the solution.

2.1.9 Nano-Au labeling of *s*NUCB1(S44C)

Heterologously purified Ca^{2+}-free *s*NUCB1(S44C) was extensively dialyzed against phosphate buffer saline (PBS) pH 7.5 and concentration of the dialyzed protein was measured using UV / VIS spectroscopy. A nano-Au maleimide solution stock was prepared according to manufacturer's protocol (Molecular Probes, Invitrogen) after which 2 nmoles of buffer dialyzed Ca^{2+}-free *s*NUCB1(S44C) protein was incubated with 6 nmoles of nano-Au maleimide in PBS supplemented with 500 μM tris carboboxyethyl phosphine (TCEP) overnight at 4 ^{o}C. After

this the reaction mixture was injected onto a PBS equilibrated Superdex200 10 / 30 GL column and the elution profiles for absorbance at 280 nm and 420 nm were recorded. The labeled protein elutes at a peak centred at 12.2 ml with the excess nano-Au eluting at higher elution volume. The efficiency of labeling was estimated using a Biorad DC assay kit. A calibration curve using serial dilutions of unlabeled Ca^{2+}-free *s*NUCB1(S44C) was prepared to use for estimation of the concentration of the labeled protein by measuring absorbance at 750 nm. The concentration of nano-Au label was estimated by measuring absorbance at 420 nm where nano-Au probe absorbs strongly. A ratio of the protein concentration to nano-Au concentration gave a value of 1.02, indicating stoichiometric labeling of Ca^{2+}-free *s*NUCB1(S44C) with each monomeric subunit labeled with one nano-Au probe.

2.1.10 Nano-Au labeling of hIAPP

32 µM of hIAPP was incubated in 20 mM Tris pH 7.5 buffer solution at room temperature. After fibrils were formed, the reaction mixture was sonicated for 15 sec and sonicated mixture was dialyzed against PBS at 4 ^{o}C. Thereafter 2 nmoles of hIAPP solution were incubated with 6 nmoles of nano-Au maleimide in PBS supplemented with TCEP overnight at 4 ^{o}C. The excess nano-Au was removed through extensive dialysis. The labeled solution was then used to "seed" a hIAPP aggregation reaction and the

incorporation of nano-Au labeled hIAPP fragment into growing fibril was observed using TEM.

2.1.11 Scanning Transmission Electron Microscopy (STEM) and mass per unit length measurements

Dark-field micrographs of unstained freeze-dried specimens together with Tobacco Mosaic Virus (TMV) particles as a mass standard were prepared according to the standard "wet film" method of the Brookhaven STEM facility. This involved freeze-drying the sample with TMV on titanium grids supporting a 2 - to 3 - nm carbon film as described by Wall and Hainfeld. Grids were scanned at - 150 °C on a custom-built STEM at 40 kV with a probe focused to 0.25 nm with a dwell time of 30 μs / pixel. Digital dark-field micrographs of freeze-dried specimens were recorded with 512 × 512 pixels at raster steps of 1.0 or 2.0 nm per pixel and an average radiation dose of 1×10^2 to 5×10^2 electron / nm^2. The images were analyzed using the PCMass30 software (Brookhaven STEM resource). The resulting data were normalized to the known mass per unit length of TMV (131.4 kDa / nm).

2.1.12 BODIPY FL-Casein based Protease assay

An experimental stock of 1 µg / µl was prepared for BODIPY FL-Casein (Molecular Probes), Trypsin (Sigma, NJ) and Ca^{2+}-free *s*NUCB1 in digestion buffer (10 mM Tris pH 7.8, 100 µM NaN_3). Thereafter 10 µg of BODIPY FL Casein substrate was incubated in digestion buffer at 25 ^oC and the fluorescence readout was measured with λ_{ex} = 505 nm and λ_{em} = 513 nm. After 60 sec, 100 µg of Ca^{2+}-free *s*NUCB1 or 10 µg of Trypsin was added to the reaction mixture and enhancement in fluorescence was recorded. In addition, BODIPY FL Casein was also incubated with Trypsin, or with varying concentrations of *s*NUCB1(tetramutant) or Ca^{2+}-free *s*NUCB1 and samples were withdrawn after 5 min and 60 min and subjected to SDS-PAGE analysis followed by coomassie staining.

2.1.13 Liquid chromatography Mass Spectrometry (LC-MS)

HPLC-MS analysis was performed using an Acquity UPLC System (Waters, Milford, MA) in combination with a QSTAR QqTOF mass spectrometer (Applied Biosystems). The column used was a 150 mm × 2.1 mm BEH C18 column. The LC was coupled with the mass spectrometer using a Pico Tip sprayer (New Objective, Woburn, MA) with an inner diameter of 15 µm. UPLC-MS / MS analysis was carried out at a flow rate of 100 µl / min. Samples were loaded directly on the analytical column. After a washing period of 1 min with 1% B (acetonitrile with 0.01%

TFA), a linear gradient was from 99% A (water with 0.01% TFA), 1%B to 30% A, 70% B in 10 minutes, respectively. Similar results were also obtained with nano-HPLC coupled to a LTQ mass spectrometer at 250 nanoliter/minute and a linear gradient was from 99% A (water with 0.01% TFA), 1%B to 30% A, 70% B in 40 minutes.

2.1.14 Matrix Metallaproteinase (MMP) assay

The Sensolyte® 520 Matrix Metalloproteinase (MMP) substrate kit (AnaSpec) was used to assay for MMP activity of Ca^{2+}-free *s*NUCB1. Sixteen synthetic FRET peptide (5-aminocarboxy fluorescein or 5-FAM and QXL™520 are used as the fluorophore / quencher pair) substrates were used as fluorogenic indicators to assay MMP activities. Within the peptide, QXL™520 quenches the fluorescence readout of 5-FAM whereas upon MMP mediated proteolytic cleavage of the peptide this internal quenching is be relieved and the fluorescence emission readout for 5-FAM can be monitored at Ex / Em wavelengths = 490 / 520 nm. The assay was done in a 96-well plate format. A serial dilution of the reference standard was done in the assay buffer to calibrate the optimal concentration of the substrate needed for the reaction. Thereafter we incubated the optimal concentration of each FRET peptide substrate with either 15 ng / 50 µl / well of MMP-1 or with 7.5 or 750 ng / 50µl / well of Ca^{2+}-free *s*NUCB1 and the fluorescence emission was recorded at 10 min time intervals for 90

min. In order to eliminate the contribution from the background, the fluorescence emission for each FRET peptide alone was subtracted from all monitored reactions.

2.1.15 Luciferase Assay

The Luciferase assay kit was bought from Promega and the Luciferin (substrate) stock was prepared in the assay buffer according to the manufacturer's protocol. Thereafter a serial dilution curve for Luciferase activity was generated by incubating the substrate with varying cconcentrations of Luciferase and quatifying the chemiluminiscence readout 10 min after substrate addition with an EnVision Multimode Plate Reader (Perkin Elmer). The analysis showed that 0.7 nM concentration of Luciferase was optimal and was used in all subsequent experiments. For renaturation assay, native Luciferase was denatured by incubating it at 40 ^{o}C for 10 min. Thereafter, denatured Luciferase (0.7 nM) was independently incubated with 0.7 nM, 7 nM or 70 nM concentration of Ca^{2+}-free *s*NUCB1 in a reaction mixture with substrate present and the chemiluminiscence recorded after 10 min, 20 min and 30 min. The chemiluminiscence of the substrate alone was substracted from each monitored reactions. In addition, we also tested for the ability of Ca^{2+}-free *s*NUCB1 towards inhibiting heat denaturation of Luciferase. We preincubated 0.7 nM Luciferase separately with 0.7 nM and 70 nM

concentration of Ca^{2+}-free *s*NUCB1 and heated each reaction mixture at 42 ^{o}C for 10 min. The chemilumiscience from each reaction was monitored 10 min after addition of substrate post incubation period. Each experiment was repeated atleast 3 times. The error bars represent mean ± S.E.M. of independent measurements.

2.2 RESULTS

2.2.1 Ca^{2+}-free *s*NUCB1 inhibits hIAPP fibril formation at sub-stoichiometric concentrations

hIAPP is a 37-amino-acid long neuroendocrine hormone that readily aggregates into characteristic amyloid fibrils with β-sheet morphology. The aggregation kinetics of hIAPP alone or in the presence of equimolar or sub-stoichiometric amounts of Ca^{2+}-free *s*NUCB1 were monitored using thioflavin-T binding assay (Fig.2.2A). For hIAPP alone, aggregation starts with a nucleation phase of "seed" formation within 5 min that extends into a rapidly growing elongation phase between 5 and 20 min. The growth phase finally plateaus into a stationary phase indicative of extensive fibril formation. Interestingly, in the presence of equimolar amount (32 μM) of Ca^{2+}-free *s*NUCB1, there is significant decrease in the enhancement of thioflavin-T fluorescence suggesting that Ca^{2+}-free *s*NUCB1 inhibits aggregation of hIAPP into amyloid fibrils. The inhibition persists even at sub-stoichiometric concentrations of 10.7 μM, 6.4 μM and 3.2 μM Ca^{2+}-free *s*NUCB1 with 32 μM hIAPP in the reaction mixture (Fig.2.2A). Interestingly, incubation with limiting concentration of 0.64 μM results in a similar aggregation profile as observed for hIAPP alone, suggesting that at this concentration Ca^{2+}-free *s*NUCB1 cannot inhibit fibril formation. Subsequent TEM analysis of samples withdrawn from individual reactions show that hIAPP alone (32 μM) aggregates to

Figure 2.2. Concentration dependent inhibition of hIAPP fibril formation by Ca^{2+}-free *s*NUCB1. **(A)** We monitored the kinetics of hIAPP aggregation using enhancement in thioflavin-T fluorescence. The aggregation of 32 μ M hIAPP alone (blue) shows an initial nucleation phase which then extends into a rapid growth phase. The aggregation continues and reaches a plateau indicating the completion of aggregation with the formation of hIAPP amyloid fibrils. We then incubated hIAPP with different concentrations of Ca^{2+}-free *s*NUCB1, ranging from equimolar (32 μ M) (black) to sub-stoichiometric amounts. The aggregation profiles show that Ca^{2+}-free *s*NUCB1 effectively inhibits hIAPP aggregation when present at equimolar (32 μ M) concentrations. However, relative enhancement in thio-T fluorescence was observed when 6.4 μM (green) or 3.2 μ M (orange) Ca^{2+}-free *s*NUCB1 was used. Interestingly, incubation with 0.64 μ M (pink) concentration of Ca^{2+}-free *s*NUCB1 results in an aggregation profile similar to hIAPP alone. We also monitored each reaction using TEM. As a control **(B)** hIAPP (32 μM) and Ca^{2+}-free *s*NUCB1 were incubated alone and reaction was monitored by withdrawing samples at 7 min, 13 min and 60 min. hIAPP alone (32 μM) aggregates rapidly to form oligomers within 7 min which associate to form protofibrils and protofilaments within 13 min. These intermediates rapidly associate to form amyloid fibrils within 60 min. Unlike hIAPP, Ca^{2+}-free *s*NUCB1 alone (32 μ M) does not aggregate to form higher order aggregates. **(C)** We also used TEM to monitor inhibition of hIAPP aggregation by varying concentrations of Ca^{2+}-free *s*NUCB1. The micrographs show that Ca^{2+}-free *s*NUCB1 when incubated with hIAPP at equimolar (32 μ M) or sub-stoichiometric concentration upto 3.2 μM concentration effectively inhibits hIAPP fibril formation. However at the limiting concentration of 0.64 μ M, fibril formation is uninhibited as seen by the presence of amyloid fibrils in the 60 min sample. Thus inhibition of amyloid formation is a dose-dependent process. The scale bar represents 200 nm.

Figure 2.2

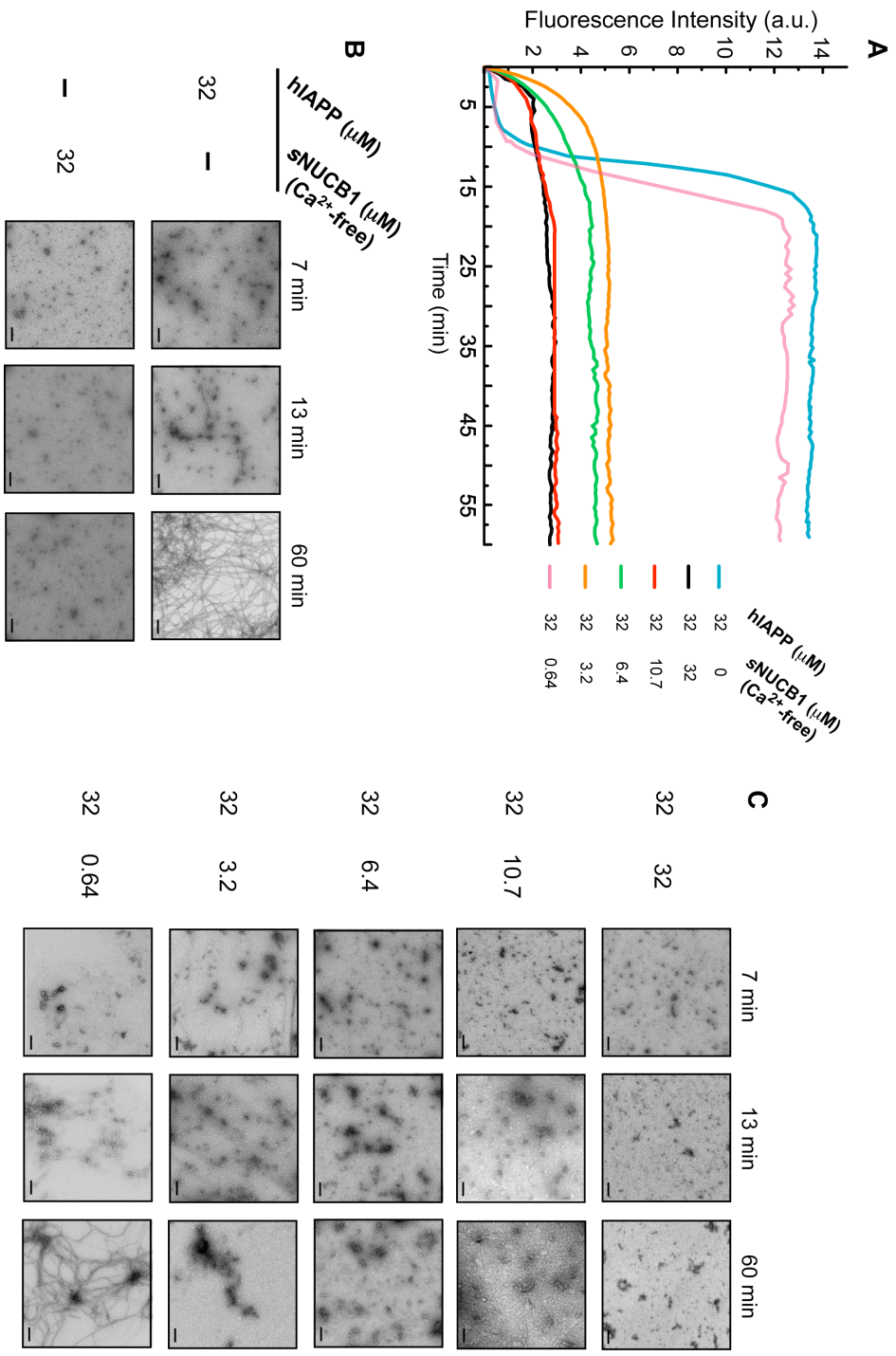
A
Fluorescence Intensity (a.u.)
Time (min)
hIAPP (μM)
sNUCB1 (μM) (Ca2+-free)
32 0
32 32
32 10.7
32 6.4
32 3.2
32 0.64
B
hIAPP (μM)
sNUCB1 (μM) (Ca2+-free)
32 –
– 32
7 min
13 min
60 min
C
7 min
13 min
60 min
32 32
32 10.7
32 6.4
32 3.2
32 0.64

form oligomers within 7 min, which continue to grow and form higher order intermediates protofilaments and protofibrils as shown for the sample at 13 min. These protofibrillar intermediates associate and extend into mature amyloid fibrils within 60 min. In a control experiment, 32 μM Ca^{2+}-free *s*NUCB1 alone does not aggregate when incubated at room temperature (Fig.2.2B). Thereafter, the reaction mixtures with stoichiometric or lower concentrations of Ca^{2+}-free *s*NUCB1 preincubated with hIAPP (32 μM) were analyzed through TEM (Fig.2.2C). The samples withdrawn at 7 min and 13 min for reaction mixtures with 32 μM, 10.7 μM, 6.4 μM and 3.2 μM concentration of Ca^{2+}-free *s*NUCB1 show oligomeric species and the 60 min sample shows the presence of high order prefibrillar species in the reaction mixture. The formation of prefibrillar species in each of these reactions explains the observed increase in the thioflavin-T fluorescence as shown in Fig.2.2A. Furthermore, the absence of a lag phase in the presence of Ca^{2+}-free *s*NUCB1 suggests towards a facilitated rapid association of hIAPP towards forming prefibrillar species by Ca^{2+}-free *s*NUCB1. Interestingly, when 0.64 μM concentration of Ca^{2+}-free *s*NUCB1 was used, fibrils were observed in the 60 min sample, showing that at this concentration Ca^{2+}-free *s*NUCB1 does not inhibit fibril formation by 32 μM hIAPP. Thus Ca^{2+}-free *s*NUCB1 inhibits fibril formation by hIAPP in a dose-dependent manner.

2.2.2 Ca^{2+}-bound *s*NUCB1 does not inhibit hIAPP fibril formation

NUCB1 is a multi-domain protein with two Ca^{2+}-binding EF hand domains (Fig.2.1). Ca^{2+} readily binds to *s*NUCB1 and induces conformational change within the protein subunit (Fig.1.2C,D). As shown earlier, Ca^{2+}-free *s*NUCB1 effectively inhibits hIAPP aggregation into amyloid fibrils (Fig.2.2). In order to investigate the effect of Ca^{2+}-binding on the functional efficacy of *s*NUCB1, we monitored inhibition of hIAPP aggregation by equimolar amounts (32 μM) of *s*NUCB1 in the absence or presence of 3 mM Ca^{2+} in the reaction mixture. The experiment was setup by first incubating Ca^{2+}-free *s*NUCB1 in 20 mM Tris pH 7.5 supplemented with or without 3 mM Ca^{2+}. Thereafter stoichiometric amount (32 μ M) of hIAPP was added to each reaction mixture and samples were withdrawn at 15 min, 30 min and 60 min time points for analysis using TEM (Fig.2.3A). As shown, Ca^{2+}-free *s*NUCB1 effectively inhibits fibril formation as only characteristic protofibrillar species are seen even at 60 min time point. In contrast, Ca^{2+}-bound *s*NUCB1 does not inhibit fibril formation. TEM images for 15 min sample show presence of protofibrils and protofilaments, which continue to grow into fibrillar structures seen in coexistence with protofibrillar intermediates in the 30 min sample. These eventually combine to form mature amyloid fibrils as shown for 60 min sample (Fig.2.3B). Thus Ca^{2+}-binding nullifies the functional ability of *s*NUCB1 to effectively inhibit hIAPP fibril formation.

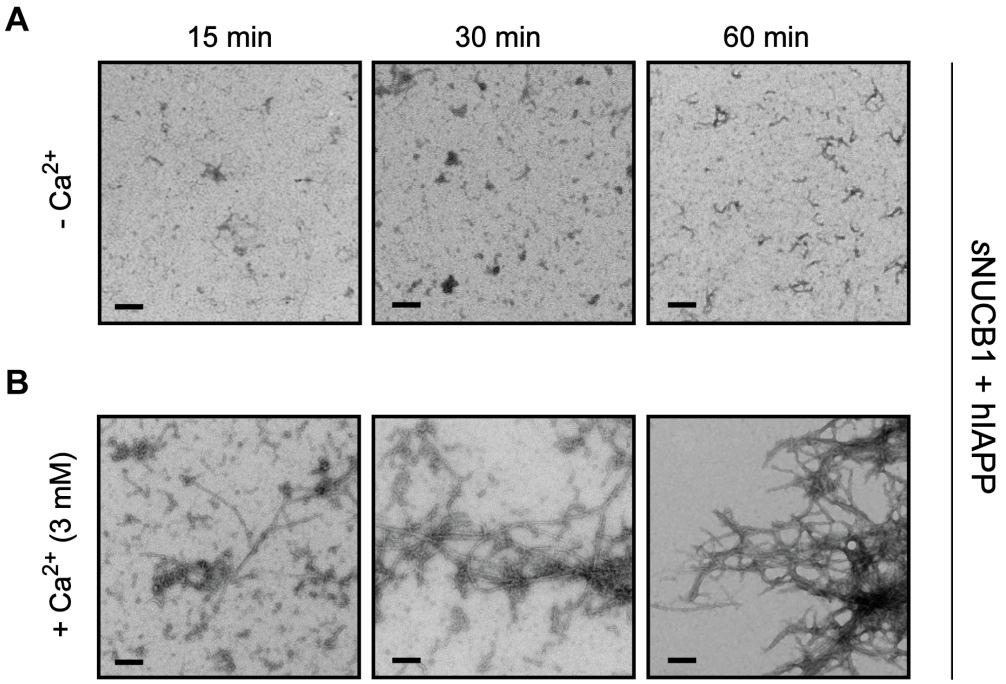

Figure 2.3. Ca^{2+}-binding prevents *s*NUCB1 from inhibiting hIAPP fibril formation. We monitored aggregation of hIAPP in the presence of *s*NUCB1. **(A)** In the absence of Ca^{2+}, equimolar amount (32 μ M) of *s*NUCB1 preincubated with hIAPP effectively inhibits aggregation of hIAPP into fibrils. The micrographs corresponding to 15 min and 30 min show the presence of oligomeric and protofibrillar species that do not progress to form fibrils as shown by the micrograph corresponding to the 60 min sample. **(B)** However, in the presence of excess Ca^{2+} (3 mM) in the reaction mixture, *s*NUCB1 is unable to inhibit hIAPP aggregation. hIAPP aggregates to form protofibrils and protofilaments as observed at 15 min and 30 min respectively which eventually grow into mature fibrils within 60 min. The scale bar on each micrograph represents 200 nm.

2.2.3 Engineered *s*NUCB1 Ca^{2+}-insensitive mutant, *s*NUCB1(tetramutant), inhibits hIAPP fibril formation in a Ca^{2+}-independent manner

*s*NUCB1 consists of two EF hand domains that bind to Ca^{2+}. The sequence alignment of the 12-amino-acid long Ca^{2+}-binding EF hand loops of NUCB1 with known Ca^{2+}-binding proteins highlights the presence of completely conserved Asp residue at the 1st position followed by a Glu at the 12th position (marked by asterisk) (Fig2.4A). In order to disrupt the Ca^{2+}-binding ability of *s*NUCB1, we mutated the Ca^{2+}-coordinating Asp253 and Asp305 in each EF hand domain to a Lys and Glu264 and Glu316 into Ala to generate a tetramutant namely *s*NUCB1(tetramutant) (Fig.2.1). The far-UV CD spectra of homogenously purified *s*NUCB1(tetramutant) showed a majorly helical structure (Fig.2.4B) similar to Ca^{2+}-free *s*NUCB1 itself (Fig.1.3A). Furthermore, the folding of *s*NUCB1(tetramutant) was observed to be non-cooperative and irreversible with an apparent T_m of 48.7 ^oC (Fig. 2.4B,inset). In addition, we performed ITC experiment to test for the ability of *s*NUCB1(tetramutant) to bind Ca^{2+}. 5 µl aliquots of 500 µM solution of Ca^{2+} were injected into a buffered solution of *s*NUCB1(tetramutant) in the reaction cell and the heat released per injection was recorded. The observed isotherm shows no significant heat release due to complete absence of Ca^{2+}-binding to *s*NUCB1(tetramutant) (Fig.2.4C). Thereafter, in order to investigate the functional efficacy of *s*NUCB1(tetramutant)

Figure 2.4. *s*NUCB1(tetramutant) is majorly helical and does not bind to Ca^{2+}. (A) A sequence alignment of the 12-residue Ca^{2+}-binding loop within the EF hand domains of NUCB1 with similar regions from several known Ca^{2+}-binding proteins is shown. The alignment highlights the presence of highly conserved aspartic acid at the beginning (pink) and glumatic acid (brown) at the end of the loop sequence. Interestingly, NUCB1 EF hand 1 loop sequence contains a conserved glycine at the 6^{th} position (green) whereas it is an Arg (blue) in the EF hand 2 sequence. The respective aspartic and glutamic acid residues were mutated to generate *s*NUCB1(tetramutant). **(B)** The secondary structure analysis for *s*NUCB1(tetramutant) (8 μ M) was done using CD spectroscopy. The recorded spectrum shows that *s*NUCB1(tetramutant) is fully folded with a majorly helical secondary structure highlighted by the characteristic minima at 208 nm and 222 nm respectively. The inset shows the thermal unfolding transition for 8 μ M recombinant *s*NUCB1(tetramutant) monitored by recording CD signal at 222 nm at a heating rate of 1 ^{o}C / min. The trace is indicative of a multistep non-cooperatively folded protein with an apparent T_m of 48.7 ^{o}C. *s*NUCB1(tetramutant) was generated to nullify the Ca^{2+}-binding ability of *s*NUCB1. Thus, **(C)** we used isothermal titration calorimetry (ITC) to measure the Ca^{2+}-binding affinity of *s*NUCB1(tetramutant). 5 μl aliquots of 500 μ M $CaCl_2.6H_2O$ were injected into the reaction cell containing 50 μ M solution of *s*NUCB1(tetramutant) at 25 ^{o}C and the heat released per injection was recorded. The inset shows effectively no release of energy as Ca^{2+} is injected into the sample cell containing *s*NUCB1(tetramutant), indicating the absence of any binding event.

Figure 2.4

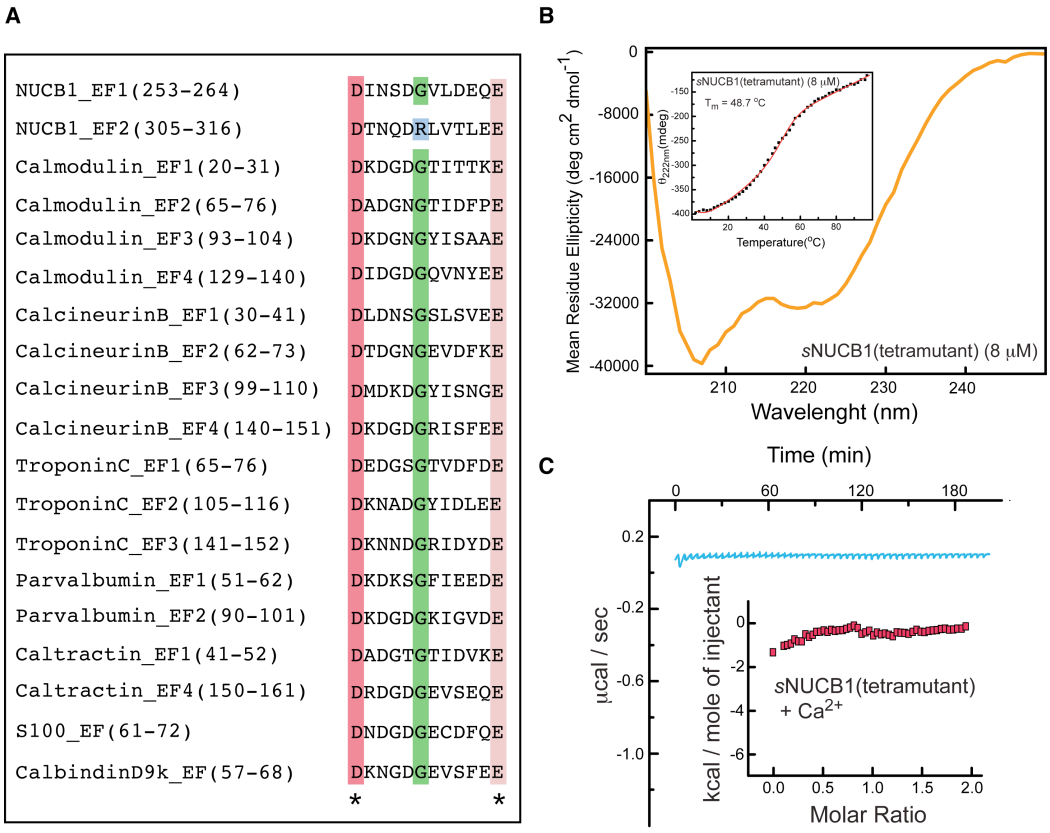
A
NUCB1_EF1(253-264) DINSDGVLDEQE
NUCB1_EF2(305-316) DTNQDRLVTLEE
Calmodulin_EF1(20-31) DKDGDGTITTKE
Calmodulin_EF2(65-76) DADGNGTIDFPE
Calmodulin_EF3(93-104) DKDGNGYISAAE
Calmodulin_EF4(129-140) DIDGDGQVNYEE
CalcineurinB_EF1(30-41) DLDNSGSLSVEE
CalcineurinB_EF2(62-73) DTDGNGEVDFKE
CalcineurinB_EF3(99-110) DMDKDGYISNGE
CalcineurinB_EF4(140-151) DKDGDGRISFEE
TroponinC_EF1(65-76) DEDGSGTVDFDE
TroponinC_EF2(105-116) DKNADGYIDLEE
TroponinC_EF3(141-152) DKNNDGRIDYDE
Parvalbumin_EF1(51-62) DKDKSGFIEEDE
Parvalbumin_EF2(90-101) DKDGDGKIGVDE
Caltractin_EF1(41-52) DADGTGTIDVKE
Caltractin_EF4(150-161) DRDGDGEVSEQE
S100_EF(61-72) DNDGDGECDFQE
CalbindinD9k_EF(57-68) DKNGDGEVSFEE
* *
B
Mean Residue Ellipticity (deg cm2 dmol-1)
0
-8000
-16000
-24000
-32000
-40000
210
220
230
240
Wavelenght (nm)
sNUCB1(tetramutant) (8 μM)
sNUCB1(tetramutant) (8 μM)
Tm = 48.7 °C
θ222nm (mdeg)
Temperature(°C)
C
Time (min)
0
60
120
180
0.2
-0.2
-0.6
-1.0
μcal / sec
kcal / mole of injectant
sNUCB1(tetramutant)
+ Ca2+
0.0
0.5
1.0
1.5
2.0
Molar Ratio

towards inhibiting hIAPP fibril formation we incubated equimolar amounts of hIAPP with *s*NUCB1(tetramutant) in the absence and presence of 3 mM Ca^{2+} in the reaction mixture. Samples were withdrawn at 15 min, 30 min and 60 min time points and analyzed using TEM (Fig.2.5). As shown, *s*NUCB1(tetramutant) effectively inhibits hIAPP fibril formation in the absence of Ca^{2+} since no fibrillar aggregates are observed for the 60 min sample (Fig.2.5A). Intriguingly, unlike *s*NUCB1, *s*NUCB1(tetramutant) also inhibits fibril formation in the presence of excess Ca^{2+} in the reaction mixture. TEM images of the samples withdrawn at various time points show complete absence of amyloid fibrils (Fig.2.5B). Hence the engineered *s*NUCB1(tetramutant) effectively inhibits hIAPP fibrils formation but unlike *s*NUCB1 is insensitive to the presence of Ca^{2+} in the reaction mixture.

2.2.4 *s*NUCB1 and *s*NUCB1(tetramutant) disaggregate hIAPP fibrils

hIAPP rapidly aggregates *in vitro* to form amyloid fibrils. As shown earlier, *s*NUCB1 and *s*NUCB1(tetramutant) effectively inhibit hIAPP fibril formation (Fig.2.3,2.5). We further investigated the functional ability of these proteins towards disaggregating preformed fibrils. 32 μM hIAPP was incubated in 20 mM Tris pH 7.5 buffer for 60 min to form mature amyloid fibrils. Thereafter, equimolar amounts of Ca^{2+}-free *s*NUCB1 or *s*NUCB1(tetramutant) were added to the reaction mixture and samples were withdrawn after 15 min, 30 min and 60 min for analysis using TEM.

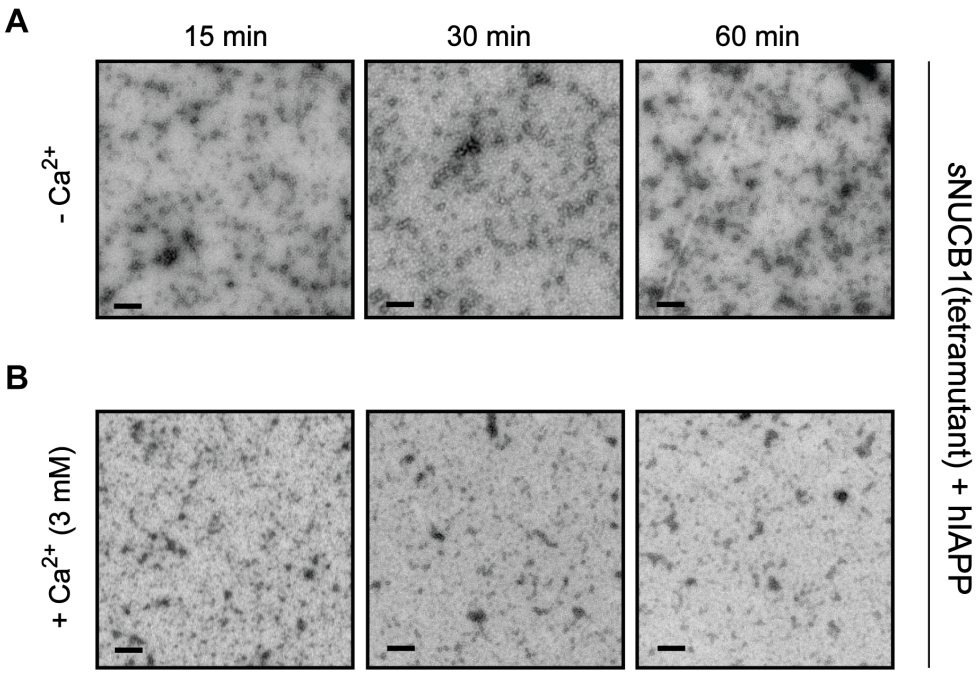

Figure 2.5. Ca^{2+} does not prevent *s*NUCB1(tetramutant) from inhibiting hIAPP aggregation. We monitored aggregation of hIAPP in the presence of *s*NUCB1(tetramutant). **(A)** In the absence of Ca^{2+}, equimolar amount (32 μ M) of *s*NUCB1(tetramutant) preincubated with hIAPP effectively inhibit aggregation of hIAPP into fibrils. The micrographs corresponding to 15 min and 30 min show the presence of oligomeric and protofibrillar species that do not progress to form fibrils as shown by the micrograph corresponding to the 60 min sample. **(B)** Interestingly, even in the presence of excess Ca^{2+} (3 mM in the reaction mixture, *s*NUCB1(tetramutant) is still effective at inhibiting fibril formation. The micrographs for the samples withdrawn at 15 min, 30 min and 60 min time points show complete absence of fibril formation. The scale bar on each micrograph represents 200 nm.

The micrographs show that in the absence of Ca^{2+} both *s*NUCB1 and *s*NUCB1(tetramutant) effectively disaggregate hIAPP fibrils into smaller molecular species within 15 min. These species do not associate to form fibrils even at 60 min time point (Fig.2.6A and B). Interestingly, Ca^{2+}-binding nullifies the functional ability of *s*NUCB1 towards disaggregating hIAPP fibrils. TEM images corresponding to samples withdrawn after addition of equimolar amount of *s*NUCB1 to fibrils in the presence of 3 mM Ca^{2+} show fibrillar species in the micrographs at all monitored time points. Intriguingly, *s*NUCB1(tetramutant) is insensitive to the presence of Ca^{2+} in the reaction mixture and disaggregates hIAPP fibrils even in the presence of 3 mM Ca^{2+}. TEM images for 15 min, 30 min and 60 min time point show that *s*NUCB1(tetramutant) effectively disaggregates hIAPP fibrils into smaller molecular species within 15 min which continue to exist even at 60 min (Fig2.6A and B). Thus Ca^{2+}-binding disrupts the ability of sNUCB1 to disaggregate amyloid fibrils but *s*NUCB1(tetramutant) continues to perform its function even in the presence of excess Ca^{2+} in the reaction mixture.

Figure 2.6. Ca^{2+} prevents *s*NUCB1 but not *s*NUCB1(tetramutant) from disaggregating hIAPP fibrils. We monitored disaggregation of hIAPP fibrils in the presence of (A) *s*NUCB1 or (B) *s*NUCB1(tetramutant). In the absence of Ca^{2+}, equimolar amount (32 μM) of *s*NUCB1 or *s*NUCB1(tetramutant) incubated with hIAPP fibrils effectively disaggregates them into smaller molecular species. The disaggregation was observed within 15 min of incubation and continues with effective disaggregation seen in 30 min and 60 min micrographs corresponding to samples withdrawn from the reaction mixture. However, when excess Ca^{2+} (3 mM) is present in the reaction mixture, *s*NUCB1 is unable to disaggregate hIAPP fibrils as shown by the presence of aggregates characteristic of fibrils for all monitored time points. Unlike *s*NUCB1, *s*NUCB1(tetramutant) is still effective at disaggregating hIAPP fibrils even in the presence of 3 mM Ca^{2+} in the reaction mixture. The microgrpahs for the 15 min, 30 min and 60 min show complete absence of any fibrillar aggregates, indicating that potent activity of *s*NUCB1(tetramutant) persists even in the presence of Ca^{2+}. The scale bar represents 200 nm.

Figure 2.6

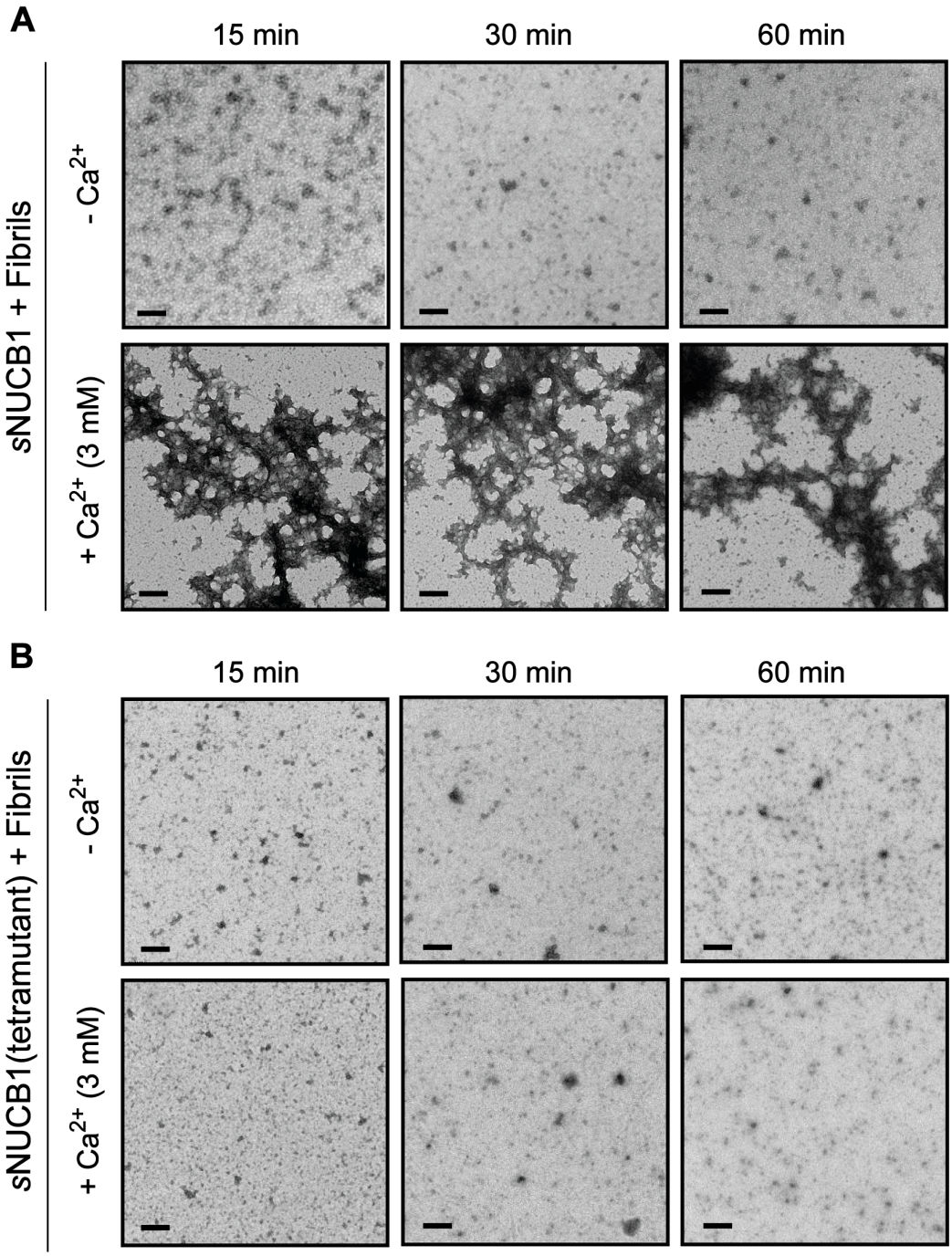
A
15 min
30 min
60 min
sNUCB1 + Fibrils
- Ca2+
+ Ca2+ (3 mM)
B
15 min
30 min
60 min
sNUCB1(tetramutant) + Fibrils
- Ca2+
+ Ca2+ (3 mM)

2.2.5 Ca^{2+}-free *s*NUCB1 inhibits hIAPP fibrillization along any stage of amyloid formation pathway

We monitored the aggregation of 32 μM hIAPP in 20 mM Tris pH 7.5 using thioflavin-T binding assay (Fig.2.7). The aggregation curve represented by solid spheres shows the nucleation phase in blue, growth phase in green and the saturation phase corresponding to formation of mature amyloid fibrils in yellow. In order to monitor the functional ability of Ca^{2+}-free *s*NUCB1 towards inhibiting fibril formation when added at different states along the hIAPP aggregation pathway, 32 μM Ca^{2+}-free *s*NUCB1 was individually added to hIAPP aggregation reaction in the nucleation phase at 7 min, middle of growth phase at 13 min and in the steady-state phase at 40 min (pink spheres). As a control, TEM micrographs for samples prior to the addition of Ca^{2+}-free *s*NUCB1 show presence of oligomers at 7 min, protofibrillar intermediates in 13 min and mature fibrils in 40 min. Subsequently each of these species was incubated with equimolar amount (32 μM) of Ca^{2+}-free *s*NUCB1 and samples were withdrawn after 60 min for TEM analysis (Fig.2.7). Interestingly, TEM analysis for each reaction mixture shows complete absence of amyloid fibrils. This suggests that Ca^{2+}-free *s*NUCB1 is effective at inhibiting fibril formation even when added at any intermediate state along the aggregation pathway. Moreover, as shown earlier, once the fibrils are formed Ca^{2+}-free *s*NUCB1 can effectively disaggregate them into smaller molecular species, which do not aggregate into amyloid fibrils.

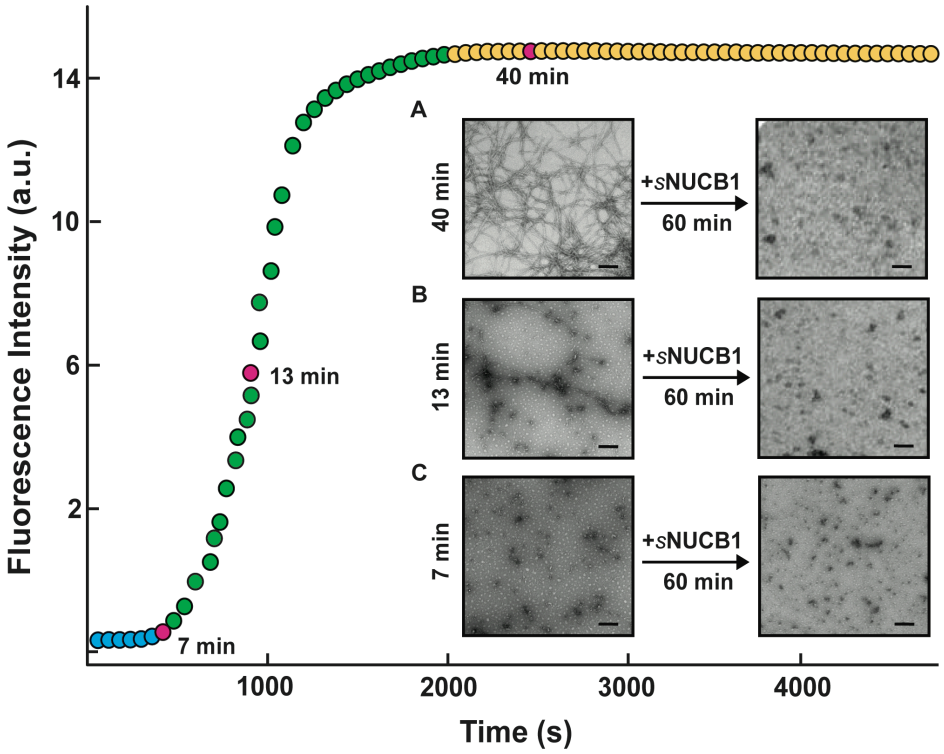

Figure 2.7. Ca^{2+}-free *s*NUCB1 inhibits hIAPP amyloidogenesis in a state-independent manner. (A) We monitored hIAPP (32 μM) aggregation using thioflavin-T (32 μM) with the lag phase in blue, growth phase in green and stationary phase in yellow. The circles in pink indicate the corresponding time points at which *s*NUCB1 was added to the aggregation reaction. hIAPP (32 μM) aggregation was allowed to proceed to **(A)** nucleation phase at 7 min, **(B)** mid-point of growth phase at 15 min and **(C)** initiation of stationary phase at 40 min after which equimolar amount (32 μM) of Ca^{2+}-free *s*NUCB1 was added to the reaction mixture. TEM images were collected immediately before addition of *s*NUCB1 and 60 min after incubation with Ca^{2+}-free *s*NUCB1. The micrographs corresponding to samples withdrawn at 60 min after addition show that Ca^{2+}-free *s*NUCB1 both effectively inhibits the progression of seeds into mature fibrils and also disaggregates amyloid fibrils. The scale bar represents 200 nm.

Thus Ca^{2+}-free *s*NUCB1 possesses the unique ability to inhibit amyloidogenesis of hIAPP at any stage of fibril formation.

2.2.6 Ca^{2+}-free *s*NUCB1 inhibits fibril formation by stabilizing hIAPP prefibrillar species

Our earlier results showed that Ca^{2+}-free *s*NUCB1 effectively inhibits hIAPP fibril formation and TEM analysis of samples withdrawn from the reaction mixture after 60 min show the presence of molecular species much smaller than the mature fibrils. Hence to characterize these observed molecular species we incubated 32 μM of Ca^{2+}-free *s*NUCB1 with 32 μM hIAPP in 20 mM Tris pH 7.5 buffer at room temperature for 60 min. Thereafter, we injected 200 μ l of reaction mixture onto a buffer equilibrated Superose6 10 / 30 GL column and the elution profile corresponding to absorbance at 280 nm was recorded (Fig.2.8A, blue curve). Since hIAPP does not have any Trp residues, absorbance at 280 nm must primarily result from contribution of Trp residues of *s*NUCB1. Injection of 32 μM solution of Ca^{2+}-free *s*NUCB1 alone onto the column generates a peak centered at 12 ml (Fig.2.8A, dotted red curve) (Peak2). In order to determine the molecular constituents of Peak1 and Peak2, we fractionated the individual peaks and performed dot blot analysis. The results show that Ca^{2+}-free *s*NUCB1 was present in both Peak1 and Peak2 fractions whereas hIAPP was present only in the Peak1 fraction

Figure 2.8. Biophysical characterization of Ca^{2+}-free *s*NUCB1 stabilized hIAPP protofibrillar species. (A) We used size exclusion chromatography using Superose6 10/30 GL column to elute Ca^{2+}-free *s*NUCB1 alone (32 μM) (red dotted curve). Thereafter a 60 min sample from a reaction mixture with equimolar concentration of hIAPP and Ca^{2+}-free sNUCB1 incubated at t = 0 was injected and the fractions corresponding to the eluting peaks were collected (blue curve). Ca^{2+}-free *s*NUCB1 alone elutes in Peak2 centered at 12 ml while the reaction mixture gives an additional peak namely Peak1 eluting at 7.8 ml. We further investigated the molecular constituents within each peak using dot-blot assay. **(B)** We blotted 5 μl of Peak1 and Peak2 fractions on a PVDF membrane and probed each of them with either anti-*s*NUCB1 antibody or anti-hIAPP antibody. The upper blot shows that *s*NUCB1 is present in both peak fractions whereas the lower blot shows that hIAPP is present only in Peak1 and not Peak2 fractions. As controls, hIAPP and *s*NUCB1 were blotted to show that the antibodies are specific with no cross-reactivity. Thereafter **(C)** we used TEM to analyze both Peak1 and Peak2 fractions. Micrograph corresponding to Peak1 shows the presence of oligomeric and prefibrillar species whereas Peak2 fraction shows no higher order structures. As a control, hIAPP fibrils formed within 60 min with hIAPP alone are shown in the inset for micrograph corresponding to Peak1. **(D)** We used both multi-angle light scattering (MALS) (left) and dynamic light scattering (DLS) (right) analysis across Peak1 and Peak2 respectively. MALS analysis across Peak1 estimates a molecular mass in the range of 2 - 6 MDa and DLS predicts hydrodynamic radii in the range of 22 - 42 nm. These numbers point towards an isolated *s*NUCB1-bound prefibrillar species of hIAPP. In addition, MALS analysis of Peak2 predicts a molecular mass in the range of 97 - 99 kDa, which corresponds to the molecular mass of a dimer of Ca^{2+}-free *s*NUCB1. DLS analysis gives an invariant hydrodynamic radius of 6.2 nm, which is characteristic for Ca^{2+}-free *s*NUCB1 dimer. Thereafter we utilized STEM to quantitatively determine a mass / unit length (M / L) distribution of

prefibrillar species in Peak1 fraction. **(E)** The analysis shows the presence of prefibrillar species with M / L ranging from 1 - 7 kDa / Å with species predominantly ranging from 2 - 5 kDa / Å. The adjacent micrograph shows a typical large-angle dark-field cryo-STEM image of Peak1 fraction with tobacco mosaic virus (TMV) helical rod as the calibration control for data analysis. The scale bar represents 100 nm. Furthermore, the images below represent examples of prefibrillar species observed in STEM wherein the width of each box represents 200 nm. **(F)** We further investigated the stability of the Peak1 fraction by incubating it at room temperature for 7 days with constant stirring. Thereafter, we injected the reaction mixture onto a buffer pre-equilibrated Superose6 10/30 GL column and the elution profile at 280 nm was recorded. The trace shows that Peak1 is reproduced suggesting that Ca^{2+}-free *s*NUCB1 bound hIAPP prefibrillar species is highly stable and does not proceed to form fibrillar aggregates as shown by the TEM of the eluting Peak1 fraction.

Figure 2.8

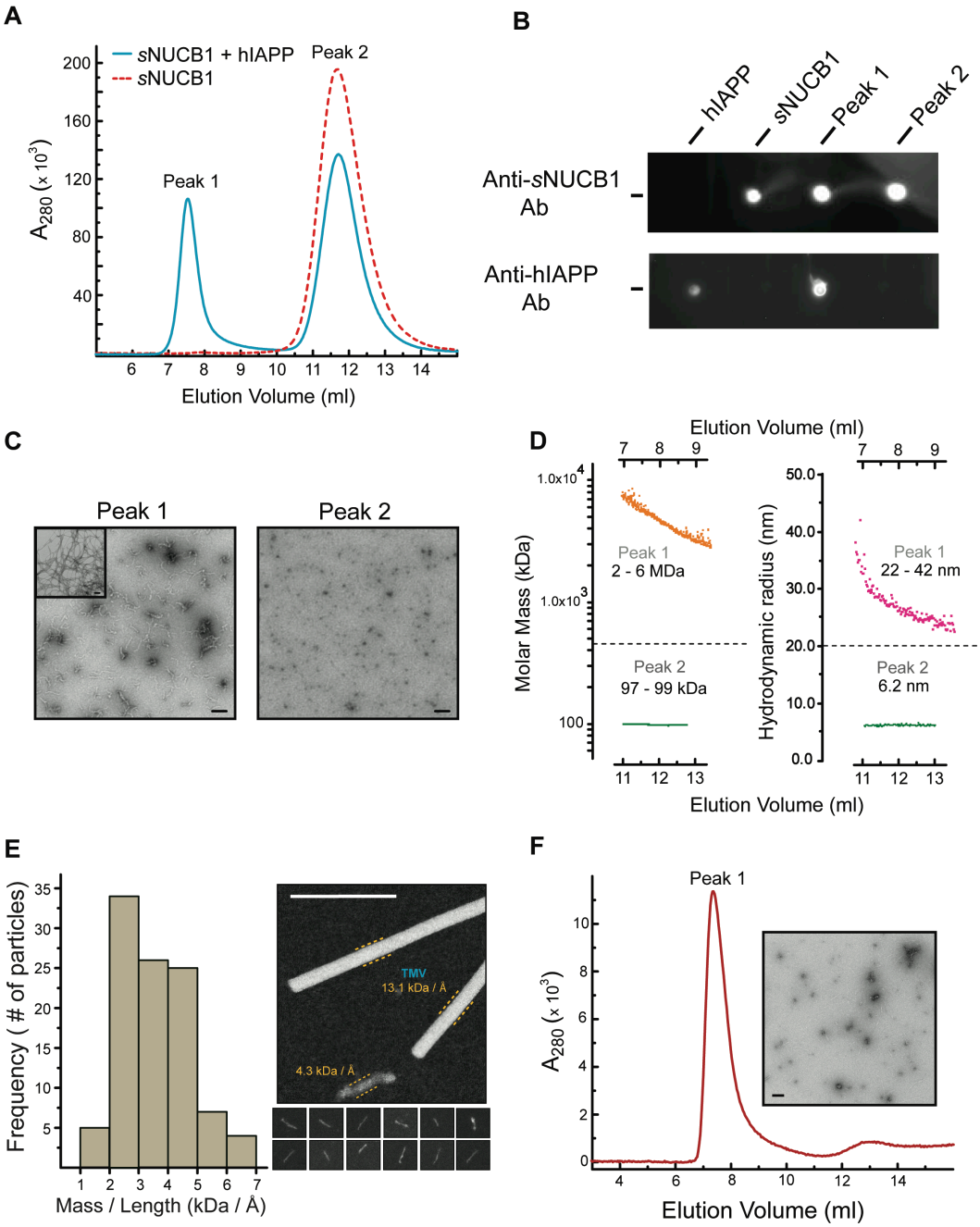
A
sNUCB1 + hIAPP
sNUCB1
Peak 1
Peak 2
A_{280} (x 10^3)
Elution Volume (ml)
B
hIAPP
sNUCB1
Peak 1
Peak 2
Anti-sNUCB1 Ab
Anti-hIAPP Ab
C
Peak 1
Peak 2
D
Elution Volume (ml)
Molar Mass (kDa)
Peak 1
2 - 6 MDa
Peak 2
97 - 99 kDa
Hydrodynamic radius (nm)
Peak 1
22 - 42 nm
Peak 2
6.2 nm
E
Frequency (# of particles)
Mass / Length (kDa / Å)
TMV
13.1 kDa / Å
4.3 kDa / Å
F
Peak 1
A_{280} (x 10^3)
Elution Volume (ml)

(Fig.2.8B). As a control, Ca^{2+}-free *s*NUCB1 and hIAPP alone were blotted onto the membrane to test for the cross-reactivity of each antibody. Both Peak1 and Peak2 fractions were further subjected to TEM analysis. The corresponding micrograph shows the presence of only prefibrillar species in Peak1 fraction whereas Peak2 fraction shows a typical image corresponding to Ca^{2+}-free *s*NUCB1 without any aggregates (Fig.2.8C).

In order to characterize the species constituting the Peak1 and Peak2 fractions, we performed multi-angle light scattering (MALS) and dynamic light scattering (DLS) analysis to estimate the average molecular mass and the hydrodynamic radii of the eluting species. MALS analysis across Peak1 estimates a molecular mass in the range of 2 - 6 MDa for the eluting species with the hydrodynamic radii of 22 - 42 nm obtained from the DLS analysis across Peak1 (Fig.2.8D). These numbers suggest that Ca^{2+}-free *s*NUCB1 binds to and stabilizes a high molecular mass prefibrillar hIAPP aggregate. Similar analysis across Peak2 fraction gave a 97 - 99 kDa molecular mass species with a hydrodynamic radii of 6.2 nm (Fig.2.8D), characteristic for a dimer of Ca^{2+}-free *s*NUCB1 alone (Fig.1.4). We further performed scanning transmission electron microscopy (STEM) analysis on Peak1 fraction to estimate the mass per unit length (M / L) for the observed prefibrillar species. Dark field images were collected for Peak1 fraction with Tobacco Mosaic Virus (TMV) as an internal standard and PCMass30 software was used for image analysis. The M / L data was

pooled and is presented in histograms. A typical dark field micrograph is shown with several prototypical examples with mass densities corresponding to the prefibrillar species shown below it. The data shows that Peak1 fraction comprises of molecular species with M / L ranging from 1 - 7 kDa / Å with predominant species varying from 2 - 5 kDa / Å (Fig.2.8E). Earlier, similar analysis by Goldsbury *et al.* on 100 nm long hIAPP fibril segments reported a M / L in the range of 2 - 5 kDa / Å with a median at 3 kDa / Å (*86*). This suggests that *s*NUCB1 stabilized prefibrillar species is comparable in mass density to the reported protofibrils. However, these 40-80 nm long prefibrillar species are stabilized by bound *s*NUCB1. Thus the M / L contributed by hIAPP alone to the prefibrillar species would be less when compared to protofibrils alone. We thus refer to this species as prefibrillar. We further investigated the stability of these Ca^{2+}-free *s*NUCB1 bound prefibrillar species by incubating Peak1 fraction at room temperature to facilitate their association into mature fibrils. The reaction mixture was constantly stirred for 7 days after which it was injected onto a buffer equilibrated Superose6 10 / 30 GL column. Interestingly, we were able to reproducibly generate the Peak1 as earlier. TEM analysis of the sample before and after elution from the column shows the characteristic prefibrillar species as observed before for Peak1 (Fig.2.8F). This shows that Ca^{2+}-free *s*NUCB1 bound prefibrillar species is highly stable and does not associate further to form fibrils. These biophysical experiments prove that Ca^{2+}-free *s*NUCB1

inhibits hIAPP fibril formation by stabilizing a high molecular mass prefibrillar species of hIAPP.

As a control, we performed ITC experiments with Pramlintide (Fig2.1), a non-aggregating analog of hIAPP. We injected Pramlintide into a reaction cell with buffered solution of Ca^{2+}-free sNUCB1 and heat released per injection was recorded. The result shows that Pramlintide does not interact with Ca^{2+}-free sNUCB1 (Fig.2.9A). In addition, we also performed SEC experiments similar to as shown in Fig.2.8A. We incubated 32 μM of pramlintide with equimolar amount of Ca^{2+}-free sNUCB1 for 3 h after which the reaction mixture was injected onto a buffer equilibrated Superose6 10 / 30 GL column. Unlike earlier, we did not observe an elution profile with Peak1 suggesting that Ca^{2+}-free sNUCB1 interacts only with an aggregated form of hIAPP and probably not the monomeric form (Fig.2.9B).

2.2.7 *s*NUCB1 does not possess protease activity and cannot cleave hIAPP

The above-proposed mechanism of inhibition of hIAPP fibril formation does not rule out the possibility of a proteolytic activity of *s*NUCB1. An alternate hypothesis might be that *s*NUCB1 proteolytically cleaves hIAPP into smaller fragments, which can still aggregate to form protofibrils

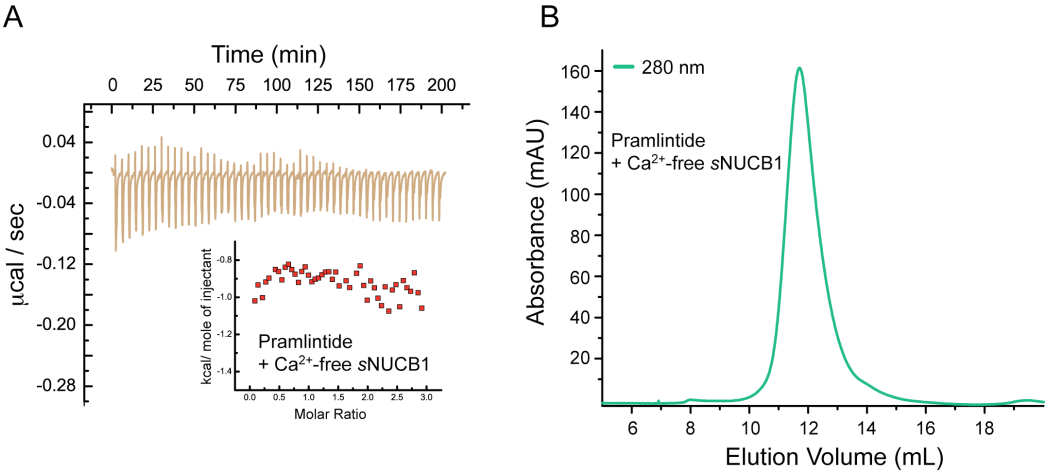

Figure 2.9. Pramlintide does not bind to Ca^{2+}-free *s*NUCB1. (A) We used isothermal titration calorimetry (ITC) to measure the binding affinity of the non-aggregating analog of hIAPP namely Pramlintide to Ca^{2+}-free *s*NUCB1. 5 µl aliquots of 600 µ M Pramlintide solution were injected into the reaction cell containing 40 µM solution of Ca^{2+}-free *s*NUCB1 at 25 ^{o}C and the heat released per injection was recorded. The inset shows effectively no release of energy as Pramlintide is injected into the reaction cell containing Ca^{2+}-free *s*NUCB1, indicating the lack of any binding event. In addition, **(B)** we incubated Pramlintide with equimolar amount (32 µM) of Ca^{2+}-free *s*NUCB1 for 5 h. 200 µl of the reaction was injected onto a buffer equilibrated Superose6 10 / 30 GL column and the chromatogram corresponding to sample absorbance at 280 nm was recorded. The plot shows the presence of only a single peak centered at the characteristic volume (~12 ml) for elution of Ca^{2+}-free *s*NUCB1 alone. The absence of a lower elution volume peak suggests that Pramlintide does not aggregate into higher order structures due to which Ca^{2+}-free *s*NUCB1 does not bind to it.

Figure 2.10. Ca^{2+}-free *s*NUCB1 / *s*NUCB1(tetramuant) do not possess protease activity. (A) We incubated 10 µg of BODIPY FL-Casein substrate in digestion buffer (10 mM Tris pH 7.8, 100 µM NaN_3) for 5 min at 25 ^oC followed by time-based fluorescence emission measurement with λ_{ex} = 505 nm and λ_{em} = 513 nm. After 60 sec, 100 µg of Ca^{2+}-free *s*NUCB1 (green) or 10 µg of Trypsin (orange) was added to the reaction mixture and enhancement in fluorescence was recorded. As shown, addition of Trypsin causes significant enhancement in the observed fluorescence intensity whereas even 10-fold excess of Ca^{2+}-free *s*NUCB1 did not result in any notable enhancement in fluorescence intensity. This suggests that Ca^{2+}-free *s*NUCB1 possibly does not proteolytically cleave BODIPY FL-Casein. In addition, **(B)** protease digestion assays were setup with 20 µg of either Trypsin or *s*NUCB1(tetramuant) incubated with 20 µg BODIPY FL-Casein substrate and samples were withdrawn at different subsequent time points for SDS-PAGE analysis. The Coomassie stained gel shows that Trypsin rapidly cleaves the substrate into smaller molecular fragments whereas *s*NUCB1(tetramutant) is unable to cleave the substrate even after 60 min of incubation. Similarly, **(C)** 30 µg BODIPY FL-Casein substrate was incubated with 3 µg or 30 µg of Ca^{2+}-free *s*NUCB1 and samples were withdrawn after 5 min and 60 min for SDS-PAGE analysis. As earlier, the Coomassie stained gel image shows that similar to *s*NUCB1(tetramutant), Ca^{2+}-free *s*NUCB1 also does not possess any proteolytic activity. In addition, **(D)** the proteolytic activity of Ca^{2+}-free *s*NUCB1 towards hIAPP was also investigated using LC-MS. We incubated equimolar amount (32 µM) of Ca^{2+}-free *s*NUCB1 with hIAPP and sample was withdrawn after 2 h for analysis using LC-MS. The mass spectrum shows characteristic peak pattern for *s*NUCB1 (pink) and a single peak for hIAPP (blue). The spectrum shows a complete absence of any smaller fragments of hIAPP confirming that Ca^{2+}-free *s*NUCB1 does not protealytically cleave hIAPP.

Figure 2.10

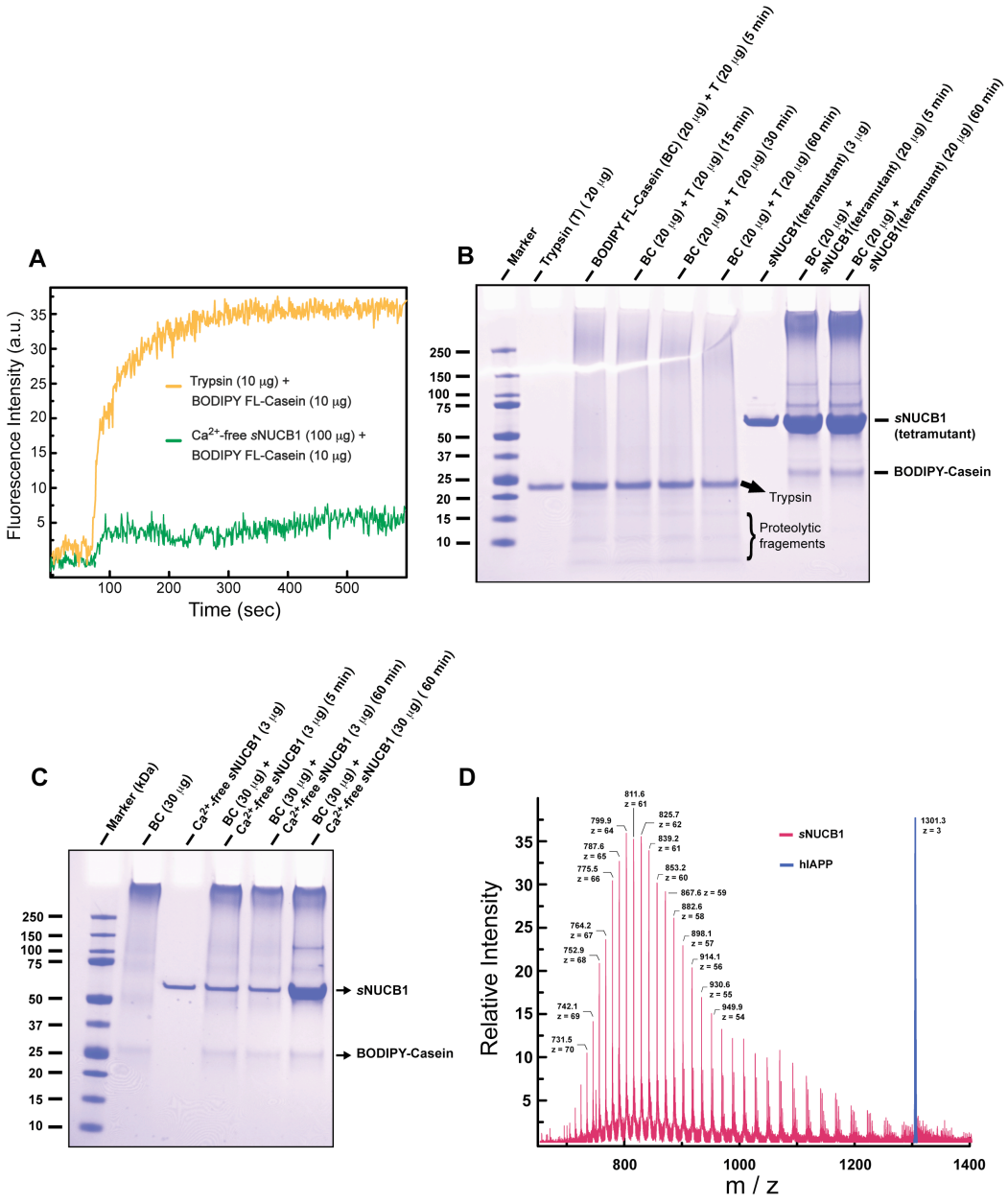
A
Fluorescence Intensity (a.u.)
Time (sec)
Trypsin (10 μg) + BODIPY FL-Casein (10 μg)
Ca2+-free sNUCB1 (100 μg) + BODIPY FL-Casein (10 μg)
B
Marker
Trypsin (T) (20 μg)
BODIPY FL-Casein (BC) (20 μg) + T (20 μg) (5 min)
BC (20 μg) + T (20 μg) (15 min)
BC (20 μg) + T (20 μg) (30 min)
BC (20 μg) + T (20 μg) (60 min)
sNUCB1(tetramutant) (3 μg)
BC (20 μg) + sNUCB1(tetramutant) (20 μg) (5 min)
BC (20 μg) + sNUCB1(tetramuant) (20 μg) (60 min)
sNUCB1 (tetramutant)
BODIPY-Casein
Trypsin
Proteolytic fragements
C
Marker (kDa)
BC (30 μg)
Ca2+-free sNUCB1 (3 μg)
BC (30 μg) + Ca2+-free sNUCB1 (3 μg) (5 min)
BC (30 μg) + Ca2+-free sNUCB1 (3 μg) (60 min)
BC (30 μg) + Ca2+-free sNUCB1 (30 μg) (60 min)
sNUCB1
BODIPY-Casein
D
Relative Intensity
m / z
sNUCB1
hIAPP

similar to the observed *s*NUCB1-bound prefibrillar species. We thereby investigated for any proteolytic activity of Ca^{2+}-free *s*NUCB1 by first using a fluorescence based protease assay with BODIPY FL-Casein as the substrate. In principle, if Ca^{2+}-free *s*NUCB1 proteolytically cleaves Casein, the intrinsic quenching of the BODIPY fluorophore label on Casein would be relieved, resulting in enhanced fluorescence readout. As shown in figure 2.10A, addition of stoichiometric amount of Trypsin, a serine-protease, to a buffered solution of BODIPY FL-Casein substrate causes a significant enhancement in the fluorescence intensity. In contrast, addition of even 10-fold molar excess of Ca^{2+}-free *s*NUCB1 does not result in any notable enhancement in the fluorescence intensity of labeled Casein. SDS-PAGE analysis of the samples withdrawn from the reaction mixtures with equimolar or excess Ca^{2+}-free *s*NUCB1 incubated with BODIPY FL-Casein substrate show that unlike Trypsin (Fig.2.10B), neither *s*NUCB1(tetramuant) (Fig.2.10B) nor Ca^{2+}-free *s*NUCB1 (Fig.2.10C) cleave BODIPY FL-Casein. Reaction mixtures containing Trypsin show generation of lower molecular mass fragments due to proteolytic cleavage of BODIPY FL-Casein which is not observed upon incubation with either *s*NUCB1(tetramuant) or Ca^{2+}-free *s*NUCB1. However, to directly rule out the proteolysis of hIAPP monomer by Ca^{2+}-free *s*NUCB1 as a contributing factor towards inhibition of fibril formation, we incubated Ca^{2+}-free *s*NUCB1 with equimolar concentration (32 μM) of hIAPP for 45 min and subjected the reaction mixture to liquid

chromatography-mass spectrometry (LC-MS). As shown in figure 2.10D, the mass spectrum shows the peaks characteristic for *s*NUCB1 (pink spectrum) and a peptide peak for hIAPP alone (purple peak). This suggests that inhibition of hIAPP aggregation by Ca^{2+}-free *s*NUCB1 does not involve proteolysis of hIAPP as no other cleavage products for hIAPP were observed. Thus *s*NUCB1 inhibits hIAPP fibril formation by capping the ends of a high molecular mass soluble prefibrillar species of hIAPP and thereby inhibiting their further association into mature amyloid fibrils.

NUCB1 is a ubiquitously expressed protein, which is found both intracellularly and extracellularly. The above results show that NUCB1 is not an intracellular endopeptidase but since NUCB1 possesses a N-terminal (NT) signal sequence and is found extracellularly, we could not rule out the possibility of it being an extracellular protease like a matrix metalloproteinase (MMP). MMPs are extracellular endopeptidases whose ability to proteolytically cleave their substrates is dependent on their ability to bind to Zn^{2+}. Hence in order to test for matrix metalloproteinase activity of *s*NUCB1, we first measured the Zn^{2+}-binding ability of Ca^{2+}-free *s*NUCB1 using ITC. 5 µl aliquots of 400 µM $ZnCl_2$ solution were injected into a buffered solution of 50 µM Ca^{2+}-free *s*NUCB1 in the reaction cell and heat released per injection was recorded. The data fit to a "one-set-of-site" model show binding of a monomer of *s*NUCB1 to one Zn^{2+}-cation (N = 0.99 ± 0.08) with a K_d value of 22 ± 1.89 µM

Figure 2.11. Ca^{2+}-free *s*NUCB1 binds to Zn^{2+} but is not a Matrix Metalloproteinase. (A) We used isothermal titration calorimetry (ITC) to measure the Zn^{2+}-binding affinity of *s*NUCB1. 5 µl aliquots of 400 µM $ZnCl_2$ were injected into the reaction cell containing 50 µM solution of Ca^{2+}-free *s*NUCB1 at 25 ^{o}C and the heat released per injection was recorded. The *inset* shows a fit of the data using "one-set of sites" model using the concentration for Ca^{2+}-free *s*NUCB1 monomer as the interacting subunit. The calculated dissociation constant for Zn^{2}-binding to Ca^{2+}-free *s*NUCB1 was 22µM ± 1.96 µM with a stoichiometry of N = 0.99 ± 0.07 suggesting that each subunit of a dimer of Ca^{2+}-free *s*NUCB1 binds to one Zn^{2+}-cation. Thereafter we used FRET based assay to investigate the MMP activity of Zn^{2+}-bound *s*NUCB1. Sixteen synthetic FRET peptide substrates were incubated with either (B) 15 ng MMP-1, (C) 7.5 ng Zn^{2+}-bound *s*NUCB1 or (D) 750 ng Zn^{2+}-bound *s*NUCB1 and the fluorescence readout was recorded at 10 min intervals for 90 min at room temperature (λ_{ex} = 490 nm, λ_{em} = 520 nm). The results show that (B) incubation of the peptide substrates with MMP-1 results in significant enhancement in the fluorescence readout for a number of substrates due to their proteolytic cleavage. However incubation with both (C) 7.5 ng and (D) 750 ng Zn^{2+}-bound *s*NUCB1 did not cause any enhancement. The fluorescence emission recorded for the substrate alone was subtracted from each monitored time point. The results show that unlike MMP-1, Zn^{2+}-bound *s*NUCB1 does not possess any MMP activity.

Figure 2.11

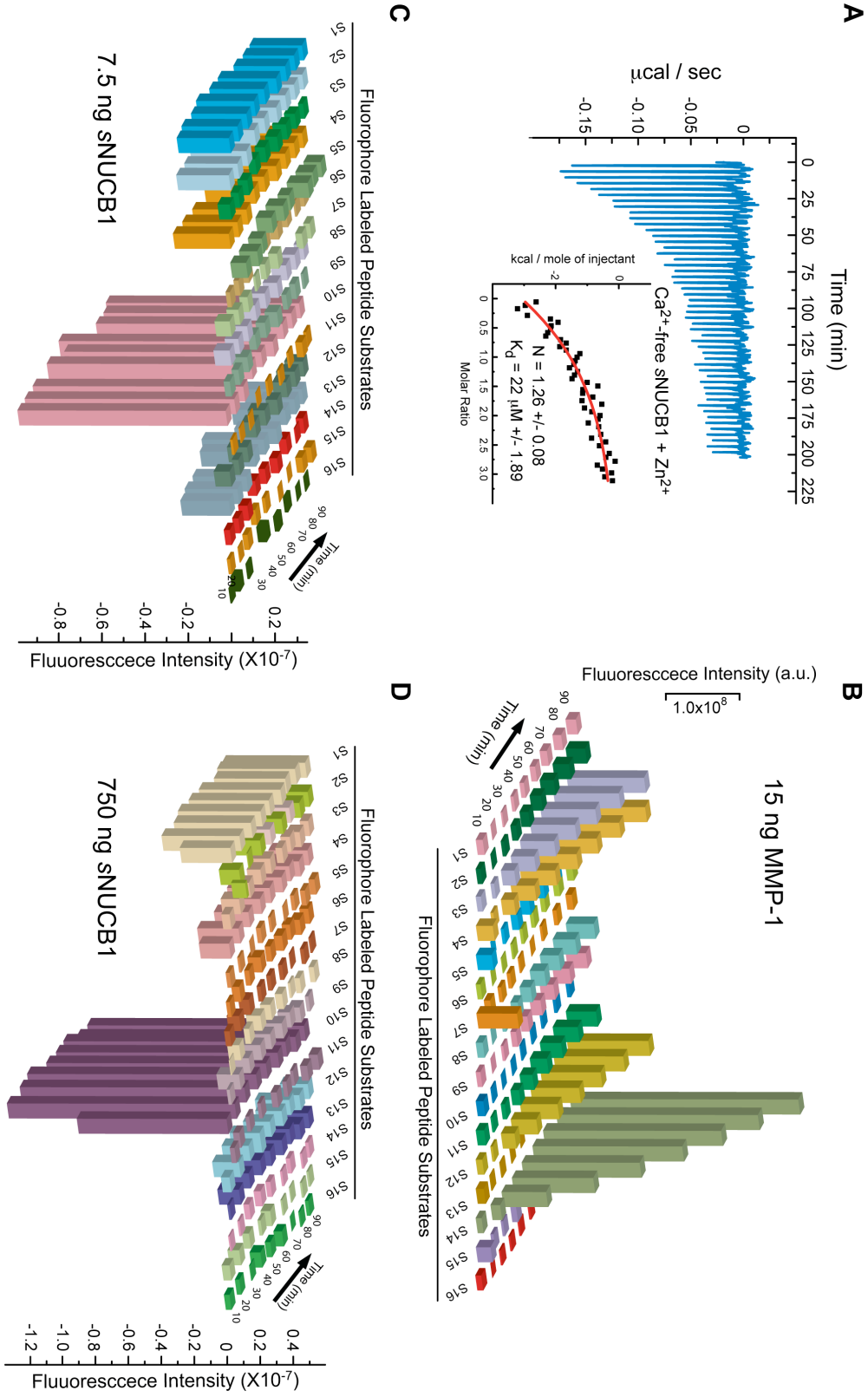
A
µcal / sec
Time (min)
Ca2+-free sNUCB1 + Zn2+
kcal / mole of injectant
Molar Ratio
N = 1.26 +/- 0.08
Kd = 22 µM +/- 1.89
B
15 ng MMP-1
Fluuoresccece Intensity (a.u.)
1.0x10^8
Time (min)
Fluorophore Labeled Peptide Substrates
C
7.5 ng sNUCB1
Fluuoresccece Intensity (X10-7)
Time (min)
Fluorophore Labeled Peptide Substrates
D
750 ng sNUCB1
Fluuoresccece Intensity (X10-7)
Time (min)
Fluorophore Labeled Peptide Substrates

(Fig.2.11A). Thereafter, in order to check for matrix metalloproteinase activity of Zn^{2+}-bound *s*NUCB1 we performed a MMP test assay using sixteen synthetic FRET peptides wherein 5-FAM (5-aminocarboxy fluorescein) and QXL™520 are used as the fluorophore / quencher pair. Within the peptide, QXL™520 quenches the fluorescence readout of 5-FAM whereas upon MMP mediated proteolytic cleavage of the peptide this internal quenching is relieved and the fluorescence emission readout for 5-FAM can be monitored at Ex / Em wavelengths = 490 / 520 nm. As a control we incubated 15 ng of MMP-1 in 50 µl of reaction volume with optimal concentration of each substrate at room temperature and the fluorescence emission readout was recorded for 90 min at 10 min time intervals. As shown in Figure 2.11B, MMP-1 has strong proteolytic activity towards Substrate 14 and relatively weaker activity towards Substrates 3, 4, 11 and 12. The fluorescence emission readout for the peptide substrates alone was substracted at each monitored time point. Thereafter the MMP activity of Zn^{2+}-bound *s*NUCB1 was monitored in an identical experimental setup. We incubated either 7.5 ng or 750 ng of Zn^{2+}-bound *s*NUCB1 with the peptide substrates and the fluorescence emission readout was recorded. The results show that unlike MMP-1, Ca^{2+}-free *s*NUCB1 does not cleave any of the peptide substrates (Fig.2.11C,D). This is in agreement with earlier observations that Ca^{2+}-free *s*NUCB1 does possess protease activity. Thus Ca^{2+}-free *s*NUCB1 can bind to Zn^{2+} but is not a MMP.

2.2.8 Ca^{2+}-free *s*NUCB1 binds to ATP with low affinity but neither reverts nor inhibits Luciferase heat denaturation

NUCB1 is a multi-domain protein with an extended CT domain (Fig2.1, 1.4). Our results so far do not rule out the possibility that *s*NUCB1 can have chaperone like activity wherein it can utilize energy from ATP hydrolysis to perform its function. Therefore, we investigated the ATP-binding ability of Ca^{2+}-free *s*NUCB1 using ITC. 5 µl aliquots of 600 µM solution of ATP were injected into a buffered solution of 40 µM Ca^{2+}-free *s*NUCB1 in the reaction cell and the heat released per injection was recorded. The plotted data was fit to a "one-set-of-sites" model wherein the concentration of dimeric Ca^{2+}-free *s*NUCB1 was used to obtain the fit. The results show that a dimer of Ca^{2+}-free *s*NUCB1 binds to one (N= 1.26 ± 0.12) ATP molecule with a K_d value of 18.3 ± 0.86 µM (Fig.2.12A). In addition, Figure 2.12B shows that Ca^{2+}-free *s*NUCB1 does not bind to ADP. Thereafter, the ATP-binding to Ca^{2+}-free *s*NUCB1 was extended to test for its ability to refold denatured proteins using firefly Luciferase based chemiluminiscence assay (Fig.2.12C). Recombinant Luciferase was heat denatured at 42 ^{o}C for 10 min. The denatured Luciferase was then incubated in ATP containing buffer either alone or with Ca^{2+}-free *s*NUCB1 and the chemiluminiscence of luciferin was recorded at different time intervals. The green bar in Fig.2.12C shows chemiluminiscence of heat denatured Luciferase at t = 0 in comparison to recombinant Luciferase chemiluminiscence (yellow bar). The significant decrease in

Figure 2.12. Ca^{2+}-free *s*NUCB1 binds to ATP but cannot refold denatured Luciferase or protect it against heat denaturation. We used isothermal titration calorimetry (ITC) to measure the **(A)** ATP-binding or **(B)** ADP-binding affinity of Ca^{2+}-free *s*NUCB1. 40 μM Ca^{2+}-free *s*NUCB1 was titrated with 600 μM ATP / ADP solution at 25 ^{o}C and the heat released per injection was recorded and integrated. The isotherms show that Ca^{2+}-free *s*NUCB1 binds only to ATP and does not bind ADP. A non-linear least squares fit of the calculated values using the "one-set of sites" model by using the concentration for Ca^{2+}-free *s*NUCB1 dimer resulted in an excellent fit as shown in the *inset*. The calculated dissociation constant for ATP-binding to Ca^{2+}-free *s*NUCB1 was 18.4 ± 0.86 μM with a stoichiometry of N = 1.26 ± 0.12 suggesting that each dimer of Ca^{2+}-free *s*NUCB1 binds to one ATP molecule. Thereafter we used a Luciferase activity assay to test for the ability of Ca^{2+}-free *s*NUCB1 to affect the **(C)** refolding or **(D)** heat denaturation of Luciferase. **(C)** We incubated 0.7 nM of native (yellow) or heat denatured (green) firefly Luciferase with the substrate and the chemiluminiscence was recorded. Thereafter 0.7 nM of heat denatured Luciferase was incubated with 0.7 nM (blue), 7 nM (orange) or 70 nM (red) of Ca^{2+}-free *s*NUCB1 in a reaction mixture with the substrate and the chemiluminiscence was recorded after 10 min, 20 min and 30 min. The results show that Ca^{2+}-free *s*NUCB1 does not influence refolding of denatured Luciferase. Subsequently, **(D)** we investigated the ability of Ca^{2+}-free *s*NUCB1 to affect Luciferase heat denaturation. In the control experiment, similar chemiluminiscence was recorded for reaction with 0.7 nM Luciferase alone (yellow) or Luciferase incubated with 70 nM Ca^{2+}-free *s*NUCB1 (grey). Subsequently, Luciferase alone (brown) or with Ca^{2+}-free *s*NUCB1 (pink) was incubated at 42 ^{o}C for 10 min and the chemiluminiscence was monitored. The results show significant and similar decrease in the recorded chemiluminiscence suggesting that Ca^{2+}-free *s*NUCB1 does not protect Luciferase against heat denaturation.

Figure 2.12

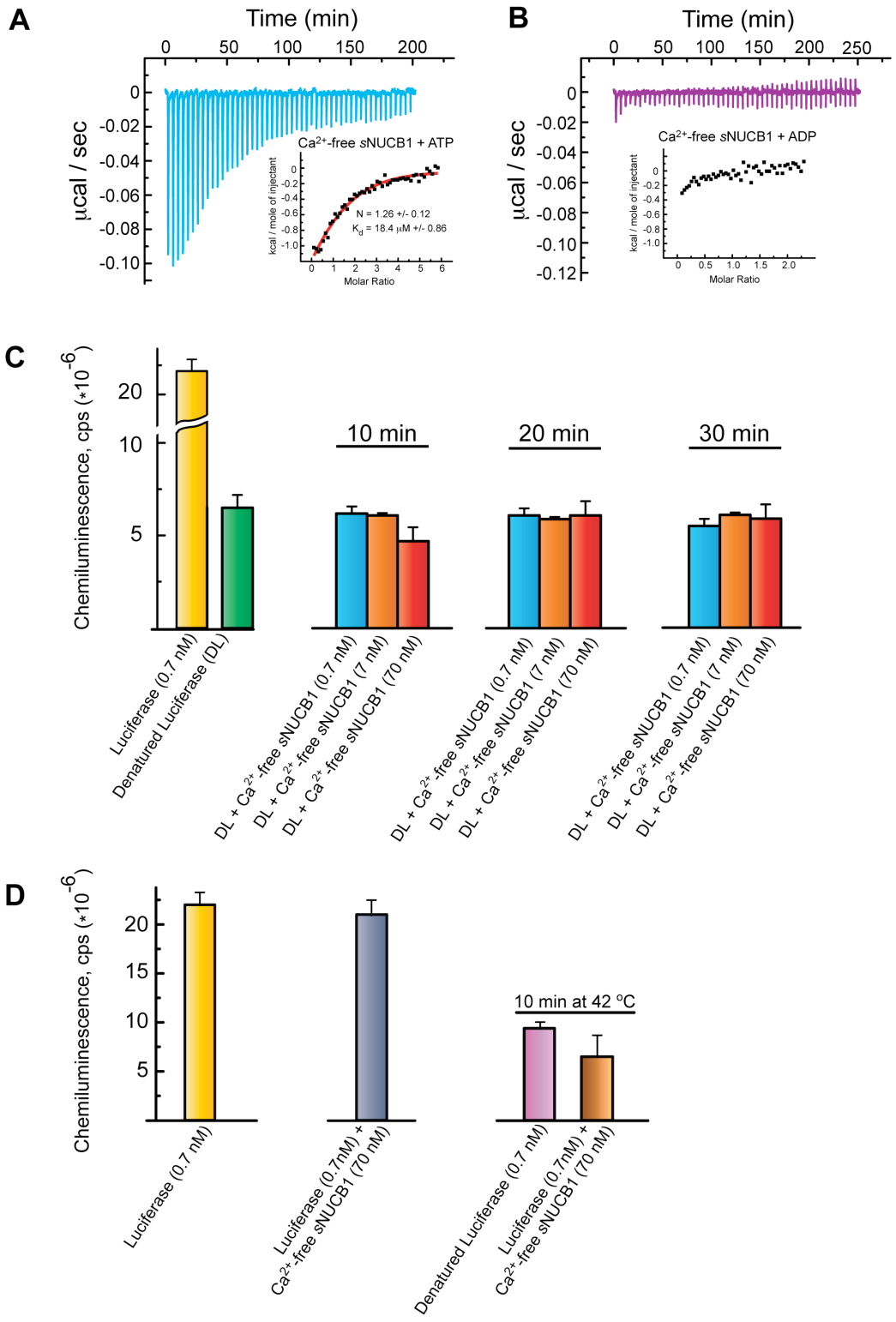
A
Time (min)
0 50 100 150 200
µcal / sec
0 -0.02 -0.04 -0.06 -0.08 -0.10
Ca2+-free sNUCB1 + ATP
kcal / mole of injectant
N = 1.26 +/- 0.12
Kd = 18.4 µM +/- 0.86
Molar Ratio
B
Time (min)
0 50 100 150 200 250
µcal / sec
0 -0.02 -0.04 -0.06 -0.08 -0.10 -0.12
Ca2+-free sNUCB1 + ADP
kcal / mole of injectant
Molar Ratio
C
Chemiluminescence, cps (*10-6)
20 10 5
10 min
20 min
30 min
Luciferase (0.7 nM)
Denatured Luciferase (DL)
DL + Ca2+-free sNUCB1 (0.7 nM)
DL + Ca2+-free sNUCB1 (7 nM)
DL + Ca2+-free sNUCB1 (70 nM)
D
Chemiluminescence, cps (*10-6)
20 15 10 5
10 min at 42 °C
Luciferase (0.7 nM)
Luciferase (0.7nM) + Ca2+-free sNUCB1 (70 nM)
Denatured Luciferase (0.7 nM)
Luciferase (0.7nM) + Ca2+-free sNUCB1 (70 nM)

the recorded chemiluminiscence confirms the heat denaturation of Luciferase. Thereafter we incubated heat denatured Luciferase with 0.7 nM (blue bar), 7 nM (orange bar) or 70 nM (red bar) Ca^{2+}-free *s*NUCB1 in the presence of luciferin and ATP and the chemilumiscence was recorded at 10 min, 20 min and 30 min time points. The absence of any relative enhancement in the recorded chemiluminiscence with time suggests that Ca^{2+}-free *s*NUCB1 cannot refold heat denatured Luciferase.

In an additional experiment, we also investigated the ability of Ca^{2+}-free *s*NUCB1 to inhibit heat denaturation of Luciferase (Fig.2.13D). As a control, we incubated 0.7 nM of Luciferase alone (yellow bar) or in the presence of 70 nM Ca^{2+}-free *s*NUCB1 (grey bar) with the substrate and recorded the chemiluminiscence output. The results show that Ca^{2+}-free *s*NUCB1 alone does not affect the enzymatic activity of Luciferase. Thereafter, we incubated 0.7 nM Luciferase alone (pink bar) or with 70 nM Ca^{2+}-free *s*NUCB1 (brown) at 42 ^{o}C for 10 min after which substrate was added to each solution and the chemiluminiscence recorded. As shown, incubation of Luciferase alone or with Ca^{2+}-free *s*NUCB1 results in similar reduction in the recorded chemiluminiscence suggesting that Ca^{2+}-free *s*NUCB1 does not inhibit Luciferase against heat denaturation. Hence although Ca^{2+}-free *s*NUCB1 does not affect the catalytic activity of Luciferase, it cannot protect it against heat denaturation**.**

2.2.9 Ca^{2+}-free *s*NUCB1 inhibits fibril formation by "capping" the ends of prefibrillar intermediates

NUCB1 is a 461-amino-acid long polypeptide, which lacks cysteine residues in its primary sequence. This provides an opportunity to site-specifically introduce cysteine residues that can be used for labeling the homogenously purified protein subunit. We generated a mutant of *s*NUCB1 namely *s*NUCB1(S44C) wherein a Ser44 residue was mutated to a Cys (Fig2.1). Ca^{2+}-free *s*NUCB1(S44C) similar to *s*NUCB1, is stable in solution and does not aggregate. TEM analysis of a solution of 32 μM of Ca^{2+}-free *s*NUCB1(S44C) incubated alone does not show any aggregation (Fig.2.13A). Thereafter we investigated inhibition of hIAPP fibril formation by incubating Ca^{2+}-free *s*NUCB1(S44C) with equimolar concentration (32 μM) of hIAPP in 20 mM Tris pH 7.5 buffer solution. TEM analysis of sample withdrawn after 60 min shows complete absence of fibrillar aggregates, which suggests that Ca^{2+}-free *s*NUCB1(S44C) can inhibit hIAPP fibril formation (Fig.2.13A).

In order to chemically label Ca^{2+}-free *s*NUCB1(S44C), we incubated the protein overnight at 4 ^{o}C with molar excess of nano-Au maleimide to covalently conjugate nano-Au to the cysteine residue. Thereafter the labeled subunit was separated from excess nano-Au in the reaction mixture by injecting the reaction mixture onto a Superose6 10 / 30 GL

Figure 2.13. Nano-Au labeled *s*NUCB1(S44C) "caps" hIAPP prefibrillar species. We designed a single-point mutant of *s*NUCB1 namely *s*NUCB1(S44C) whereby a Ser44 was mutated to a Cys in the primary sequence of *s*NUCB1. **(A)** Ca^{2+}-free *s*NUCB1(S44C) alone does not aggregate and upon incubation with equimolar concentration (32 μM) of hIAPP effectively inhibits fibril formation as seen by the complete absence of fibrillar species from a 60 min sample of the reaction mixture (Scale bar : 200 nm). We then utilized the presence of Cys44 in *s*NUCB1(S44C) to nano-Au label the protein. **(B)** Nano-Au labeled *s*NUCB1(S44C) was purified through SEC using Superose6 10/30 GL column. The elution chromatogram shows the co-elution of a characteristic 280 nm peak for the protein (black) and the 420 nm peak for nano-Au (red). The inset shows a schematic of the typical conjugation reaction that happens to covalently link the nano-Au to an unlabeled macromolecule through a Cys residue. Thereafter, **(C)** we prepared a calibration curve (blue) from a serial dilution series of unlabeled *s*NUCB1(S44C) to estimate the concentration of the nano-Au labeled protein in the eluting peak for the labeled protein. As shown, the concentration for the labeled protein is 751.9 μg / μl which is equivalent to 14.7 μM. The concentration of nano-Au in the labeled protein sample (15.08 μM) was estimated from the UV-Vis absorption of the sample at λ_{420nm} , a wavelength at which only the nano-Au probe absorbs energy. The labeling efficiency from the ratio of the concetration of the labeled protein to the concentration of nano-Au which gives a value of 1.02, showing that we have stoichiometric labeling of Ca^{2+}-free *s*NUCB1(S44C). **(D)** TEM analysis of the labeled sample shows the presence of two typical nano-Au densities next to each other corresponding to a dimer of a labeled Ca^{2+}-free *s*NUCB1(S44C). In addition **(E)** we used the labeled protein to investigate the inhibition of hIAPP aggregation into fibrils. Nano-Au labeled Ca^{2+}-free *s*NUCB1(S44C) was incubated with equimolar (32 μM) amount of hIAPP

for 60 min after which samples were withdrawn from the reaction mixture. TEM analysis of the negatively stained samples show high molecular mass prefibrillar species with labeled ends. This suggests that *s*NUCB1(S44C) "caps" the ends of the prefibrillar species and possibly inhibits further aggregation into fibrils by preventing end-to-end association of prefibrillar species into mature fibrils. The scale bar represents 100 nm.

Figure 2.13

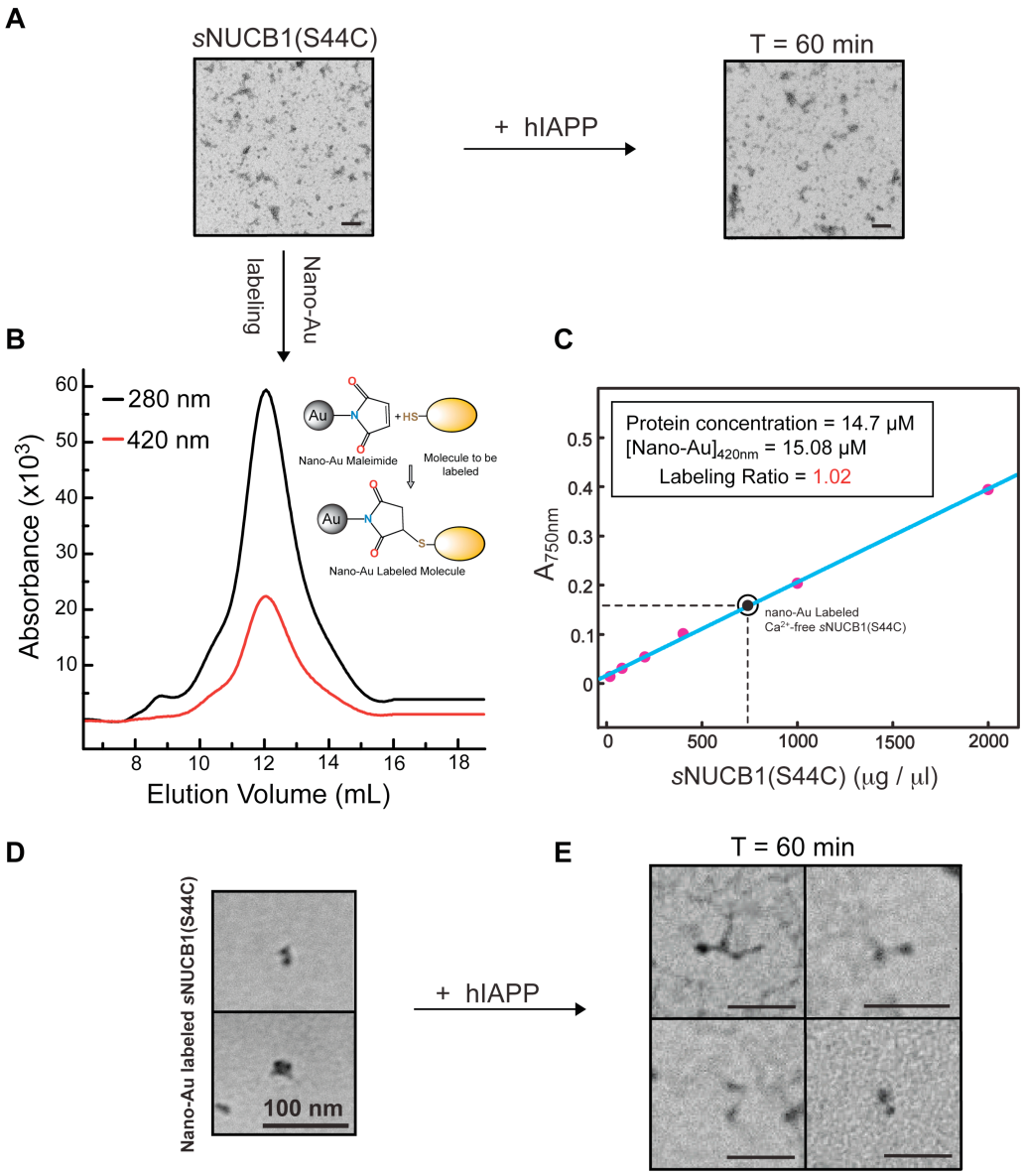
A
sNUCB1(S44C)
+ hIAPP
T = 60 min
labeling
Nano-Au
B
280 nm
420 nm
Absorbance (x10³)
Elution Volume (mL)
Nano-Au Maleimide
Molecule to be labeled
Nano-Au Labeled Molecule
C
Protein concentration = 14.7 μM
[Nano-Au]420nm = 15.08 μM
Labeling Ratio = 1.02
A750nm
nano-Au Labeled Ca²⁺-free sNUCB1(S44C)
sNUCB1(S44C) (μg / μl)
D
Nano-Au labeled sNUCB1(S44C)
100 nm
+ hIAPP
E
T = 60 min

column equilibrated with phosphate buffer saline (PBS) pH 7.5. The recorded chromatograms show co-elution of 280 nm peak corresponding to elution of the protein and a 420 nm peak corresponding to nano-Au (Fig.2.13B). Since nano-Au label absorbs at 280 nm, we used BioRad DC assay to estimate the protein concentration by measuring absorbance at 750 nm. The concentration of nano-Au was calculated by measuring absorbance at 420 nm. Using these we calculated a labeling efficiency of 1.02, which suggests that each Ca^{2+}-free *s*NUCB1(S44C) subunit has a nano-Au label attached to it (Fig.2.13C). TEM analysis of the collected peak fraction shows density for two nano-Au molecules next to each other consistent with the labeling of each protein subunit in a *s*NUCB1(S44C) dimer (Fig.2.13D). Thereafter we incubated equimolar amount (32 μM) of nano-Au labeled *s*NUCB1(S44C) with hIAPP to investigate inhibition of aggregation. TEM analysis of sample withdrawn at 60 min shows the presence of prefibrillar species with characteristic nano-Au density present at their ends (Fig.2.13E). This suggests that mechanistically *s*NUCB1(S44C) inhibits hIAPP fibril formation by stably interacting with and capping the ends of high molecular mass prefibrillar species. The capping probably inhibits further association to form mature fibrils. This provides evidence for a possible mechanism of action by which *s*NUCB1 inhibits hIAPP fibril formation.

2.2.10 Ca^{2+}-free *s*NUCB1 inhibits hIAPP fibrillization by promoting formation of Dead-End Prefibrillar (DEP) species

hIAPP is a 37-amino-acid long peptide with two N-terminal cysteine residues which can be used for labeling the peptide (Fig.2.1). We incubated 32 μ M of hIAPP in a buffer solution to allow for fibril formation. Once fibrils were formed, we sonicated the fibrils for 15 s to generate smaller molecular mass protofibrillar fragments, which were used for nano-Au labeling. The labeled protofibrils were then used to "seed" a hIAPP aggregation reaction for fibril formation. As shown, the labeled protofibrils can get incorporated into a growing fibril with the presence of the characteristic nano-Au density distributed along the length of the fibril (Fig.2.14A). As above, we incubated 32 μM Ca^{2+}-free *s*NUCB1 with 32 μM hIAPP and monitored the reaction for 2 h. Thereafter, we injected 200 μl of the reaction volume onto a Superose6 10 / 30 GL column resulting in an elution profile with characteristic Peak1 and Peak2 as earlier (Fig.2.8A). We then collected the Peak1 fraction (Fig.2.14B) and used it for nano-Au labeling of hIAPP. TEM analysis of samples withdrawn from the labeling reaction shows the presence of multiple nano-Au labels per prefibrillar species (Fig.2.14C). We then used the labeled protofibrils as "seed" in a hIAPP fibrillization reaction. TEM analysis of samples withdrawn from the aggregation reaction shows the presence of extensive fibrils which do not possess nano-Au label possibly due to inability of the *s*NUCB1 stabilized nano-Au labeled prefibrillar species to get

Figure 2.14. Ca^{2+}-free *s*NUCB1 stabilized hIAPP prefibrillar species are not incorporated into growing fibrils. (A) We incubated hIAPP monomers at room temperature to form fibrils, which were then sonicated to generate protofibrils, and oligomers. These were then labeled with nano-Au and used to seed the fibril assembly reaction upon incubation with soluble hIAPP. TEM analysis of the fibril formation reaction shows incorporation of the nano-Au labeled protofibrils into the fibrils. **(B)** Equimolar concentration (32 μM) of Ca^{2+}-free *s*NUCB1 was incubated with hIAPP for 60 min and the reaction mixture was subsequently injected onto a Superose6 10/30 GL column. The chromatogram shows Peak1 consisting of Ca^{2+}-free *s*NUCB1 stabilized hIAPP prefibrillar species and Peak2 corresponding to unbound Ca^{2+}-free *s*NUCB1. **(C)** We subsequently collected the Peak1 fraction and labeled the Cys of hIAPP with nano-Au. TEM analysis of the reaction shows Ca^{2+}-free *s*NUCB1 stabilized nano-Au labeled protofibrils. **(D)** We then used these Ca^{2+}-free *s*NUCB1 stabilized labeled protofibrils as seed in hIAPP aggregation reaction. TEM analysis of a 60 min reaction sample shows presence of mature hIAPP fibrils without the incorporation of nano-Au labeled protofibrils. The scale bar represents 200 nm. Thereafter, we used both post sonication hIAPP fragments and Peak1 fraction as seeds in independent hIAPP aggregation reactions monitored using thio-T binding assay. **(E)** The results show hIAPP aggregation (black, inset) gets accelerated in the presence of both 20 μl (blue) or 50 μl (red) seed as observed by a decreased lag phase of the process. Interestingly, even when 50 μl (orange), 100 μl (purple) or 200 μl (green) of Peak1 fraction was added to hIAPP aggregation reaction, no effect was observed on the lag phase of the process. This shows that *s*NUCB1 stabilized high molecular mass prefibrillar aggregate of hIAPP cannot get incorporated into a growing fiber and hence does not seed the aggregation reaction.

Figure 2.14

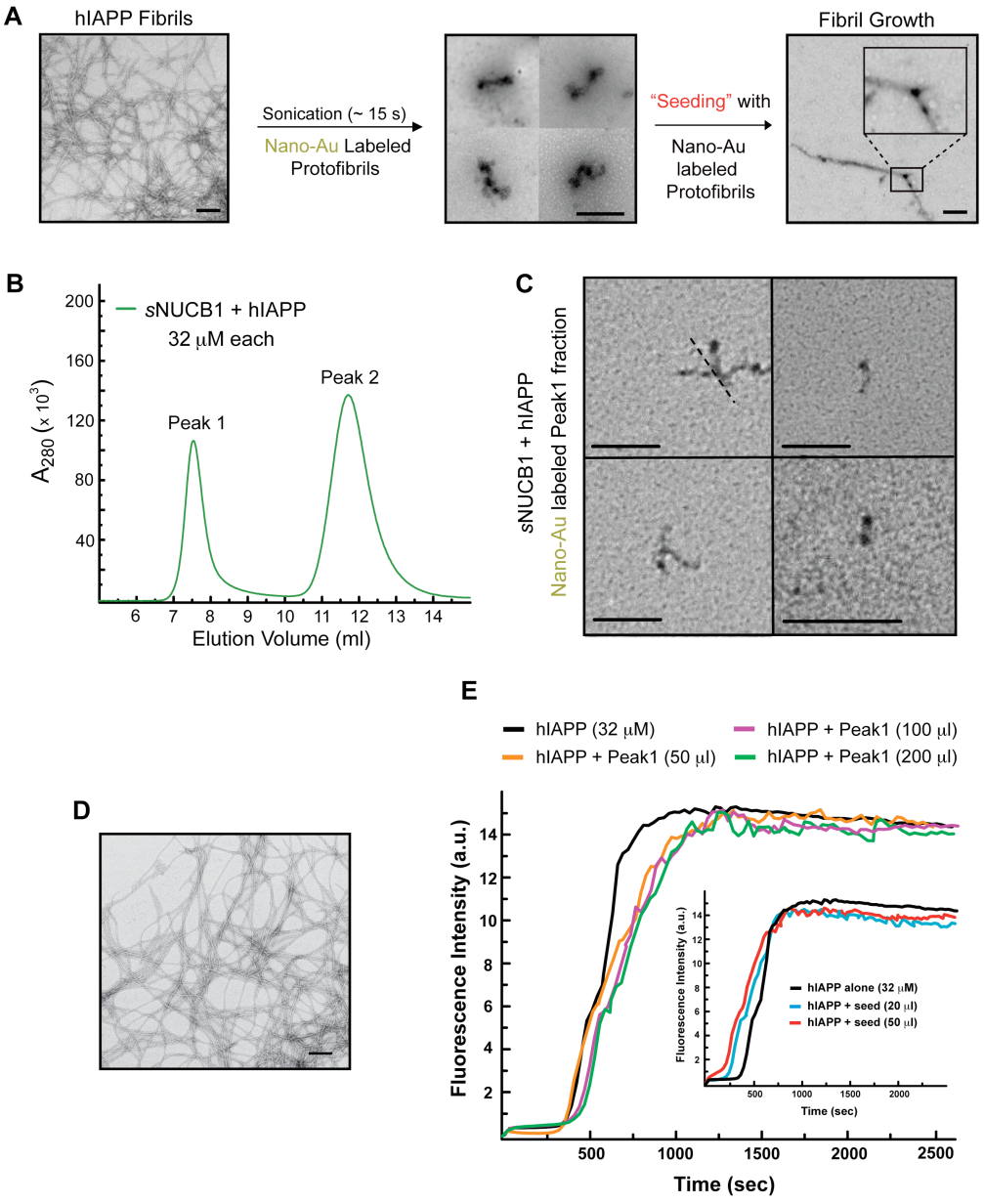
A
hIAPP Fibrils
Sonication (~ 15 s)
Nano-Au Labeled Protofibrils
"Seeding" with
Nano-Au labeled Protofibrils
Fibril Growth
B
sNUCB1 + hIAPP
32 μM each
Peak 1
Peak 2
A280 (x 10^3)
Elution Volume (ml)
C
sNUCB1 + hIAPP
Nano-Au labeled Peak1 fraction
D
E
hIAPP (32 μM)
hIAPP + Peak1 (50 μl)
hIAPP + Peak1 (100 μl)
hIAPP + Peak1 (200 μl)
Fluorescence Intensity (a.u.)
Time (sec)
hIAPP alone (32 μM)
hIAPP + seed (20 μl)
hIAPP + seed (50 μl)

incorporated into a growing fibril (Fig2.14D). This suggests that Ca^{2+}-free *s*NUCB1 stabilizes an intermediate that is a Dead End Prefibrillar (DEP) species and cannot be incorporated into a growing hIAPP amyloid fibril. In addition, we also monitored the effect of SEC purified prefibrillar species in Peak1 fraction on hIAPP aggregation by recording the enhancement in thioflavin-T fluorescence (Fig.2.14E). In principle, if a species can act as a seed for aggregation reaction it should shorten the lag phase of the process since nucleation is the rate limiting step in amyloid formation. The plot shows that incubation of hIAPP with increasing amounts of Peak1 fraction has little to no affect on the lag phase of the process. This suggests that in agreement with the above results, the prefibrillar species cannot "seed" a fibrillization reaction. As a control, incubation of hIAPP with seeds generated from sonication of hIAPP fibrils shorten the lag phase of the aggregation process (Fig.2.14E,inset).

2.2.11 A CT peptide fragment of NUCB1 namely NUCB1(381-419) effectively inhibits hIAPP fibril formation and also disaggregates amyloid fibrils

Our earlier results showed that Ca^{2+}-free *s*NUCB1 effectively inhibits hIAPP fibril formation and also disaggregates preformed amyloid fibrils. However we are interested in isolating a smaller fragment of Ca^{2+}-free *s*NUCB1 that exhibits similar activity. The CT of Ca^{2+}-free *s*NUCB1 is

Figure 2.15. NUCB1(381-419) inhibits hIAPP aggregation and disaggregates hIAPP amyloid fibrils. NUCB1(381-419) is a CT peptide fragment from *s*NUCB1. **(A)** We investigated the secondary structure of NUCB1(381-419) using CD spectroscopy. The spectra recorded for a 50 μM solution of NUCB1(381-419) shows that the peptide is essentially unstructured. Thereafter we incubated 32 μM **(B)** hIAPP for 1 h or **(C)** NUCB1(381-419) for 5 h alone in 50 mM Tris pH 8.0 at room temperature after which samples were withdrawn and monitored using TEM. The corresponding micrographs show that **(B)** hIAPP alone forms typical amyloid fibrils within 1 h whereas **(C)** NUCB1(381-419) does not aggregate to form higher molecular mass structrues. **(D)** We then incubated equimolar amount (32 μM) of hIAPP with NUCB1(381-419) in the buffer at room temperature and sample was withdrawn after 2 h for TEM analysis. The corresponding micrographs show that NUCB1(381-419) inhibits hIAPP amyloid formation by stabilizing high molecular mass intermediates. Furthermore, we added **(E)** equimolar amount of NUCB1(381-419) to hIAPP fibrils. TEM analysis of sample withdrawn after 1 h of incubation shows that NUCB1(381-419) effectively disaggregates hIAPP fibrils into smaller molecular fragments. The scale bar represents 200 nm.

Figure 2.15

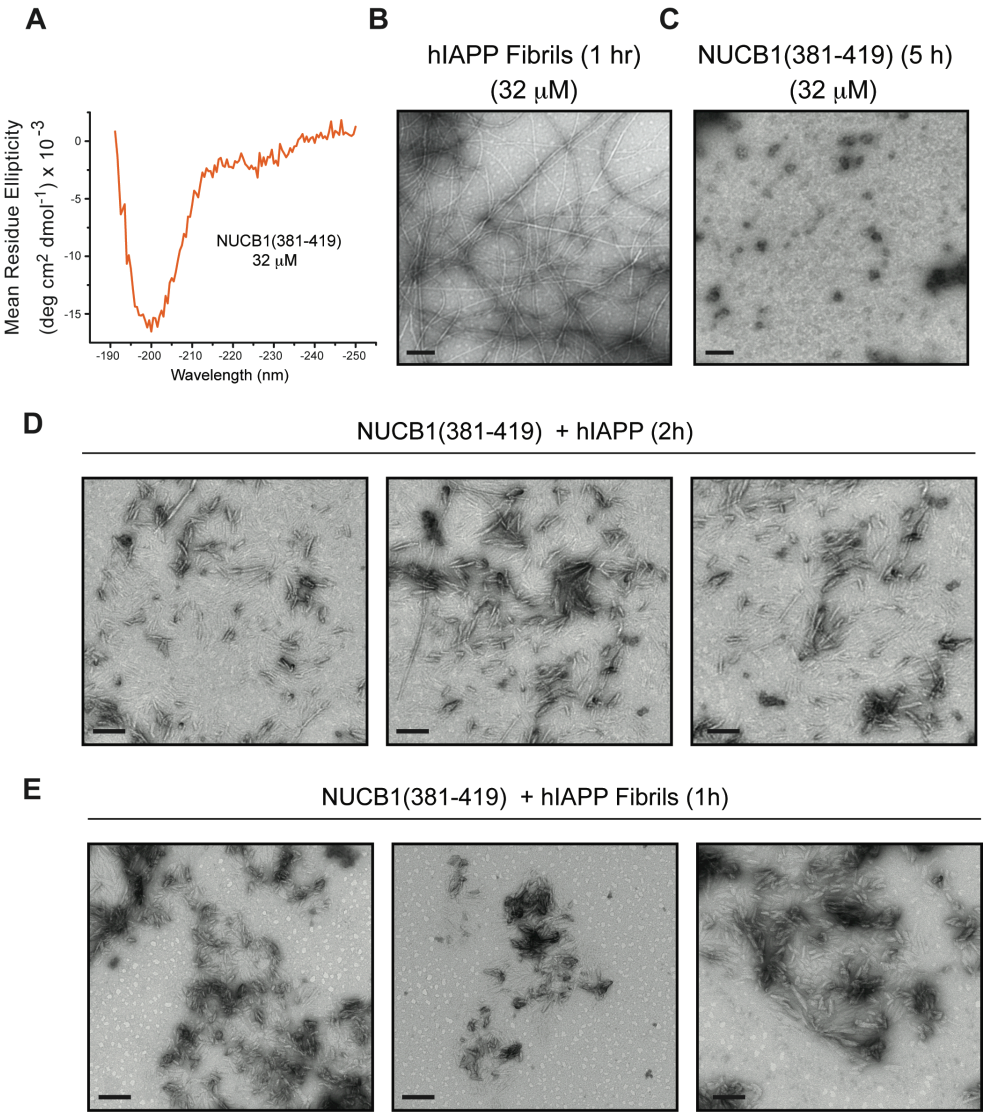
A
B
C
hIAPP Fibrils (1 hr)
(32 μM)
NUCB1(381-419) (5 h)
(32 μM)
Mean Residue Ellipticity
(deg cm² dmol⁻¹) x 10⁻³
0
-5
-10
-15
-190
-200
-210
-220
-230
-240
-250
Wavelength (nm)
NUCB1(381-419)
32 μM
D
NUCB1(381-419) + hIAPP (2h)
E
NUCB1(381-419) + hIAPP Fibrils (1h)

majorly unstructured and has an unusual PolyQ (residues 401-407) stretch (Fig.2.1) that may have important functional implications. Hence we designed a peptide fragment namely NUCB1(381-419) from the CT of *s*NUCB1 to test for its ability to inhibit or disaggregate hIAPP fibrils. As shown in Figure 2.15B, hIAPP alone (32 μ M) forms characteristic amyloid fibrils within 1 h. Interestingly, 32μM of NUCB1(381-419) even though unstructured (Fig.2.15A), does not aggregate even after 5 h as shown by the complete absence of higher order amyloid structures in the micrograph (Fig.2.15C). Thereafter we incubated equimolar amounts (32 μM) of hIAPP with NUCB1(381-419) at room temperature and sample was withdrawn after 2 h for TEM analysis. The corresponding micrographs show that NUCB1(381-419) effectively inhibits hIAPP fibril formation by stabilizing high molecular mass protofibril like species (Fig.2.15D). Additionally, we also investigated the ability of NUCB1(381-419) to disaggregate hIAPP fibrils. We incubated equimolar amount (32 μM) of NUCB1(381-419) with hIAPP amyloid fibrils at room temperature and sample was withdrawn after 1 h for TEM analysis. The recorded micrographs show presence of smaller molecular mass fragments and complete absence of any amyloid fibrils suggesting that NUCB1(381-419) can disaggregate hIAPP amyloid fibrils (Fig.2.15E). Hence NUCB1(381-419) similar to Ca^{2+}-free *s*NUCB1 has the functional ability to inhibit hIAPP fibril formation and also disaggregate amyloid fibrils.

2.3 DISCUSSION

IAPP is a neuroendocrine peptide hormone expressed in pancreatic islets of all mammals and can aggregate to form amyloid deposits depending on species-specific amino acid sequence. Amongst all naturally occurring hormones, hIAPP has the most hydrophobic and highly amyloidogenic sequence. It thus provides a useful model system to test for molecules with potent inhibitory acitivity against fibril formation. In the present study we report the anti-amyloidogenic property of Ca^{2+}-free *s*NUCB1 towards inhibiting hIAPP fibril formation and disaggregate the preformed amyloid fibrils. In addition, our results show that *s*NUCB1 assisted inhibition of hIAPP fibril formation is dose-dependent and observed even at sub-stoichiometric concentrations. Thus inhibition of hIAPP aggregation by *s*NUCB1 presents a crucial and interesting finding, possibly one of the several mechanisms at work in keeping these naturally occurring amyloidogenic peptides from aggregating into insoluble amyloid fibrils. Importantly, Ca^{2+}-free *s*NUCB1 can inhibit fibril formation even when added either during nucleation or growth phase of amyloidogenesis. Thus if aggregation of hIAPP has been initiated, Ca^{2+}-free *s*NUCB1 can prevent the growth of existing amyloidogenic intermediates into fibrils. Functionally, this ability is very unique and significant as it may not only assist in clearing the existing amyloid aggregates but also prevent further sequestration of functional monomers into amyloid deposits. It has been reported that IAPP monomers released during β-cell secretion can be

rapidly seeded at the nucleation site and assembled into fibrils (*87*). Several drug-based approaches to reduce IAPP secretion in animal models by increasing insulin sensitivity caused a marked reduction and retardation in islet amyloid formation. However, the cytotoxic effects of small IAPP amyloid aggregates were still observed. This suggests that therapeutic approaches to preventing β-cell loss not only require clearance of mature islet amyloid deposits but inhibition of formation of early aggregates as well (*80*). In this regard, the functional ability of NUCB1 to target both amyloid fibrils and intermediates may provide a therapeutically relevant approach to circumvent islet amyloidosis.

Physiologically, both hIAPP and insulin are secreted as precursor pro-peptides whose proteolytic processing by proconvertases generates the mature hormone (*58*) The disproportionate release of proinsulin relative to mature insulin is well documented in T2D (*88-92*). Functionally, it has been shown that only insulin and not proinsulin can inhibit fibril formation (*68, 93*). Thus incomplete processing of Insulin may promote Islet amyloid formation. In addition, recently it was shown that Insulin only impedes but does not completely inhibit IAPP fibril formation (*94*). Thus additional factors may be necessary towards keeping IAPP in a non-aggregated and soluble form at millimolar concentrations in the secretory granules (*95*). Moreover, incomplete processing of proIAPP has also been postulated as a possible cause for facilitating amyloid formation.

Immunostaining assays have shown that proIAPP ubiquitinated at N-terminus to be a component of intracellular fibrils (*96*). These intracellular fibrils are located in pre-Golgi part of the secretory pathway to be directed for lysosomal degradation (*97*). Lysosomal enzymes are however less efficient in clearing these aggregates whose accumulation results in cellular disintegration and apoptosis (*68, 98*). This release of hIAPP from intracellular compartments can stimulate IAPP aggregation. Thus inhibition of intracellular aggregation and clearance of fibrillar aggregates are both essential in preventing loss of β-cell mass. Physiologically, NUCB1 is present in both Golgi and ER (*23, 26*). RT-PCR of total RNA from rat insulinoma (RIN-m5F) cells and western blot analysis of RIN-m5F cell lysate revealed presence of both NUCB1 mRNA and protein. Thus anti-amyloidogenic activity of NUCB1 could be crucial in preventing intracellular aggregation and clearing fibrillar aggregates of hIAPP in conjunction with the cellular chaperone machinery. We have shown that Ca^{2+}-binding regulates the anti-amyloidogenic ability of *s*NUCB1. Both disruption of Ca^{2+}-homeostasis in the cells and generation of reactive oxygen species have been shown to significantly contribute to the cytotoxicity associated with hIAPP (*99*). Higher concentrations of Ca^{2+} have been shown to promote aggregation of hIAPP (*68*). Under these conditions, our engineered Ca^{2+}-insensitive mutant *s*NUCB1(tetramutant) can effectively inhibit hIAPP fibrillization and also dissociate the preformed amyloid fibrils. The Ca^{2+}-insensitive mutant

*s*NUCB1(tetramutant) provides a handle for overriding the functional dependence of *s*NUCB1 on Ca^{2+} without any loss of anti-amyloidogenic ability.

NUCB1 is a novel Ca^{2+}-binding protein whose precise physiological role(s) is still poorly understood. Since it shows potential for anti-amyloidogenic properties and can bind to ATP even though with weak affinity, we also investigated the ability of *s*NUCB1 to refold or inhibit denaturation of natively folded proteins. Using firefly Luciferase as a model system we showed that even though Ca^{2+}-free *s*NUCB1 does bind to ATP, it alone cannot help refolding of denatured Luciferase or protect it against heat denaturation. This suggests that Ca^{2+}-free *s*NUCB1 unlike several chaperones like Hsp70 lacks the ability to refold denatured or aggregated proteins (*74, 75*). However there is a possibility that similar to Hsp70 it may also require certain other cofactors to robustly perform its function (*100*). Future work pertaining to understanding the *in vivo* functional role of NUCB1 would be immensely helpful towards establishing it.

Our biochemical results show that both Ca^{2+}-free *s*NUCB1 and *s*NUCB1(tetramutant) possess anti-amyloidogenic properties but neither exhibited any proteolytic activity. Using BODIPY FL-Casein as a

substrate to test for proteolytic activity showed that unlike Trypsin, both Ca^{2+}-free *s*NUCB1 and *s*NUCB1(tetramutant) lack the functional ability to cleave it. In addition, LC-MS analysis directly showed that Ca^{2+}-free *s*NUCB1 does not proteolytically cleave hIAPP as evident from the complete absence of any smaller molecular fragments of hIAPP detected through LC-MS. Interestingly, our control experiments with the non-aggregating analog of hIAPP namely Pramlintide also showed that Ca^{2+}-free *s*NUCB1 does not bind to it. It hints towards a preferential interaction of Ca^{2+}-free *s*NUCB1 only with intermediate oligomeric species of hIAPP and not with monomeric hIAPP. Functionally, the ability of Ca^{2+}-free *s*NUCB1 to bind to Zn^{2+} alongwith the observation that NUCB1 has a signal sequence and is found extracellularly raises a possibility that NUCB1 may act as a MMP. However our studies using fluorescently modified natural substrates of MMPs showed that unlike MMP-1, Ca^{2+}-free *s*NUCB1 does not proteolytically cleave them. Hence unlike the native Zn^{2+}-dependent metalloproteases like IDE and Neprilysin, which facilitate clearance of amyloidogenic peptides like IAPP and Aβ by cleaving them (*79*) (Neprilysin), NUCB1 does not possess any proteolytic activity against Amylin. Thus the observed anti-amyloidogenic functionality of Ca^{2+}-free *s*NUCB1 is not due to its protease activity.

The biophysical characterization of Ca^{2+}-free *s*NUCB1 stabilized prefibrillar species using light scattering analysis shows that Ca^{2+}-free

*s*NUCB1 interacts with hIAPP to form a 2 - 6 MDa complex, which can be isolated by SEC. In addition, Ca^{2+}-free *s*NUCB1 stabilized soluble species of hIAPP range from 40 - 80 nm in length with a predominant mass density of 2 - 5 kDa / Å. Mechanistically, the stabilization of the prefibrillar species is achieved by "capping" its ends as shown by our inhibition experiments followed by TEM analysis using nano-Au labeled Ca^{2+}-free *s*NUCB1(S44C). Interestingly, these capped prefibrillar species neither aggregate when incubated for over a week nor seed the aggregation of hIAPP monomers to form amyloid fibrils. This presents a unique mechanism of action for activity of an amyloidogenesis inhibitor, in preventing the aggregation of hIAPP. In addition, the ability of *s*NUCB1 to disaggregate would further assist in clearing the pre-formed amyloid fibrils. Physiologically, Insulin degrading enzyme (IDE) can proteolytically cleave hIAPP, which provides a cellular mechanism to clear excess peptide from the system. However, IDE can only degrade monomeric hIAPP and is ineffective when hIAPP aggregates into higher order structures (*79*). We have shown that Ca^{2+}-free *s*NUCB1 does not possess any proteolytic activity but is effective at inhibiting amyloid formation. Alternatively, several heat shock proteins (Hsps), small heat shock proteins (sHsps) and chaperones have been reported to inhibit aggregation of several amyloidogenic peptides. Both Hsp70 and extracellular chaperone Clusterin bind to prefibrillar species and prevent the formation of amyloid fibrils (*76, 77*). The results shown in the present

study however do not rule out the role of NUCB1 as a chaperone. It is possible that similar to sHsps, NUCB1 stabilizes the prefibrillar species and delivers them to Hsps for clearance from the system. These hypotheses will be addressed in our future studies.

Ca^{2+}-free *s*NUCB1 is a ~ 100 kDa protein which can limit its potency and usefulness towards usage as a therapeutic agent. Hence in search of a smaller molecular fragment of NUCB1 which retains the functional ability and efficacy to inhibit hIAPP fibril formation and preferably also dissociates amyloid fibrils, we isolated a 39-amino-acid long polypeptide namely NUCB1(381-419) from CT domain of NUCB1. Intriguingly, similar to Ca^{2+}-free *s*NUCB1, the peptide inhibits hIAPP fibril formation as well as effectively dissociates amyloid fibrils at sub-stoichiometric concentrations. In addition to this functional ability, NUCB1(381-419) also provides a tool to override the inherent Ca^{2+}-dependence on the functional efficacy of *s*NUCB1. It provides a molecular handle, which in its present or an altered form can be useful in designing agents for inhibiting amyloidogenesis of hIAPP. The extension of these *in vitro* results in relevant animal models will be useful in testing their *in vivo* efficacy. Future work pertaining to continuation of these results to other amyloidogenic proteins / peptides like Aβ and Tau as relevant to pathology of AD would be particularly interesting in understanding if the observed ability is specific or generic.

T2D is commonly associated with insulin resistance and reduced insulin secretion causing increase in plasma glucose levels. Thus most drugs administered to diabetic patients either stimulate β-cells to release more insulin or act as insulin sensitizers to promote skeletal muscle glucose uptake (*80*). However loss of β-cell mass is tightly correlated with IAPP cytotoxicity and islet amyloid formation (*101*). Transgenic mice over expressing hIAPP in their islet cells show amyloid deposits, β-cell depletion and develop non-insulin dependent diabetes mellitus (*102, 103*). The depletion of β-cells contributes to insulin resistance and decreased effectiveness of the administered drugs with time. This underlines the significance of strategies aimed at decreasing or preventing islet amyloid formation. The ability of Ca^{2+}-free *s*NUCB1 to inhibit fibrillization of hIAPP at any stage of aggregation is therefore therapeutically relevant. It would be interesting to test for *s*NUCB1's functional efficacy towards inhibiting the formation of amyloid plaques and disaggregating islet amyloids in relevant mouse models of diabetes. As shown here, the mechanism employed by *s*NUCB1 is unique and offers insights into designing strategies for inhibiting amyloidogenesis. However, the need for inhibition of aggregation and disaggregation of fibrillar deposits would require a molecule, which can effectively work under conditions of Ca^{2+} flux. The designed *s*NUCB1(tetramutant) or the isolated CT peptide fragment namely NUCB1(381-419) are Ca^{2+}-insensitive and may efficiently execute the anti-amyloidogenic activity in the presence of high

concentrations of Ca^{2+}. Interestingly, the truncation mutant *s*NUCB1(W333Ter) (Fig.1.1) neither inhibits not disaggregates hIAPP amyloid fibrils (data not shown). This can be explained by the possible role of the CT region comprising of residues 381-419 in *s*NUCB1 that is absent in the heterologously expressed *s*NUCB1(W333Ter).

In vivo, the presence of amyloid fibrils leads to generation of reactive oxygen species. The particular susceptibility of β-cells to these species results from the physiologically low levels of antioxidant enzymes such as superoxide dismutase and catalase (*104, 105*). Hence the anti-amyloidogenic properties of NUCB1 along with other contributing factors might be part of physiological machinery that protects the highly susceptible pancreatic β-cells from amyloid mediated toxicity. In conclusion, our data provides evidence that NUCB1 has novel anti-amyloidogenic functional ability and provides opportunity to understand the possible defense mechanisms against islet amyloidosis as relevant to T2D. If apoptosis and β-cell depletion due to islet amyloid formation contribute to the observed loss of β-cell function, then the anti-amyloidogenic activity of *s*NUCB1, its engineered mutant *s*NUCB1(tetramutant) or the isolated CT peptide fragment NUCB1(381-419) can be crucial in designing therapeutics towards targeting islet amyloidosis.

CHAPTER 3

Nucleobindin 1 and its Engineered Mutant Inhibit Aβ42 Aggregation and Disaggregate Aβ42 Fibrils into Non-toxic Species

3.0 INTRODUCTION

Alzheimer's disease (AD) is a neurodegenerative disorder characterized by the presence of extracellular β -amyloid (Aβ) fibril deposits with subsequent intra-neuronal accumulation of hyperphosphorylated tau into neurofibrillary tangles (NFTs), both of which trigger neuronal dystrophy (*106*). Evidently, a role of extracellular Aβ fibrillar deposits on intracellular tau hyperphosphorylation has been postulated (*101, 107*). In tissue culture experiments with hippocampal neurons from transgenic mice, it was shown that tau is essential to β-amyloid induced neurotoxicity (*108*). AD is a synaptic failure disease in which aggregation of Aβ, both intracellularly and extracellularly, causes neuritic and synaptic pathology through reduction in synaptic plasticity and associated proteins (*109-111*). Aβ is a 38 - 43 residue (~ 4 kDa) proteolytic fragment generated by the sequential cleavage of single-span transmembrane Amyloid Precursor Protein (APP) by membrane aspartyl proteases namely β- and γ-secretases respectively (*112-119*). Cell biological studies have shown that Aβ generation occurs majorly in *trans*-Golgi network (TGN) with much less in endoplasmic reticulum (ER). However, ER seems to be more selective

towards generation of more amyloidogenic Aβ42 than Aβ40. Mechanistically, Aβ40 has been shown to be the predominantly secreted form of Aβ peptide (*120, 121*). In a recent study, Cirrito *et al.* showed that synaptic activity increases the cell-surface levels of APP by stimulating its anterogade transport to synapses and plasma membrane. APP is then internalized from cell surface into endosomes where it is proteolytically cleaved to generate Aβ for release into the brain interstitial fluid (*122*). Functionally, Aβ42 monomers have also been shown to protect mature neurons from excitotoxicity and support the survival of developing neurons under trophic conditions (*123*). However, when Aβ monomers oligomerize into amyloidogenic intracellular aggregates, they cause neuritic dystrophy. Numerous studies have reported behavioral, physiological, oxidative and plaque mediated abnormalities in transgenic mouse models of AD much before the appearance of Aβ amyloid deposits (*124-129*). These observations point towards the pathogenic activity of intracellular Aβ aggregation in promoting cytotoxicity. Thereafter, the subsequent release of these aggregates into the extracellular space, possibly due to neuronal apoptosis or membrane disruption, impairs processes involved in learning and memory. Thus both intracellular and extracellular Aβ deposits contribute to cognitive impairment but early events involving intracellular amyloidogenesis initiate synaptic pathology as observed in AD (*130, 131*). Hence, preventing intraneuronal Aβ aggregation in addition to eliminating extracellular amyloid deposits might

be therapeutically relevant for the treatment and control of AD. Therefore the leading target of emerging AD therapies is the suppression of Aβ by reduced generation or enhanced degradation.

Several decades of research in understanding AD has put forth different Aβ lowering strategies for potential drug development. These include suppression of Aβ generation by employing β- or γ-secretase inhibitors, preventing Aβ aggregation and immunization based approaches (*132-134*). Several small molecule inhibitors have been explored and tested that prevent Aβ fibril formation and seem to partially reverse the cognitive impairment (*101*). Naturally occurring Zn^{2+}-dependent endopeptidases namely Insulin Degrading Enzyme (IDE) and Neprilysin (NEP) decrease amyloid load in the brain by proteolytically cleaving Aβ (*79, 135-139*). Recently, several heat shock proteins (Hsp's) and small heat shock proteins (sHsp's) have also been shown to effectively inhibit aggregation of amyloidogenic peptides. Interestingly, several members of sHsp's like αB-crystallin, Hsp27, Hsp20 and HspB8 completely inhibit Aβ40 amyloidogensis by binding to and stabilizing prefibrillar species (*74, 75*). In addition, extracellular chaperone clusterin has been shown to inhibit the fibril formation by prion protein, Aβ and apolipoprotein CII. Along with Hsp70, clusterin has been shown to bind to prefibrillar species and prevent the formation of amyloid fibrils. The stabilization of these prefibrillar species, however, resulted in enhanced toxicity in a cell culture based

assay (*76, 77*). Importantly, a direct role of apolipoprotein E (apoE) and its isoforms in differentially promoting clearance of Aβ from extracellular space has also been established (*140, 141*).

In a recent study Lin *et al.* showed that overexpression of a novel Ca^{2+}-binding protein Nucleobindin 1 or NUCB1 in an *in vitro* setup reduces APP mRNA level and regulates APP biosynthesis. This consequently causes a reduction in the proteolytic metabolites of APP including Aβ. Intriguingly, the expression level of NUCB1 was also reported to decrease by 50% in the brains of AD patients (*28*). NUCB1 is a 55 kDa multi-domain protein that was first reported as a growth and differentiation factor associated with lupus syndrome in mice (*18*). Since its discovery, NUCB1 has been reported to be widely expressed in cells and tissues and is conserved from flies to humans (*85*). NUCB1 is primarily a Golgi-resident protein also found in both cytosolic and membrane fractions (*142*). NUCB1 has been shown to function as a matrix modulator and may act as a Ca^{2+}-buffer in Golgi (*16, 46*). In both sporadic and familial AD, Ca^{2+}-dysregulation has been known to play a critical role. Abnormal Ca^{2+}-homeostasis has been observed in the dendritic spines adjacent to the amyloid plaques (*143*). Since NUCB1 interacts with APP in a Ca^{2+}-dependent manner and has been shown to regulate Aβ generation (*28*), we proceeded to test the effect of NUCB1 on the amyloidogenesis of synthetic Aβ42. In the present study, we use the heterologously expressed

and purified *s*NUCB1, a soluble form of NUCB1 without the signal sequence (residues 1-31) (Fig.3.1) and show that *s*NUCB1 in its Ca^{2+}-free form completely inhibits Aβ fibril formation as well as effectively disaggregates pre-formed amyloid fibrils. We further engineered a Ca^{2+}-independent mutant of *s*NUCB1, namely *s*NUCB1(tetramutant), which continues to inhibit Aβ42 amyloidogenesis and disaggregates preformed Aβ42 fibrils even in the presence of Ca^{2+}. In addition, in a tissue-culture based assay, the species generated upon Aβ42 fibril disaggregation by *s*NUCB1 or *s*NUCB1(tetramutant) were non-toxic. Finally, this anti-amyloidogenic property of *s*NUCB1 was also tested against aggregation of tau K19(C322S), a heterologously expressed construct corresponding to the microtubule binding domain of human tau (htau) with only 3 repeat domains (Fig.3.1) (*144*). Our results show that similar to Aβ, Ca^{2+}-free *s*NUCB1 inhibits fibrillarization of tau K19(C322S).

Figure 3.1. **Domain architecture of human NUCB1 and engineered NUCB1 variants, human tau and tauK19.** The modular nature of the NUCB1 protein structure is depicted schematically with its N-terminal signal sequence (grey square), putative DNA binding domain (green square), two EF hand loops (magenta rectangles), acidic region (blue oval) and leucine zipper domain (yellow hexagon). The amino acid residues at domain borders are numbered. We engineered a construct for expression in *E. coli* of a soluble form of NUCB1 that included an N-terminal hexa-His tag and a PreScission protease recognition sequence with an intervening spacer sequence as shown. Endoprotease cleavage yields a soluble form of NUCB1 that begins with the amino acid sequence GPHMAS and continues with the remainder of the native sequence beginning at Gly32. We refer to this expressed protein construct as soluble NUCB1 or *s*NUCB1 throughout the text. Furthermore we used the *s*NUCB1 template to make point mutations in each EF hand as indicated by the arrows to generate *s*NUCB1(tetramutant) which lacks the ability to bind to calcium. Thereafter the domain diagram of the longest form of human Tau protein shows three alternatively spliced exons (exon 1, 2 and 3) along with proline rich domains P1 and P2. The CT proximal microtubule-binding repeat domains are labeled R1-R4 followed by a low homology repeat domain namely R'. The domain diagram of tauK19 consists of repeat domains R1, R3 and R4 followed by three residues KIE (370-372) from the R' domain at its CT end.

Figure 3.1

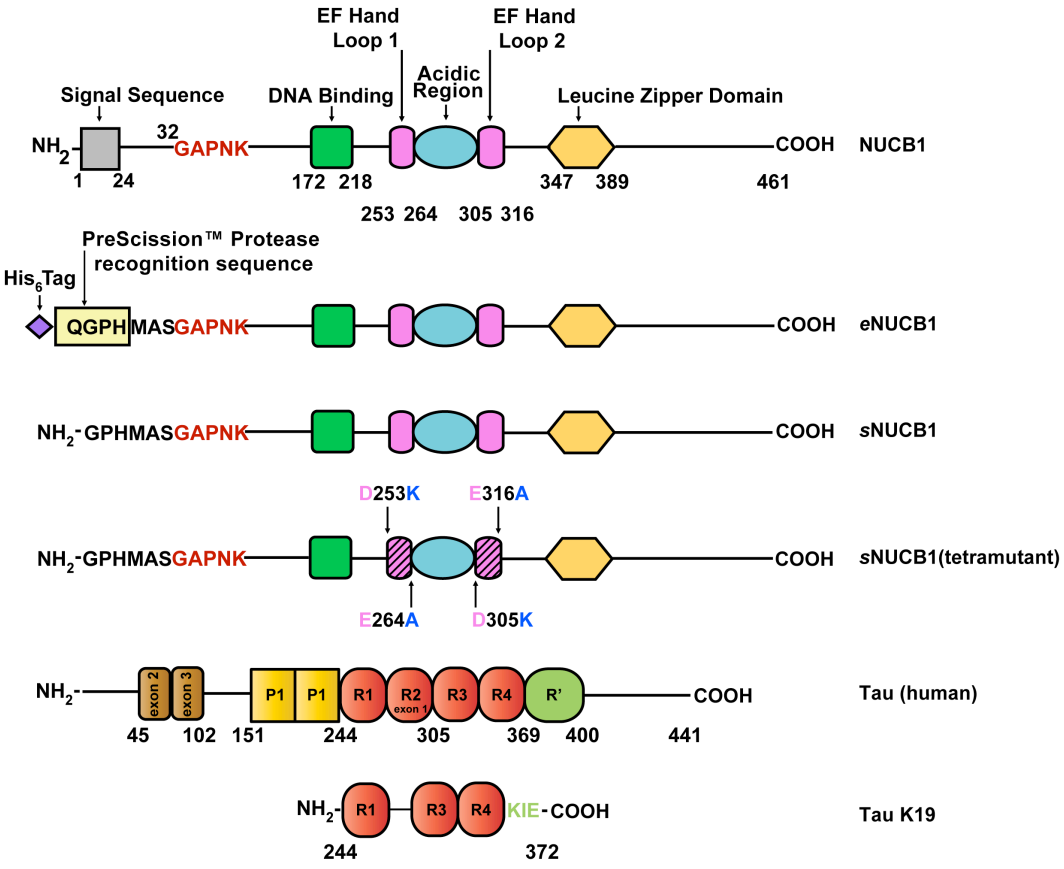
EF Hand Loop 1
EF Hand Loop 2
Acidic Region
Signal Sequence
DNA Binding
Leucine Zipper Domain
NH2
32
GAPNK
COOH
NUCB1
1 24
172 218
253 264 305 316
347 389
461
PreScission™ Protease recognition sequence
His6Tag
QGPHMASGAPNK
COOH
eNUCB1
NH2-GPHMASGAPNK
COOH
sNUCB1
D253K
E316A
NH2-GPHMASGAPNK
COOH
sNUCB1(tetramutant)
E264A
D305K
NH2-
exon 2
exon 3
P1
P1
R1
R2
exon 10
R3
R4
R'
COOH
Tau (human)
45 102 151 244 305 369 400 441
NH2-
R1
R3
R4
KIE-COOH
Tau K19
244 372

3.1 MATERIALS AND METHODS

3.1.1 REAGENTS

Thioflavin-T was purchased from Fisher Scientific and Uranyl Acetate was purchased from SPI-Chem^{TM}. For TEM, 300 mesh carbon coated Cu grids were purchased from EMS diasum (Hatfield, PA). Nano-Au Maleimide was purchased from Molecular Probes. Aβ42 peptide was purchased from the Keck peptide synthesis facility at Yale university, New Haven CT. Heterologously expressed, purified and lyophilized tauK19(C322S) was a generous gift from Dr David Eliezer (Weill, Cornell). All reagents and chemicals used were of the highest available purity.

3.1.2 Heterologous expression and purification of *s*NUCB1 and its variants

The cDNA clone for human NUCB1 was obtained from ATCC and the DNA fragment for the soluble form of NUCB1 or sNUCB1, corresponding to residues 31-461 of the human NUCB1 protein without the N-terminal signal sequence (residues 1-31) was cloned into a pET28a(+) expression vector (Amersham Biosciences) to generate a N-terminal His_6-tagged construct. The construct for *s*NUCB1 served as a template to generate the His_6-tagged mutant of *s*NUCB1 namely *s*NUCB1(tetramutant. For *s*NUCB1(tetramuant) the coding sequence

changes leading to generation of D253K, E264A, D305K and E316A mutations were introduced by site-directed mutagenesis using the Quick Change system (Stratagene, La Jolla, CA). The vectors were then used to transform BL21 (DE3) cells to express a N-terminal His_6-tag protein containing a PreScission protease site following the His_6-tag. Both proteins were expressed in BL21 (DE3) cells grown in the presence of 50 μg / ml kanamycin. Cells were grown at 37 ^oC to A_{600nm} of ~ 0.7 and then induced with 500 μ M isopropylthio-β-D-galactoside (IPTG) (US Biological). Post induction the culture was grown overnight at 17 ^oC and subsequently harvested. The resulting pellets were re-suspended in a buffer containing 50 mM Tris-HCl pH 8.0, 150 mM NaCl, 50 mM β-mercaptoethanol, bovine lung aprotinin (20 mg/ml), 2 mM phenylmethane sulfonyl fluoride (PMSF) and complete EDTA-free protease inhibitor cocktail tablets (Roche). Thereafter the cells were lysed and the expressed His_6-tag protein was purified from crude extract by using affinity chromatography using Ni-NTA column pre-equilibrated with buffer A (50 mM Tris, pH 8.0, 150 mM NaCl, 50 mM β-mercaptoethanol). The bound His_6-tag protein was eluted from the column by using buffer A supplemented with 500 mM imidazole. The His_6-tag was cleaved by PreScission^{TM} protease, which was subsequently removed. In order to remove Ca^{2+} from *s*NUCB1 or its variant, the proteins were extensively dialyzed against buffer A supplemented with 5 mM EGTA and 1 mM EDTA, which were also eventually removed through dialysis. Finally, size

exclusion chromatography (SEC) was done using Superdex 200 26 / 60 HR column equilibrated with buffer S (50 mM Tris, pH 8.0, 150 mM NaCl, 1 mM DTT) to obtain homogenously pure protein. The typical yield for sNUCB1 and its variant was ~ 5 mg / L. The purity of the proteins was assessed by Coomassie brilliant blue staining after the proteins were separated through SDS-PAGE. The purity of both the proteins was greater than 95%.

3.1.3 Aβ42 fibril formation protocol

In order to produce homogeneous Aβ fibrils, purified and lyophilized Aβ42 peptide (0.6 mg) was added to DDI water (0.2 ml) in a polypropylene eppendorf tube and allowed to stand for 2 min. Thereafter the sample was vortexed for 10 s, and an equal volume of 200 mM Tris pH 7.4 was added, followed by another round of vortexing for 10 s. The sample was then filtered through a 10 kDa cutoff filter by spinning it at 17,200 g in a benchtop microcentrifuge for 3.5 min. Subsequently, the flowthrough was collected and the peptide concentration was determined by absorbance at 280 nm. This solution was used within 5-10 min to set up the fibrillization reaction to obtain mature, elongated and well resolved Aβ42 fibrils within 24 h.

3.1.4 tau K19(C322S) neurofibrillary tangle (NFT) formation protocol

Lyophilized tau K19(C322S) was reconsistuted in a buffer solution (100 mM NaH_2PO_4 pH 7.4, 150 mM NaCl) at a concentration of 50 μM. The reaction mixture was constantly stirred at room temperature and samples were withdrawn at successive time points and analyzed using TEM to confirm formation of NFTs. The analysis shows that tau K19(C322S) forms NFTs within 27 h as shown in the corresponding micrographs.

3.1.5 Transmission Electron Microscopy (TEM)

TEM was performed at the Bioimaging facility at Rockefeller University. Samples were prepared by placing 5 μl of solution onto formvar coated 300 mesh copper grids and counterstained with 2% aqueous uranyl acetate solution. Samples were viewed with a FEI Tecnai12 BioTwinG^2 transmission electron microscope at 80 kV. Digital images were acquired with an AMT XR-60 CCD Digital Camera System and compiled using Adobe Photoshop CS2 and Image J.

3.1.6 MTT Assay

In this assay, 7000 to 9000 undifferentiated PC12 cells in 100 μl were plated in each well of a 96-well plate. Thereafter, cells were grown for an additional 12-16 h at 37 ^oC in an incubator with 5 % CO_2 supply. To test

for toxicity, samples were added to the cells at a concentration of 10 µM / well followed by incubation for 4 h. Thereafter, 10 µl of the MTT (3-(4,5-Dimethyl-2-thiazolyl)-2,5-diphenyl-2H-tetrazolium bromide) stock solution (Sigma-Aldrich, Cat # CGD1) was added to the cells followed by incubation for an additional 4 h. Finally, the media was withdrawn and 200 µl of DMSO was added to each well to dissolve the reduced MTT (formazan) crystals giving a characteristic purple color. Spectrophotometric measurement of the absorbance at 570 nm was done for each well and cell viability was calculated with respect to vehicle alone as the control.

3.2.1 Ca^{2+}-free *s*NUCB1 inhibits Aβ42 fibril formation and disaggregates Aβ42 fibrils

Aβ42 is the most amyloidogenic isoform generated from APP proteolytic cleavage and is the predominant species present in amyloid deposits in AD. APP mutants associated with early-onset AD show increased production of Aβ42 (*145*). Interestingly, preplaque increases in soluble Aβ42 but not Aβ40 are also observed in patients with Down's Syndrome (*146*). Biochemically, Aβ42 forms fibrils at pH 7.4 much more rapidly than Aβ40. In addition, Aβ42 fibrils are comparatively more stable and resistant to sodium dodecyl sulphate treatment (*147, 148*). Hence, Aβ42 was chosen to test the inhibitory activity of *s*NUCB1 in preventing fibril formation. Initially, *in vitro* aggregation of Aβ42 alone (32 μ M) was monitored using TEM analysis of samples withdrawn at time zero, 5 h, 12h and 24 h respectively (Fig.3.2A). The corresponding micrographs show presence of oligomers and protofibrils for the 5h and 12 h sample respectively which eventually grow into long, unbranched and well-resolved fibrils within 24 h (Fig.3.2A). Thereafter, we incubated equimolar (32 μM) amount of Ca^{2+}-free *s*NUCB1 with Aβ42 and samples were withdrawn at time zero, 5 h 12 h and 24 h as above. TEM analysis of samples withdrawn at various time points show presence of high molecular mass species which do not progress to form fibrils even at 24 h (Fig.3.2B). Interestingly, samples withdrawn even after 24 h of incubation

Figure 3.2. Ca^{2+}-free *s*NUCB1 inhibits Aβ42 fibril formation and disaggregates Aβ42 fibrils. Aβ42 alone slowly aggregates *in vitro* to form amyloid fibrils. **(A)** We monitored aggregation of 32 μM solution of Aβ42 with time using TEM. Samples withdrawn at time zero contain low molecular weight species. Thereafter as the aggregation of Aβ42 proceeds, the 5 h sample shows the presence of both oligomers and protofibrils. These continue to form and associate into fibrils as seen in the 12 h sample containing fibrils along with protofibrils and oligomers. The aggregation in complete at 24 h with the formation of characteristic amyloid fibrils. Thereafter, **(B)** we monitored inhibition of Aβ42 fibril formation in the presence of equimolar amount of Ca^{2+}-free *s*NUCB1 (32 μM) added at time zero. TEM images collected after 5 h, 12 h and 24 h of incubation show no trace of fibril formation. Finally, **(C)** disaggregation of Aβ42 fibrils by Ca^{2+}-free *s*NUCB1 was monitored with time using TEM. Aβ42 aggregates to form fibrils within 24 h, which were then incubated with equimolar amount (32 μM) of Ca^{2+}-free *s*NUCB1. Samples withdrawn at 60 min time point show that *s*NUCB1 effectively dissociates Aβ42 fibrils into smaller molecular mass fragments, which continue to exist even at 5 h or 24 h time point without reassociation to form fibrils. The scale bar represents 200 nm.

Figure 3.2

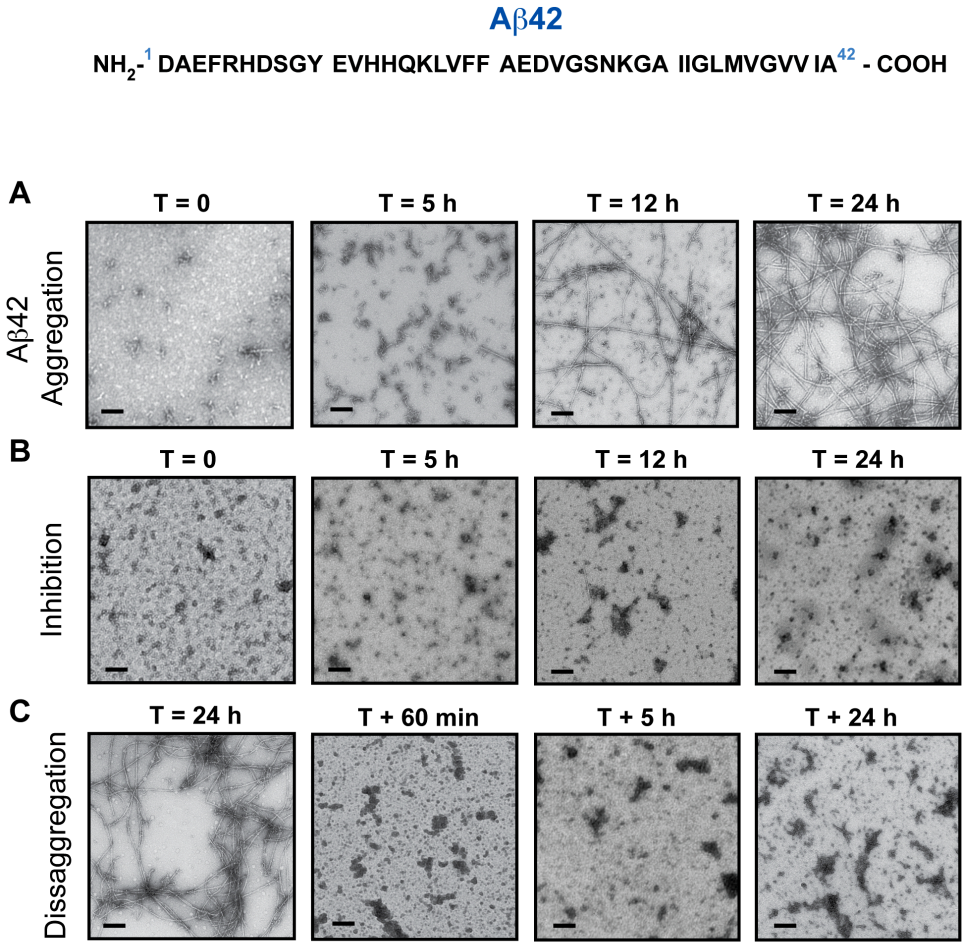
Aβ42
NH2-1 DAEFRHDSGY EVHHQKLVFF AEDVGSNKGA IIGLMVGVV IA42 - COOH
A
Aβ42 Aggregation
T = 0
T = 5 h
T = 12 h
T = 24 h
B
Inhibition
T = 0
T = 5 h
T = 12 h
T = 24 h
C
Dissaggregation
T = 24 h
T + 60 min
T + 5 h
T + 24 h

continued to show inhibition of fibril formation. This shows that Ca^{2+}-free *s*NUCB1 effectively inhibits Aβ42 fibril formation. Subsequently, to explore the effect of Ca^{2+}-free *s*NUCB1 towards disaggregating preformed Aβ42 fibrils, we added equimolar amount (32μM) of Ca^{2+}-free *s*NUCB1 to Aβ42 fibrils in a reaction mixture. TEM analysis shows that Ca^{2+}-free *s*NUCB1 can effectively dissociate Aβ42 fibrils within 60 min and the disaggregated species continue to exist without progressing to form fibrils even at 24 h time point (Fig. 3.2C). Thus functionally, Ca^{2+}-free *s*NUCB1 inhibits Aβ42 aggregation and also effectively disaggregates the preformed fibrils.

3.2.2 Ca^{2+} disrupts inhibition and disaggregation of Aβ42 fibrils by *s*NUCB1

NUCB1 is a multi-domain protein with two characteristic Ca^{2+}-binding EF hand motifs (Fig.3.1). Ca^{2+}-binding to *s*NUCB1 has been shown to induce structural rearrangement in the protein (Fig.1.2). Hence, the effect of Ca^{2+}-binding on the anti-amyloidogenic properties of *s*NUCB1 was investigated. As earlier, Aβ42 was incubated with equimolar amount (32 μM) of *s*NUCB1 in the presence of 1 mM Ca^{2+} in the reaction mixture.

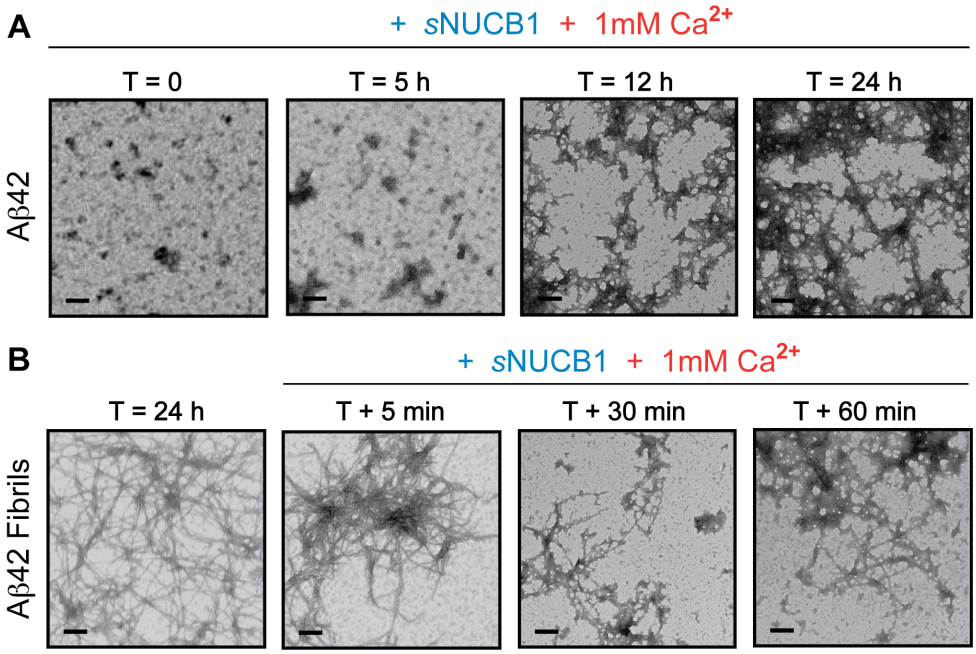

Figure 3.3. Ca^{2+} prevents the ability of *s*NUCB1 to inhibit aggregation and dissociate Aβ42 fibrils. (A) 32 μM Ca^{2+}-free *s*NUCB1 was incubated with 1 mM Ca^{2+} in the reaction mixture at 25 ^{o}C with the subsequent addition of equimolar amount of Aβ42. Samples were withdrawn at the indicated time points and analyzed using TEM. As shown, Ca^{2+}-bound *s*NUCB1 does not inhibit aggregation of Aβ42 as fibrils are present in the 12 h sample, which continue to grow extensively as seen in the 24 h sample. In addition, the ability of Ca^{2+}-bound *s*NUCB1 towards **(B)** disaggregating Aβ42 fibrils was monitored using TEM. Equimolar amount of Ca^{2+}-bound *s*NUCB1 (32 μM) was added to Aβ42 fibrils and samples were withdrawn at the indicated time points. As shown, fibrils are still present in the reaction mixture after 60 mins of incubation showing that Ca^{2+}-bound *s*NUCB1 cannot dissociate Aβ42 fibrils. The scale bar represents 200 nm.

Unlike with Ca^{2+}-free *s*NUCB1, the TEM analysis of samples withdrawn from the reaction mixture at various time points show initiation of fibril formation within 12 h with extensive Aβ42 fibrils present at 24 h (Fig.3.3A), which is similar to the time frame of fibril formation by Aβ42 alone (Fig.3.2A). This shows that binding of Ca^{2+} to *s*NUCB1 disrupts its functional ability towards inhibiting Aβ42 fibril formation and points towards Ca^{2+}-free *s*NUCB1 as being the only functionally adept form in preventing Aβ42 amyloidogenesis. In addition, disaggregation of preformed Aβ42 fibrils by equimolar (32 μM) *s*NUCB1 was also examined in the presence of 1 mM Ca^{2+} in the reaction mixture. TEM analysis clearly shows that unlike Ca^{2+}-free *s*NUCB1, Ca^{2+}-bound *s*NUCB1 cannot dissociate Aβ42 fibrils as observed by the presence of fibrils in samples withdrawn after 5 min, 30 min and 60 min of incubation. Thus Ca^{2+}-binding nullifies the anti-amyloidogenic properties of *s*NUCB1.

3.2.3 *s*NUCB1(tetramutant) is insensitive to Ca^{2+} but functionally similar to *s*NUCB1

Our earlier results showed that heterologously expressed and purified *s*NUCB1(tetramutant) is correctly folded and unlike *s*NUCB1, lacks the ability to bind to Ca^{2+}. Hence in order to test the anti-amyloidogenic properties of *s*NUCB1(tetramutant) towards Aβ42 in the presence of excess Ca^{2+}, we incubated equimolar amount (32 μM) of Aβ42 with

Figure 3.4. Ca^{2+}-insensitive anti-amyloidogenic activity of *s*NUCB1(tetramutant). *s*NUCB1(tetramutant) does not bind to Ca^{2+} and was tested for its ability to affect Aβ42 amyloid formation. We incubated Aβ42 with equimolar concentration of *s*NUCB1(tetramutant) (32 μM), both in the **(A)** absence and **(B)** presence of 1 mM Ca^{2+}. TEM analysis of samples withdrawn from each reaction mixture at T = 0 h, 5 h, 12 h and 24 h time points show complete inhibition of fibril formation. Subsequently, the ability of *s*NUCB1(tetramutant) to disaggregate fibrils was investigated. Thereafter, we incubated stoichiometric amount of *s*NUCB1(tetramutant) (32 μM) with fibrils in a reaction mixture, both in the **(C)** absence or **(D)** presence of 1 mM Ca^{2+}. As a control, micrographs with Aβ42 fibrils before addition of *s*NUCB1(tetramutant) are shown on the left. TEM images corresponding to samples withdrawn after 30 min and 60 min of *s*NUCB1(tetramutant) addition show that *s*NUCB1(tetramutant) can efficiently dissociate the preformed fibrils of Aβ42. The scale bar represents 200 nm.

Figure 3.4

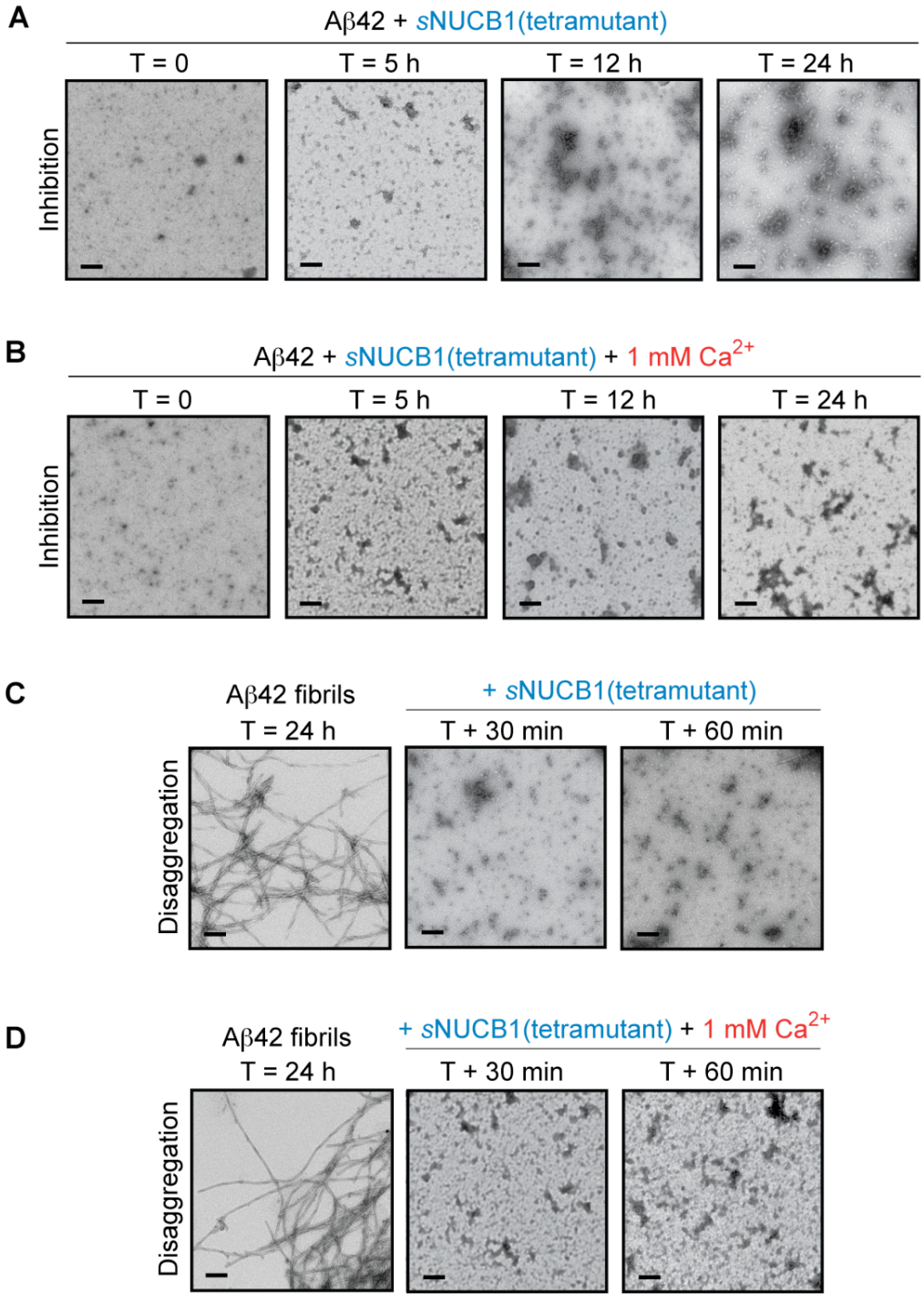
A
Aβ42 + sNUCB1(tetramutant)
T = 0
T = 5 h
T = 12 h
T = 24 h
Inhibition
B
Aβ42 + sNUCB1(tetramutant) + 1 mM Ca2+
T = 0
T = 5 h
T = 12 h
T = 24 h
Inhibition
C
Aβ42 fibrils
T = 24 h
+ sNUCB1(tetramutant)
T + 30 min
T + 60 min
Disaggregation
D
Aβ42 fibrils
T = 24 h
+ sNUCB1(tetramutant) + 1 mM Ca2+
T + 30 min
T + 60 min
Disaggregation

*s*NUCB1(tetramutant) in a reaction mixture in the absence and presence of 1 mM Ca^{2+}. Samples were withdrawn at the indicated time points and effect of *s*NUCB1(tetramutant) on aggregation was analyzed using TEM. The corresponding micrographs show that similar to *s*NUCB1, *s*NUCB1(tetramutant) also effectively inhibits aggregation of Aβ42 to form amyloid fibrils (Fig.3.4A). However more importantly, even in the presence of excess Ca^{2+} in the reaction mixture, *s*NUCB1(tetramutant) continues to be functionally active and inhibits Aβ42 fibril formation as shown by the complete absence of any fibrillar aggregates in the micrograph corresponding to 24 h sample (Fig.3.4B). Thereafter we investigated the functional ability of *s*NUCB1(tetramutant) towards disaggregating Aβ42 fibrils and the effect of Ca^{2+} on it. Aβ42 alone (32 μM) aggregates within 24 h to form fibrils. We then added equimolar amount (32 μ M) of *s*NUCB1(tetramutant) to it in the absence and presence of 1 mM Ca^{2+} in the reaction mixture (Fig.3.4C,D). Samples from each reaction were withdrawn after 30 min and 60 min for analysis using TEM. The corresponding micrographs show that *s*NUCB1(tetramutant) effectively disaggregates Aβ42 fibrils both in the absence (Fig.3.4C) and presence of Ca^{2+} (Fig.3.4D). Hence unlike *s*NUCB1, the functional ability of *s*NUCB1(tetramutant) is unaffected by Ca^{2+} and it retains its anti-amyloidogenic properties towards Aβ42 even in the presence of high concentrations of Ca^{2+} in the reaction mixture.

3.2.4 *s*NUCB1 / *s*NUCB1(tetramutant) mediated Aβ42 fibril dissociation generates non-toxic species

Aβ42 aggregation leads to fibril formation through association of oligomers and protofibrils. Tissue culture based MTT assay can provide quantitative calorimetric estimate of the toxicity of intermediate species along with the fibrillar aggregates (*149*). As shown earlier, Ca^{2+}-free *s*NUCB1 inhibits Aβ42 fibril formation and effectively disaggregates preformed Aβ42 fibrils. However, TEM analysis cannot rule out the presence of oligomeric species stabilized by *s*NUCB1 in the reaction mixture. Several studies have shown that along with fibrils, oligomeric species are also cytotoxic (*150, 151*). Hence, to test the potential toxicity of the species generated after Aβ42 fibril dissociation by Ca^{2+}-free *s*NUCB1 or *s*NUCB1(tetramutant), MTT assays were conducted with undifferentiated PC12 cells. As a control, administration of either *s*NUCB1 or *s*NUCB1(tetramutant) to the cells showed that they are completely non-toxic to the cells. Thereafter in the first set of experiments, samples from Aβ42 aggregation reaction alone were withdrawn at time zero, 5 h and 24 hours and administered to cells at a final concentration of 10 μM to assay for cytotoxicity by monitoring reduction of MTT. For time zero sample, neuronal cells showed 80% viability. As aggregation continues, monomers assemble into oligomers within 5 h for which the cell viability decreased to 60%. Eventually, administration of sample containing Aβ42 fibrils at 24 h further reduced the cell viability to 40%

Figure 3.5. Inhibition of cytotoxicity of Aβ42 fibrils by *s*NUCB1 and *s*NUCB1(tetramutant). We measured the cell viability of PC12 cells using the standard MTT reduction assay. The delivery vehicle alone was administered to the cells as the control. Both *s*NUCB1 and *s*NUCB1(tetramutant) individually resulted in 90% to 95% final cell viability, showing that each of the protein subunits by themselves are non-toxic. Thereafter, we administered samples withdrawn from a Aβ42 aggregation reaction at 0 h, 5 h and 24 h to PC12 cells such that the final concentration for each is 10 μM. Cell viability measurements using MTT reduction estimate that T = 0 h sample decreases the cell viability to 80%. The subsequent addition of samples consisting of essentially oligomers (T = 5h) and fibrils (T = 24h) continue to decrease cell viability to 55% and 39% respectively. We then incubated the Aβ42 fibrils at T = 24 h with equimolar (32 μ M) amounts of *s*NUCB1 or *s*NUCB1(tetramutant) and samples were withdrawn after 5 min, 15 min, 30 min and 60 min respectively. Each sample was then administered to PC12 cells in culture at a final concentration of 10 μM and cell viability was estimated using MTT reduction. The results show ~ 90 % cell viability for samples withdrawn from reaction mixture containing *s*NUCB1 were administered whereas cell viability of ~ 95 % was observed for *s*NUCB1(tetramuant) containing samples. Each experiment was repeated atleast 3 times and the data was plotted as the mean ± S.E.M.

Figure 3.5

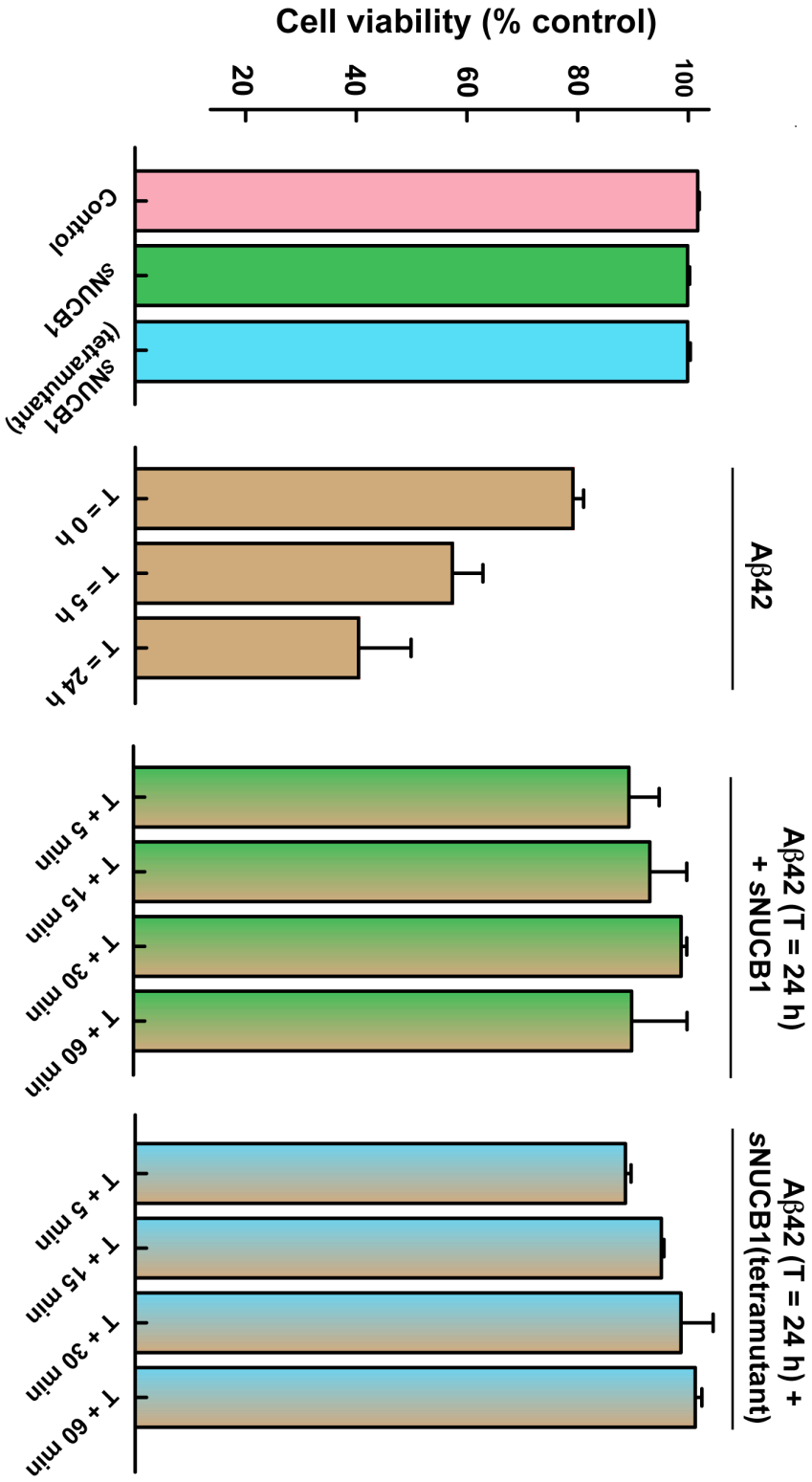
Cell viability (% control)
20
40
60
80
100
Control
sNUCB1
sNUCB1 (tetramutant)
Aβ42
T = 0 h
T = 5 h
T = 24 h
Aβ42 (T = 24 h) + sNUCB1
T + 5 min
T + 15 min
T + 30 min
T + 60 min
Aβ42 (T = 24 h) + sNUCB1(tetramutant)
T + 5 min
T + 15 min
T + 30 min
T + 60 min

(Fig.3.5). In the next set of experiments, Aβ42 fibrils were incubated with equimolar amount of Ca^{2+}-free *s*NUCB1 or *s*NUCB1(tetramutant) and samples were withdrawn at 5 min, 15 min, 30 min and 60 min time points for administration to PC12 cells at a final concentration of 10 μM. Intriguingly, MTT reduction dependent cell viability measurements estimated ~ 90 % viability for 5 min sample from the disaggregation reaction with either *s*NUCB1 or *s*NUCB1(tetramutant) and greater than 95 % viability for later time points showing that disaggregated species are essentially non-toxic to PC12 cells (Fig.3.5). Thus, MTT assay shows that both *s*NUCB1 and *s*NUCB1(tetramutant) disaggregate cytotoxic Aβ42 fibrillar aggregates into non-toxic species.

3.2.5 Ca^{2+}-free *s*NUCB1 inhibits tau K19(C322S) NeuroFibrillary Tangle (NFT) formation

Human tau is a multi-domain protein with 31-32 residue long repeat regions (R1-R4) at the CT constituting the microtubule-association domain (Fig.3.1). Tau K19 represents a synthetic and truncated form of tau, which can aggregate *in vitro* to form NFTs. A growing role of tau in AD pathology has recently been reported. Hence in order to investigate the functional ability of Ca^{2+}-free *s*NUCB1 towards inhibiting aggregation of

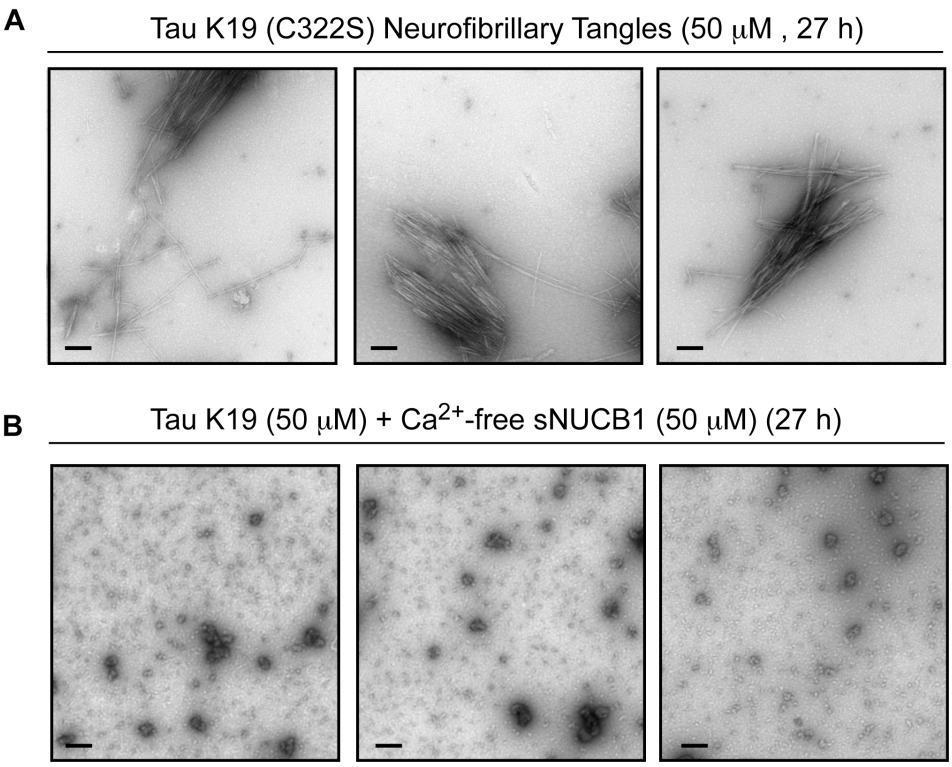

Figure 3.6. Ca^{2+}-free *s*NUCB1 inhibits tau K19(C322S) neurofibrillary tangle (NFT) formation. Tau K19(C322S) slowly aggregates *in vitro* to form NFTs. **(A)** We monitored aggregation of 50 μM tau K19(C322S) in solution with time using TEM. Samples withdrawn from a constantly stirred solution at room temprature after 27 h show presence of NFTs of tau K19(C322S). In order to monitor the effect of Ca^{2+}-free *s*NUCB1 on aggregation of tau K19(C322S) to form NFTs, **(B)** we incubated equimolar amount (50 μM) of tau K19(C322S) with Ca^{2+}-free *s*NUCB1 for 27 h. Samples were withdrawn after 27 h and analyzed using TEM. The micrographs show complete absence of any NFTs. This suggests that Ca^{2+}-free *s*NUCB1 can effectively inhibit NFT formation by tau K19(C322S). The scale bar represents 200 nm.

tauK19 towards forming NFTs, we used the mutant tau K19(C322S), which lacks the ability to form intermolecular disulphide bonds. We incubated 50 μ M tau K19(C322S) alone or with equimolar amount of Ca^{2+}-free *s*NUCB1 in 100 mM NaH_2PO_4 pH 7.4, 150 mM NaCl for 27 h at room temperature with constant stirring. TEM analysis of samples withdrawn from the reaction mixtures show that tau K19(C322S) alone aggregates within 27 h to form NFTs (Fig. 3.6A). However, incubation of tau K19(C322S) with Ca^{2+}-free *s*NUCB1 completely inhibits NFT formation as seen by the complete absence of any fibrillar aggregates in the corresponding micrographs for the 27 h sample (Fig.3.6B). Hence, Ca^{2+}-free *s*NUCB1 effectively inhibits *in vitro* formation of NFTs by tau K19(322S).

3.3 DISCUSSION

Amyloid hypothesis has been the central dogma of AD research. Both Aβ oligomers and fibrillar aggregates have been shown to exert neurotoxic effects (*150, 152*). For decades, generation of Aβ was thought to be a non-essential product resulting from the erroneous cleavage of APP by γ-secretase. However, recent work has revealed the neuroprotective role of monomeric Aβ and has highlighted the involvement of APP in synaptic transmission (*110, 123*). Thus neuritic dystrophy observed in AD can result from both the loss of function of Aβ and the neurotoxic effects of Aβ aggregates. In addition, a secondary role of tau hyperphosphorylation and its aggregation into NFTs dependent on Aβ fibril formation has also been postulated and shown to exacerbate cytotoxicity (*153*). Hence, preventing the aggregation of Aβ is the primary therapeutic target with significant interest in understanding and controlling intracellular tau aggregation. Our results show that the soluble form of NUCB1 can both inhibit Aβ42 aggregation and effectively disaggregate the pre-formed fibrils in a Ca^{2+}-dependent manner. In addition, Ca^{2+}-free *s*NUCB1 also inhibits aggregation of a truncated form of tau namely tauK19(C322S) into NFTs and thus might inhibit aggregation of hyperphosphorylated intracellular pool of full-length tau as relevant to AD pathology. Thus this dual anti-amyloidogenic functionality of *s*NUCB1 presents an ideal target that may be therapeutically relevant and useful. Clinically, the symptoms of cognitive impairment in an AD patient appear years after initiation of

Aβ aggregation, tau hyperphosphorylation, synaptic loss and neurite dystrophy (*154*). Thus prevention of neurodegeneration requires the clearance of deposited Aβ aggregates and inhibition of any further Aβ aggregation to restore physiological Aβ function. In accordance with this observation, our data shows that Ca^{2+}-free *s*NUCB1 possesses the ability to both inhibit fibril formation and disaggregate them into non-toxic species.

AD research in the past decade has unraveled the neurotoxicity effects of Aβ oligomers and fibrils. However, the events that initiate Aβ aggregation are still not clearly understood. In 2006, Yankner and coworkers showed that Ca^{2+} enhanced the aggregation of early protofibrillar species and increased their association to form fibrils. They proposed a potential role of Ca^{2+} in Aβ aggregation and toxicity in the AD brains (*155*). It is known that Ca^{2+}-homeostasis plays a central role in many aspects of brain physiology including growth, plasticity, learning and memory as well as cell death and degeneration. Ca^{2+} ions are essential during signal transmission from one neuron to another and Ca^{2+}-dysregulation has been repeatedly observed in AD research (*156, 157*). Aβ is believed to cause Ca^{2+}-dysregulation either by interacting with cell surface receptors coupled with Ca^{2+}-flux or by forming leaky membrane pores (*56*). NUCB1 is a Ca^{2+}-binding protein, which maintains Ca^{2+}-homeostasis and Ca^{2+}-storage in Golgi (*16, 46*). NUCB1 is ubiquitously expressed, found

in ER and resides in Golgi for more than 12 hours (*23*). APP is synthesized in ER, transported through the Golgi apparatus into the TGN. Immunofluorescence assays have shown that Aβ42 generated from APP is present in ER under steady state conditions and is also localized in TGN (*158*). Co-localization of NUCB1 and APP has been reported in both cultured cells and mouse brains (*28*). Thus the role of NUCB1 in maintaining Ca^{2+}-homeostasis and its interaction with APP and Aβ suggests towards a possible involvement of NUCB1 in AD pathology.

An alternative hypothesis to initiation of Aβ aggregation could be the disruption of cellular machinery involving Hsps, sHsps, cellular proteases and trafficking molecules that normally prevent the aggregation and accumulation of Aβ. Both extracellular and intracellular chaperones have been shown to co-localize with Aβ deposits in senile plaques and inhibit Aβ aggregation and are involved in its clearance across the blood-brain barrier (*74, 159*). In addition, Zn^{2+}-dependent metalloprotease Neprilysin targets Aβ diffuse deposits and neuritic plaques for their catalytic degradation (*137*). Synaptic activity has been shown to decrease intracellular Aβ levels. Upon APP cleavage, Aβ40 is generated which is secreted while intraneuronal Aβ42 is subjected to Neprilysin mediated degredation (*110*). Overexpression of IDE decreases the extracellular levels of both Aβ40 and Aβ42 monomers. The current prevailing evidence

also suggests a differential role of apolipoprotein E (apoE) isoforms in mediating clearance of Aβ from the extracellular space. Importantly, the apoE4 isoform, which is associated with increased risk for AD, has been shown to exhibit an impaired ability to promote Aβ proteolysis and thus clearance from the extracellular space compared to apoE2 and apoE3 (*140, 141*). Furthermore, Low-density lipoprotein receptor-related protein 1 or LRP1, was shown to bind Aβ or to its chaperone complex with β2 Microglobulin or apoE4 and deliver the complex to lysosomes for degradation (*160*). A soluble form of LRP1 sequesters 70-90 % of plasma Aβ peptides and its levels and capacity to bind Aβ are reduced in AD brains (*161*). In a recent study, Brodeur *et al.* showed that NUCB1 strongly binds to LRP, assists in its endosomal sorting and consequently prevents its lysosomal degradation (*27*). Functionally, NUCB1 has also been shown to affect the biogenesis of APP, which in turn attenuates Aβ production (*28*). Thus physiologically, NUCB1 can possibly regulate Aβ production, assist in its clearance through reduced degradation of LRP and inhibit the deposition of Aβ aggregates. Future work investigating the physiological role of NUCB1 should provide evidence in favor or against these hypotheses.

Our results show that NUCB1 inhibits Aβ42 fibril formation only in its Ca^{2+}-free form. This is consistent with the reported interaction of NUCB1 with APP only in the absence of Ca^{2+}. Physiologically, neuronal Ca^{2+}

levels vary from 100 nM intracellular to 1 mM extracellular concentration. Given the K_d values of Ca^{2+}-binding to *s*NUCB1 of 6.3 μM and 73.5 μM respectively (Fig1.3), NUCB1 should primarily exist in a Ca^{2+}-free form intraneuronally and Ca^{2+}-bound in the extracellular environment. This implies that NUCB1 can interact with Aβ42 intraneuronally but extracellular Ca^{2+} levels may inhibit this interaction. However, our engineered Ca^{2+}-insensitive mutant, *s*NUCB1(tetramutant) should be functional both intra- and extracellularly. The role of intraneuronal and extracellular Aβ in facilitating tau hyperphosphorylation, mitochondrial and proteosomal disruption, dysregulation of Ca^{2+} homeostasis, synaptic failure and cognitive dysfunction has placed it at the forefront of AD research. Additionally, it has been shown that Aβ42 when generated is poorly secreted and has a high tendency to aggregate under physiological conditions. Thus the discovery of the functional role of NUCB1 in inhibiting Aβ42 aggregation and disaggregating its fibrils into non-toxic species becomes increasingly important. Furthermore, the ability of Ca^{2+}-free *s*NUCB1 towards inhibiting tau K19(C322S) aggregation to form NFTs suggests that NUCB1 might have some role in regulating the aggregation of full-length tau upon hyperphosphorylation. Future work investigating this observation both in an *in vitro* and *in vivo* model would be useful towards understanding and establishing the physiological role of NUCB1. In addition, the observed reduction of NUCB1 levels in the brains of AD patients along with the disruption of Ca^{2+}-homeostasis could

individually or together cause progression of the diseased state in AD patients. *s*NUCB1(tetramutant) circumvents the Ca^{2+}-dependence of the anti-amyloidogenic properties of NUCB1 and should be functional under disrupted Ca^{2+}-homeostasic conditions. This can be a useful molecular handle and future studies with both *s*NUCB1 and *s*NUCB1(tetramutant) in relevant mouse models of AD should provide important insights into their functional capabilities. Hence understanding of the role of NUCB1 in AD pathology can be useful in designing novel and effective therapeutics.

APPENDIX

doi:10.1016/j.jmb.2009.08.043 J. Mol. Biol. (2009) 393, 882–897

JMB

Available online at www.sciencedirect.com

ScienceDirect

ELSEVIER

Structural Evidence for a Sequential Release Mechanism for Activation of Heterotrimeric G Proteins

Neeraj Kapoor[1], Santosh T. Menon[1], Radha Chauhan[2], Pallavi Sachdev[1] and Thomas P. Sakmar[1]*

[1]*Laboratory of Biochemistry and Molecular Biology, Rockefeller University, 1230 York Avenue, New York, NY 10065, USA*

[2]*Laboratory of Cell Biology, Rockefeller University and Howard Hughes Medical Institute, 1230 York Avenue, New York, NY 10065, USA*

Received 20 June 2009; received in revised form 13 August 2009; accepted 17 August 2009
Available online 22 August 2009

Edited by I. Wilson

Heptahelical G-protein (heterotrimeric guanine nucleotide-binding protein)-coupled receptors couple to heterotrimeric G proteins to relay extracellular signals to intracellular signaling networks, but the molecular mechanism underlying guanosine 5′-diphosphate (GDP) release by the G protein α-subunit is not well understood. Amino acid substitutions in the conserved α5 helix of G_i, which extends from the C-terminal region to the nucleotide-binding pocket, cause dramatic increases in basal (receptor-independent) GDP release rates. For example, mutant $G\alpha_{i1}$-T329A shows an 18-fold increase in basal GDP release rate and, when expressed in culture, it causes a significant decrease in forskolin-stimulated cAMP accumulation. The crystal structure of $G\alpha_{i1}$-T329A·GDP shows substantial conformational rearrangement of the switch I region and additional striking alterations of side chains lining the catalytic pocket that disrupt the Mg^{+2} coordination sphere and dislodge bound Mg^{+2}. We propose a "sequential release" mechanism whereby a transient conformational change in the α5 helix alters switch I to induce GDP release. Interestingly, this mechanistic model for heterotrimeric G protein activation is similar to that suggested for the activation of the plant small G protein Rop4 by RopGEF8.

Keywords: G-protein-coupled receptors (GPCRs); heterotrimeric G-proteins; α5 helix; X-ray crystallography; activation mechanism

Introduction

Heterotrimeric guanine nucleotide-binding regulatory proteins, G proteins ($G\alpha\beta\gamma$),[1,2] relay signals from heptahelical transmembrane G-protein-coupled receptors (GPCRs) to downstream effector molecules.[3,4] GPCRs activate G proteins by inducing the release of guanosine 5′-diphosphate (GDP) from the Gα subunit in the active receptor (R*)–G protein complex.[5–7] Guanosine 5′-triphosphate (GTP) uptake by Gα leads to the dissociation of the heterotrimer into the Gα and $G\beta\gamma$ subunits, making them available to interact with various downstream effectors. The interface between the cytoplasmic structure of an active GPCR and its bound G protein might be as far as 30 Å away from the bound GDP.[8,9] The agonist ligand-binding site on the receptor, as judged by the crystal structures of inverse-agonist-bound rhodopsin[10] and adrenergic receptors,[11,12] are approximately an additional 40 Å away from the inner surface of the bilayer. How does ligand binding to a GPCR induce GDP release from Gα at a distance of ~70 Å?

Although the crystal structures of several G protein subunit isoforms,[13–18] complexes[19–22] and mutants with altered exchange rates[23,24] have been solved, we still lack a mechanistic understanding of how active GPCRs stimulate nucleotide

*Corresponding author. E-mail address: sakmar@mail.rockefeller.edu.

Abbreviations used: G protein, heterotrimeric guanine nucleotide-binding protein; GPCR, G-protein-coupled receptor; GDP, guanosine diphosphate; GTP, guanosine 5′-triphosphate; CT, C-terminus; G_t, transducin; EPR, electron paramagnetic resonance; WT, wild type; FRET, fluorescence resonance energy transfer; FK, forskolin; GTPase, guanosine triphosphatase; AC, adenylyl cyclase; SEAP, secreted alkaline phosphatase; ITC, isothermal titration calorimetry; GEF, guanine nucleotide exchange factor; FCS, fetal calf serum.

exchange by the Gα subunit. Nevertheless, these structural studies have identified state-dependent conformational differences within the Gα subunit and suggest allosteric coupling of well-defined switch regions to the activation process.[15] The exchange of GDP for GTP induces ordering in the switch regions, making the GTP-bound state conformationally more rigid.

During activation, R* engages the C-terminus (CT) of G protein α-subunit. Earlier mutagenesis work with transducin (G_t) showed that activation signal is transferred to the catalytic pocket via the α5 helix that connects the CT to the nucleotide-binding β6–α5 loop.[25] Additionally, site-directed mutagenesis of α5 helix residues of G_t showed drastic alterations in the basal rates of nucleotide exchange.[26,27] Previous electron paramagnetic resonance (EPR) studies with site-directed spin-labeled G protein α-subunits proposed a rigid-body movement of the α5 helix upon binding of receptor during activation.[28–30] Furthermore, the crystal structure of Q333C–I56C $G\alpha_{i1}$, a mimic of EPR-measured receptor-associated conformation, suggests a shift of α5 helix toward the bound nucleotide.[31] The recent structure of ligand-free opsin in complex with a peptide analogue of the CT tail of the α-subunit of G_t shows, as shown earlier by NMR,[32] that the G_t peptide binds at an angle of ~40° to the hypothetical plane of the bilayer and makes contacts with several conserved amino acid residues on the receptor transmembrane border regions, notably R135. The structure also suggests how the G protein heterotrimer might dock to R*.[33] However, the lack of a crystal structure of an active GPCR in complex with the full-length G protein α-subunit or heterotrimer limits our understanding of the exact molecular determinants of receptor-mediated G protein activation.

We present here the molecular details of a probable intermediate state along the G protein activation pathway. We carried out Ala-scanning mutagenesis to make a panel of site-specific mutants of the α5 helix of $G\alpha_{i1}$ and identified a number of mutants with orders-of-magnitude increases in basal exchange rates of guanine nucleotides in the absence of receptor. The mutant $G\alpha_{i1}$-T329A, for example, showed a nearly 20-fold increase in receptor-independent basal nucleotide-exchange rate. In cell-based assays, $G\alpha_{i1}$-T329A significantly attenuated forskolin (FK)-induced cAMP accumulation and lowered basal cellular cAMP levels. We then solved high-resolution crystal structures of $G\alpha_{i1}$-T329A in both GDP- and guanosine GTPγS-bound states and compared the structures with other available G protein structures. The T329A mutation caused significant alterations in the structure of the switch I region and affected the complex Mg^{2+} coordination sphere in the nucleotide-binding site. Based on the new structures, we propose a "sequential release" mechanism for receptor-induced nucleotide exchange where specific structural changes mediated by the α5 helix destabilize bound Mg^{2+}, which exits the active site to facilitate GDP release.

Results

Fluorescence measurement of nucleotide binding

We first constructed a set of single point mutants of $G\alpha_{i1}$ in which residues T329, V332 and F336 on the α5 helix and residue Q52 on the α1 helix were replaced with Ala (Fig. 1). A double-mutant construct with both Q52 and T329 residues replaced with alanine was also engineered. All single and double mutants were expressed as recombinant proteins in *Escherichia coli* and purified to homogeneity. The intrinsic fluorescence of W211, which is present in the switch II region of $G\alpha_{i1}$, increases upon GTP binding due to its movement from a solvent-exposed environment to a hydrophobic pocket in the nucleotide-binding pocket[14] and has been used to measure the kinetics of GTP uptake reaction.[34] The rate of basal nucleotide exchange for each mutant was measured by monitoring its fluorescence in the presence of GTPγS (a nonhydrolyzable analogue of GTP) (Fig. 2a). Pseudo-first-order rate constants for GTPγS uptake by wild-type (WT) $G\alpha_{i1}$ and the single and double $G\alpha_{i1}$ mutants were calculated.

The nucleotide-exchange reaction was also monitored using the fluorescence nucleotide analogue, mant [2′,3′-*O*-(*N*-methyl-anthraniloyl)]-GTPγS (Fig. S1). As Gα takes up mant-GTPγS, W211 moves into its characteristic hydrophobic pocket in the nucleotide-binding site. Since the excitation spectrum of mant-GTPγS overlaps with the emission spectrum of Trp, fluorescence resonance energy transfer (FRET) is observed upon mant-GTPγS binding to $G\alpha_{i1}$. Higher rates of FRET increase were observed for the $G\alpha_{i1}$ mutants compared with that of the WT $G\alpha_{i1}$, thereby corroborating the results of the GTPγS uptake assay. In general, we observed multifold increases in basal nucleotide-exchange rates in the mutants compared with that in WT $G\alpha_{i1}$. In particular, $G\alpha_{i1}$-T329A displayed an 18-fold increase in its rate of GTPγS uptake compared with that of WT $G\alpha_{i1}$ and appeared to be stable in solution over extended time periods (data not shown). Therefore, we chose the $G\alpha_{i1}$-T329A mutant for additional detailed studies.

Physiological role of $G\alpha_{i1}$-T329A

To investigate the potential physiological relevance of the T329A mutation, we expressed the human $G\alpha_{i1}$-T329A mutant in mammalian HEK 293 cells. In control experiments, HEK cells were transfected with WT $G\alpha_{i1}$ or a constitutively active, guanosine triphosphatase (GTPase)-deficient mutant, $G\alpha_{i1}$-Q204L.[35] We next measured FK-stimulated intracellular cAMP levels in the transfected cells. FK directly activates adenylyl cyclase (AC) and is commonly used as an adjunct in assays designed to evaluate the ability of G_s and G_i to activate or inhibit, respectively, cellular AC activity. GTP-bound, active WT $G\alpha_{i1}$ acts to

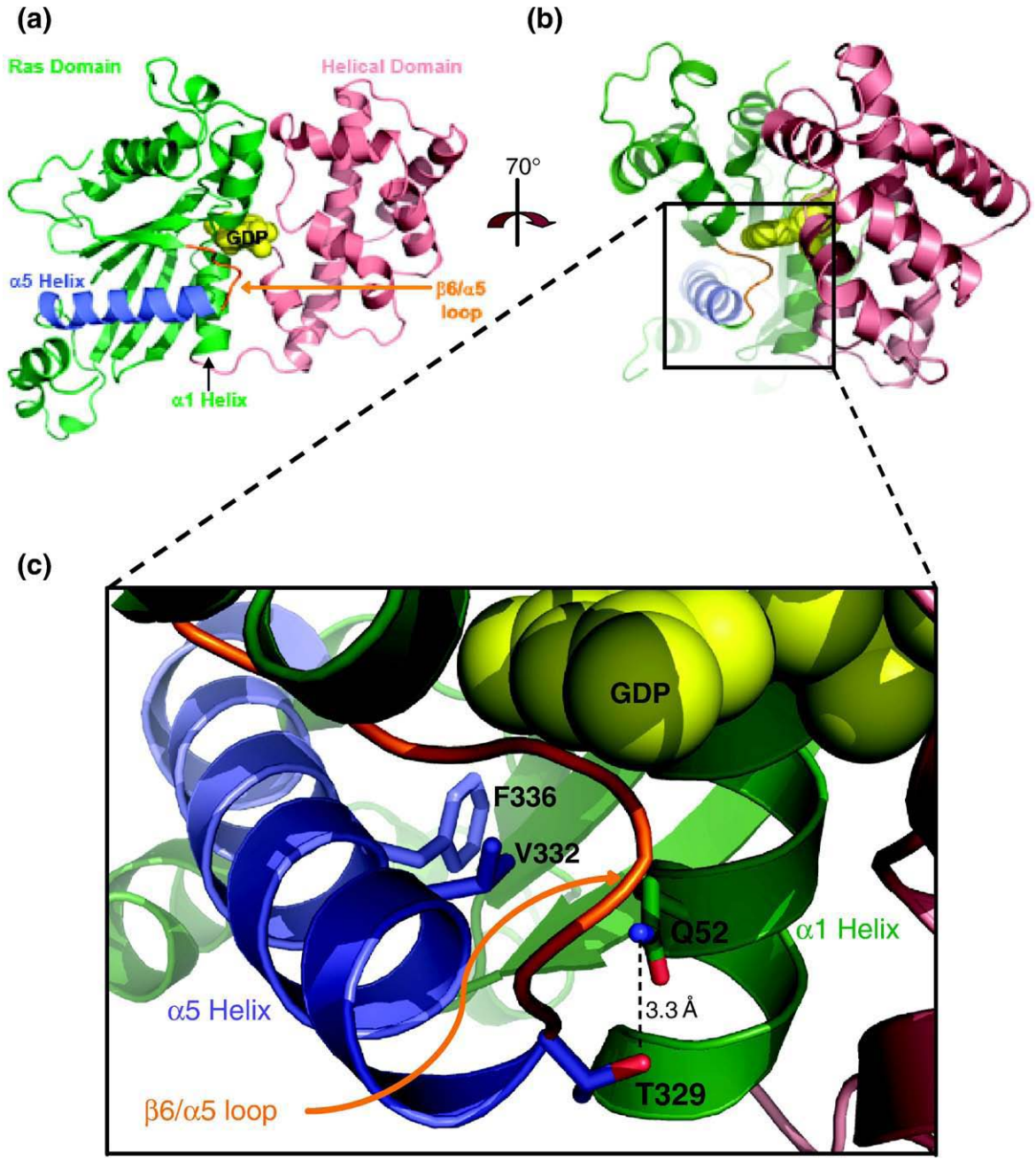

Fig. 1. The structure of $G\alpha_{i1}$ showing sites of amino acid substitution on the α5 helix. (a) The structure of the GDP-bound form of WT $G\alpha_{i1}$ consists of the GTPase domain (green) and the helical domain (salmon) with the nucleotide shown as a ball-and-stick model (yellow) sandwiched between them. The α5 helix (blue) connects the receptor interacting C-terminal tail with the GDP-interacting β6–α5 loop (orange). (b) The structure in (a) has been rotated clockwise by 70° along the vertical axis. The α5 helix, lying in a trough formed by the α1 helix and β1–β6 strands, is ~50% solvent-exposed and oriented in an N- to C-terminal order coming out of the plane of paper. (c) A zoom into the α5 helix region shows the sites of mutations on the α5 helix (F336, V332, T329) and the neighboring α1 helix (Q52A). As shown, T329 and Q52 residues could be involved in a possible H-bonding interaction via their side-chain groups that are placed 3.3 Å apart. Each of the residues was mutated to alanine for generation of single- and double-point mutants. The bound nucleotide close to the CT of the α1 helix is shown as a ball-and-stick model (yellow).

inhibit AC, resulting in a decreased concentration of intracellular cAMP.[36,37] We tested the ability of the $G\alpha_{i1}$-T329A mutant to affect FK-stimulated cellular cAMP levels, using a highly sensitive gene reporter assay that relies on secreted alkaline phosphatase (SEAP) to report intracellular cAMP concentration.[38,39] Compared with WT, expression of the constitutively active $G\alpha_{i1}$-Q204L mutant caused a dramatic decrease in FK-stimulated cAMP levels (Fig. 2b and c). This effect is presumed to be a direct result of increased inhibition of AC by the $G\alpha_{i1}$-Q204L mutant. Interestingly, the $G\alpha_{i1}$-T329A mutant mimics the effect of the Q204L mutant in its ability to inhibit FK-stimulated cAMP production. Also, unlike

residue Q204, T329 is not in close proximity to the bound nucleotide and hence cannot directly influence the stability of the bound nucleotide even though the T329A-$G\alpha_{i1}$ mutant mimics a constitutively active state. This suggests that the mutation somehow allosterically modulates the fast rates of nucleotide exchange on the $G\alpha_{i1}$ subunit.

Crystal structure of $G\alpha_{i1}$-T329A in the GDP- or GTPγS-bound form

To probe the molecular determinants and structural basis for the increased rates of nucleotide exchange observed in the mutant $G\alpha_{i1}$ proteins, we determined the crystal structures of $G\alpha_{i1}$-T329A in both the GDP- and the GTPγS-bound forms (Table 1). The intended mutation of Thr to Ala in the protein was confirmed by the crystal structure, where electron density at position 329 corresponded to Ala (Fig. S2A). The structure of the GDP-bound form of $G\alpha_{i1}$-T329A was refined to 2.5-Å resolution using the structure of $G\alpha_{i1}$·GDP·Mg^{2+} [Protein Data Bank (PDB) code 1BOF] as a template for molecular replacement. In the final model, the region corresponding to amino acids M1–L5, Q204–C217 and V233–E239 is missing due to lack of electron density for these residues. Similarly, the structure of the GTPγS·Mg^{2+}-bound form of $G\alpha_{i1}$-T329A was refined to a resolution of 2.3 Å, using the structure of $G\alpha_{i1}$-G42V·GTPγS·Mg^{2+} (PDB code 1AS0) as a template. In the final model, the region corresponding to amino acids M1–R32 and K349–F354 is missing due to lack of electron density for these residues. The GDP- and GTPγS-bound structures for T329A-$G\alpha_{i1}$ were solved in space groups identical to those of the WT $G\alpha_{i1}$ structures. We systematically compared and contrasted the structures of the WT and mutant $G\alpha_{i1}$ proteins.

Although the switch II (residues 199–219) and switch III (residues 231–242) regions of $G\alpha_{i1}$-T329A·GDP are essentially disordered as in the WT $G\alpha_{i1}$·GDP, both of these switch regions are nicely ordered and resolved in the active GTPγS-bound states of both proteins.[15] Interestingly, a well-defined electron density for switch I (residues 177–187) shows that it has moved away from the nucleotide in $G\alpha_{i1}$-T329A·GDP compared with switch I in WT $G\alpha_{i1}$ (Fig. 3). Overall the root-mean-square deviation (r.m.s.d.) between WT $G\alpha_{i1}$·GDP and $G\alpha_{i1}$-T329A·GDP was 0.79 Å, whereas it was only 0.29 Å for their GTPγS-bound structures. Hence, overall the GTPγS-bound-state structures WT $G\alpha_{i1}$ and $G\alpha_{i1}$-T329A are essentially identical

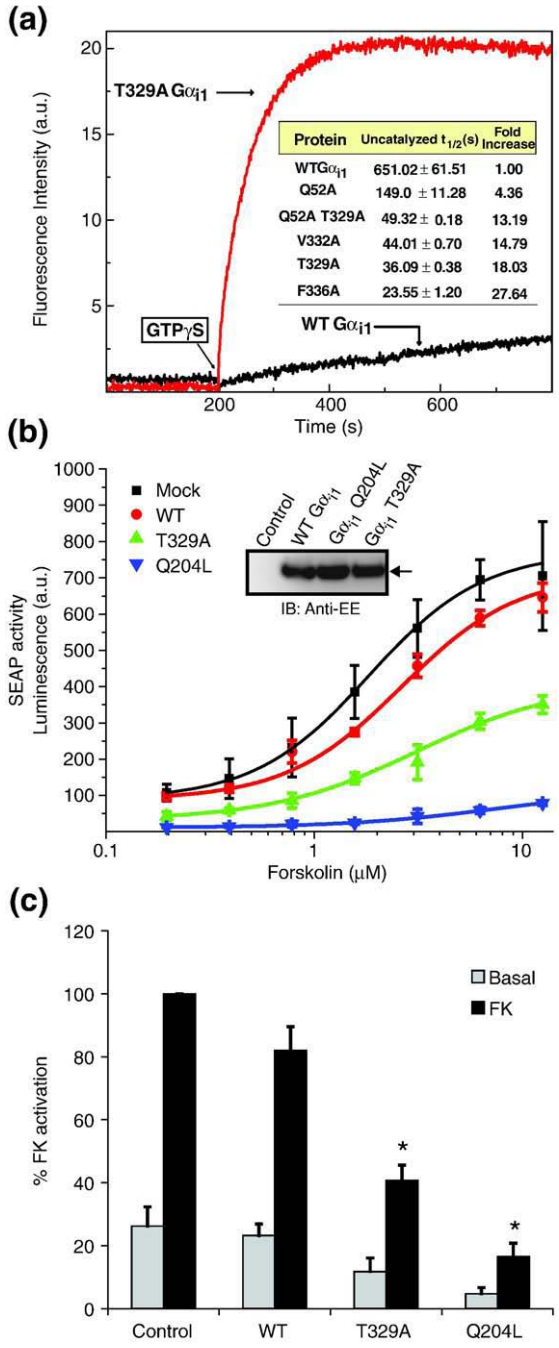

Fig. 2. Fluorescence assay of nucleotide uptake rates and forskolin (FK)-induced SEAP assay. (a) Nucleotide exchange was monitored by measuring the enhancement in intrinsic Trp fluorescence as a function of time after addition of GTPγS. Traces show the activation of the WT $G\alpha_{i1}$ (black) and T329A mutant (red) and rates of exchange for all proteins studied are given in the table (inset). Uncatalyzed $t_{1/2}$ values are presented as the mean±SEM of at least three independent experiments. As observed, substitutions of residues on the α5 helix (T329, V332, F336) or residues in close proximity to the α5 helix (Q52) increase the basal rate of exchange, indicating a possible involvement of the α5 helix during the receptor-catalyzed nucleotide-exchange process. (b) $G\alpha_{i1}$ mutants, T329A and Q204L, show increased inhibition of FK-induced cAMP-dependent SEAP activity. Mock (black), WT (red), T329A (green), Q204L (blue) and pCRE-SEAP cotransfected cells were incubated for 6 h in the presence of FK ranging from 0 to 12.5 μM prior to SEAP activity measurement. Inset: expression levels were similar based on immunoblot analysis. (c) Increased inhibition of basal as well as FK-stimulated SEAP activity is observed in cells transfected with Q204L and T329A $G\alpha_{i1}$ mutants. SEAP activity is expressed as a percentage of the activity obtained with 12.5 μM FK stimulation in mock-transfected cells. Data are mean + SEM from three independent experiments done in triplicate.

Table 1. Crystallographic data and refinement statistics

	T329A $G\alpha_{i1}$ (GDP)	T329A $G\alpha_{i1}$ (GTPγS)
Data processing[a]		
Space group	*I*4	$P3_221$
Unit cell dimensions		
a, *b*, *c* (Å)	121.76, 121.76, 68.71	79.29, 79.29, 105.6
α, β, γ (degrees)	90, 90, 90	90, 90, 120
Crystal dimensions (mm)	0.2×0.5×0.7	0.1×0.2×0.3
Total no. of reflections	118,368	92,656
Unique reflections	16,157	17,460
No. of molecules per asymmetric unit	1	1
R_{merge} on *I*[b]	6.0 (27.5)	8.3 (22.6)
Mean $I/\sigma I$[c]	8.4 (2.6)	6.7 (3.3)
Completeness (%)	100 (100)	100(100)
Multiplicity	7.3 (7.5)	5.3 (5.5)
Model for MR (PDB)	1BOF	1AS0
Refinement statistics		
Resolution (Å)	59.8–2.5	68.4–2.3
Reflections in file	16,157	17,447
Reflections used	15,346	16,564
R_{work} (%)[d]	18.1	18.5
R_{free} (5% of data)	22.6	25.2
No. of atoms		
Protein	2690	2627
Ions		
Mg^{2+}	0	1
SO_4^{2-}	1	1
Ligand (GDP/GTPγS)	1	1
Water	46	49
B-factor		
Average	40.0	30.0
Ligand	27.0	12.0
r.m.s.d.'s		
Bond lengths (Å)	0.02	0.02
Bond angles (°)	1.79	1.82
Chiral angles (°)	0.11	0.11

[a] Numbers in parentheses indicate statistics for the highest-resolution shell.
[b] $R_{merge} = \sum_{hkl}\sum_i |I(hkl)i - \langle I(hkl)\rangle| / \sum hkl \sum i \langle I(hkl)i\rangle$.
[c] $I/\sum I$, signal-to-noise ratio, where I is the integrated intensity of a measured reflection and σI is the estimated error in measurement.
[d] $\sum |F_P - F_{P(calc)}| / \sum F_P$, where F_P and $F_{P(calc)}$ are the observed and calculated structure factor amplitudes. R_{free} is calculated similarly using test set reflections never used during refinement.

(Fig. S3), whereas significant differences are observed in the GDP-bound-state structures (Fig. S4).

Changes in conformation of switch I region

Superimposition of the $G\alpha_{i1}$·GDP·Mg^{2+}, $G\alpha_{i1}$·GTPγS·Mg^{2+}, $G\alpha_{i1}$-T329A·GDP and $G\alpha_{i1}$-T329A·GTPγS·Mg^{2+} structures shows striking differences in the conformations of the switch I region (Fig. 3a). The T329A replacement on the α5 helix allosterically induces an extensive outward movement of the switch I region away from the nucleotide in the GDP-bound state of the mutant $G\alpha_{i1}$-T329A compared with the GDP-bound state of WT $G\alpha_{i1}$. This conformational change leads to an overall increase in the catalytic pocket size, thereby destabilizing the bound nucleotide to facilitate faster GDP release. Interestingly, the switch I regions in the activated forms of the mutant $G\alpha_{i1}$-T329A·GTPγS·Mg^{2+} and WT $G\alpha_{i1}$·GTPγS·Mg^{2+} exhibit identical conformational states. Switch I is tightly positioned in close proximity to the nucleotide, probably due to the bound Mg^{2+} divalent cation in the catalytic pocket. Hence, the T329A substitution affects the conformational state of the switch I region only in the GDP-bound form. An electrostatic potential surface rendering of $G\alpha_{i1}$-T329A·GDP and WT $G\alpha_{i1}$·GDP·Mg^{2+} structures also highlights extensive outward movement of the switch I region, allowing access for a possible exit route of the bound GDP (Fig. 3b).

Changes in GDP interactome within the catalytic pocket

The T329A substitution also induced structural changes in several key amino acid side chains in the catalytic pocket (Fig. 3c and d). Foremost is an inversion (~180°) of the guanidinium side chain of R178, thereby preventing H-bonding interactions with the oxygen of the α- and β-phosphate on GDP demonstrated in the WT $G\alpha_{i1}$·GDP·Mg^{2+} crystal structure. This conformational flip of R178 causes a loss of stabilization of the bound GDP. The dramatic movement of switch I in the $G\alpha_{i1}$-T329A mutant also orients the side chain of K180 away from the catalytic pocket (Fig. 4a). The other residues participating in electrostatic interactions with the guanine ring of GDP (N269, D272, K270 and A326) have similar orientations in the $G\alpha_{i1}$-T329A mutant and the WT $G\alpha_{i1}$, although shorter H-bonding distances in the mutant promote stronger interactions with the bound GDP. Also, unlike the case in WT $G\alpha_{i1}$, the side chains of R178 and L273 in the $G\alpha_{i1}$-T329A mutant seem to be involved in hydrophobic interactions with the guanine ring along with K270 and T327. In WT $G\alpha_{i1}$, the GDP ribose engages its 2′- and 3′-hydroxyl groups in an H-bond network with the backbone carbonyl groups of L175 and R176. These stabilizing interactions are substituted by the single side-chain hydroxyl group of S151 in the $G\alpha_{i1}$-T329A mutant, resulting in weaker H-bonding potential (Fig. 3c and d). Thus, despite apparent gains in hydrophobic interactions, the loss of favorable electrostatic and H-bonding interactions in $G\alpha_{i1}$-T329A destabilizes the bound GDP, resulting in a faster rate of release from the catalytic pocket.

Loss of Mg^{2+} from the catalytic pocket in the $G\alpha_{i1}$-T329A·GDP structure

Mg^{2+} was absent from the catalytic pocket in the crystal structure of $G\alpha_{i1}$-T329A·GDP (Fig. S2b and c). Two key residues of the Mg^{2+} coordination sphere in WT $G\alpha_{i1}$·GDP·Mg^{2+}, T181 (on the switch I region) and S47 (on the α1 helix), display considerable structural alterations upon substitution of T329 (Fig. 4a). T181 moves away from the Mg^{2+}-binding site due to the extensive outward movement of the switch I region. The S47 side chain also orients away from the Mg^{2+}-binding site, disrupting the favorable interaction present in WT $G\alpha_{i1}$. The displacement of nucleotide in the catalytic pocket also compromises the favorable interactions between the β-phosphate

and bound Mg^{2+} (Fig. 4a). The integration of these changes essentially dismantles the Mg^{2+} coordination sphere in the $G\alpha_{i1}$-T329A mutant, and the loss of bound Mg^{2+} further decreases the stability of the bound GDP. In the WT $G\alpha_{i1}$·GDP·Mg^{2+}structure (PDB code 1BOF), several water molecules populate the catalytic pocket, with water molecules W801, W802 and W803 forming part of the octahedral coordination sphere of Mg^{2+}. These water molecules are completely absent from the catalytic pocket of the $G\alpha_{i1}$-T329A·GDP structure (Fig. 4b), further corroborating the loss of Mg^{2+} from the catalytic pocket. Other proximal residues, including the highly conserved D200, which is part of the conserved DXXG sequence motif found in all the regulatory G proteins of the Ras superfamily, adopt similar side-chain conformations in the $G\alpha_{i1}$-T329A mutant and WT proteins.

1n 1998, Coleman and Sprang solved structures of WT $G\alpha_{i1}$ in the presence of different concentrations of Mg^{2+}.[40] They showed that the Mg^{2+}-binding site in the catalytic pocket of WT $G\alpha_{i1}$ has 70% occupancy at 10 mM Mg^{2+} concentration and 100% occupancy at 100 mM Mg^{2+} or above in the crystallization buffer.[40] To address the issue of Mg^{2+} binding, we solved the structure of the GDP-bound form of the $G\alpha_{i1}$-T329A mutant with 10 mM Mg^{2+} in the crystallization buffer. The structure still revealed a complete absence of Mg^{2+} from the catalytic pocket, which was consistent with our primary crystallographic data set at 2 mM Mg^{2+}. We also saw similar secondary-structural and side-chain orientations in the crystals grown at 10 mM $MgCl_2$, as in the structure from the crystal with 2 mM Mg^{2+} (data not shown). This confirms the observation that the T329A mutation indeed disrupts the Mg^{2+}

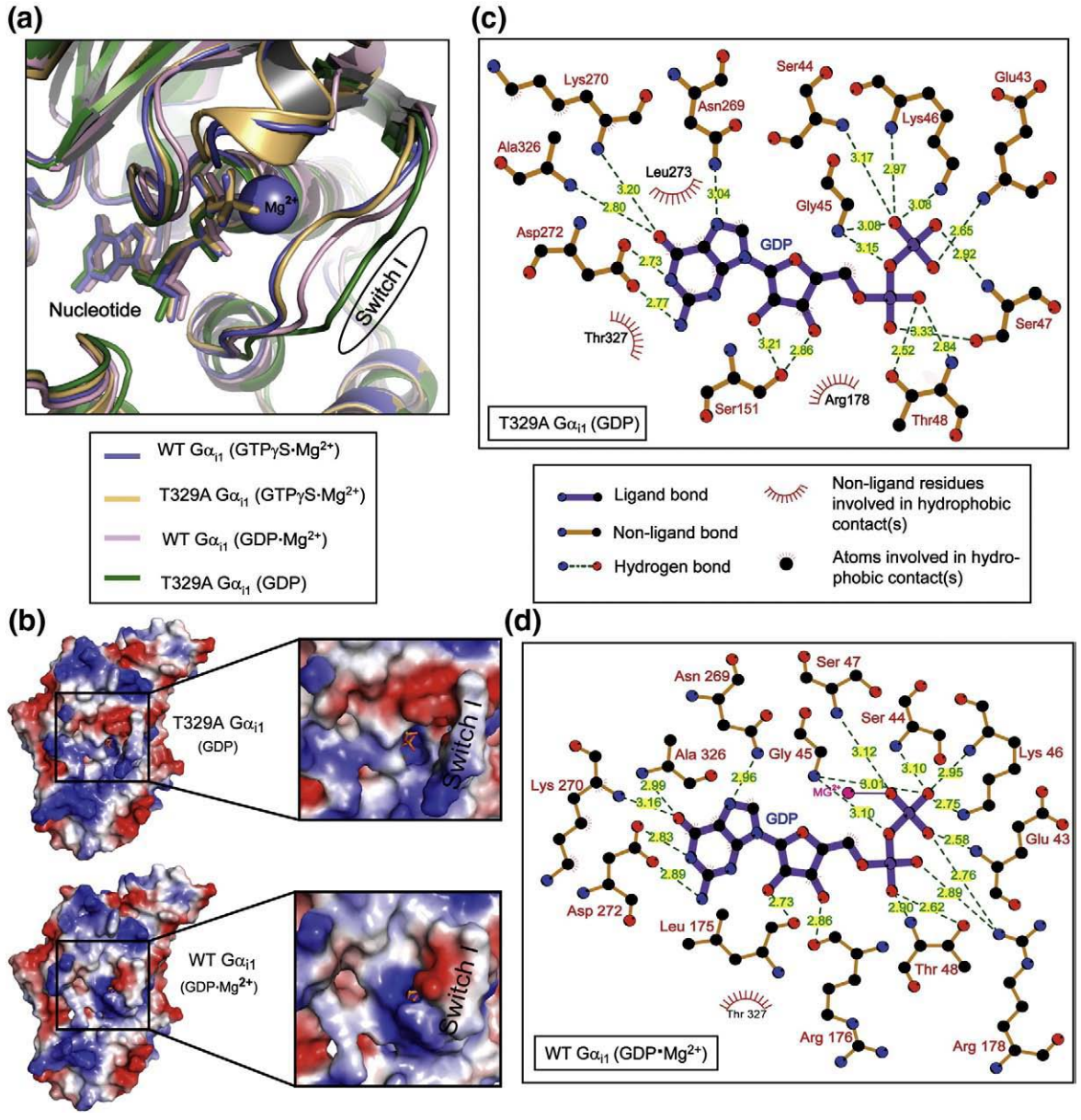

Fig. 3 *(legend on next page)*

coordination sphere in the catalytic pocket. The absence of Mg^{2+}, in conjunction with other destabilizing structural changes, facilitates the release of bound GDP from the catalytic pocket, explaining the increase in release rates of GDP from the mutant $G\alpha_{i1}$ proteins.

To investigate the influence of Mg^{2+} on the kinetics of the nucleotide-exchange process, we performed the GTPγS-binding assay on the WT and mutant $G\alpha_{i1}$ proteins as a function of Mg^{2+} concentration. Interestingly, the results showed that the rates of exchange depended significantly on the concentration of Mg^{2+} present in the reaction buffer. In general, increasing Mg^{2+} concentration decreased the rate of GDP release (Fig. 4c). The greatest decrease in the rate of exchange as a function of increasing concentrations of Mg^{2+} was observed for the WT $G\alpha_{i1}$. The effect of increasing Mg^{2+} concentration can be rationalized by our earlier structural observations. The high concentration of Mg^{2+} might induce order in the structure and stabilize the GDP-bound state. This would make the rate of nucleotide exchange slower at higher concentrations of Mg^{2+}. The induction of similar structural changes due to increasing Mg^{2+} concentration was also shown earlier by Coleman and Sprang.[40] Interestingly, the rate of nucleotide exchange for the slower-exchange mutants (Q52A, V332A, Q52A/T329A) was also influenced by the concentration of Mg^{2+} present in the reaction mixture. This may be due to a partially intact Mg^{2+} coordination sphere where binding of Mg^{2+}, albeit with lower affinity, might stabilize the bound nucleotide. The rates of nucleotide exchange for the rapid-exchange mutants $G\alpha_{i1}$-T329A and $G\alpha_{i1}$-F336A are, by and large, unaffected by increasing Mg^{2+} concentrations. This substantiates the structural findings related to the disruption of the Mg^{2+} coordination sphere in the $G\alpha_{i1}$-T329A·GDP structure as noted above. We thus propose that the accelerated rate of the activation process in the mutants is coherently coupled in part to the loss of Mg^{2+} from the catalytic pocket. In receptor-induced nucleotide exchange, the receptor might possibly be inducing similar structural rearrangements to facilitate a faster nucleotide exchange.

As stated earlier, the superimposition of the static secondary-structural elements in the crystal structure of the $G\alpha_{i1}$-T329A·GTPγS·Mg^{2+} and WT $G\alpha_{i1}$·GTPγS·Mg^{2+} complexes revealed an r.m.s.d. of only 0.29 Å. There were no observable significant secondary-structural differences between these two structures (Fig. S3). This highlights the fact that the activated state is well ordered and almost identical for WT $G\alpha_{i1}$ and the $G\alpha_{i1}$-T329A mutant. The mutation affects only the less ordered GDP-bound form of the protein, inducing an increased rate of nucleotide exchange. The presence of an intact Mg^{2+} coordination sphere in the activated form leads to tight ordering of the switch I region, which is conformationally more dynamic in the GDP-bound form. The residues that constitute the GTPγS-binding domain have identical orientation with minimal conformational differences. The nucleotide positioning in the catalytic pocket is more definitive and static, with complete overlap between the respective nucleotides in the mutant and WT $G\alpha_{i1}$ structures (Fig. 4d).

Thermodynamics and kinetics of the activation process

The mutations of the α5 helix residues cause disruption of certain key electrostatic interactions within the Gα subunit. The influence of the mutation on the rate of activation suggests that the mutation

Fig. 3. Switch I movement and changes in GDP interactome within the catalytic pocket. (a) The T329A mutation on the α5 helix allosterically induces an extensive outward movement of the switch I region of $G\alpha_{i1}$-T329A·GDP (green) in comparison to the switch I regions of WT $G\alpha_{i1}$·GDP·Mg^{2+} (salmon) (PDB code 1BOF), $G\alpha_{i1}$-T329A·GTPγS·Mg^{2+} (orange) or WT $G\alpha_{i1}$·GTPγS·Mg^{2+} (blue) (PDB code 1ASO). This movement of a key structural determinant in $G\alpha_{i1}$-T329A·GDP leads to changes in the orientation of side chains of the residues lying along the switch I region in the $G\alpha_{i1}$-T329A·GDP in comparison to other forms of $G\alpha_{i1}$. (b) A zoom into switch I consisting of electrostatic potential surface of $G\alpha_{i1}$-T329A·GDP and WT $G\alpha_{i1}$·GDP·Mg^{2+} shows extensive movement of the switch I corresponding region on the proteins. The outward movement of switch I in the mutant exposes an exit route readily available for the bound nucleotide, which could facilitate faster rates of nucleotide exchange. However, in WT $G\alpha_{i1}$, switch I is rigidly positioned to act as a lid on the exit channel, thereby limiting the kinetics of the nucleotide-exchange process. The residues interacting with the guanine ring (N269, D272, K270 and A326) are the same in both (c) the mutant and (d) the WT $G\alpha_{i1}$, although the H-bond stabilizing interactions are slightly stronger (due to closer proximity of interacting ends) in the mutant. In the T329A mutant, additional residues, namely, R178, L273, T327 and K270, are involved in hydrophobic interactions with the guanine ring through their side chains than in WT $G\alpha_{i1}$. In WT $G\alpha_{i1}$, the ribose ring of GDP engages the 2′- and 3′-hydroxyl groups in a H-bonding network with the backbone carbonyls of L175 and R176, whereas this bicentric stabilizing interaction is replaced by a single side-chain hydroxyl group of S151 in T329A, contributing to the decreased stability of the nucleotide in the pocket. The α- and β-phosphates interact with multiple amino acid side chains and backbones. A crucial H-bonding interaction between the oxygen atoms of the α- and β-phosphates on GDP and the protonated side chain of R178 is lost in the mutant, contributing further to the decrease in the stability of the bound nucleotide. The flipping of the R178 side chain outside the pocket also contributes to a larger pocket size in comparison to WT $G\alpha_{i1}$, where this interaction is tightly regulated. These effects of the mutation at a distance are tremendous, and overall cause the loss of Mg^{2+} from the binding pocket. The lack of Mg^{2+} in turn disrupts multiple electrostatic interactions with amino acid residues, such as S47 and T181, along with the oxygen atoms present on the β-phosphate of GDP. The T329A mutation overall lowers the activation barrier of nucleotide exchange by allosterically modulating the orientation and general conformation of the residues constituting the GDP interactome.

might be affecting the activation energy for the nucleotide-exchange process. In order to analyze quantitatively the effect of mutation on the activation energy, we performed GTPγS-binding assays over a linear temperature gradient. The fluorescence enhancement of W211 due to activation was monitored and rates were calculated. Experiments were performed for the WT $G\alpha_{i1}$ and $G\alpha_{i1}$-T329A mutant and k_{app} values were calculated for each data set at different temperatures. A plot of ln k *versus* $1/T$ was fit to the Arrhenius equation to give activation energies for both WT and mutant. The analysis revealed that the barrier for activation of the mutant is lower by 5.1 kcal/mol than that of the WT

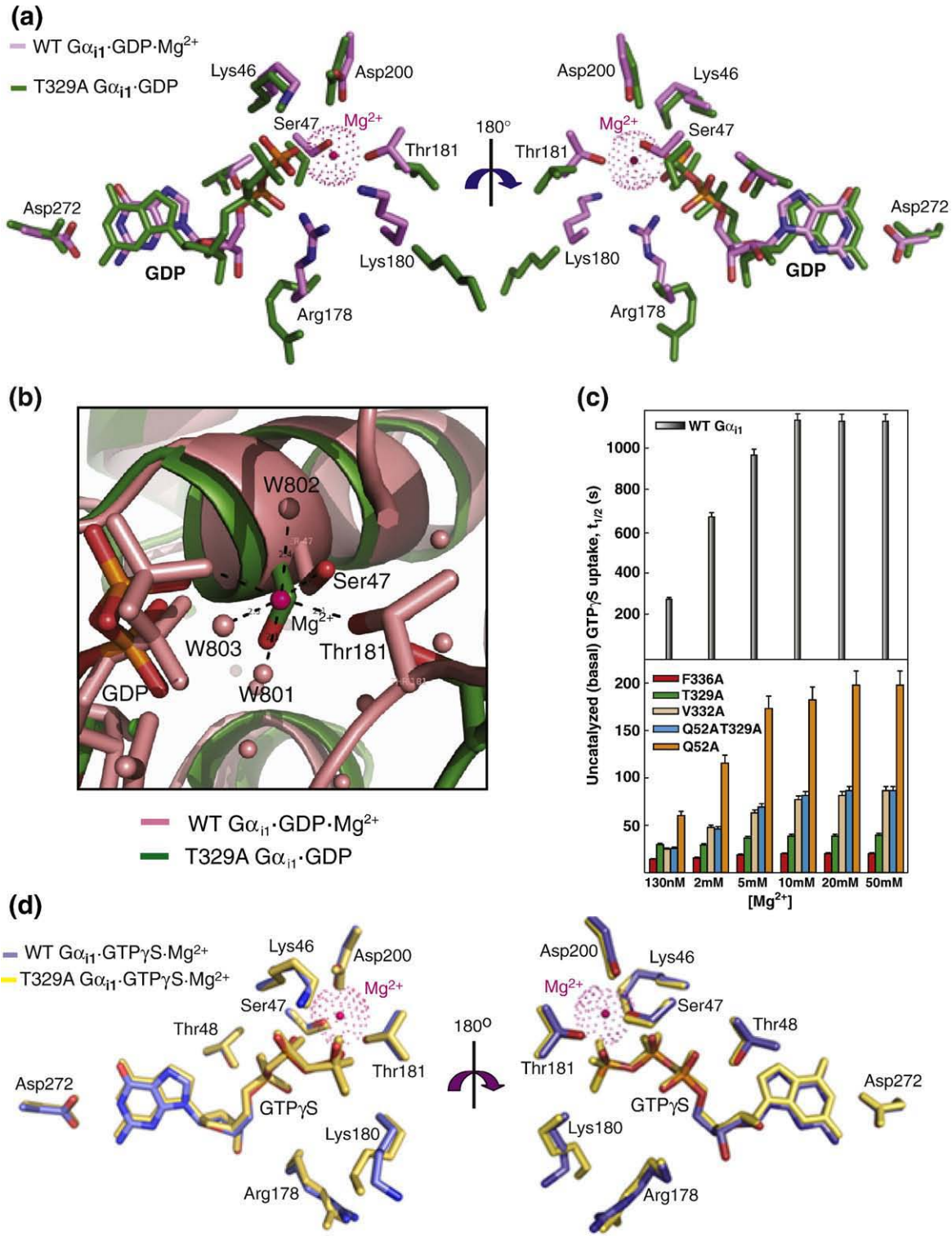

Fig. 4 *(legend on next page)*

(Fig. S5a). This implies that the T329A mutation causes allosteric modulation of residues defining the catalytic pocket, which leads to destabilization of interactions involved in GDP binding. The net effect is a lowering of the activation threshold, thereby resulting in faster rates of nucleotide exchange.

We performed isothermal titration calorimetry (ITC) to analyze the effect of amino acid replacement on the apparent binding affinity of the nucleotide ligand and its influence on the nucleotide-exchange process. ITC experiments, in principle, give the net change in the enthalpy for this exchange reaction (Fig. S5b). The binding of GTPγS to the $G\alpha_{i1}$-T329A mutant was more exothermic than GTPγS binding to WT $G\alpha_{i1}$ (data not shown). The crystal structures of $G\alpha_{i1}$-T329A·GTPγS·Mg^{2+} and WT $G\alpha_{i1}$·GTPγS·Mg^{2+} are almost identical, with an r.m.s.d. of 0.29 Å. Thus, the final GTPγS-bound states of the two complexes can be assumed to have the same energy level on a reaction profile diagram. However, the crystal structure of the GDP-bound form of the $G\alpha_{i1}$-T329A mutant displays significant conformational changes that destabilize its GDP-bound state. Hence, transition from the energetically higher GDP-bound state should give larger reaction enthalpy. Our ITC data are in excellent agreement with this rationale. The high activation barrier for the WT protein makes the process of spontaneous basal nucleotide exchange slow and unfavorable, although we observe strong binding constants for α5 helix mutants $G\alpha_{i1}$-T329A, $G\alpha_{i1}$-Q52A/T329A and $G\alpha_{i1}$-V332A (Fig. S4b). The loss of favorable interactions caused by each α5 helix amino acid replacement promotes faster release of the bound GDP, which creates a nucleotide-free pocket readily available for GTPγS binding. This observation is in excellent agreement with the kinetic analysis of the exchange process for different mutants as shown earlier. Hence, the ITC experiments along with the Arrhenius analysis show that thermodynamic gain also contributes to faster rates of nucleotide exchange for the mutants in comparison to the WT protein.

Discussion

Over the years, several hypothetical models have been proposed to explain receptor-induced G protein activation. One model elucidates the role of the Gβγ subunit as a "lever" to reorient a cognate exit route in Gα during receptor-promoted GDP–GTP exchange. The β3–α2 loop or the "lip" of this contact surface (between Gα and Gβγ subunits) and switch I occlude the exit route for GDP. The receptor-mediated exchange promotes alterations in this region to facilitate the activation of G proteins.[8,41] Alternatively, a "gear-shift" model has also been proposed where R* binds to Gα and induces a hinge motion at the Gα N-terminal tail. This leads to tight packing of the Gα–Gβ subunits, and the N-terminal tail of the Gγ subunit is engaged to displace the Gα helical domain. The opening of the cleft between the GTPase domain and the helical domain allows for GDP release.[42]

Mutations of the α5 helix residues of G_t facing into the protein cause a multifold increase in the basal rate of nucleotide exchange.[26,27] This suggests that the α5 helix comprises a functional microdomain in G proteins that affects basal nucleotide release rates and mediates receptor-catalyzed nucleotide exchange at a distance from the nucleotide-binding pocket. Interestingly binding to Gβγ or the receptor is largely unaffected by these mutations. In 2006,

Fig. 4. Changes in catalytic pocket residues in $G\alpha_{i1}$-T329A and WT $G\alpha_{i1}$ and loss of Mg^{2+}. (a) A superposition of the side chains of residues in close proximity with GDP and those forming the coordination spheres of Mg^{2+} in the WT $G\alpha_{i1}$·GDP·Mg^{2+} and $G\alpha_{i1}$-T329A·GDP structures reveals some key differences. The protonated side chain of R178 involved in forming H-bonding interactions with the oxygen of the α- and β-phosphate on GDP in the WT $G\alpha_{i1}$·GDP·Mg^{2+} rotates by almost 180° in T329A, thus nullifying this stabilizing interaction. Extensive movement of switch I leads to flipping of the K180 side chain away from the catalytic pocket into a more solvent-exposed environment. A key residue of the Mg^{2+} coordination sphere, T181, orients away from the Mg^{2+} binding site as well. The side chain of S47, a direct Mg^{2+}-binding ligand, undergoes a conformational switch orienting it away from the Mg^{2+} binding site. All other proximal residues adopt a side-chain conformation in the mutant similar to that observed in the WT protein. Concomitantly, the T329A substitution also leads to the displacement of the nucleotide in the catalytic pocket, indicative of the disruptions in the cooperative H-bond network within the catalytic pocket in the mutant. (b) A superposition of the WT $G\alpha_{i1}$·GDP·Mg^{2+} (green) structure with the $G\alpha_{i1}$-T329A·GDP structure (salmon) shows distinct organization of the water molecules within the catalytic pocket. The mutant structure shows absence of Mg^{2+} coordinating water molecules, namely, W801, W802 and W803, further substantiating the observation of loss of Mg^{2+} from the catalytic pocket. (c) Coleman and Sprang showed that with increasing concentrations of Mg^{2+}, WT $G\alpha_{i1}$ undergoes conformational changes inducing order in the structure reminiscent of the activated WT $G\alpha_{i1}$·GTPγS·Mg^{2+} state.[40] The rate of nucleotide exchange for the WT $G\alpha_{i1}$ protein and the slow-exchange mutants (Q52A, V332A and Q52A T329A) is very much dependent on the concentration of Mg^{2+} present in the reaction buffer, possibly due to the influence of a completely or partially intact Mg^{2+} coordination sphere stabilizing the bound nucleotide. The rates of exchange for the rapid-exchange mutants, T329A and F336A, remain by and large unaffected by increasing Mg^{2+} concentrations, substantiating the structural determinants, consistent with the disruption of the Mg^{2+} coordination sphere in the $G\alpha_{i1}$-T329A·GDP structure as shown above. (d) Unlike the GDP-bound state, the residues aligned along the catalytic pocket involved in both electrostatic and hydrophobic interactions with the bound nucleotide in the GTPγS-bound state are much more static. The side-chain orientations are similar or identical, with no displacement of the bound nucleotide in either the $G\alpha_{i1}$-T329A·GTPγS·Mg^{2+} or WT $G\alpha_{i1}$·GTPγS·Mg^{2+}. These results show that even if the rates of nucleotide exchange are different, post-exchange a higher degree of order is restored in the structure, which is independent of amino acid substitution on the α5 helix.

Hubbell and coworkers conducted a site-directed spin-label EPR study of α5 helix residues and suggested that R∗-stimulated activation causes a rigid-body movement of the α5 helix, which perturbed the β6–α5 loop and thereby decreased GDP stability in the catalytic pocket.[28] In addition, allosteric changes at the Gα–Gβγ interface triggered by interactions with R∗ were observed, along with significant changes even in the dynamics of residues (A300 on the α4 helix) distant to the receptor or the Gα–Gβγ interface.[29,30] An alternative hypothesis suggested that the receptor first engages Gβγ and then triggers the GDP release by interacting with the CT of Gα in a "sequential" manner.[43,44] All of these studies suggest a potential important role for the α5 helix of Gα in the activation pathway. The receptor would engage the CT of Gα (connecting to the α5 helix) to induce conformational changes facilitating the release of bound GDP from the catalytic pocket.

In the absence of R∗, the CT is unstructured and becomes mainly helical upon binding to the activated receptor.[45,46] This binding also induces conformational rearrangement within the receptor.[33] However, intriguingly, the CT interacts with the receptor primarily through its backbone atoms, which suggests that the CT alone cannot provide specificity and selectivity to the binding event coupled to G protein activation. In contrast to this observation, Conklin *et al.* earlier demonstrated through a series of experiments that only a minimum of three amino acid substitutions in the C-terminal region switches the receptor specificity of $G\alpha_q$ to that of $G\alpha_i$, highlighting the contribution of CT.[47] However, in $G\alpha_{i2}$ and G_t, the last eight residues are identical, but the α_2-adrenergic receptor only activated $G\alpha_{i2}$ selectively.[48] All these observations suggest that the CT alone cannot be the sole determinant of R∗–G protein specificity, and other regions of the α-subunit along with contributions from the Gβγ subunit[49] must provide elements that contribute to the overall selectivity of this interaction.

The α5 helix of Gα is directly proximal to the CT and is highly structured, pointing directly from the N-terminal portion of CT into the nucleotide-binding pocket. Therefore, we hypothesized earlier that α5 might be a key structural element in transmitting the signal of Gα binding to R∗ to the nucleotide-binding pocket. This hypothesis was supported by the results of mutagenesis experiments showing that amino acid substitutions in the α5 helix resulted in dramatically enhanced rates of nucleotide exchange even in the absence of receptor. Mutagenesis of G_t[26,27] and follow-up computational molecular dynamics studies[50] suggested that a receptor-induced movement of the α5 helix of the Gα subunit might affect the local structure of the GDP-binding pocket via the α1 helix and β2 and β3 strands. Although biophysical studies of the A326S $G\alpha_{i1}$ mutant suggested that it might be a mimic of the receptor-bound activated state, a follow-up crystal structure of $G\alpha_{i1}$-A326S·GDP showed that its GDP-binding pocket was no different from that of WT $G\alpha_{i1}$.[23]

Structural studies on the $G\alpha_{i1}$-T329A mutant presented here show extensive movement of the switch I region and disruption of the Mg^{2+} coordination sphere within the catalytic pocket. There are also drastic changes in the conformations of side chains of residues lining the catalytic pocket, also resulting in decreased stability of the bound GDP nucleotide. Interestingly, the residue R178 even in the structure of the heterotrimer (PDB code 1GG2) adopts a conformation where it is oriented away from the catalytic pocket, as shown in Fig. S6. As shown by Abdulaev *et al.*, Gα adopts a "preactivated" conformation when associated with Gβγ.[51] An altered conformation of R178 might contribute to acquiring this state. These changes concomitantly cause the destabilization and displacement of the bound nucleotide.

Also, the results from the cell-based *in vitro* SEAP assay (Fig. 2b and c) show that ligand-stimulated inhibition is much stronger for the mutants in comparison to the WT protein. This must be possible only because the mutant, similar to WT protein, can interact with the receptor and the Gβγ subunit. As shown in Fig. S7, both WT and $G\alpha_{i1}$-T329A subunits can interact with Gβγ subunit *in vitro*, leading to substantial inhibition of activation. The observation and rationalization of these changes in the $G\alpha_{i1}$-T329A mutant suggest that the T329A replacement has stabilized a structural intermediate along the activation pathway. The structure of the mutant subunit provides a plausible insight into the mechanism of nucleotide exchange and allows us to explain convincingly the allosteric effect of the α5 helix on the basal rate of exchange.

We did not observe any substantial movement of the α5 helix itself or of the nucleotide-interacting β6–α5 loop within the structures, probably because the structure of the $G\alpha_{i1}$-T329A mutant represents an intermediate along the activation pathway and not a true transition state in the exchange process. We presume that a transient movement of α5 along with other contributing conformational changes must occur earlier in the process, which could not be trapped in the crystal structure of the T329A-$G\alpha_{i1}$ mutant. In support of this explanation, a recent molecular dynamics simulation reported by Scheerer *et al.* shows that the α5 helix might act as a transmission rod that undergoes both translation and rotation upon engagement of G protein by the activated receptor.[52]

Recently, Johnston and Siderovski solved the crystal structure of the WT $G\alpha_{i1}$·GDP subunit bound to two peptides corresponding to the N-terminal region of the third intracellular loop of the D2-dopamine receptor and a Gβγ surrogate peptide (KB-752).[22] Each of these peptides can act as a Gα guanine nucleotide exchange factor (GEF). Their work showed that binding of the peptides to the GDP-bound form displaces the β6 strand away from the α4 helix and toward the α5 helix from its position in the unbound protein. The $G\alpha_{i1}$-T329A replacement described here promotes a similar movement of the β6 strand in the GDP-bound

structure (Fig. S8), which further supports the hypothesis that the mutation most likely traps an intermediate along the activation pathway.

Based on our analysis, we propose a sequential release model for G protein activation (Fig. 5). Initially, the activated receptor interacts with the heterotrimer (Gαβγ) and induces a helical conformation into the unstructured CT of the α-subunit. This binding event translates to an activation signal, which we propose is transmitted to the catalytic pocket via the α5 helix. During activation, the switch I region of the α-subunit undergoes extensive

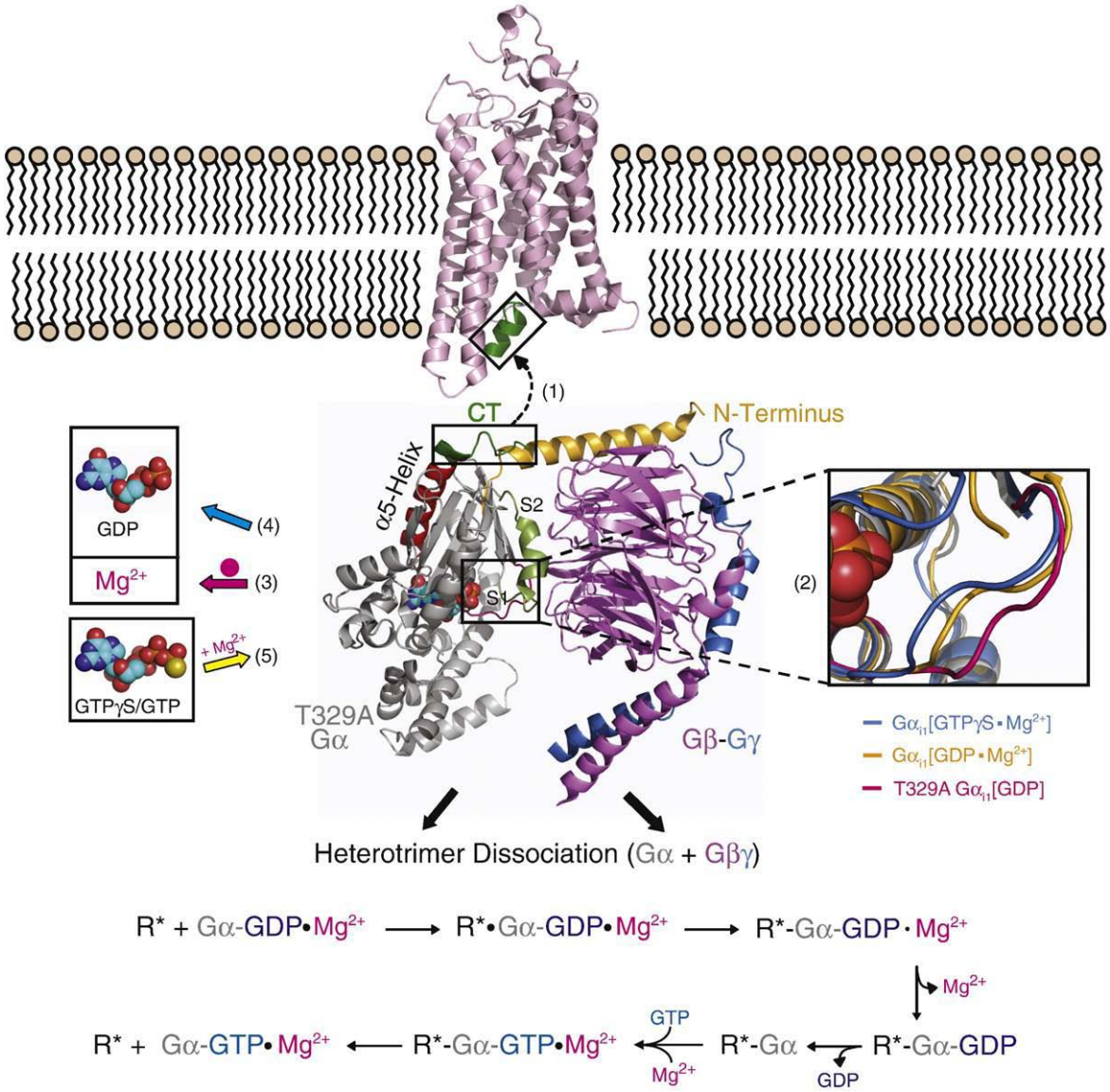

Fig. 5. A proposed sequential release model of G protein activation by GPCRs. The prototypical GPCR opsin (salmon) complexed with the C-terminal (CT) peptide (residues 340–350) from transducin (G_t) (green) (PDB code 3DQB) is depicted as a ribbon diagram in a cartoon. The heterotrimeric G protein subunits Gα (gray), Gβ (light pink) and Gγ (blue) are shown as a complex (PDB code 1GG2) with $Gα_{i1}$·GDP replaced with the mutant $Gα_{i1}$-T329A·GDP structure. The α5 helix of $Gα_{i1}$ is highlighted in red. Since the CT is not resolved in the structure of the heterotrimer, the G protein is docked to the active receptor (R∗) as suggested by Scheerer *et al.*[33] Upon G protein activation, switch I (S1, dark pink) and switch II (S2, light green) of the α subunit undergo conformational changes. The switch I region is highlighted to show the extent of movement. In our proposed model of the G protein activation cycle: (1) The receptor first engages the CT of the α subunit, which brings the α5 helix directly to the surface of R∗. (2) Receptor binding along with docking of the Gβγ subunit facilitates allosteric structural modulation of the α subunit to cause an outward movement of its switch I region. (3) These accumulating conformational changes disrupt the Mg^{2+} binding site in the catalytic pocket leading to its dissociation. (4) The loss of Mg^{2+} and structural rearrangements of key residues (S47, T181, R178) overall destabilizes the bound GDP and facilitates its faster release from the catalytic pocket. (5) The transient intermediate of empty pocket Gαβγ bound to R∗ is formed. GTP and Mg^{2+} rebind to Gα leading to the dissociation of the heterotrimer into the Gα and Gβγ subunits. Finally, the bound GTP is hydrolyzed to GDP + Pi and the inactive Gα·GDP subunit can reassociate with Gβγ to initiate another G protein activation cycle. The structure of the T329A mutant, which shows an increased rate of receptor-independent GDP release, may represent an intermediate that mimics the Mg^{2+} free state of the G protein during the activation cycle.

outward movement away from the catalytic pocket, as seen on comparison of $G\alpha_{i1}$-T329A·GDP and $G\alpha_{i1}$·GDP·Mg^{2+}structures. This spatial rearrangement of switch I coupled to conformational changes in the side chains of key residues (S47, T181, R178) lining the catalytic pocket together disrupt the coordination sphere of Mg^{2+}. The loss of Mg^{2+} along with the accumulating conformational changes destabilizes the bound GDP, which can now be exchanged for GTP at a much more rapid rate to accelerate G protein activation. This activation triggers the dissociation of the heterotrimer into the Gα and Gβγ subunits, rendering them available for interacting with their respective downstream effectors.

As expected, the kinetics of the overall process of nucleotide exchange is modulated by the presence of Mg^{2+}. However, the rapid-exchange mutants ($G\alpha_{i1}$-T329A and $G\alpha_{i1}$-F336A) show an increased rate of activation independent of the concentration of Mg^{2+}. This can be rationalized by the absence of a coordination sphere for Mg^{2+} in the crystal structure of $G\alpha_{i1}$-T329A. However, as seen in WT $G\alpha_{i1}$, GTPγS binding assays with the slow-exchange mutants ($G\alpha_{i1}$-Q52A, $G\alpha_{i1}$-V332A, $G\alpha_{i1}$-Q52A/T329A) show a decrease in the rate of activation with increasing concentration of Mg^{2+}, probably due to a partially intact Mg^{2+} coordination sphere in the catalytic pocket. This model suggests the existence of an "allosteric switch," meaning that a transient ternary complex with a finite lifetime should exist between GDP-bound G protein and R∗ complex, as suggested earlier by Heck and Hofmann using a kinetic analysis.[53] The alternate model would be a so-called hit-and-run model, where R∗ and GDP binding to Gα would be mutually exclusive. Our structural studies suggest, in fact, a transient state between R∗·G[GDP-Mg^{2+}] and R∗·G[empty], namely, R∗·G[GDP-], where Mg^{2+} has exited and GDP remains, causing destabilization of the GDP-binding pocket.

G proteins comprise a superfamily consisting of both the heterotrimeric and small monomeric G proteins.[54,55] Similar to heterotrimeric G proteins, small G proteins also undergo conformational changes in switch regions upon activation. Binding to GTPγS induces order in both switch I and switch II regions.[56,57] Recently, Thomas *et al.* solved the co-crystal structure of a plant small G protein Rop4 (Rho of plants) in complex with the catalytic PRONE domain of RopGEF8.[58] The structure of this never previously observed ternary complex of Rop4, PRONE domain and GDP suggested a general mechanism of small G protein activation. Namely, Rop4 binding to RopGEF8 causes displacement of Mg^{2+} through steric hindrance of its binding site, moves switch I away from the nucleotide and pushes switch II toward the conserved phosphate-binding P-loop. The extended movement of the switch I region further facilitates the sequential exit of Mg^{2+} followed by GDP from the catalytic pocket, leading to accelerated exchange of nucleotide. Our structural studies of a heterotrimeric G protein α-subunit mutant also highlight the disruption of the Mg^{2+} coordination sphere and movement of the switch I region with concomitant destabilization of the bound nucleotide. These independent, yet obviously related, observations hint at a similar shared mechanism of activation for the two subclasses of G proteins, heterotrimeric G proteins and small, single-subunit G proteins.

In summary, our results provide novel structural insights toward understanding the mechanism of nucleotide exchange by heterotrimeric G proteins. The structural studies reported here, supplemented with biophysical data, demonstrate a critical dependence of basal nucleotide exchange rate on Mg^{2+}. As observed in the high-resolution crystal structure of the $G\alpha_{i1}$-T329A mutant, with an amino acid replacement in the α5 helix, movement in the switch I region disrupts the coordination sphere of Mg^{2+} and increases the effective size of the nucleotide-binding pocket. These changes, in association with the conformational changes of other binding pocket residues, result in overall destabilization of the bound GDP, leading to rapid exchange of GDP for GTPγS. The complete conservation of residues T329 and F336 across different classes of G protein α-subunits suggests a critical role of these residues (Fig. S9). Furthermore, our mutational analysis suggests that similar mechanisms of activation might be utilized for the different α-subunits. We believe that the novel mechanistic aspects highlighted here, along with the observations from other relevant studies on related systems, allow a greater understanding of the allosteric mechanism of nucleotide exchange by G proteins.

Materials and Methods

Reagents

GDP sodium salt and GTPγS tetralithium salt were purchased from Sigma-Aldrich (St. Louis, MO). The fluorescent GTPγS analogue, mant-GTPγS was purchased from Jena Biosciences (Jena, Germany). The His_6-tagged mutants of WT $G\alpha_{i1}$ were generated by site-directed mutagenesis using the high-fidelity thermostable DNA polymerase *Pfu* (Stratagene, CA). All crystallographic reagents were purchased from Hampton Research (Aliso Viejo, CA). All reagents and chemicals used were of highest available purity.

Construction, expression and purification of $G\alpha_{i1}$ proteins

The DNA fragment containing the WT rat $G\alpha_{i1}$ subunit (residues 1–354) was amplified by PCR and cloned into the pET28a(+) expression vector (Amersham Biosciences, Piscataway, NJ) with the BamHI and NotI restriction sites. The vector was used to transform BL21 (DE3) cells to express an N-terminal His_6-tag WT $G\alpha_{i1}$ protein containing a PreScission protease site directly after the His_6-tag. The same construct served as a template for introducing site-specific mutations in the protein with the QuickChange system (Stratagene, La Jolla, CA) according to the

manufacturer's protocol. The mutations were confirmed by DNA sequencing (DNA Sequencing Facility, Genelink, NJ). The WT and the mutants were expressed in BL21 (DE3) cells grown in the presence of kanamycin (50 μg/ml). Cells were grown at 37 °C to $A_{600\ nm}$ of ~0.7 and then induced with 400 μM isopropyl-β-D-thiogalactoside (IPTG) (US Biological). The culture was then grown overnight at 17 °C at an agitation speed of 180 rpm. Cells were harvested by centrifugation, and the resulting pellets were resuspended on ice in a buffer containing 50 mM Tris–HCl (pH 8.0), 150 mM NaCl, 2 mM $MgCl_2$, 10 μM GDP, 50 mM β-mercaptoethanol, bovine lung aprotinin (20 mg/ml), 2 mM PMSF and complete EDTA (ethylenediaminetetraacetic acid)-free protease inhibitor cocktail tablets (Roche). The cells were snap-frozen in liquid nitrogen and stored at −80 °C. For purification, the cells were thawed on ice and lysed with a French press (Avestin). The lysate was spun for 90 min at 16,500 rpm. The resulting supernatant fraction was filtered through a 0.45-μm filter (Nalgene) and loaded onto a nickel–nitrilotriacetic acid (Ni–NTA) Superflow resin column (GE Healthcare) that was equilibrated with buffer A [50 mM Tris–HCl (pH 8.0), 150 mM NaCl, 2 mM $MgCl_2$, 10 μM GDP, 50 mM β-mercaptoethanol]. The protein-loaded resin was washed with buffer A and the bound protein was eluted, using a gradient of buffer B (buffer A supplemented with 500 mM imidazole). The eluted protein fractions were pooled, extensively dialyzed against buffer A and cleaved with 1:1000 A_{280} unit of glutathione *S*-transferase PreScission protease for 48 h in order to remove the N-terminal his-tag. The sample was then loaded onto a Ni–NTA column to separate the cleaved protein from the cleaved His-tag and any uncleaved fraction. Next, the protein solution was loaded onto a glutathione Sepharose 4B column (GE Healthcare) to separate the glutathione *S*-transferase fusion PreScission protease protein from the cleaved protein. The resin was equilibrated with buffer A. The resin was first washed in buffer A and the bound PreScission protease was eluted using a gradient of buffer B (buffer A supplemented with 20 mM reduced glutathione). SDS-PAGE was used to test the purity of the chromatography fractions. Thereafter, the appropriate fractions were pooled and concentrated to a volume of less than 5 ml and loaded onto a Superdex 200 26/60 column (GE Healthcare) that was equilibrated in buffer C [50 mM Tris–HCl (pH 8.0), 150 mM NaCl, 2 mM $MgCl_2$, 10 μM GDP, 2 mM DTT]. After elution, the protein-containing fractions were pooled, concentrated to >50 mg/ml, snap-frozen in liquid nitrogen and stored at −80 °C. The average yield for WT $G\alpha_{i1}$ and each mutant was >10 mg/l of culture.

Fluorescence-based kinetic assays

Time-based fluorescence measurements were performed in a SPEX Fluorolog-2 spectrofluorometer (SPEX Industries, Edison, NJ) at 25 °C. WT $G\alpha_{i1}$ was incubated in the reaction buffer [50 mM Tris–HCl (pH 8.0), 150 mM NaCl, 2 mM $MgCl_2$ and 1 mM DTT] for 5 min with constant stirring. GTPγS (178 μM) was added to the reaction mixture with WT $G\alpha_{i1}$ (178 nM) and the relative increase in intrinsic fluorescence (λ_{ex} = 295 nm, λ_{em} = 340 nm) was measured as a function of time. The same procedure was carried out for all $G\alpha_{i1}$ mutants. Mg^{2+}-dependent nucleotide exchange rates were determined by varying the concentration of Mg^{2+} in the reaction buffer. Pseudo-first-order exchange rates were determined by fitting the data to an exponential association curve, $Y = Y_0 + a[1-\exp(-k_{app}t)]$, using Sigma Plot 10.0, where k_{app} is the apparent rate constant and t is the time in seconds. The $t_{1/2}$ values were calculated using $t_{1/2} = (\ln 2)/k_{app}$. The pseudo-first-order kinetic analysis was valid due to the presence of excess GTPγS in the reaction mixture. The data are reported as the average value obtained from three to five experiments. The GTPγS-binding assay was also done with a linear temperature gradient from 5 to 35 °C with the same method. A k_{app} was calculated for each temperature step at intervals of 5 °C by pseudo-first-order kinetic analysis. The activation energy for reaction E_a was calculated using $k_{app} = A \exp[-E_a/(RT)]$ for the Arrhenius analysis, where A is the preexponential factor, E_a is the activation energy of the exchange reaction, R is the universal gas constant (8.314 J mol^{-1} K^{-1}) and T is the temperature in kelvins. For mant-GTPγS binding assays, $G\alpha_{i1}$ protein samples (178 nM) were incubated for 5 min (same buffer as the GTPγS binding assay) at 25 °C, followed by the addition of mant-GTPγS (300 nM). FRET was monitored by exciting the intrinsic Trp fluorescence at 295 nm and measuring the mant-GTPγS fluorescence from 310 to 540 nm. In all cases, blank spectra containing buffer alone were subtracted from the final spectra.

Cell-based assay of $G\alpha_{i1}$-T329A

The EE-tagged WT and constitutively active (GTPase deficient) human Q204L expression constructs were obtained from the Missouri S&T cDNA Resource Center†. The T329A point mutation was generated with site-directed mutagenesis and confirmed by sequencing. HEK293 cells (ATCC) were maintained in Dulbecco's modified Eagle's medium (Invitrogen) with 10% (v/v) fetal calf serum (FCS) at 37 °C and 5% CO_2. For the SEAP assay described below, cells were plated in 10-cm dishes and transiently transfected with pCRE-SEAP (BD Biosciences) and pcDNA3.1(+) control, WT $G\alpha_{i1}$ or mutant-$G\alpha_{i1}$ expression constructs using Lipofectamine Plus (Invitrogen). Briefly, 3.5 μg of total DNA (0.5 μg of pCRE-SEAP + 3 μg of G protein expression vector) was complexed with 10 μl of PLUS reagent and 17 μl of Lipofectamine reagent and incubated for 15 min at room temperature before addition of the DNA–lipid mixture to cells. Cells were plated 24 h after transfection at a density of 20,000 cells per well in poly-D-lysine-coated 384-well plates. Cells were serum-starved in 0.1% FCS overnight and subjected to the SEAP assay, which was performed as described previously with some modifications to employ a 384-well format. About 48 h after transfection, cells were left untreated (basal) or stimulated with FK for 6 h in 0.1% FCS. Briefly, 2 μl of culture medium supernatant fractions were transferred to white 384-well low-volume ProxiPlate (PerkinElmer) containing 5 μl of dilution buffer [150 mM NaCl and 40 mM Tris–HCl (pH 7.2)] and heat inactivated at 65°C for 20 min (to heat inactivate the endogenous alkaline phosphatase). Equal volumes (7 μl) of assay buffer (2 M diethanolamine, 10 mM $MgCl_2$, 20 mM L-homo-Arg, adjusted to pH 9.8), reaction solution containing enhancer solution (Tropics, Bedford, MA) and 0.4 mM SEAP chemiluminescent substrate (Tropics) were added to each well. Luminescence was quantified 15 min after substrate addition with an EnVision Multimode Plate Reader (Perkin Elmer). To allow comparison between different experiments and to assess the effect of different mutant G proteins, data were normalized relative to signal obtained in mock-transfected cells in the presence of 12.5 μM FK, defined as 100%. Dose response experiments

† www.cdna.org

were performed with FK ranging from 0.2 to 25 μM. Assays were performed in triplicate and data were analyzed using Origin 7.0 software.

Crystallization and structural determination

The protein stock solution of $G\alpha_{i1}$-T329A·GDP at 120 mg/ml in storage buffer (50 mM Tris–HCl, 150 mM NaCl, 2 mM $MgCl_2$, 10 μM GDP, 2 mM DTT) was diluted to 10 mg/ml using the dilution buffer [50 mM EPPS (pH 8.0), 1 mM EDTA, 2 mM $MgCl_2$, 5 mM GDP, 5 mM DTT]. Crystals of $G\alpha_{i1}$-T329A bound to GDP were obtained by the hanging-drop vapor-diffusion method in 1.8–2.1 M $(NH_4)_2SO_3$ and 100 mM sodium acetate (pH 5.9–6.3), as described earlier by Sprang and coworkers.[59] Crystals of size 0.2 mm × 0.5 mm × 0.5 mm formed in 5–7 days at 20 °C in the space group $I4$ ($a=b=120.4$ Å, $c=69.8$ Å, $\alpha=\beta=\gamma=90°$) with one $G\alpha_{i1}$-T329A·GDP molecule in the asymmetric unit. Crystals for $G\alpha_{i1}$-T329A·GDP at 10 mM $MgCl_2·6H_2O$ in the dilution buffer were grown under similar conditions and showed the same space group. A similar strategy was used to grow crystals of $G\alpha_{i1}$-T329A·GTPγS·Mg^{2+} by preparing a solution of 10 mg/ml by incubating the protein stock for 60 min with 5 mM GTPγS in storage buffer instead of GDP. The $G\alpha_{i1}$-T329·GTPγS·Mg^{2+} complex crystallized in the space group $P3_221$ ($a=b=78.93$ Å, $c=105.62$ Å) with one $G\alpha_{i1}$-T329A·GTPγS·Mg^{2+} molecule in the asymmetric unit. For data collection at 100 K, crystals were transferred to well solution supplemented with 20% glycerol and 2.5 M $(NH_4)_2SO_3$ for ~30 s followed by immersion in liquid nitrogen. The native data sets were collected at beam line NE-CAT (24ID) of the Advanced Photon Source (APS) at Argonne National Laboratory. The data sets were indexed and processed using HKL2000[60] and Mosflm.[61] The structures of $G\alpha_{i1}$-T329A·GDP and $G\alpha_{i1}$-T329A· GTPγS·Mg^{2+} complexes were determined by molecular replacement using only the C^{α} backbone from 1BOF (WT $G\alpha_{i1}$·GDP·Mg^{2+}) and 1AS0 ($G\alpha_{i1}$-G42V·GTPγS·Mg^{2+}) structures as search models for Phaser in the CCP4 suite‡. Thereafter, CNS was utilized to obtain simulated annealing generated models for both GDP- and GTPγS-bound states of $G\alpha_{i1}$-T329A. Finally, model building was performed in Coot,[62] wherein nucleotide and Mg^{2+} were fitted into the observed densities with refinement conducted by Refmac5 in CCP4 as well as a combination of rigid-body, simulated annealing, energy minimization, and *B*-factor protocols in CNS.[63] The structural superpositions were done using SSM superposition for C^{α} carbon backbone in Coot. All structural images were made with PyMOL§ unless otherwise indicated. The ligand coordination images for GDP and GTPγS were made using Ligplot.[64]

PDB accession numbers

Structure factors and coordinates are deposited in the Research Collaboratory for Structural Bioinformatics protein database with PDB codes 3FFA ($G\alpha_{i1}$-T329A·GTPγS·Mg^{2+}) and 3FFB ($G\alpha_{i1}$-T329A·GDP) for the respective structures.

‡ http://www.ccp4.ac.uk
§ http://www.pymol.org

Acknowledgements

Use of the APS is supported by the U.S. Department of Energy, Office of Science, Office of Basic Energy Sciences, under W-31-109-Eng-38. Use of the Northeastern Collaborative Access Team (NE-CAT) beam line at Sector 24 is based on research conducted at the NE-CAT beam lines of the APS, which is supported by award RR-15301 from the National Center for Research Resources at the National Institutes of Health. Purified $G\beta_1\gamma_2$ subunit was a generous gift of Xin-Yun Huang of Cornell–Weill Medical College. We thank Ethan P. Marin and K. Christopher Min for helpful discussions on crystallographic and structural analysis.

Supplementary Data

Supplementary data associated with this article can be found, in the online version, at doi:10.1016/j.jmb.2009.08.043

References

1. Gilman, A. G. (1987). G proteins: transducers of receptor-generated signals. *Annu. Rev. Biochem.* **56**, 615–649.
2. Birnbaumer, L. (1993). Heterotrimeric G proteins. Molecular diversity and functional correlates. *J. Recept. Res.* **13**, 19–26.
3. Birnbaumer, L. (1992). Receptor-to-effector signaling through G proteins: roles for beta gamma dimers as well as alpha subunits. *Cell*, **71**, 1069–1072.
4. Birnbaumer, L., Abramowitz, J. & Brown, A. M. (1990). Receptor-effector coupling by G proteins. *Biochim. Biophys. Acta*, **1031**, 163–224.
5. Oldham, W. M. & Hamm, H. E. (2006). Structural basis of function in heterotrimeric G proteins. *Q. Rev. Biophys.* **39**, 117–166.
6. Oldham, W. M. & Hamm, H. E. (2008). Heterotrimeric G protein activation by G-protein-coupled receptors. *Nat. Rev. Mol. Cell Biol.* **9**, 60–71.
7. Johnston, C. A. & Siderovski, D. P. (2007). Receptor-mediated activation of heterotrimeric G-proteins: current structural insights. *Mol. Pharmacol.* **72**, 219–230.
8. Bourne, H. R. (1997). How receptors talk to trimeric G proteins. *Curr. Opin. Cell Biol.* **9**, 134–142.
9. Hamm, H. E. (1998). The many faces of G protein signaling. *J. Biol. Chem.* **273**, 669–672.
10. Palczewski, K., Kumasaka, T., Hori, T., Behnke, C. A., Motoshima, H., Fox, B. A. *et al.* (2000). Crystal structure of rhodopsin: a G protein-coupled receptor. *Science*, **289**, 739–745.
11. Cherezov, V., Rosenbaum, D. M., Hanson, M. A., Rasmussen, S. G., Thian, F. S., Kobilka, T. S. *et al.* (2007). High-resolution crystal structure of an engineered human beta2-adrenergic G protein-coupled receptor. *Science*, **318**, 1258–1265.
12. Rasmussen, S. G., Choi, H. J., Rosenbaum, D. M., Kobilka, T. S., Thian, F. S., Edwards, P. C. *et al.* (2007). Crystal structure of the human beta2 adrenergic G-protein-coupled receptor. *Nature*, **450**, 383–387.
13. Noel, J. P., Hamm, H. E. & Sigler, P. B. (1993). The 2.2 Å crystal structure of transducin-alpha complexed with GTP gamma S. *Nature*, **366**, 654–663.

14. Lambright, D. G., Noel, J. P., Hamm, H. E. & Sigler, P. B. (1994). Structural determinants for activation of the alpha-subunit of a heterotrimeric G protein. *Nature*, **369**, 621–628.
15. Mixon, M. B., Lee, E., Coleman, D. E., Berghuis, A. M., Gilman, A. G. & Sprang, S. R. (1995). Tertiary and quaternary structural changes in G_i alpha 1 induced by GTP hydrolysis. *Science*, **270**, 954–960.
16. Sunahara, R. K., Tesmer, J. J., Gilman, A. G. & Sprang, S. R. (1997). Crystal structure of the adenylyl cyclase activator $G_s$alpha. *Science*, **278**, 1943–1947.
17. Kreutz, B., Yau, D. M., Nance, M. R., Tanabe, S., Tesmer, J. J. & Kozasa, T. (2006). A new approach to producing functional G alpha subunits yields the activated and deactivated structures of G alpha (12/13) proteins. *Biochemistry*, **45**, 167–174.
18. Raw, A. S., Coleman, D. E., Gilman, A. G. & Sprang, S. R. (1997). Structural and biochemical characterization of the GTPgammaS-, GDP·Pi-, and GDP-bound forms of a GTPase-deficient Gly42→Val mutant of $G_i$alpha1. *Biochemistry*, **36**, 15660–15669.
19. Wall, M. A., Coleman, D. E., Lee, E., Iniguez-Lluhi, J. A., Posner, B. A., Gilman, A. G. & Sprang, S. R. (1995). The structure of the G protein heterotrimer G_i alpha 1 beta 1 gamma 2. *Cell*, **83**, 1047–1058.
20. Sondek, J., Bohm, A., Lambright, D. G., Hamm, H. E. & Sigler, P. B. (1996). Crystal structure of a G-protein beta gamma dimer at 2.1Å resolution. *Nature*, **379**, 369–374.
21. Lambright, D. G., Sondek, J., Bohm, A., Skiba, N. P., Hamm, H. E. & Sigler, P. B. (1996). The 2.0 Å crystal structure of a heterotrimeric G protein. *Nature*, **379**, 311–319.
22. Johnston, C. A. & Siderovski, D. P. (2007). Structural basis for nucleotide exchange on G alpha i subunits and receptor coupling specificity. *Proc. Natl Acad. Sci. USA*, **104**, 2001–2006.
23. Posner, B. A., Mixon, M. B., Wall, M. A., Sprang, S. R. & Gilman, A. G. (1998). The A326S mutant of $G_i$alpha1 as an approximation of the receptor-bound state. *J. Biol. Chem.* **273**, 21752–21758.
24. Thomas, C. J., Du, X., Li, P., Wang, Y., Ross, E. M. & Sprang, S. R. (2004). Uncoupling conformational change from GTP hydrolysis in a heterotrimeric G protein alpha-subunit. *Proc. Natl Acad. Sci. USA*, **101**, 7560–7565.
25. Natochin, M., Moussaif, M. & Artemyev, N. O. (2001). Probing the mechanism of rhodopsin-catalyzed transducin activation. *J. Neurochem.* **77**, 202–210.
26. Marin, E. P., Krishna, A. G. & Sakmar, T. P. (2001). Rapid activation of transducin by mutations distant from the nucleotide-binding site: evidence for a mechanistic model of receptor-catalyzed nucleotide exchange by G proteins. *J. Biol. Chem.* **276**, 27400–27405.
27. Marin, E. P., Krishna, A. G. & Sakmar, T. P. (2002). Disruption of the alpha5 helix of transducin impairs rhodopsin-catalyzed nucleotide exchange. *Biochemistry*, **41**, 6988–6994.
28. Oldham, W. M., Van Eps, N., Preininger, A. M., Hubbell, W. L. & Hamm, H. E. (2006). Mechanism of the receptor-catalyzed activation of heterotrimeric G proteins. *Nat. Struct. Mol. Biol.* **13**, 772–777.
29. Oldham, W. M., Van Eps, N., Preininger, A. M., Hubbell, W. L. & Hamm, H. E. (2007). Mapping allosteric connections from the receptor to the nucleotide-binding pocket of heterotrimeric G proteins. *Proc. Natl Acad. Sci. USA*, **104**, 7927–7932.
30. Van Eps, N., Oldham, W. M., Hamm, H. E. & Hubbell, W. L. (2006). Structural and dynamical changes in an alpha-subunit of a heterotrimeric G protein along the activation pathway. *Proc. Natl Acad. Sci. USA*, **103**, 16194–16199.
31. Preininger, A., Funk, M., Meier, S., Oldham, W., Johnston, C., Adhikary, S. *et al.* (2009). Helix dipole movement and conformational variability contribute to allosteric GDP release in G_i subunits. *Biochemistry*, **48**, 2630–2642.
32. Koenig, B. W., Kontaxis, G., Mitchell, D. C., Louis, J. M., Litman, B. J. & Bax, A. (2002). Structure and orientation of a G protein fragment in the receptor bound state from residual dipolar couplings. *J. Mol. Biol.* **322**, 441–461.
33. Scheerer, P., Park, J. H., Hildebrand, P. W., Kim, Y. J., Krauss, N., Choe, H. W. *et al.* (2008). Crystal structure of opsin in its G-protein-interacting conformation. *Nature*, **455**, 497–502.
34. Fahmy, K. & Sakmar, T. P. (1993). Light-dependent transducin activation by an ultraviolet-absorbing rhodopsin mutant. *Biochemistry*, **32**, 9165–9171.
35. Coleman, D. E., Berghuis, A. M., Lee, E., Linder, M. E., Gilman, A. G. & Sprang, S. R. (1994). Structures of active conformations of Gi alpha 1 and the mechanism of GTP hydrolysis. *Science*, **265**, 1405–1412.
36. Insel, P. A. & Ostrom, R. S. (2003). Forskolin as a tool for examining adenylyl cyclase expression, regulation, and G protein signaling. *Cell. Mol. Neurobiol.* **23**, 305–314.
37. Levitzki, A. (1987). Regulation of adenylate cyclase by hormones and G-proteins. *FEBS Lett.* **211**, 113–118.
38. Gupta, A., Decaillot, F. M. & Devi, L. A. (2006). Targeting opioid receptor heterodimers: strategies for screening and drug development. *AAPS J.* **8**, E153–E159.
39. Durocher, Y., Perret, S., Thibaudeau, E., Gaumond, M. H., Kamen, A., Stocco, R. & Abramovitz, M. (2000). A reporter gene assay for high-throughput screening of G-protein-coupled receptors stably or transiently expressed in HEK293 EBNA cells grown in suspension culture. *Anal. Biochem.* **284**, 316–326.
40. Coleman, D. E. & Sprang, S. R. (1998). Crystal structures of the G protein G_i alpha 1 complexed with GDP and Mg^{2+}: a crystallographic titration experiment. *Biochemistry*, **37**, 14376–14385.
41. Rondard, P., Iiri, T., Srinivasan, S., Meng, E., Fujita, T. & Bourne, H. R. (2001). Mutant G protein alpha subunit activated by Gbeta gamma: a model for receptor activation? *Proc. Natl Acad. Sci. USA*, **98**, 6150–6155.
42. Cherfils, J. & Chabre, M. (2003). Activation of G-protein Galpha subunits by receptors through Galpha-Gbeta and Galpha-Ggamma interactions. *Trends Biochem. Sci.* **28**, 13–17.
43. Nanoff, C., Koppensteiner, R., Yang, Q., Fuerst, E., Ahorn, H. & Freissmuth, M. (2006). The carboxyl terminus of the Galpha-subunit is the latch for triggered activation of heterotrimeric G proteins. *Mol. Pharmacol.* **69**, 397–405.
44. Herrmann, R., Heck, M., Henklein, P., Kleuss, C., Hofmann, K. P. & Ernst, O. P. (2004). Sequence of interactions in receptor-G protein coupling. *J. Biol. Chem.* **279**, 24283–24290.
45. Dratz, E. A., Furstenau, J. E., Lambert, C. G., Thireault, D. L., Rarick, H., Schepers, T. *et al.* (1993). NMR structure of a receptor-bound G-protein peptide. *Nature*, **363**, 276–281.
46. Kisselev, O. G., Kao, J., Ponder, J. W., Fann, Y. C., Gautam, N. & Marshall, G. R. (1998). Light-activated rhodopsin induces structural binding motif in G protein alpha subunit. *Proc. Natl Acad. Sci. USA*, **95**, 4270–4275.
47. Conklin, B. R., Farfel, Z., Lustig, K. D., Julius, D. & Bourne, H. R. (1993). Substitution of three amino acids

switches receptor specificity of G_q alpha to that of G_i alpha. *Nature*, **363**, 274–276.
48. Cerione, R. A., Staniszewski, C., Benovic, J. L., Lefkowitz, R. J., Caron, M. G., Gierschik, P. *et al.* (1985). Specificity of the functional interactions of the beta-adrenergic receptor and rhodopsin with guanine nucleotide regulatory proteins reconstituted in phospholipid vesicles. *J. Biol. Chem.* **260**, 1493–1500.
49. Kleuss, C., Scherubl, H., Hescheler, J., Schultz, G. & Wittig, B. (1992). Different beta-subunits determine G-protein interaction with transmembrane receptors. *Nature*, **358**, 424–426.
50. Ceruso, M. A., Periole, X. & Weinstein, H. (2004). Molecular dynamics simulations of transducin: interdomain and front to back communication in activation and nucleotide exchange. *J. Mol. Biol.* **338**, 469–481.
51. Abdulaev, N. G., Ngo, T., Zhang, C., Dinh, A., Brabazon, D. M., Ridge, K. D. & Marino, J. P. (2005). Heterotrimeric G-protein alpha-subunit adopts a "preactivated" conformation when associated with betagamma-subunits. *J. Biol. Chem.* **280**, 38071–38080.
52. Scheerer, P., Heck, M., Goede, A., Park, J. H., Choe, H. W., Ernst, O. P., Hofmann, K. P. & Hildebrand, P. W. (2009). Structural and kinetic modeling of an activating helix switch in the rhodopsin-transducin interface. *Proc. Natl. Acad. Sci. USA*, **106**, 10660–10665.
53. Heck, M. & Hofmann, K. P. (2001). Maximal rate and nucleotide dependence of rhodopsin-catalyzed transducin activation: initial rate analysis based on a double displacement mechanism. *J. Biol. Chem.* **276**, 10000–10009.
54. Vetter, I. R. & Wittinghofer, A. (2001). The guanine nucleotide-binding switch in three dimensions. *Science*, **294**, 1299–1304.
55. Wennerberg, K., Rossman, K. L. & Der, C. J. (2005). The Ras superfamily at a glance. *J. Cell Sci.* **118**, 843–846.
56. Wittinghofer, F. (1998). Ras signalling. Caught in the act of the switch-on. *Nature*, **394**(317), 319–320.
57. Cherfils, J. & Chardin, P. (1999). GEFs: structural basis for their activation of small GTP-binding proteins. *Trends Biochem. Sci.* **24**, 306–311.
58. Thomas, C., Fricke, I., Scrima, A., Berken, A. & Wittinghofer, A. (2007). Structural evidence for a common intermediate in small G protein-GEF reactions. *Mol. Cell*, **25**, 141–149.
59. Coleman, D. E., Lee, E., Mixon, M. B., Linder, M. E., Berghuis, A. M., Gilman, A. G. & Sprang, S. R. (1994). Crystallization and preliminary crystallographic studies of Gi alpha 1 and mutants of G_i alpha 1 in the GTP and GDP-bound states. *J. Mol. Biol.* **238**, 630–634.
60. Minor, Z. O. a. W. (1997). Processing of X-ray diffraction data collected in oscillation mode. *Methods Enzymol.* **276**, 307–326.
61. Leslie, A. G. W. (1992). Recent changes to MOSFLM package for processing film and image plate data. *Joint CCP4 + ESF-EAMCB Newslett. Protein Crystallogr.* **26**.
62. Emsley, P. & Cowtan, K. (2004). Coot: model-building tools for molecular graphics. *Acta Crystallogr., Sect. D: Biol. Crystallogr.* **60**, 2126–2132.
63. Brunger, A. T., Adams, P. D., Clore, G. M., DeLano, W. L., Gros, P., Grosse-Kunstleve, R. W. *et al.* (1998). Crystallography & NMR system: a new software suite for macromolecular structure determination. *Acta Crystallogr., Sect. D: Biol. Crystallogr.* **54**, 905–921.
64. Wallace, A. C., Laskowski, R. A. & Thornton, J. M. (1995). LIGPLOT: a program to generate schematic diagrams of protein-ligand interactions. *Protein Eng.* **8**, 127–134.

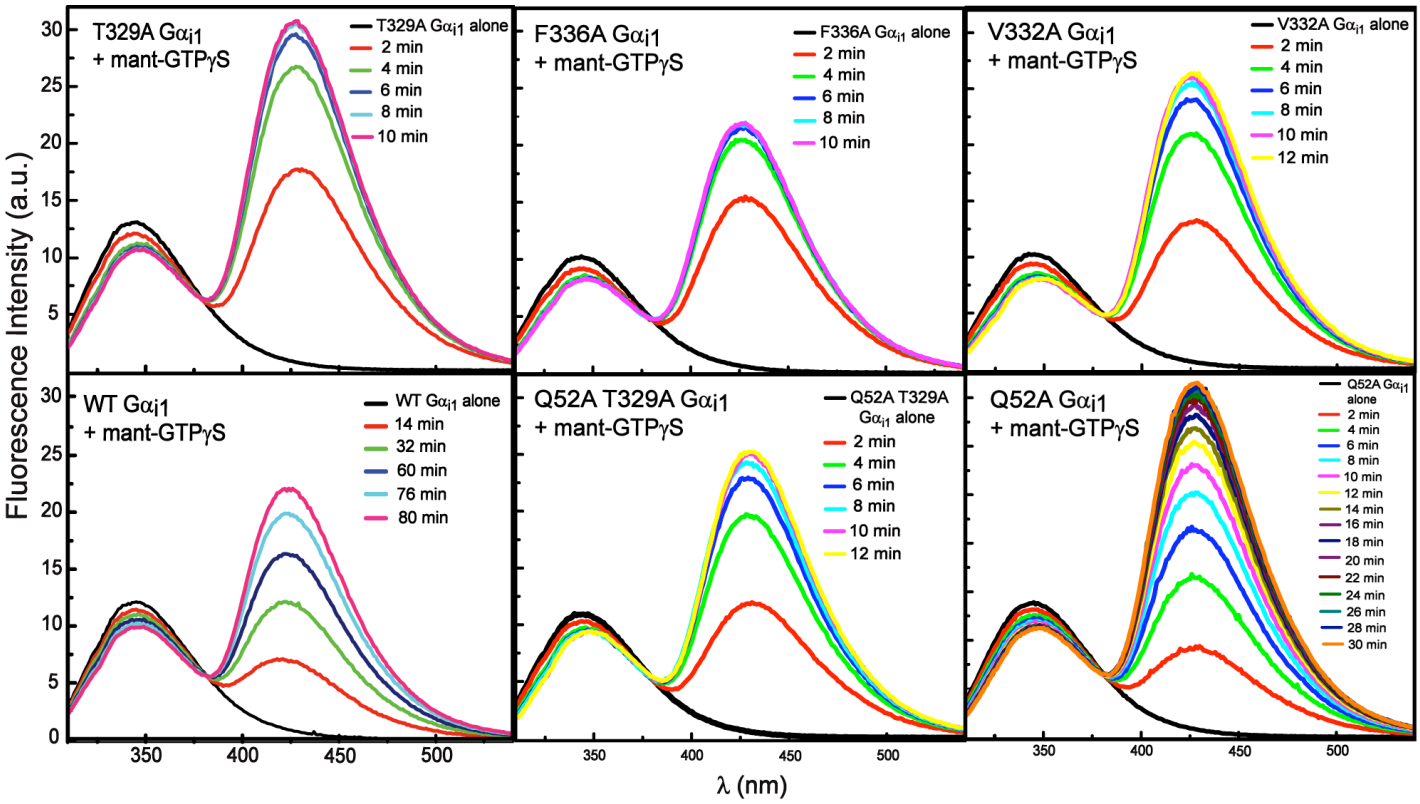
T329A Gαi1
+ mant-GTPγS
T329A Gαi1 alone
2 min
4 min
6 min
8 min
10 min
F336A Gαi1
+ mant-GTPγS
F336A Gαi1 alone
2 min
4 min
6 min
8 min
10 min
V332A Gαi1
+ mant-GTPγS
V332A Gαi1 alone
2 min
4 min
6 min
8 min
10 min
12 min
WT Gαi1
+ mant-GTPγS
WT Gαi1 alone
14 min
32 min
60 min
76 min
80 min
Q52A T329A Gαi1
+ mant-GTPγS
Q52A T329A Gαi1 alone
2 min
4 min
6 min
8 min
10 min
12 min
Q52A Gαi1
+ mant-GTPγS
Q52A Gαi1 alone
2 min
4 min
6 min
8 min
10 min
12 min
14 min
16 min
18 min
20 min
22 min
24 min
26 min
28 min
30 min
Fluorescence Intensity (a.u.)
λ (nm)

Figure S1. mant-GTPγS uptake by α5 helix mutants. Fluorescently-labeled nucleotide (mant-GTPγS) was used to do FRET studies for monitoring rates of nucleotide exchange. The α5 helix mutants $G\alpha_{i1}$-T329A (top left), $G\alpha_{i1}$-F336A (top middle), $G\alpha_{i1}$-V332A (top right), $G\alpha_{i1}$-(Q52A T329A) (bottom middle) and $G\alpha_{i1}$-Q52A (bottom right) all show overall fast rates of nucleotide exchange in comparison to WT $G\alpha_{i1}$ protein (lower left panel).

(a)

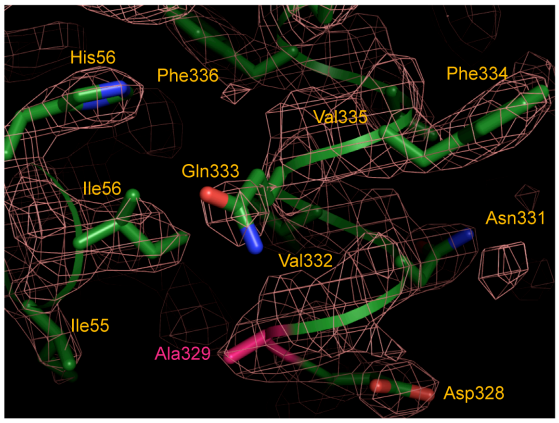
His56
Phe336
Phe334
Val335
Gln333
Ile56
Asn331
Val332
Ile55
Ala329
Asp328

(b)

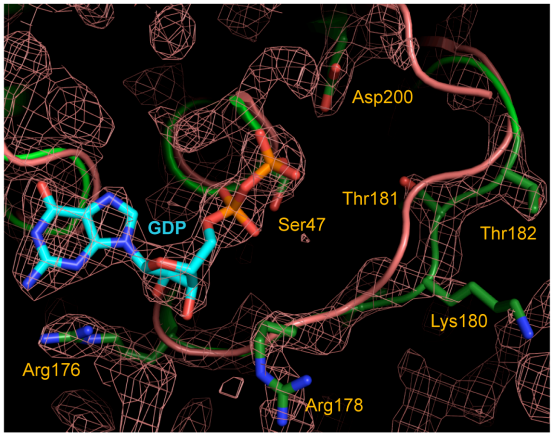
Asp200
Thr181
GDP
Ser47
Thr182
Lys180
Arg176
Arg178

(c)

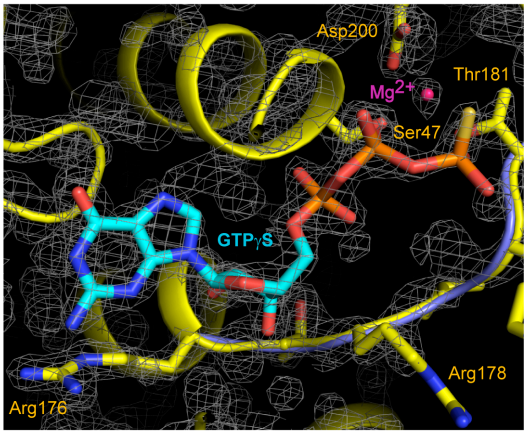
Asp200
Thr181
Mg2+
Ser47
GTPγS
Arg178
Arg176

(d)

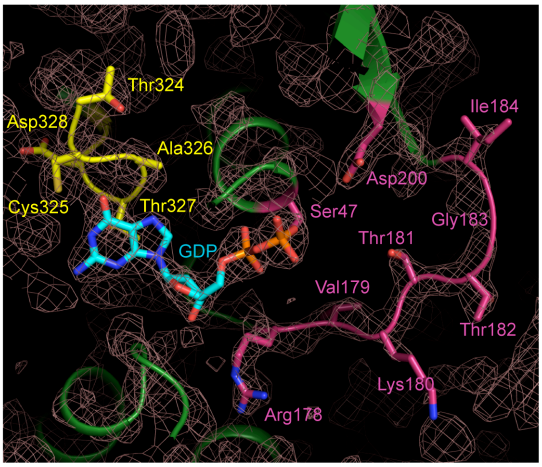
Thr324
Ile184
Asp328
Ala326
Asp200
Cys325
Thr327
Ser47
Gly183
GDP
Thr181
Val179
Thr182
Lys180
Arg178

(e)

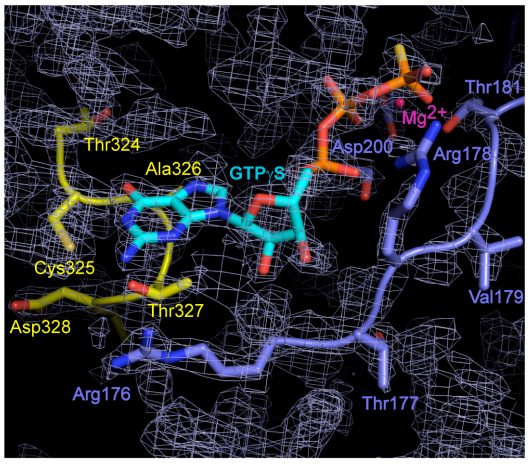
Thr181
Mg2+
Thr324
Asp200
Arg178
Ala326
GTPγS
Cys325
Val179
Thr327
Asp328
Arg176
Thr177

Figure S2. The T329A mutation and model building. The crystal structure of heterologously expressed $G\alpha_{i1}$-T329A shows (a) density for alanine at the 329 position in its protein sequence confirming the correctly characterized and crystallized protein. Simulated Annealing OMIT-maps were generated for $G\alpha_{i1}$-T329A•GDP while omitting GDP from the analysis and for $G\alpha_{i1}$-T329A•GTPγS•Mg^{2+} while excluding GTPγS and Mg^{2+}. A $2F_o$-F_c simulated annealing OMIT-map contoured at 2σ for (b) $G\alpha_{i1}$-T329A•GDP (green) and (c) $G\alpha_{i1}$-T329A•GTPγS•Mg^{2+} (yellow) is shown. The structures for WT $G\alpha_{i1}$•GDP (salmon) and WT $G\alpha_{i1}$•GTPγS•Mg^{2+} (blue) are also superimposed. The fit of the final model into the electron density is presented for the critical regions close to the nucleotide for each structure. The nucleotide interacting β6/α5 loop is shown in yellow. The residues corresponding to Switch 1 and Mg^{2+} coordination sphere are shown in (d) pink for $G\alpha_{i1}$-T329A•GDP and shown in (e) blue for $G\alpha_{i1}$-T329A•GTPγS•Mg^{2+}.

(a)

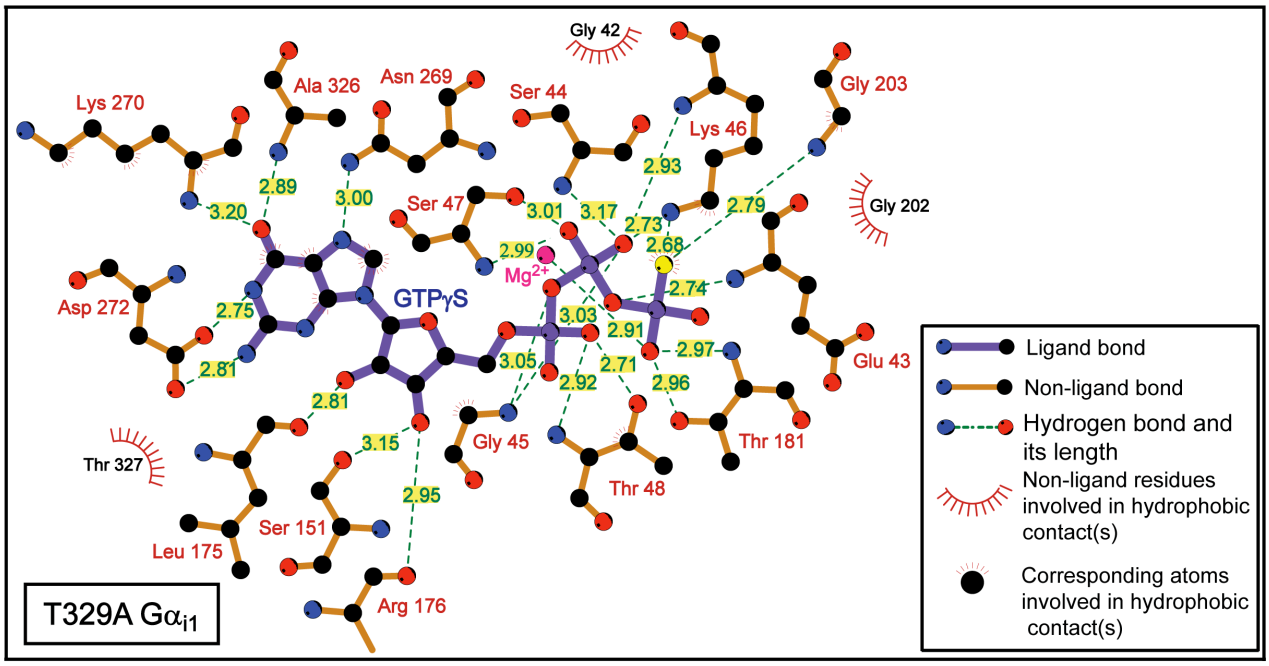
Gly 42
Lys 270
Ala 326
Asn 269
Ser 44
Gly 203
Lys 46
Gly 202
Ser 47
GTPγS
Mg2+
Asp 272
Glu 43
Thr 327
Gly 45
Thr 181
Thr 48
Ser 151
Leu 175
Arg 176
T329A Gαi1
Ligand bond
Non-ligand bond
Hydrogen bond and its length
Non-ligand residues involved in hydrophobic contact(s)
Corresponding atoms involved in hydrophobic contact(s)

(b)

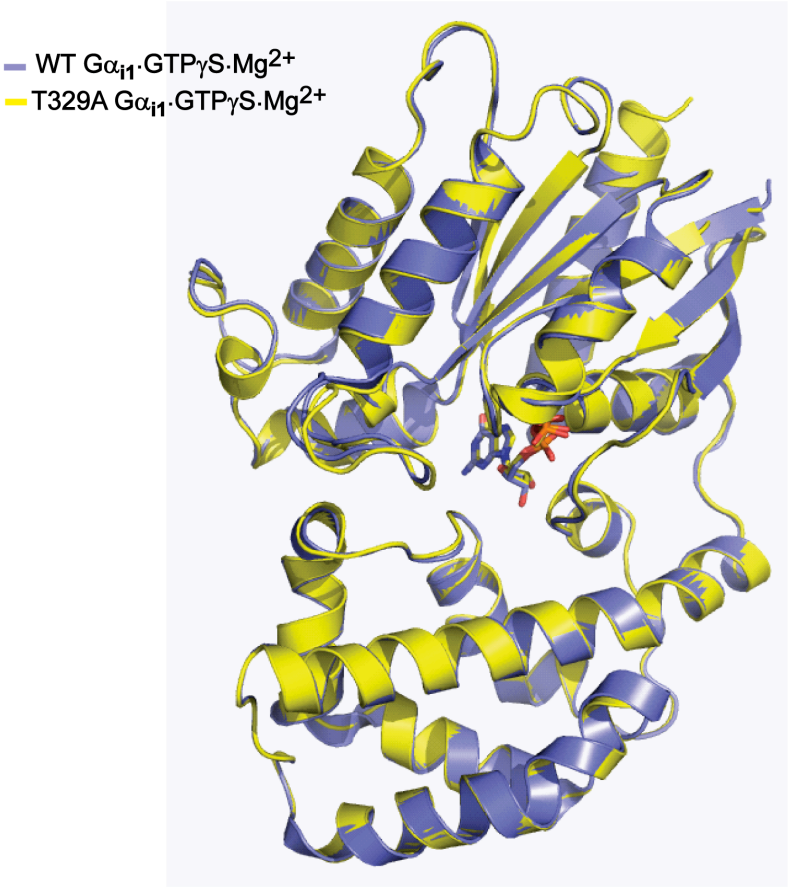
WT Gαi1·GTPγS·Mg2+
T329A Gαi1·GTPγS·Mg2+

Figure S3. Structural changes in the GTPγS-bound form of WT $G\alpha_{i1}$ and $G\alpha_{i1}$-T329A structures. (A) The catalytic pocket of the GTPγS•Mg^{2+} bound (activated) form of $G\alpha_{i1}$-T329A shows the expected conservation of residues involved in the interaction with both diphosphate and triphosphate nucleosides. The presense of Mg^{2+} also promotes a greater degree of order and coordination density within the catalytic pocket, increasing the overall stability of the state. (B) A superposition of the WT $G\alpha_{i1}$-GTPγS•Mg^{2+} and $G\alpha_{i1}$-T329A-GTPγS•Mg^{2+} structures shows almost identical secondary structures. There are also no observable differences in the orientation of the bound nucleotide.

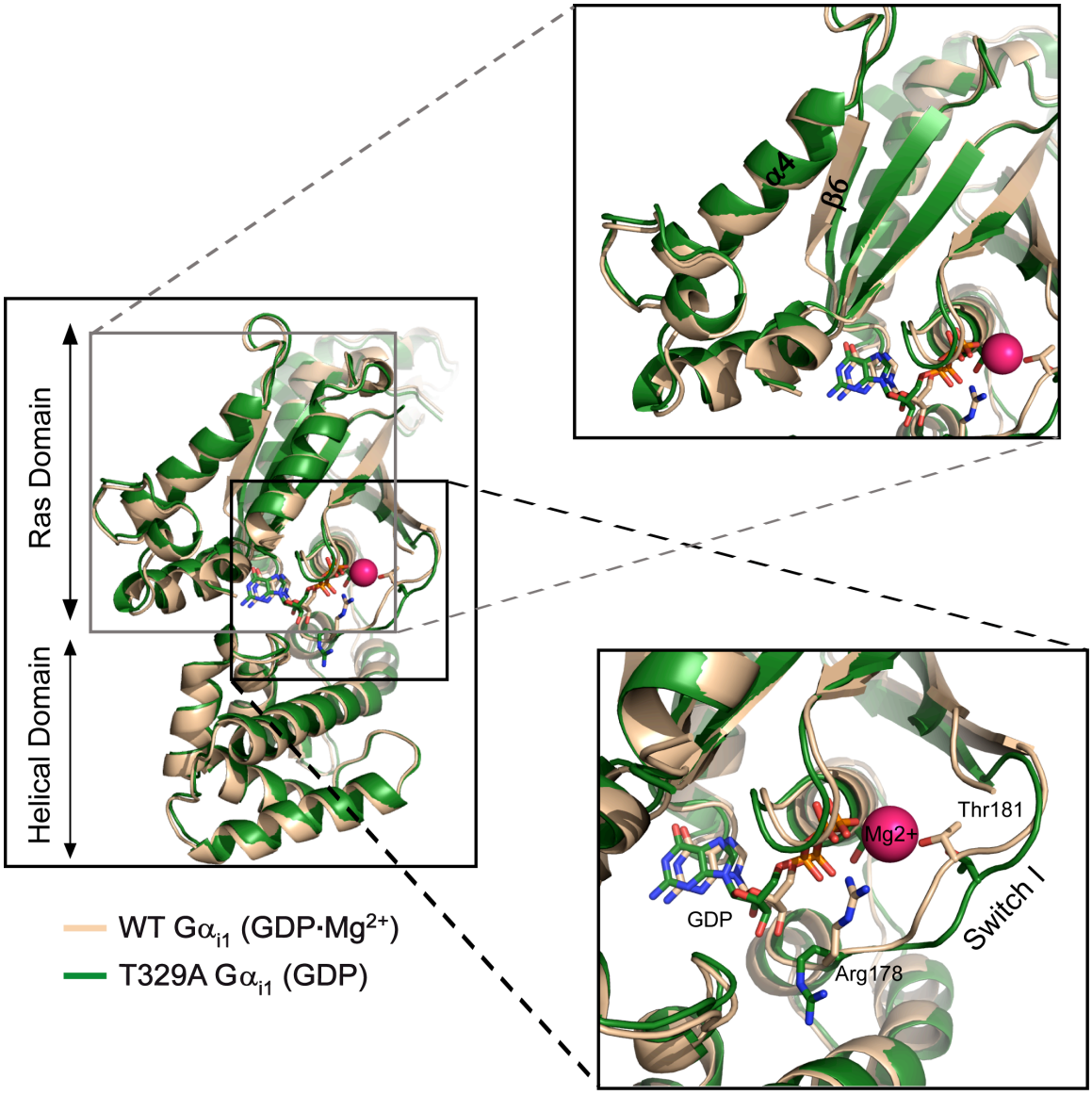
α4
β6
Ras Domain
Helical Domain
WT Gαi1 (GDP·Mg2+)
T329A Gαi1 (GDP)
Thr181
Mg2+
GDP
Switch I
Arg178

Figure S4. Structural changes amongst the GDP-bound forms of WT $G\alpha_{i1}$ and $G\alpha_{i1}$-T329A. The superposition of WT $G\alpha_{i1}$•GDP and $G\alpha_{i1}$-T329A•GDP shows key structural differences. A zoom into the Ras domain (top) (and removal of the a3 helix for clarity) reveals the displacement observed in the β6 strand between the structures. A zoom into the catalytic pocket (below) shows a drastically altered switch 1 conformation between the WT $G\alpha_{i1}$•GDP and $G\alpha_{i1}$-T329A•GDP structures. The superposition also shows the bound Mg^{2+} in the WT $G\alpha_{i1}$•GDP structure along with key residues, namely R178 and T181, lining the catalytic pocket. A small displacement in position of the bound nucleotide can also be observed.

(a)

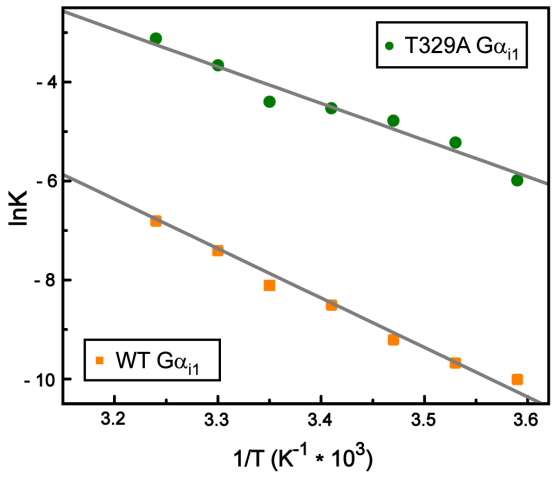

(b)

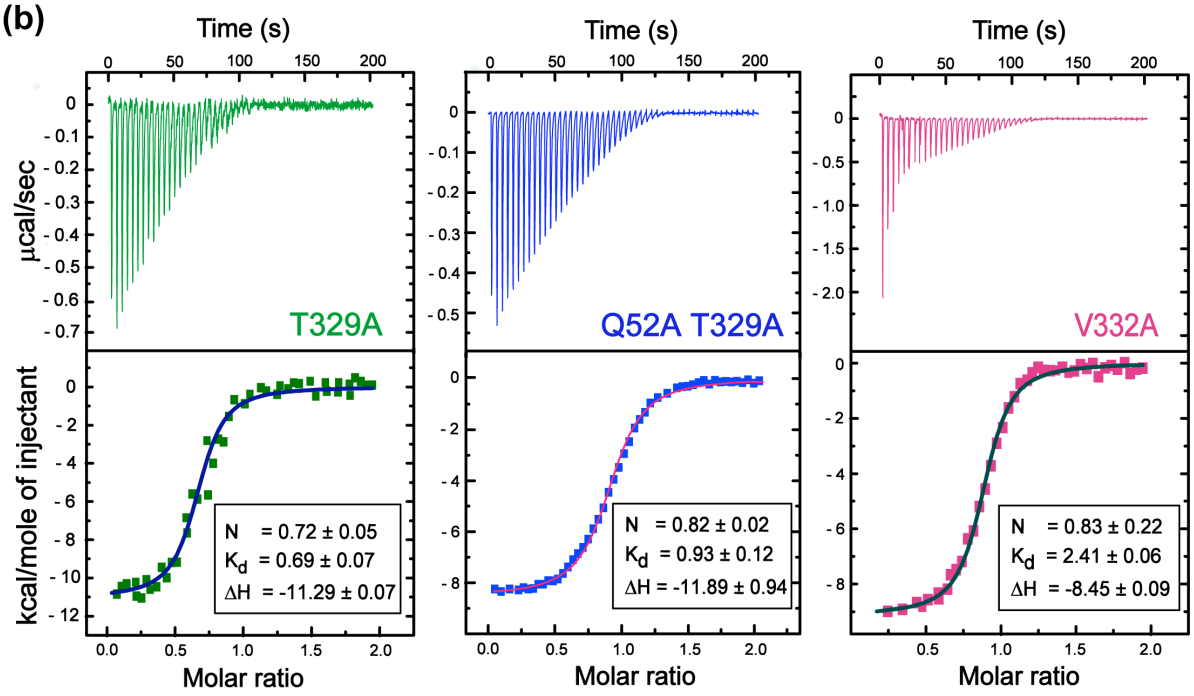

Protein	N	K_d (µM)	ΔH (kcal mol^{-1})
T329A	0.70 ± 0.05	0.69 ± 0.07	-11.29 ± 0.20
Q52A T329A	0.82 ± 0.02	0.93 ± 0.12	-8.45 ± 0.09
V332A	0.83 ± 0.22	2.41 ± 0.06	-11.89 ± 0.94

Figure S5. Thermodynamics analysis of the activation process. (A) In order to analyze quantitatively the effect of mutation on the activation energy for the nucleotide exchange process, we performed GTPγS-binding assays over a linear temperature gradient. The fluorescence enhancement of W211 due to activation was monitored and rates were calculated. Experiments were performed for the WT $G\alpha_{i1}$ and $G\alpha_{i1}$-T329A mutant and k_{app} values were calculated for each data set at different temperatures. A plot of lnk versus 1/T was fit to the Arrhenius equation to give activation energies for both WT and mutant T329A $G\alpha_{i1}$. The analysis revealed that the barrier for activation of the mutant was lower by 5.1 kcal/mol compared to the WT.

Isothermal titration calorimetry (ITC) was performed to analyze the effect of amino acid replacement on the apparent binding affinity of the nucleotide ligand and its influence on the nucleotide exchange process. (B) ITC experiments of the binding of GTPγS to three mutant $G\alpha_{i1}$ subunits are shown along with their calculated thermodynamic parameters. The binding of GTPγS to the $G\alpha_{i1}$-T329A mutant was more exothermic than GTPγS binding to WT $G\alpha_{i1}$ (data not shown), possibly because it does not exchange as rapidly as the mutants. The crystal structures of $G\alpha_{i1}$-T329A•GTPγS•Mg^{2+} and WT $G\alpha_{i1}$•GTPγS•Mg^{2+} are almost identical, with an r.m.s.d. of 0.29 Å. Thus, the final GTPγS-bound states of the two complexes can be assumed to have the same energy level on a reaction profile diagram. However, the crystal structure of the GDP-bound form of the $G\alpha_{i1}$-T329A mutant displays significant conformational changes that destabilize its GDP-bound state. Hence, transition from the energetically higher GDP-bound state should give larger reaction enthalpy. Our ITC data are in excellent agreement with this rationale. The high activation barrier for the WT protein

makes the process of spontaneous basal nucleotide exchange slow and unfavorable, although we observe strong binding constants for $G\alpha_{i1}$-T329A. Since both the GTPγS-bound states of the WT $G\alpha_{i1}$ and $G\alpha_{i1}$-T329A proteins show almost identical structures, the higher affinity of $G\alpha_{i1}$-T329A can be explained by the initial lower affinity for the bound GDP. The loss of favorable interactions caused by the α 5 helix amino acid replacement promotes faster release of the bound GDP. This creates a nucleotide-free pocket readily available for GTPγS binding. The initial higher affinity of WT $G\alpha_{i1}$ for GDP explains its lower binding affinity for GTPγS, resulting in lower enthalpy of reaction. The kinetically slower mutants $G\alpha_{i1}$-Q52A/T329A and $G\alpha_{i1}$-V332A display lower apparent binding affinities for the triphosphate ligand than does $G\alpha_{i1}$-T329A, suggesting that replacements of Q52 and V332 destabilize the GDP-bound state to a lesser extent than the T329A replacement.

ITC was performed at 25°C (298 K) using a MicroCal VP-ITC (MicroCal, Northhampton, MA) calorimeter. Protein samples were dialyzed against the titration buffer (50 mM Tris-HCl, pH8.0, 150 mM NaCl, 2 mM $MgCl_2$, 10 μM GDP, 1 mM TCEP (Tris-(2-carboxyethyl) phosphine)). Three buffer exchanges (each 4 hrs or more) were done to remove DTT from the protein stock. GTPγS was not dialyzed due to its small size. The GTPγS stock solution was prepared using the final dialysis buffer for the protein solution. Both the experimental protein and GTPγS samples were thoroughly degassed. Contents of the sample cell were stirred continuously at 280 rpm during the experiment. A typical titration of $G\alpha_{i1}$ mutants with GTPγS involved 50 injections each of 5 μl of GTPγS solution (500 μM) into a sample cell containing 1.4 ml of WT or mutant $G\alpha_{i1}$ (50 μM). The heat of dilution of the titrant (GTPγS) was subtracted from the

titration data for base-line correction. The base line-corrected data were analyzed with MicroCal OriginTM 6.0 software to determine the enthalpy (ΔH), association constant (K_a), and stoichiometry of binding (N). Thermal titration data were fit to single site binding model and thermodynamic parameters Δ H, K_d and entropy change (Δ*S*) were obtained from the fits to the model. The parameters were calculated based on three or more independent titration experiments. Each numerical value reported is the mean experimental value ± S.E.M from three independent data sets. $G\alpha_{i1}$-T329A displays highest affinity for GTPγS in comparison with Q52A T329A and V332A mutant $G\alpha_{i1}$ subunits. WT $G\alpha_{i1}$ could not be tested because of its low affinity for the nucleotide and its very slow basal GTPγS uptake rate.

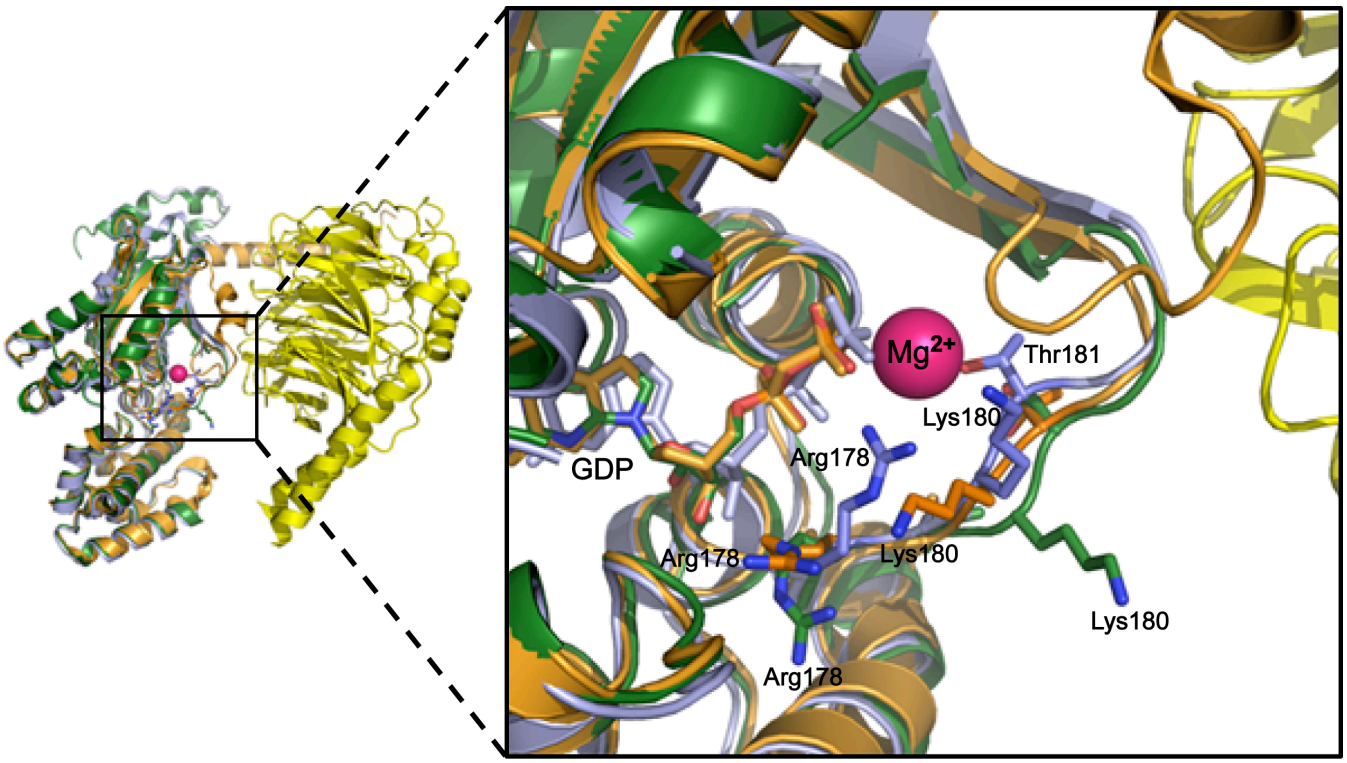

Color Code

- WT $G\alpha_{i1}$·GDP·Mg^{2+}
- WT $G\alpha_{i1}$·GDP·Mg^{2+} ($G\beta\gamma$ Complex)
- T329A $G\alpha_{i1}$·GDP
- $G\beta\gamma$

Figure S6. Differential orientation of R178 residue. A superposition of α-subunits from WT $G\alpha_{i1}$•GDP•Mg^{2+} (PDB Code 1BOF) (Coleman & Sprang, 1998), WT $G\alpha_{i1}$•GDP•Mg^{2+} (from the heterotrimer complex) (PDB Code 1GG2) (Wall et al, 1995) and $G\alpha_{i1}$-T329A•GDP structures show differential orientation of the R178 residue. In the WT $G\alpha_{i1}$•GDP•Mg^{2+} structure R178 points into the catalytic pocket making electrostatic interactions with the α- and β-phosphates of GDP whereas in the heterotrimer the R178 is flipped outwards by 90^0 away from the catalytic pocket. Even in the $G\alpha_{i1}$-T329A•GDP structure the R178 residue flips away by almost 180^0 and moves away from the catalytic pocket.

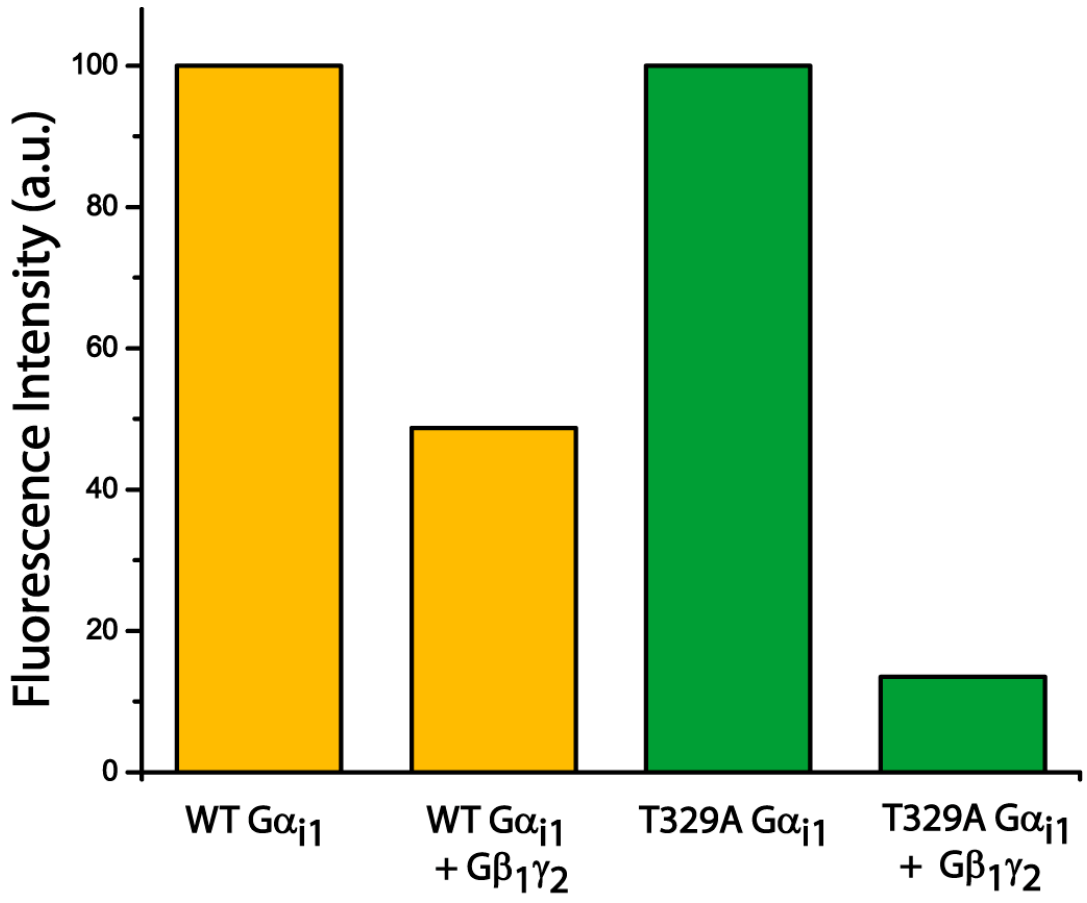
Fluorescence Intensity (a.u.)
100
80
60
40
20
0
WT Gαi1
WT Gαi1 + Gβ1γ2
T329A Gαi1
T329A Gαi1 + Gβ1γ2

Figure S7. Inhibition of G protein activation in the presence of Gβγ. WT G protein α-subunit or the T329A-$G\alpha_{i1}$ in the GDP bound form are mixed with equimolar (178nM each) quantities of $G\beta_1\gamma_2$ and $AlF4^-$ uptake is monitored by measuring the fluorescence enchancement. Both WT and T329A-$G\alpha_{i1}$ exhibit decrease in the fluorescence enhancement observed in the presence of $G\beta_1\gamma_2$ in comparison to the α-subunits alone suggesting a direct interaction between these difference components of the heterotrimeric G proteins.

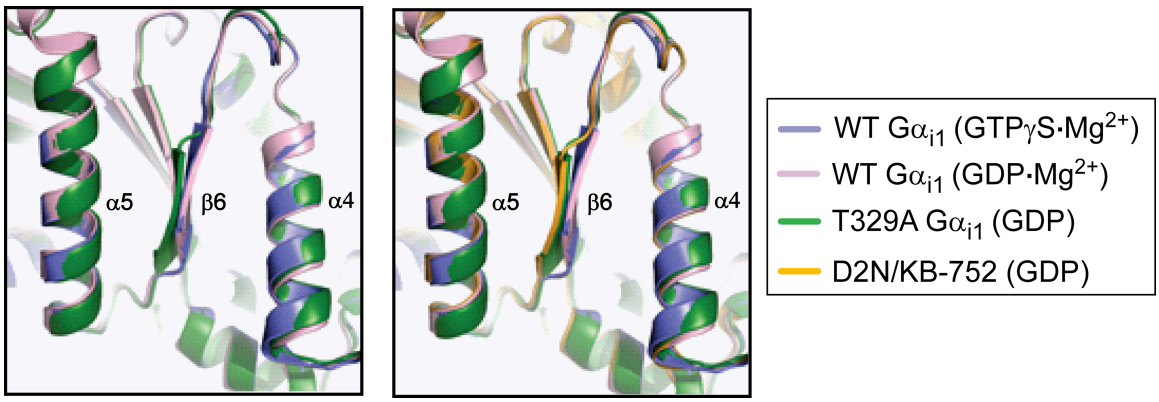
α5
β6
α4
α5
β6
α4
WT Gαi1 (GTPγS·Mg2+)
WT Gαi1 (GDP·Mg2+)
T329A Gαi1 (GDP)
D2N/KB-752 (GDP)

Figure S8. Structural changes facilitating nucleotide exchange. The structure of WT $G\alpha_{i1}$•GDP bound to two peptides (KB-752 and D2N) which interact with different regions of the protein and synergistically cause an increase in the nucleotide exchange rates, apparently acting as GEFs (guanine-nucleotide exchange factors) was recently solved (Johnston & Siderovski, 2007) (PDB code 2hlb). Superimposition of the α5-β6-α4 domain of WT $G\alpha_{i1}$•GTPγS•Mg^{2+}, WT $G\alpha_{i1}$•GDP•Mg^{2+}, $G\alpha_{i1}$-T329A•GDP and WT $G\alpha_{i1}$•GDP/KB-752/D2N shows a similar orientation of β6 strand for the T329A mutant as observed by Siderovski *et al.* Unlike the case of T329A, the β6 strand in the active and inactive forms of WT $G\alpha_{i1}$ do not undergo any conformational changes.

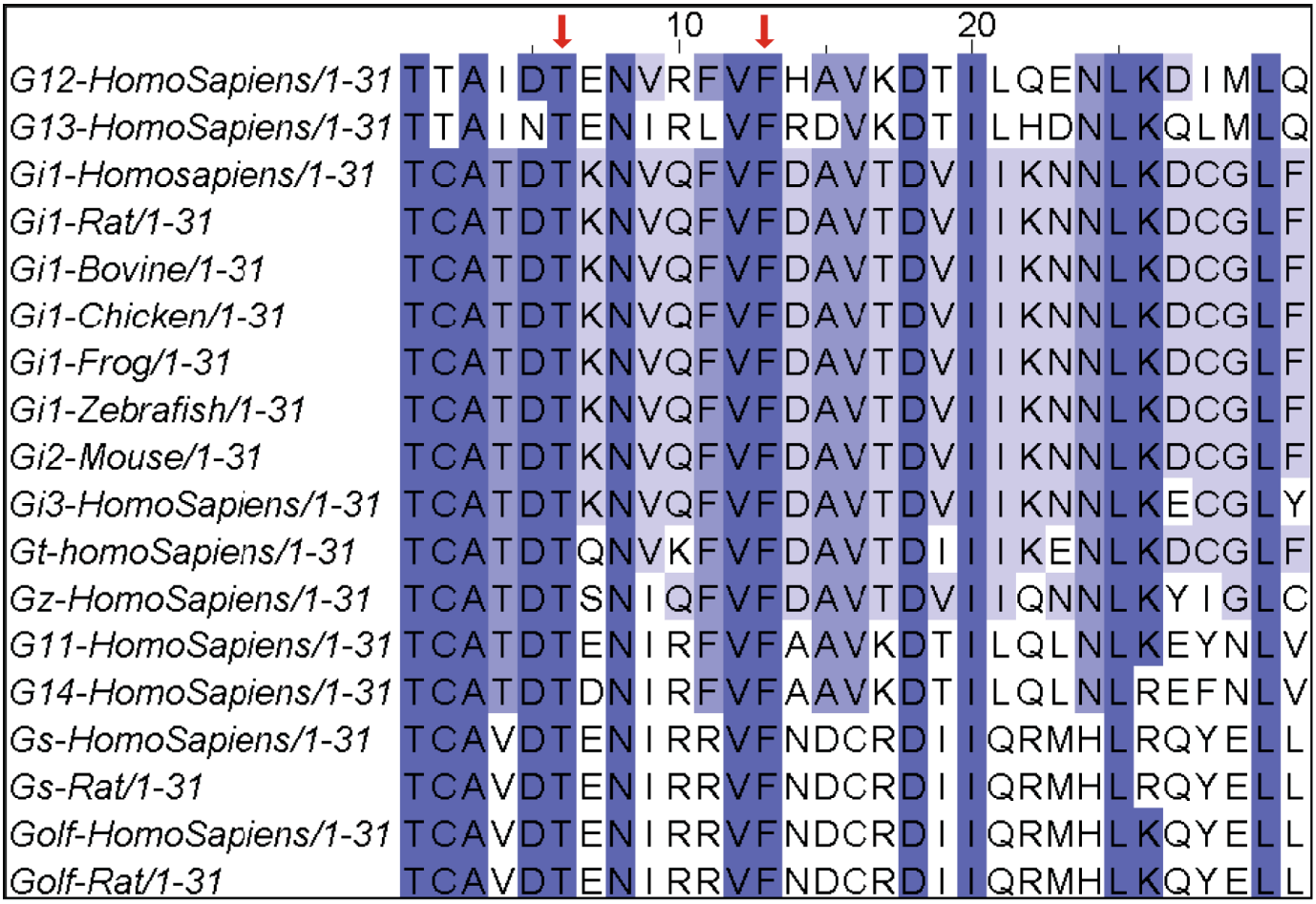
10
20
G12-HomoSapiens/1-31 TTAIDTENVRFVFHAVKDTILQENLKDIMLQ
G13-HomoSapiens/1-31 TTAINTENIRLVFRDVKDTILHDNLKQLMLQ
Gi1-Homosapiens/1-31 TCATDTKNVQFVFDAVTDVIIKNNLKDCGLF
Gi1-Rat/1-31 TCATDTKNVQFVFDAVTDVIIKNNLKDCGLF
Gi1-Bovine/1-31 TCATDTKNVQFVFDAVTDVIIKNNLKDCGLF
Gi1-Chicken/1-31 TCATDTKNVQFVFDAVTDVIIKNNLKDCGLF
Gi1-Frog/1-31 TCATDTKNVQFVFDAVTDVIIKNNLKDCGLF
Gi1-Zebrafish/1-31 TCATDTKNVQFVFDAVTDVIIKNNLKDCGLF
Gi2-Mouse/1-31 TCATDTKNVQFVFDAVTDVIIKNNLKDCGLF
Gi3-HomoSapiens/1-31 TCATDTKNVQFVFDAVTDVIIKNNLKECGLY
Gt-homoSapiens/1-31 TCATDTQNVKFVFDAVTDIIIKENLKDCGLF
Gz-HomoSapiens/1-31 TCATDTSNIQFVFDAVTDVIIQNNLKYIGLC
G11-HomoSapiens/1-31 TCATDTENIRFVFAAVKDTILQLNLKEYNLV
G14-HomoSapiens/1-31 TCATDTDNIRFVFAAVKDTILQLNLREFNLV
Gs-HomoSapiens/1-31 TCAVDTENIRRVFNDCRDIIQRMHLRQYELL
Gs-Rat/1-31 TCAVDTENIRRVFNDCRDIIQRMHLRQYELL
Golf-HomoSapiens/1-31 TCAVDTENIRRVFNDCRDIIQRMHLKQYELL
Golf-Rat/1-31 TCAVDTENIRRVFNDCRDIIQRMHLKQYELL

Figure S9. Sequence alignment of C-terminal residues of Gα subunits. The sequence alignment of the last 31 residues of various α-subunits comprising the P-loop, α5 helix and CT shows high degree of conservation. The residues T329 and F336 in WT $G\alpha_{i1}$ show 100% conservation across various classes of α-subunits. The sequence alignment was generated using the software clustalW.

BIBLIOGRAPHY

1. W. M. Oldham, H. E. Hamm, *Nat Rev Mol Cell Biol* **9**, 60 (Jan, 2008).
2. T. P. Sakmar, S. T. Menon, E. P. Marin, E. S. Awad, *Annu Rev Biophys Biomol Struct* **31**, 443 (2002).
3. A. G. Gilman, *Annu Rev Biochem* **56**, 615 (1987).
4. K. L. Pierce, R. T. Premont, R. J. Lefkowitz, *Nat Rev Mol Cell Biol* **3**, 639 (Sep, 2002).
5. C. R. McCudden, M. D. Hains, R. J. Kimple, D. P. Siderovski, F. S. Willard, *Cell Mol Life Sci* **62**, 551 (Mar, 2005).
6. D. P. Siderovski, F. S. Willard, *Int J Biol Sci* **1**, 51 (2005).
7. L. De Vries, B. Zheng, T. Fischer, E. Elenko, M. G. Farquhar, *Annu Rev Pharmacol Toxicol* **40**, 235 (2000).
8. R. R. Neubig, D. P. Siderovski, *Nat Rev Drug Discov* **1**, 187 (Mar, 2002).
9. R. J. Kimple *et al.*, *J Biol Chem* **276**, 29275 (Aug 3, 2001).
10. F. S. Willard, R. J. Kimple, D. P. Siderovski, *Annu Rev Biochem* **73**, 925 (2004).
11. A. Takesono *et al.*, *J Biol Chem* **274**, 33202 (Nov 19, 1999).
12. J. B. Blumer, M. J. Cismowski, M. Sato, S. M. Lanier, *Trends Pharmacol Sci* **26**, 470 (Sep, 2005).
13. R. J. Kimple, F. S. Willard, D. P. Siderovski, *Mol Interv* **2**, 88 (Apr, 2002).
14. L. De Vries *et al.*, *Proc Natl Acad Sci U S A* **97**, 14364 (Dec 19, 2000).

15. N. Mochizuki, M. Hibi, Y. Kanai, P. A. Insel, *FEBS Lett* **373**, 155 (Oct 9, 1995).

16. P. Lin *et al.*, *J Cell Biol* **141**, 1515 (Jun 29, 1998).

17. P. Lin, T. Fischer, C. Lavoie, H. Huang, M. G. Farquhar, *Mol Neurodegener* **4**, 15 (2009).

18. Y. Kanai, S. Tanuma, *Immunol Lett* **32**, 43 (Mar, 1992).

19. K. Miura, K. Titani, Y. Kurosawa, Y. Kanai, *Biochem Biophys Res Commun* **187**, 375 (Aug 31, 1992).

20. K. Miura, Y. Kurosawa, Y. Kanai, *Biochem Biophys Res Commun* **199**, 1388 (Mar 30, 1994).

21. E. de Alba, N. Tjandra, *Biochemistry* **43**, 10039 (Aug 10, 2004).

22. M. Kanuru, J. J. Samuel, L. M. Balivada, G. K. Aradhyam, *FEBS J* **276**, 2529 (May, 2009).

23. C. Lavoie, T. Meerloo, P. Lin, M. G. Farquhar, *Mol Endocrinol* **16**, 2462 (Nov, 2002).

24. S. N. Wang *et al.*, *Pathol Int* **44**, 844 (Dec, 1994).

25. Y. Tsukumo, S. Tsukahara, S. Saito, T. Tsuruo, A. Tomida, *J Biol Chem*, (Aug 5, 2009).

26. P. Leclerc *et al.*, *PLoS One* **3**, e2229 (2008).

27. J. Brodeur *et al.*, *Traffic* **10**, 1098 (Aug, 2009).

28. P. Lin *et al.*, *J Neurochem* **100**, 1505 (Mar, 2007).

29. P. Lin, T. Fischer, T. Weiss, M. G. Farquhar, *Proc Natl Acad Sci U S A* **97**, 674 (Jan 18, 2000).

30. N. Kapoor, S. T. Menon, R. Chauhan, P. Sachdev, T. P. Sakmar, *J Mol Biol*, (Aug 21, 2009).

31. E. P. Marin, A. G. Krishna, T. P. Sakmar, *J Biol Chem* **276**, 27400 (Jul 20, 2001).

32. E. P. Marin, A. G. Krishna, T. P. Sakmar, *Biochemistry* **41**, 6988 (Jun 4, 2002).

33. E. Folta-Stogniew, K. Williams, *J Biomol Tech* **10**, 51 (Jun, 1999).

34. D. E. Koppel, *Journal of Chemical Physics* **57**, 4814 (1972).

35. P. G. Cummins, E. J. Staples, *Journal of Physics E-Scientific Instruments* **14**, 1171 (1981).

36. K. E. Vanholde, R. L. Baldwin, *Journal of Physical Chemistry* **62**, 734 (1958).

37. S. R. Phillips, L. J. Wilson, R. F. Borkman, *Curr Eye Res* **5**, 611 (Aug, 1986).

38. M. S. Cates *et al.*, *Structure* **7**, 1269 (Oct 15, 1999).

39. W. H. Landschulz, P. F. Johnson, S. L. McKnight, *Science* **240**, 1759 (Jun 24, 1988).

40. L. M. Siegel, K. J. Monty, *Biochim Biophys Acta* **112**, 346 (Feb 7, 1966).

41. M. Natochin, M. Moussaif, N. O. Artemyev, *J Neurochem* **77**, 202 (Apr, 2001).

42. W. M. Oldham, N. Van Eps, A. M. Preininger, W. L. Hubbell, H. E. Hamm, *Nat Struct Mol Biol* **13**, 772 (Sep, 2006).

43. F. S. Willard, A. J. Kimple, C. A. Johnston, D. P. Siderovski, *Anal Biochem* **340**, 341 (May 15, 2005).

44. F. S. Willard, R. J. Kimple, A. J. Kimple, C. A. Johnston, D. P. Siderovski, *Methods Enzymol* **389**, 56 (2004).

45. M. B. Mixon *et al.*, *Science* **270**, 954 (Nov 10, 1995).

46. P. Lin, Y. Yao, R. Hofmeister, R. Y. Tsien, M. G. Farquhar, *J Cell Biol* **145**, 279 (Apr 19, 1999).

47. R. Pezzati, M. Bossi, P. Podini, J. Meldolesi, F. Grohovaz, *Mol Biol Cell* **8**, 1501 (Aug, 1997).

48. P. E. Scherer *et al.*, *J Cell Biol* **133**, 257 (Apr, 1996).

49. Y. M. Usachev, S. M. Marchenko, S. O. Sage, *J Physiol* **489 (Pt 2)**, 309 (Dec 1, 1995).

50. T. S. Weiss *et al.*, *Proc Natl Acad Sci U S A* **98**, 14961 (Dec 18, 2001).

51. F. S. Willard, C. R. McCudden, D. P. Siderovski, *Cell Signal* **18**, 1226 (Aug, 2006).

52. C. R. McCudden *et al.*, *Biochim Biophys Acta* **1745**, 254 (Sep 10, 2005).

53. R. J. Kimple *et al.*, *Biochem J* **378**, 801 (Mar 15, 2004).

54. R. J. Kimple, M. E. Kimple, L. Betts, J. Sondek, D. P. Siderovski, *Nature* **416**, 878 (Apr 25, 2002).

55. F. Chiti, C. M. Dobson, *Annu Rev Biochem* **75**, 333 (2006).

56. B. Caughey, P. T. Lansbury, *Annu Rev Neurosci* **26**, 267 (2003).

57. A. Clark, M. R. Nilsson, *Diabetologia* **47**, 157 (Feb, 2004).

58. S. E. Kahn, S. Andrikopoulos, C. B. Verchere, *Diabetes* **48**, 241 (Feb, 1999).

59. H. Ohsawa *et al.*, *Diabetes Res Clin Pract* **15**, 17 (Jan, 1992).

60. A. Clark *et al.*, *Diabetologia* **33**, 285 (May, 1990).

61. A. L. Maloy, D. S. Longnecker, E. R. Greenberg, *Hum Pathol* **12**, 917 (Oct, 1981).

62. G. J. Cooper *et al.*, *Proc Natl Acad Sci U S A* **84**, 8628 (Dec, 1987).

63. P. Westermark *et al.*, *Proc Natl Acad Sci U S A* **84**, 3881 (Jun, 1987).

64. S. Enoki *et al.*, *Diabetes Res Clin Pract* **15**, 97 (Jan, 1992).

65. P. J. Wookey, T. A. Lutz, S. Andrikopoulos, *ScientificWorldJournal* **6**, 1642 (2006).

66. E. Hartter *et al.*, *Diabetologia* **34**, 52 (Jan, 1991).

67. A. Lorenzo, B. Razzaboni, G. C. Weir, B. A. Yankner, *Nature* **368**, 756 (Apr 21, 1994).

68. P. Westermark, Z. C. Li, G. T. Westermark, A. Leckstrom, D. F. Steiner, *FEBS Lett* **379**, 203 (Feb 5, 1996).

69. S. Janciauskiene, S. Eriksson, E. Carlemalm, B. Ahren, *Biochem Biophys Res Commun* **236**, 580 (Jul 30, 1997).

70. K. Yagui *et al.*, *Eur J Endocrinol* **132**, 487 (Apr, 1995).

71. J. W. Hoppener, B. Ahren, C. J. Lips, *N Engl J Med* **343**, 411 (Aug 10, 2000).

72. J. F. Paulsson, G. T. Westermark, *Diabetes* **54**, 2117 (Jul, 2005).

73. L. Marzban, G. Trigo-Gonzalez, C. B. Verchere, *Mol Endocrinol* **19**, 2154 (Aug, 2005).

74. M. M. Wilhelmus *et al.*, *Brain Res* **1089**, 67 (May 17, 2006).

75. M. M. Wilhelmus *et al.*, *Acta Neuropathol* **111**, 139 (Feb, 2006).

76. J. J. Yerbury *et al.*, *FASEB J* **21**, 2312 (Aug, 2007).

77. T. Oda *et al.*, *Exp Neurol* **136**, 22 (Nov, 1995).

78. R. G. Bennett, W. C. Duckworth, F. G. Hamel, *J Biol Chem* **275**, 36621 (Nov 24, 2000).

79. Y. Shen, A. Joachimiak, M. R. Rosner, W. J. Tang, *Nature* **443**, 870 (Oct 19, 2006).

80. R. L. Hull *et al.*, *Diabetes* **54**, 2235 (Jul, 2005).

81. L. A. Scrocchi *et al.*, *J Mol Biol* **318**, 697 (May 3, 2002).

82. Y. Porat, Y. Mazor, S. Efrat, E. Gazit, *Biochemistry* **43**, 14454 (Nov 16, 2004).

83. L. M. Yan, M. Tatarek-Nossol, A. Velkova, A. Kazantzis, A. Kapurniotu, *Proc Natl Acad Sci U S A* **103**, 2046 (Feb 14, 2006).

84. K. J. Potter *et al.*, *Biochim Biophys Acta* **1790**, 566 (Jun, 2009).

85. J. Kawano *et al.*, *Eur J Cell Biol* **79**, 208 (Mar, 2000).

86. C. Goldsbury *et al.*, *J Struct Biol* **130**, 352 (Jun, 2000).

87. E. Rhoades, J. Agarwal, A. Gafni, *Biochim Biophys Acta* **1476**, 230 (Feb 9, 2000).

88. R. L. Hull, G. T. Westermark, P. Westermark, S. E. Kahn, *J Clin Endocrinol Metab* **89**, 3629 (Aug, 2004).

89. W. K. Ward *et al.*, *Diabetologia* **30**, 698 (Sep, 1987).

90. N. Yoshioka, T. Kuzuya, A. Matsuda, M. Taniguchi, Y. Iwamoto, *Diabetologia* **31**, 355 (Jun, 1988).

91. M. F. Saad *et al.*, *J Clin Endocrinol Metab* **70**, 1247 (May, 1990).

92. S. E. Kahn, P. A. Halban, *Diabetes* **46**, 1725 (Nov, 1997).

93. E. T. Jaikaran, M. R. Nilsson, A. Clark, *Biochem J* **377**, 709 (Feb 1, 2004).

94. W. Cui *et al.*, *FEBS J* **276**, 3365 (Jun, 2009).

95. M. Nishi, T. Sanke, S. Nagamatsu, G. I. Bell, D. F. Steiner, *J Biol Chem* **265**, 4173 (Mar 15, 1990).

96. T. D. O'Brien, A. E. Butler, P. C. Roche, K. H. Johnson, P. C. Butler, *Diabetes* **43**, 329 (Feb, 1994).

97. R. J. Mayer, *Nat Rev Mol Cell Biol* **1**, 145 (Nov, 2000).

98. A. H. Schnell, I. Swenne, L. A. Borg, *Cell Tissue Res* **252**, 9 (Apr, 1988).

99. M. P. Mattson, Y. Goodman, *Brain Res* **676**, 219 (Apr 3, 1995).

100. R. M. Hafizur, M. Yano, T. Gotoh, M. Mori, K. Terada, *J Biochem* **135**, 193 (Feb, 2004).

101. A. Lorenzo, B. A. Yankner, *Proc Natl Acad Sci U S A* **91**, 12243 (Dec 6, 1994).

102. J. Janson *et al.*, *Proc Natl Acad Sci U S A* **93**, 7283 (Jul 9, 1996).

103. C. B. Verchere *et al.*, *Proc Natl Acad Sci U S A* **93**, 3492 (Apr 16, 1996).

104. S. Lenzen, J. Drinkgern, M. Tiedge, *Free Radic Biol Med* **20**, 463 (1996).

105. B. Xu, J. T. Moritz, P. N. Epstein, *Free Radic Biol Med* **27**, 830 (Oct, 1999).

106. S. A. Small, K. Duff, *Neuron* **60**, 534 (Nov 26, 2008).

107. J. Busciglio, A. Lorenzo, J. Yeh, B. A. Yankner, *Neuron* **14**, 879 (Apr, 1995).

108. M. Rapoport, H. N. Dawson, L. I. Binder, M. P. Vitek, A. Ferreira, *Proc Natl Acad Sci U S A* **99**, 6364 (Apr 30, 2002).

109. D. J. Selkoe, *Science* **298**, 789 (Oct 25, 2002).

110. D. Tampellini *et al.*, *J Neurosci* **29**, 9704 (Aug 5, 2009).

111. L. M. Billings, S. Oddo, K. N. Green, J. L. McGaugh, F. M. LaFerla, *Neuron* **45**, 675 (Mar 3, 2005).

112. D. J. Selkoe, *Science* **275**, 630 (Jan 31, 1997).

113. B. De Strooper, W. Annaert, *J Cell Sci* **113 (Pt 11)**, 1857 (Jun, 2000).

114. B. De Strooper, *Nature* **405**, 627 (Jun 8, 2000).

115. M. S. Wolfe, *Semin Cell Dev Biol* **20**, 219 (Apr, 2009).

116. M. S. Wolfe, *J Biol Chem* **284**, 13969 (May 22, 2009).

117. M. S. Wolfe, *Chem Rev* **109**, 1599 (Apr, 2009).

118. H. Li, M. S. Wolfe, D. J. Selkoe, *Structure* **17**, 326 (Mar 11, 2009).

119. P. Osenkowski *et al.*, *J Mol Biol* **385**, 642 (Jan 16, 2009).

120. C. A. Wilson, R. W. Doms, V. M. Lee, *J Neuropathol Exp Neurol* **58**, 787 (Aug, 1999).

121. G. K. Gouras, C. G. Almeida, R. H. Takahashi, *Neurobiol Aging* **26**, 1235 (Oct, 2005).

122. J. R. Cirrito *et al.*, *Neuron* **58**, 42 (Apr 10, 2008).

123. M. L. Giuffrida *et al.*, *J Neurosci* **29**, 10582 (Aug 26, 2009).

124. P. F. Chapman *et al.*, *Nat Neurosci* **2**, 271 (Mar, 1999).

125. D. Moechars *et al.*, *J Biol Chem* **274**, 6483 (Mar 5, 1999).

126. D. Pratico, K. Uryu, S. Leight, J. Q. Trojanoswki, V. M. Lee, *J Neurosci* **21**, 4183 (Jun 15, 2001).

127. A. Y. Hsia *et al.*, *Proc Natl Acad Sci U S A* **96**, 3228 (Mar 16, 1999).

128. D. M. Walsh, B. P. Tseng, R. E. Rydel, M. B. Podlisny, D. J. Selkoe, *Biochemistry* **39**, 10831 (Sep 5, 2000).

129. C. A. McLean *et al.*, *Ann Neurol* **46**, 860 (Dec, 1999).

130. S. Oddo, A. Caccamo, M. Kitazawa, B. P. Tseng, F. M. LaFerla, *Neurobiol Aging* **24**, 1063 (Dec, 2003).

131. S. Oddo *et al.*, *Neuron* **39**, 409 (Jul 31, 2003).

132. S. Gandy, *Neurobiol Aging* **23**, 1009 (Nov-Dec, 2002).

133. M. Citron, *Neurobiol Aging* **23**, 1017 (Nov-Dec, 2002).

134. H. L. Weiner, D. J. Selkoe, *Nature* **420**, 879 (Dec 19-26, 2002).

135. E. A. Eckman, C. B. Eckman, *Biochem Soc Trans* **33**, 1101 (Nov, 2005).

136. R. A. Marr *et al.*, *J Neurosci* **23**, 1992 (Mar 15, 2003).

137. R. A. Marr *et al.*, *J Mol Neurosci* **22**, 5 (2004).

138. N. Iwata *et al.*, *Science* **292**, 1550 (May 25, 2001).

139. W. Farris *et al.*, *Am J Pathol* **171**, 241 (Jul, 2007).

140. Q. Jiang *et al.*, *Neuron* **58**, 681 (Jun 12, 2008).

141. J. Kim, J. M. Basak, D. M. Holtzman, *Neuron* **63**, 287 (Aug 13, 2009).

142. M. Wendel, Y. Sommarin, T. Bergman, D. Heinegard, *J Biol Chem* **270**, 6125 (Mar 17, 1995).

143. K. N. Green, F. M. LaFerla, *Neuron* **59**, 190 (Jul 31, 2008).

144. P. Barre, D. Eliezer, *J Mol Biol* **362**, 312 (Sep 15, 2006).

145. Y. I. Yin *et al.*, *J Biol Chem* **282**, 23639 (Aug 10, 2007).

146. J. K. Teller *et al.*, *Nat Med* **2**, 93 (Jan, 1996).

147. C. J. Barrow, M. G. Zagorski, *Science* **253**, 179 (Jul 12, 1991).

148. D. Burdick *et al.*, *J Biol Chem* **267**, 546 (Jan 5, 1992).

149. T. Mosmann, *J Immunol Methods* **65**, 55 (Dec 16, 1983).

150. C. Haass, D. J. Selkoe, *Nat Rev Mol Cell Biol* **8**, 101 (Feb, 2007).

151. R. Kayed *et al.*, *Science* **300**, 486 (Apr 18, 2003).

152. H. W. Querfurth, F. M. LaFerla, *N Engl J Med* **362**, 329 (Jan 28).

153. E. D. Roberson *et al.*, *Science* **316**, 750 (May 4, 2007).

154. D. J. Selkoe, *Physiol Rev* **81**, 741 (Apr, 2001).

155. A. M. Isaacs, D. B. Senn, M. Yuan, J. P. Shine, B. A. Yankner, *J Biol Chem* **281**, 27916 (Sep 22, 2006).

156. L. Bojarski, J. Herms, J. Kuznicki, *Neurochem Int* **52**, 621 (Mar-Apr, 2008).

157. F. M. LaFerla, *Nat Rev Neurosci* **3**, 862 (Nov, 2002).

158. J. P. Greenfield *et al.*, *Proc Natl Acad Sci U S A* **96**, 742 (Jan 19, 1999).

159. M. M. Wilhelmus, R. M. de Waal, M. M. Verbeek, *Mol Neurobiol* **35**, 203 (Jun, 2007).

160. S. Ito, S. Ohtsuki, J. Kamiie, Y. Nezu, T. Terasaki, *J Neurochem* **103**, 2482 (Dec, 2007).

161. R. D. Bell, B. V. Zlokovic, *Acta Neuropathol* **118**, 103 (Jul, 2009).